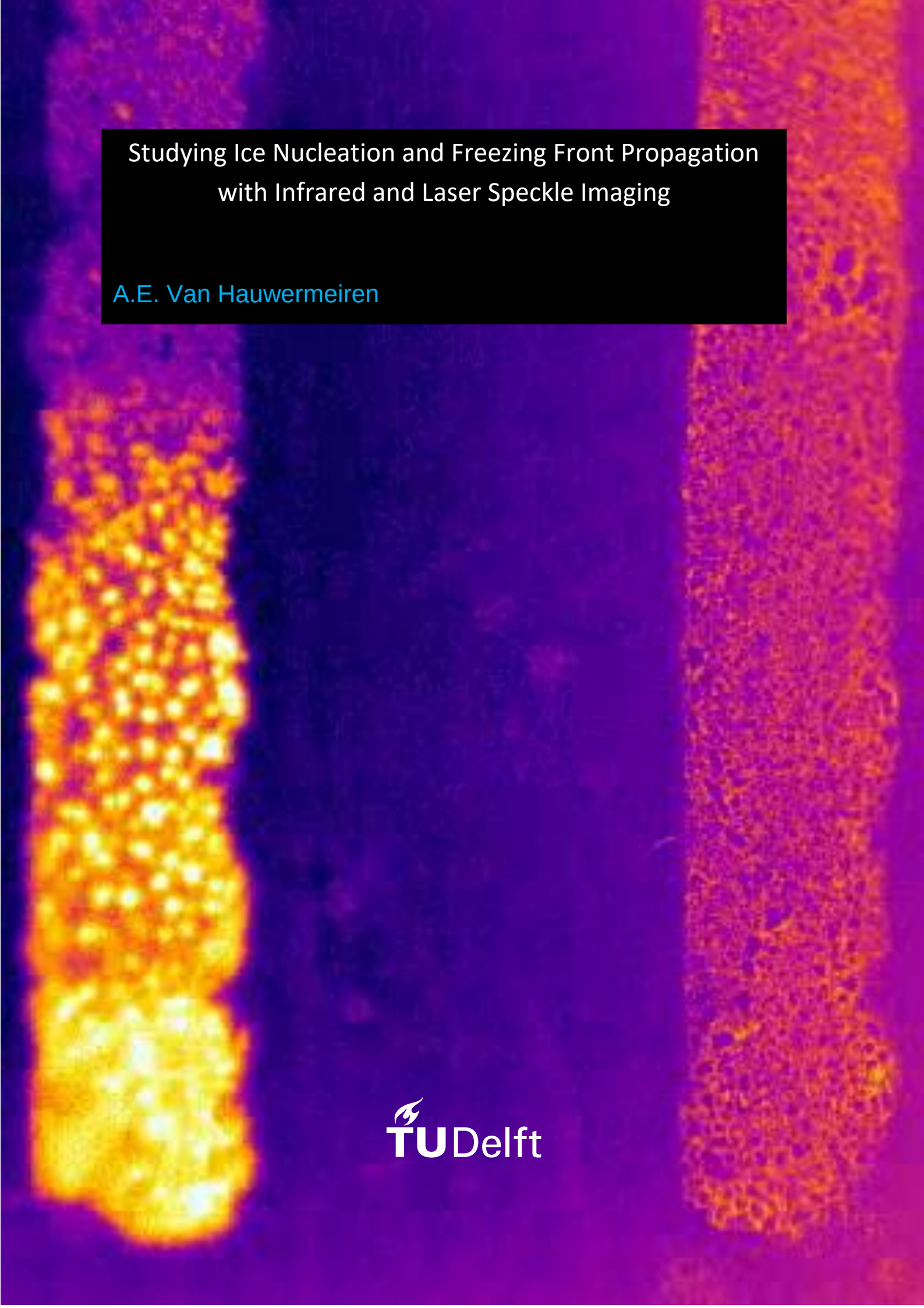

Studying Ice Nucleation and Freezing Front Propagation with Infrared and Laser Speckle Imaging

A.E. Van Hauwermeiren

TU Delft

Studying Ice Nucleation and Freezing Front Propagation with Infrared and Laser Speckle Imaging

by

A.E. Van Hauwermeiren

in partial fulfilment of the requirements for the degree of Master of Science in Aerospace Engineering
at the Delft University of Technology,
to be defended publicly on Wednesday May 23, 2018 at 13:00.

Student number:	4171616	
Project duration:	July 2017 – May 2018	
Project supervisor:	Associate professor dr. S. J. Garcia	
Faculty:	Aerospace Engineering	
Department:	Aerospace Structures and Materials	
Group:	Novel Aerospace Materials (NovAM)	
Thesis committee:	Prof. dr. ir. W. A. (Pim) Groen	Chairman | TU Delft (NovAM)
	Dr. S. J. (Santiago) Garcia Espallargas	Daily supervisor | TU Delft (NovAM)
	Ir. J. (Jos) Sinke	External member| TU Delft (SI&C)

TU Delft

Failure is an option here. If things are not failing, you are not innovating.

Elon Musk
Inc., July 14, 2015

Acknowledgements

This thesis concludes ten months of research into a new strategy to prevent clear ice from accumulating on aircraft surfaces at the department of Novel Aerospace Materials (NovAM) at the Faculty of Aerospace Engineering (AE) of the Delft University of Technology (TU Delft). Instead of preventing ice from forming, clear ice could be converted into the less dangerous rime ice. Without prior experience in the physical accretion of ice and the large thesis scope, the topic was extra challenging. Thanks to the weekly supervision and guidance of dr. Santiago Garcia Espallargas, a clear story and emerged. His help has been invaluable for finding new approaches and making results scientifically valid. Although my time was often split between the startup Qlayers and the research, he remained patient and motivating. He was and will remain a personal model for working hard and pushing for perfection.

I would like to thank prof. dr. ir. Pim Groen, dr. ir. Alexander in 't Veld, ir. Jos Sinke and dr. Elmar Bonaccurso for their useful feedback on the research approach. I would also like to thank Andrei Anisimov and dr. Roger Groves for the amazing opportunity to use the Sirius Laser Facility for drilling small holes in metal and Teflon. Thanks to dr. Marlies Mijemeisland, the LSI data gathering and analysis was possible within the available time. Furthermore, the results in this thesis would not have been achieved without the help of Johan Bijleveld, Frans Oostrum and the lab technicians of the Delft Aerospace Structures and Materials Laboratory (DASML), especially Berthil, Gertjan, Johan, Fred and Misja.

Next to the great equipment available at the Faculty of Aerospace Engineering, the most important thing that the TU Delft offered me was a place with smart, ambitious and fun people. I have to thank my fellow students at NovAM for being available in the good and frustrating times and the amazing NovAM secretary Shanta for a healthy dose of life coaching. I could not have finished this thesis without the unwavering support of ir. Ruben Geutjens and Josefien Groot, the co-founders of Qlayers. In the more demanding periods of this research, they pushed for the growth and survival of Qlayers. The vision of Qlayers is to finally start applying all the wonderful research on functional coatings to large industrial surfaces, like aircraft and wind turbines. I can't express how excited this company makes me for the future of functional coatings and will join them with all my heart in making the world more beautiful and engaged with the magic of materials science.

Lastly, I would like to thank my family and friends that were always available for professional and personal advice. My roommates and girlfriend will be royally compensated for the lack in attention they received over the past few months. Due to their personal and financial support, my parents allowed me to study abroad for seven years and close off with this thesis.

Abstract

Clear ice accretion is considered to be a critically limiting factor in the operations of aircraft. Freezing rain can cause the accretion of clear ice on aircraft wings, increasing the aerodynamic drag up to 80% and decreasing the lift force by up to 50% during take-off, ascent, approach and landing. In this thesis, Infrared imaging (IRI) and Laser Speckle Imaging (LSI) are employed to visualize several ice-related phenomena. IRI is used for the detection of nucleation events on the surface. As a novel development, IRI and LSI are combined to observed a freezing front that propagates over the whole surface. This freezing front appears to transmit nucleation through a molecular liquid layer of water (MLL) and its velocity and intensity can be followed well with IRI. Using IRI, high nucleation temperatures and short nucleation time delays are observed in cooled droplets impacting on frozen surfaces. The fast nucleation of these droplets at high temperatures links the freezing of the MLL to the formation of clear ice, which also features high nucleation temperatures.

For the design of strategies that prevent the freezing of surfaces, several surface, material and environmental properties that govern heterogeneous ice nucleation of the MLL are systematically studied. Firstly, the surface temperature greatly affects the nucleation, inducing a critical nucleation temperature between $-11°C > T_{surf} > -14°C$ and a temperature invariant region between $-14°C > T_{surf} > 27°C$. Secondly, surface vibration shows no significant effect between $5\ Hz$ and $5\ MHz$ and is not explored further. Thirdly, materials with a high contact angle increase the nucleation time delay significantly, while leaving the nucleation temperature unaffected. Fourthly, higher conductivity appears to reduce nucleation temperatures and nucleation time delays. Fifthly, lower values for the relative humidity (RH) clearly depress the critical nucleation temperature. The last parameter, sessile water droplet size, showed no significant effect on the nucleation time delay or nucleation temperature. Although nucleation in the MLL clearly can't be prevented, its transmission over the surface can be slowed down using some of the same surface, material and environmental properties. Firstly, the front velocity seems independent of surface temperature below the critical nucleation temperature of about $T_{surf} = -12°C$. Secondly, higher contact angles appear to switch the freezing front propagation mechanism from MLL freezing ($G^* > 1\ mm/s$) to the much slower dendrite growth ($G^* < 1\ mm/s$). Thirdly, at relative humidities below 40%, nucleation can't be transmitted over the surface due to a non-continuous MLL. The intensity of the MLL freezing front under IRI is also observed to depend on the amount of water condensation on the surface.

As the contact angle can be used to control the MLL freezing front velocity, patterns of hydrophilic and hydrophobic material might be able to limit the amount of frozen area available for clear ice formation. $200\ \mu m$ olive oil-filled holes in an aluminum surface inhibit the freezing front propagation by a local increase in contact angle. Locally plasma-treated PVDF thin films, as well as a permanent marker ink pattern on Teflon confirmed this ability of hydrophilic-hydrophobic boundaries to switch from a freezing MLL to the much slower dendrite freezing front propagation mechanism. Locally variable contact angles on many different scales should therefore be considered for the design of smooth, durably and non-toxic anti-icing coatings for application on aircraft.

Chapter 1 introduces the state-of-the-art in anti-icing research and defines the thesis scope and research questions. Chapter 2 introduces IRI and the novel combination of IRI and LSI to detect ice nucleation and follow a freezing front propagation through the MLL. Using the IRI observation method, chapter 3 links clear ice formation of impacting droplets to the frozen/unfrozen state of the surface. Chapter 4 explores the effect of surface, material and environmental properties on MLL nucleation and freezing front propagation. In chapter 5, the insight gained in chapters 1-4 is used to explore flat, non-toxic and durable anti-icing surface architectures. Conclusions and recommendations for future research are given in chapter 6.

Table of contents

List of figures

List of tables

List of symbols and abbreviations

Abbreviation	Unit	Full form	Explanation
d_{drop}	mm	Droplet diameter	Diameter of impacting droplet
G	mm^2/s	Area growth rate	Rate of expansion of the frozen area
$G^*_{frontline}$	mm/s	Active frontline velocity	Area growth rate, divided by the length of the active frontline
$G^*_{perimeter}$	mm/s	Average front velocity	Area growth rate, divided by the perimeter of the visible frozen area
MLL		Molecular liquid layer	Liquid layer of water on surfaces, typically 2 – 50 Å in thickness
RH	$\%$	Relative humidity	Relative humidity of the climate chamber controlled or lab environment
T_{drop}	$°C$	Droplet temperature	Temperature of droplet impacting on a surface
T_{env}	$°C$	Environmental	Temperature of the climate chamber controlled or lab environment
T_{surf}	$°C$	Surface temperature	Temperature of the tested surface
t_n	s	Nucleation time delay	Time between reaching -10°C and the nucleation event
T_n	$°C$	Nucleation temperature	Surface temperature at the moment of nucleation
V_{drop}	V	Droplet voltage	Voltage applied to the 20x20 mm to cool down impacting droplets

1. Introduction

1.1 The relevancy of icing research and thesis scope

Everyone interacts with ice in his or her daily life, although more frequently in cold seasons. A scientific mind will notice that different situations feature ice with different properties. As an example, some winter days it can be very hard to remove ice from the windshield of one's car requiring forceful mechanical removal or extensive windshield heating, while on other cold days, the layer of ice can be easily removed by hand. There is more to this than subjective experience, because there exist many different forms of ice, each forming in different circumstances. An environment with different relative humidity, exterior temperature, atmospheric pressure and source of water (rain, mist, water vapor) will result in ice with very different properties, like density, crystal structure, color, opaqueness, adhesion strength, cohesion strength, porosity, growth rate and purity. Although water is abundantly present in our daily lives, the exact formation of ice and the origin of its mechanical, chemical and physical properties is not fully understood yet. This is mainly caused by the difficulty in observation of realistic icing scenario's. The lack of understanding is also in part due to some of the exceptional properties of water, like for example a density maximum at 4°C, causing the floating of ice on water, the freezing of ice from the top and negative volume of melting. [1]

1.1.1 Identifying the governing parameters of icing on aircraft operations

Ice formation (or 'icing') presents a safety and economic threat to operations in many different sectors, such as aeronautics, wind turbines, commercial shipping, telecommunications, transmission lines, highway and building construction, oil and gas rigs, heat exchangers and even rocketry. [2,3]. As an example, the ability of Canadian wind turbines to generate power is reduced significantly by icing. Apart from the reduction of lift force by the ice, due to the change in airfoil shape, large pieces of ice that grew on the turbine blades can fall off at high lateral speeds and cause harm to people or damage to the surrounding infrastructure. To enable wind turbines to operate in icing conditions, helicopters have to be used to remove the ice. The cost of de-icing by helicopter is too high for scalable application, which makes the implementation of wind power generators much less attractive for land owners, private and public energy companies in Canada.[4]

The most relevant forms of icing on aircraft are clear ice, rime ice, beak ice, mixed ice, frost, runback ice, carburetor ice and propeller freezing. Of these forms of icing, clear ice and carburetor ice are the most dangerous, but carburetor ice is only relevant for propeller aircraft. The other dangerous form of ice, is clear ice (or 'glaze ice'). It is formed when large supercooled water droplets (or "freezing rain") impact the wings, antennas or fuselage. Due to their size, the droplets don't freeze completely immediately, but smear out and freeze at a slower rate. [5], [4]

Icing causes a wide variety of problems on aircraft at different points in the mission profile. Some of the most common problems for jet engine powered aircraft are instrument icing, loss of lift on wing or tail surfaces, increased drag and weight and the obstruction of view due to windshield icing. [6]. According to Steuernagle et al.[7], for large aircraft, the additional weight due to icing is negligible, compared to the loss in lift. Ice with a structure similar to sandpaper will already reduce the lift by 30 % and increase the drag by 40%. Ice with a topography on larger scales can increase the drag up to 80%. In this severe scenario, de-icing has to be activated as quickly as possible, but even then, a 30% additional drag increase will remain because of areas where no de-icing devices are installed, like antennas, flaps, fuselage, windshield wipers, struts and landing gear. [7] One scenario that involves a complete loss of lift, the aircraft can be forced into an attitude with an angle of attack that exceeds the stall angle of attack. Firstly, the angle of attack has to

be increased to maintain altitude due to the loss in lift at normal angles of attack. Although during the onset of icing on aircraft wings, only the frontal surfaces of the airplane are affected, the bottom of the wing is now susceptible to icing as well, further increasing the drag. Secondly, the ice on the wing has increased the stall speed and decreased the stall angle of attack. If the set angle of attack reaches the stall angle of attack, catastrophic failure might occur, with little altitude and engine power left to execute emergency procedures. In another scenario involving loss of lift, the loss of lift is due to a tail stall. The tail of an aircraft usually ices quicker than its wings, as well as being harder to observe from the cockpit. If a tail stall is induced by icing, longitudinal stability can suddenly disappear and recovery will be impossible at low altitudes.

Figure 1.1. illustrates a typical mission profile of a passenger jet aircraft, with the blue dashed arrows indicating the parts where enough humidity is present in liquid form for dangerous icing to occur. These humid regions at low altitude are unavoidable at the beginning and end of every flight of any aircraft mission profile. After take-off, the aircraft will climb to cruise altitude. The temperature and pressure continuously decrease, while the humidity can stay high enough for both rime and clear ice to grow on the wing. During this MSc thesis, an assistant professor and professional pilot at the TU Delft was interviewed to gain firsthand insight into the flight mission profile and experiences with ice formation (see appendix A). During this interview was mentioned that pilots use the rule of thumb that a significant risk of icing can be expected during climb, if the temperature on ground level is below 10°C and if there is visible moisture. It was confirmed by literature, that for icing to occur on an aircraft, it has to fly through visible water and the surface has to be cooled below 0°C. The visible moisture can be in the form of rain droplets (diameter > 40um) or cloud droplets (diameter < 40um).[8], [9].

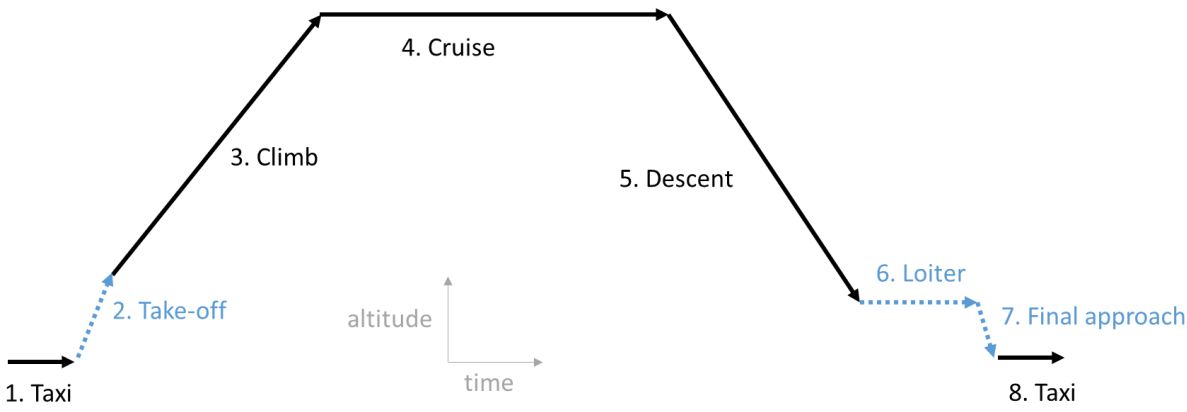

Figure 1.1: Mission profile of a typical commercial aircraft. In some Parts of the mission profile, the aircraft has to fly at low altitudes in regions with high relative humidity. Especially during loiter and final approach, where the aircraft has usually descended from an environment with a temperature of -56°C (above the tropopauze), icing can be expected to occur.

Inflight icing at low altitudes is the worst hazard when considering safety, but also from an economic viewpoint, major risk is involved with icing between flights. During taxiing or parking of the aircraft, rime and clear ice can grow on the wings. This 'ground ice' has to be removed before starting the pre-flight checks, as it is forbidden to take off with even small amounts of ice on the aircraft. For small aircraft, the ice can be removed mechanically, but operators of large aircraft need to spray de-icing fluid over the wing and fuselage. The de-icing process costs several thousands of dollars and usually renders commercial flights profitless. Even after de-icing is successful, the ice can grow back during taxiing, which can prevent take-off.

In the US from 1990 to 2000, 40% of the ice-related incidents were due to in-flight ice growth on the aircraft, 8% by ground ice and 52% by 'induction icing' of carburetors and engine air intakes [7], [10]. From the

interview of a professional aircraft pilot, documented in Appendix A, and instruction documentation for pilots available online, it was concluded that clear ice is the most dangerous form of ice that is affecting current commercial passenger aircraft. As both clear ice and rime ice are formed by impacting droplets, but clear ice presents a much more significant threat to the safe operation of aircraft than rime ice, the commonalities and difference between them are of interest. They are reviewed in Table 1.1.

	Clear ice ("glaze ice" / "freezing rain")	**Rime ice**
Environmental temperature	$0°C > T_{env} > -6°C$ [4]	$-10°C > T_{env} > -40°C$, but also below -6°C [4]
Relative humidity	High liquid water content (LWC). Only forms with visible humidity, like clouds or rain. [9]	Low LWC. Only forms with visible humidity, like clouds or rain. [9]
Droplet impact velocity	High droplet impact velocity [5]	Low droplet impact velocity [5]
Droplet size	Impacting supercooled droplets with diameters of $40 - 5000\ \mu m$ [5]	Impacting supercooled droplets of diameter $5 - 40\ \mu m$
Droplet temperature	$5°C > T_{drop} > -15°C$ [5]	$T_{drop} > -35°C$ [5]
Crystal	High density ice	Low density ice
Appearance	Smooth, lumpy, clear	White, feathery
Growth rate	Fast	Slow
Adhesion strength	High adhesion strength	Low adhesion strength

Table 1.1 Difference between clear and rime ice, according to online instructions for pilots [5] and the interview in appendix A

In the mission profile of a commercial passenger aircraft, the impacting supercooled droplets that form either rime or clear ice would come in the form of cloud or rain droplets. Table 1.1 seems to indicate that larger rain droplets ($d_{drop} > 400\ \mu m$) cause clear ice, as illustrated in Figure 1.2a. Rime ice, shown in Figure 1.2b, could be formed by smaller impacting cloud droplets ($d_{drop} < 40\ \mu m$). Small rain droplets ($40\ \mu m < d_{drop} < 400\ \mu m$) could be the origin of mixed ice.

The origin of droplets that cause rime or clear ice has been studied extensively. Cloud droplets form by condensation around hydrophilic nuclei in the air. Due to their small size in the tens of microns range, these droplets have a temperature of around $-20°C$. The droplet temperature can go down to $-40°C$ for micron size droplets of very pure water, at which point homogeneous nucleation does not allow further cooling. Rime ice is formed when these small, highly subcooled droplets impact a surface. When some of these small droplets in a cloud freeze, they become seed crystals. The water from all surrounding droplets rapidly evaporates and sublimates on the seed crystals, forming "snow". When snowflakes descend through lower and warmer layers of the atmosphere, they melt and coalesce into large droplets with diameters greater than $400\ \mu m$. If these droplets pass through an colder layer of air during their downwards fall ('inversion layer'), they can cool down below 0°C and create "freezing rain". If the droplets coalesce to smaller droplets of $50 - 400\ \mu m$, it is characterized as "freezing drizzle". [5]

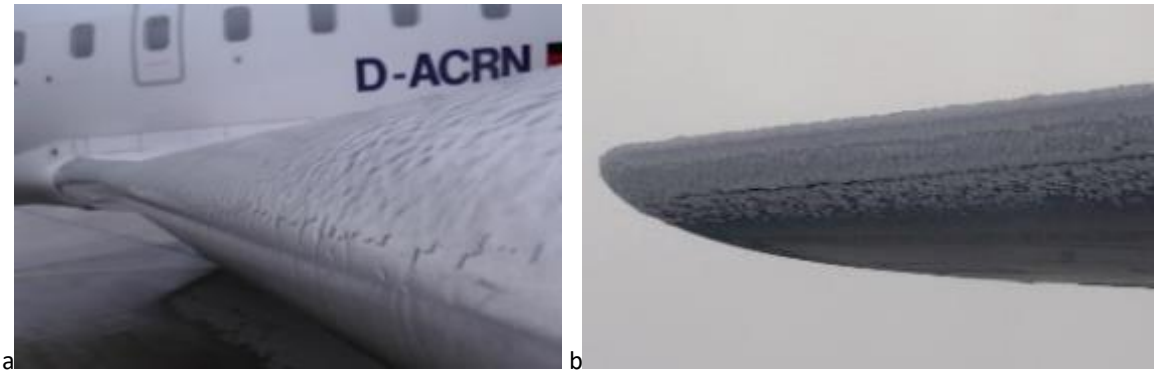

Figure 1.2 Illustration of (a) fast-growing, transparent and strongly adhered clear ice, originating from freezing rain and (b) slow-growing, feathery white, easily removable rime ice, originating from cloud droplets.

Due to the previously mentioned concerns with safety, no airplane is allowed to take off with icing. However, during flight there might not be the possibility of avoiding icing. As accurate predictive modelling techniques remain to be developed, if at all feasible, aircraft authorities have made the installation of in-flight anti-icing or de-icing equipment mandatory.

The most common de-icing method for small aircraft, is mechanical breaking of the ice with an inflatable rubber boot on the leading edge of the wing or propeller. Although rubber boots are very effective, they can't be applied on fast aircraft if the lift-producing surface is distorted too much. Another reason why rubber boots are not used on modern commercial passenger aircraft is the fast wear following from intensive operation. Also, they can only be operated above a critical temperature, below which the rubber will fracture. One of the dangers that is often taught to pilots, although reported to be untrue, is the 'bridging effect'. In this case, the ice layer would expand with the rubber boot and remain in this new shape when the boot is deflated, instead of flying off. [7] More appropriate methods to mechanically brake off ice, are the electro-expulsive separation system (EESS) and electro-impulsive system (EISS). In this case, electromagnetic coils introduce vibrations by rapidly pulsed current. Unfortunately, these systems can't be retrofitted to existing aircraft, as it might affect the structural integrity of the aircraft. [11, 12, 13].

The most reliable and widely applied de-icing and anti-icing method on large aircraft, is heating of the leading edge. This can melt attached ice or prevent freezing completely. The heating can be done by blowing bleed air from the jet engine into a piping systems that is installed in the wing. Other, less common heating methods are resistive heating, infrared lamps, microwave irradiation, ultrasonic waves or high power pulsed electrical signals through a conductive coating. [14,11]. One of the issues arising with heating the leading edge of a wing, is molten ice freezing downstream of the heater. This phenomenon is called 'runback ice' and is usually avoided by heating to higher temperatures to vaporize the ice, instead of only melting. [7. As could be expected, keeping an aircraft wing at temperatures that can quickly vaporize water while cold air rushing over the wing at high speeds, requires a lot of energy to operate. The infrastructure required for such an intensive heating process is bulky and heavy, which is always to be avoided in aeronautic design. Although innovation is slow, some alternatives are being investigated, such as a rapidly heating graphite foil, used for retrofitting on existing aircraft. [15]

Another common anti-icing method, used in both small and large aircraft, is the dispersion of freezing-point depressants. These liquids dissolve in the interfacial water layer on the aircraft wings and lower the freeze point of the layer. They can be dispersed through a perforated titanium plate on the leading edge, tail, propeller or windshield. [10] According to the interview of a professional pilot (appendix A), these de-icing systems have to be switched on in the cockpit and will operate for about 2.5, 1.5 and 0.5 hours for normal, high and maximum settings, respectively. Although being very effective, this method only gives the pilot a relatively short time to adjust the flight path and get out of the icing environment. Moreover, the fast

growth and transparency of clear ice can lead to dangerous situations in which the pilots do not notice ice on the wing until it is impacting the flight performance significantly. At this point in time the freezing-point depressant will be ineffective. Another disadvantage of using de-icing or anti-icing liquids, is that they are usually glycol-based. Glycols have been shown to have a detrimental effect on natural environments, by depleting oxygen in streams and lakes around airports. Salt-based freezing-point depressants are also used, although they corrode metal surfaces and disrupt the osmotic balance in the environment. Currently, research is being done to develop natural antifreeze proteins, which would be less toxic. [11], [16]

1.1.2 Current knowledge on heterogeneous ice nucleation

The three most well-known forms of ice are clear ice, rime ice and frost. The classification of different kinds of ice is hard, because the environmental conditions describing the ice formation and the resulting ice properties vary continuously over a large range. 'Mixed ice', for example, is the ambiguous name for a mix between clear and rime ice, not only in the aircraft pilots jargon, but also in scientific publications. It illustrates how the definition of a new kind of ice covers up the inability to explain its origin. One explanation for 'mixed ice' could for example be that clear ice and rime ice can coexist and their mechanisms are unrelated. Another point of view, could be that both forms of icing are intimately connected and only a few governing parameters differentiate between the two. In this case, every environmental or surface property that can determine whether clear ice or rime ice is formed, also has a transition zone between the two distinctive cases. Until these governing parameters are determined, the research community will find it hard to focus on the right circumstances to prevent specific types of icing.

When water is cooled down below 0°C, it becomes more energetically favorable for the water molecules to arrange in a hexagonal grid structure. Small crystals of a few water molecules, or 'ice nuclei', that float freely in the liquid are unstable and will dissolve as quickly as they were formed. Only ice nuclei with a minimal number of water molecules will be stable. As an example, at a temperature of -5°C, 50.000 water molecules have to arrange coincidentally into a nucleus. At -20°C, only a few hundred water molecules can already form a stable nucleus and at -40°C, the 'homogeneous nucleation temperature', only a few water molecules are sufficient. [14] This makes the ice nucleation of water in principle a stochastic process. [17] Homogeneous nucleation rarely occurs in reality. Solid impurities or any other solid-liquid interfaces will allow stable nanocrystals to grow on their surface at subzero temperatures above the homogeneous nucleation temperature. Continuous formation and breaking of hydrogen bonds between surface and water molecules, as well as between water molecules, also dominates the heterogeneous ice nucleation process. Recent Monte Carlo simulations of the heterogeneous ice nucleation process by Li et al., show that it takes about 175 nanoseconds for a stable molecular layer of ice to form on a surface at a temperature of -43°C. [18] For the temperatures used in this thesis, between -30°C and -10°C, it takes several orders of magnitude longer, in the regime of milliseconds to minutes.

Many surface and material properties are expected to influence heterogeneous nucleation of ice. Li et al. [18] showed in their Monte Carlo simulations how the surface energy of the substrate and its temperature influence nucleation. On the one hand, the hydrogen bond network has to be stable enough to give new layers of water molecules the time to attach to other water molecules or to the solid-water interface. This is why ice only forms below 0°C. It also prevents crystal growth when the bonding strength between the solid surface molecules and the water molecules is too low. On the other hand, the crystal shouldn't be too stable. This allows for the hydrogen bonds to continuously break and be rearranged, enabling the crystal to find the desired hexagonal structure. For this reason, a high bonding strength between water and surface molecules can prevent freezing, as the strong bonds fix the water molecules on the surface in an imperfect crystal. Analogously, the temperature of water can be too low for freezing to occur. At too low temperatures

a non-hexagonal hydrogen bond network will not be able to break up and be rearranged into a crystal that can rapidly convert bulk liquid into ice. [18] Apart from surface energy and surface temperature, the ability of interfacial water to form a stable hexagonal crystal has been shown by Reinhardt et al.[19] to depend significantly on the crystal structure of the surface, using Monte Carlo Simulations. If the arrangement of the surface molecules does not deviate more than 10 – 15% of the ice crystal structure, heterogeneous nucleation occurs easily. The crystal orientation of the surface molecules can determine whether ice nucleation occurs or not. When heterogeneous nucleation is prohibited by the crystal structure, nucleation can still occur. In the Monte Carlo simulations it seemed like an ice-like bilayer of water molecules was formed, serving as a semi-solid on which heterogeneous nucleation could occur. This bilayer of water appears also on silver iodide particles, and has been suggested as the reason why silver iodide particles can nucleate clouds. [19]

The heterogeneous nucleation on the interface between subcooled water and a solid surface has been studied in detail. The growth of a crystal through bulk water behaves like a front and propagates at a certain velocity. Pasieka et al. used infrared imaging to observe the freezing front propagation through a layer of water of $20\,mm$ thickness in a cylindrical container of diameter $200\,mm$. The bulk front velocities of $100 - 250\,mm/s$ at nucleation temperatures between $-1.5°C$ and $-7°C$ showed that the bulk front velocity strongly depends on temperature. Using a modified Noyes and Whitney growth mechanism with the temperature as driving force, they confirmed that $V = A\left(T_{eq} - T_{system}\right)^{B}$, with front velocity V, equilibrium temperature T_{eq}, subcooling temperature T_{system} and empirical constants A and B, found to be 54.3 and 0.863. The results obtained by Pasieka et al. are higher higher than the linear relationship between subcooling temperature and bulk freezing front velocity as observed by Schremb et al. with $50 - 150\,mm/s$ at nucleation temperatures between $-10°C$ and $-20°C$. [20] In the aircraft mission profile, the bulk freezing water comes in the form of small droplets. For a droplet that could be expected to create rime ice ($5\,\mu m < d_{drop} < 40\,\mu m$), the time it would take for the droplet to fully freeze after nucleation between $-1.5°C$ and $-7°C$, is between $20\,\mu s$ and $400\,\mu s$. If the model proposed by Pasieka et al. is extrapolated to the minimum rime ice droplet temperature of $-35°C$, beyond the validated lower bound of $-7°C$, the freezing times are expected to be around $5\,\mu s$. For a droplet that could produce clear ice ($d_{drop} = 40 - 5000\,\mu m$), the time it would take for full droplet freezing, would between and $160\,\mu s$ and $50\,ms$, after nucleation between $-1.5°C$ and $-7°C$. As nucleation also occurs in impacting droplets up until $T_{drop} = 5°C$, the freezing time can be expected to be even larger in specific cases of clear icing [21].

When studying the freezing of individual droplets on surfaces, the molecular layer of water that covers most materials might become relevant. This molecular liquid layer (MLL) has been observed on Mica by Hu et al. in 1995 by atomic force microscopy (AFM). They identified three phases in growth of the MLL at different relative humidities. Below $RH = 25\%$, clusters of about 1 nm grow. At higher relative humidities, large 2D islands of water grow on the surface, forming a continuous MLL at about $RH = 40\%$. They also observed these islands to take a hexagonal shape of the crystallographic orientation of the Mica substrate [22]. James et al. confirmed the presence of the MLL on many hydrophilic and hydrophobic materials. The thickness of the MLL was shown to depend on time and the surface temperature. According to their research, the contact angle of the material is not affected by the presence or thickness of the MLL. [23] No literature was found that has linked the presence, thickness and continuity of the MLL to freezing mechanisms or the icing phenomena in section 1.1.1. If a freezing front would be able to travel through this layer of water covering most surfaces, many aspects of ice formation might be affected. Firstly, the MLL would be expected to transmit nucleation between droplets. Secondly, if this transmission of the crystal occurs, it could be expected that the MLL serves as the de facto interface on which heterogeneous nucleation takes place, as it contains a much larger portion of the solid-water interface than impacting or sessile droplets. Thirdly, the presence of a frozen MLL would be expected to affect the freezing behavior of impacting subcooled droplets.

A recent study of the effect of droplet diameter on the contact angle of small water droplets might give insight into the origin of the difference clear and rime ice. Park et al. used cryo-SEM and FIB cutting to show that droplets with $d_{drop} > 40\ \mu m$ could feature contact angles between 90° and 100°, whereas the contact angles for droplets with $10\ \mu m < d_{drop} < 40\ \mu m$ went up to 120° and droplets with $d_{drop} < 1\ \mu m$ up to 165°. [24] Higher contact angles are generally connected to a reduction in ice nucleation probability, due to limited interfacial area and heat conduction between the subcooled impacting droplet and the cold surface. [16,3,25,26]. Higher contact angles have also clearly been linked to easier harmonic bouncing and thus reduction of droplet-surface contact time.[3], [16], [27] The increased contact angle of a material has also been linked to lower ice adhesion. [28], [29] Therefore, the droplet size range for rime ice with $5\ \mu m < d_{drop} < 40\ \mu m$ might cause reduced nucleation probability and higher nucleation delays, as well as lower ice adhesion strength, as compared to the larger clear ice droplets, purely because of their size-induced increased contact angle.

Most recent research results on the behavior of ice do not connect the effect of surface, material or environmental properties on nucleation to actual icing in industrial applications. Conversely, the applied research on ice accretion for aeronautic applications is performed to quantify ice accretion rate and shapes or to optimize de-icing methods, not with the goal of understanding what mechanism causes the type of icing that is observed.

1.1.3 Current state-of-the-art in passive anti-icing and de-icing research

Considering that icing is inherently an interfacial problem between impacting droplets and the topcoat of the aircraft, the path to prevent icing should start at understanding the freezing process on the interface. Although the experimental foundation for icing research was laid in the 1940s and 1950s, no anti-icing coating has been found that is durable, smooth, non-toxic, light, producible, cheap and failsafe, which indicates a lack of understanding of the freezing process. [5], [30] For this reason, old but reliable 'bulk solutions' are still applied, trading off energy consumption, volume, weight and cost in favor of safety and reliability. A solution that acts only on the interface between the droplet and the aircraft topcoat would inherently have a low weight, complexity and required material, because a surface is two-dimensional. The system would also be easily accessible for maintenance. These arguments speak strongly in favor of the pursuit of anti-icing systems using only surface and material properties. A better understanding of the impact of environmental conditions and icing classification would also allow airliners and authorities to improve safety during flight operations. Although is impractical to control environmental conditions, like relative humidity, droplet size and temperature, one could imagine approach and take-off procedures being adjusted or safety and economic risk being more accurately assessed.

In the 1940s and 1950s, the first experimental and analytical results were obtained. The models that could be constructed at the time were limited by the lack of computational power. In the 1970s, the research started to focus more on relevant geometries and models that matched the industrial demand for solutions, like helicopter blades and airfoils. Until the 1990s, the only relevant research was performed in the US, UK and France, but with increasing demand for safe transportation and reliable and cheap energy, research started in Italy, Spain, Germany and Canada. [5] Since 2002, there has been a renewed interest in icing, with fifteenfold increase of the number of papers published on the subject, according to Scopus, as illustrated in Appendix B.

The field of ice-phobicity research uses roughly three strategies to prevent or reduce icing, namely repelling droplets, preventing their nucleation or preventing strong ice adhesion. [29,31] The first strategy is to reduce the contact time between impacting water droplets and the surface and repel the droplets before ice nucleation occurs. Existing flexible coatings are an example of this approach. The droplets will be repelled from the surface before they have the chance to freeze. [11] Hairs seem to be effective in repelling

impacting droplets as well. The surprising ice-phobicity of penguin feathers, has been related to repulsion of impacting droplets and good insulation. [32], [33] Limited contact area has proven to fully prevent icing when contact time is short, by preventing ice nucleation. The high insulation by penguin feathers will decrease the ice nucleation probability even more. [16] Inspired by rain-repelling butterfly wings, Bird et al. found that the contact time of a large droplet and a superhydrophobic silicon surface can be reduced significantly when the droplet impacts on a riblet with a height of about $150\ \mu m$ and a width of $500\ \mu m$. The contact time was reduced below the theoretical limit of a harmonic. [34]

The second strategy is to delay the nucleation of impacting droplets, when they can't be repelled fast enough with the first strategy. Conductivity plays a large role in the nucleation delay. [35] Wang et. al show that feathers of penguins have six topographies that capture air to improve insulation. This property makes penguins feather a perfect example of anti-icing coating. [36]. A second method that has often been suggested to increase nucleation time delay, is the use of superhydrophobic surfaces. [3], [16] It remains unclear if they are in fact beneficial or detrimental for anti-icing. In 2010, Mishchenko et al. observed an increase in nucleation time delay, reproduced by Alizadeh et al. , no difference in nucleation time delay was observed by Heydari et al., Jung et al. and Yin et al. [3], [16], [17], [37], [38] The groups observing higher nucleation time delays worked in dry environments, with relative humidities of between 2% and 5%, whereas the groups that observed no difference, worked in relative humidities of between 40% and 80%. [29], [39], [40] Humidity is clearly connected to the effectiveness of superhydrophobic surfaces in delaying the nucleation time. However, no physical explanation has been given in literature to connect relative humidities below 40% to higher nucleation time delays. The research of Cao et al. gives a hint at the effect of humidity on ice nucleation. They observed a sharp decrease in ice nucleation probability, corresponding to a higher nucleation time delay, on a surface with nanoroughness under $100\ nm$. In their experiments a volume of 500 ml water cooled to $T_{drop} = -20$°C was poured over a surface at $T_{surf} = -20$°C, with $T_{env} = 20$°C and $RH = 30\%$. They consider these values for T_{env} and RH as uncontrolled 'normal laboratory ambient conditions', indicating that they might have a large error margin. The ratio of experiments with nucleation to the total number of experiments was considered to represent the icing probability. [41] If the MLL does indeed have the effect on freezing as introduced in section 1.1.2, the observed reduction in icing probability could be explained by a lack of condensation in pores smaller than the mean free path of water vapor, which is about 68 nm under lab atmosphere. As an alternative explanation, the effect could also be due to confined freezing in nanopores. Monodisperse cylindrical nanopores have been made recently with a tunable diameter from 2 to $10\ nm$ in MCM-41 and SBA-15 nanoporous silica. This yielded homogeneous nucleation temperatures inside the nanopores of -78°C and melting at $-50°C$. [42]

Due to the limited success of the first two strategies, a large part of anti-icing research in the past decade has focused on a third approach, namely the reduction of the adhesion force of the ice after it has formed on the surface. [16], [18], [28], [29], [30], [43], [44] In spite of the great interest in anti-icing research, no academic research is explicitly focused on the prevention of clear ice, reproducing the exact conditions at which icing occurs on aircraft. The third strategy, namely reducing ice adhesion, has developed many interesting concepts in recent years. However, the connection to their interaction with specific kinds of ice is still unclear, as the concepts are far from application. Ice adhesion strengths to standard most surfaces are around $1\ MPa$, whereas non-textured fluorinate surfaces have ice adhesion strengths of about $200\ kPa$. Below $60\ kPa$, the ice adhesion strength can be considered 'low'. Below $10\ kPa$, an ice cube that is adhered to a surface can fall off under its own weight or airflow, and ice adhesion strength is considered to be 'super low'. The ice adhesion strength reduces with increasing receding contact angle, down to about $160\ kPa$ at $\theta_R = 120°$. Unfortunately the trend of reducing the ice adhesion strength with increasing contact angle can't be continued towards desired low adhesion strengths with smooth coatings. [29]

The first and most widely suggested method to reduce ice adhesion strength, is the use of superhydrophobic surfaces. There is disagreement between publications, similar to the discussions on their ability to reduce

the ice nucleation time delay. [28] In 2010 Mishchenko et al. published a significant decrease in ice adhesion strength on superhydrophobic surfaces. [16] However, Bharatadisan et al. published higher ice adhesion strengths on similar surfaces. [28] Quite consistently, publications that report ice adhesion strength increase, work at high relative humidities between 40% and 80%, whereas the decrease in ice adhesion strength is reported for relative humidities between 2% and 5%. Unlike the ambiguous effect of superhydrophobic surfaces on the nucleation delay, the reported discrepancies in ice adhesion strength has a physical explanation in literature as condensed water mechanically locking the ice inside the micro- and nanoroughnes. [16], [39], [40] A second example of recent coating architectures developed to reduce ice adhesion, are slippery liquid infused porous surfaces (SLIPSs). High contact angle liquids are infused into a polymer or metal microtopography to increase the contact angle of the composite to above $150°$, which is in the superhydrophobic regime. [29], [32], [45], [46] However effective, these surfaces rely on a microstructure and an infused liquid that eventually has to be refilled, which yields the concept of SLIPSs in principle of low durability. As a third example, phase changing materials have been suggested as a mechanical ice removal method. To create this active coating architecture, Makkonen et al. used temperature as a trigger for local coating displacement. In their research, an epoxy matrix contracts while a solid component expands. This results in little overall displacement, but high local shear stresses on the ice interface. [11] A fourth example of a method for passive de-icing that has frequently been suggested in recent literature, uses aerodynamic forces to brake off ice. Flexible coatings have been tested where wind drag was able to remove ice, although this approach was only successful with coatings that featured low ice adhesion strength. [11] If the ice grows on the surface as crystals, the shape in which they grow could be controlled. To have high local shear stresses, ice crystals would need to grow with small base and bulky head. A suggestion to reduce the ice adhesion strength, is to blow air through the coating. This would reduce the interfacial area between the ice and substrate. [11] A fourth approach was taken by He et al., who designed PDMS (polydimethylsiloxane) topographies that initiated macrocracks between the solid and the attached ice. The stress concentrations at the solid-ice interface were initiated by controlled topography and a mismatch in stiffness between the solid and the ice, both perpendicular and parallel to the surface. This strategy allowed them to reduce ice adhesion by over 50% in vertical shear tests of water frozen on the surfaces in a mold. [29]. The fourth example of reducing ice adhesion is using superhydrophobic surfaces.

A different approach to reduce ice adhesion has been developed in the seemingly unrelated research field of fog harvesting, where patterned hydrophilic-hydrophobic coatings have been inspired by banana leaves, spider webs and the Stenocara beetle shield. [40], [47], [48], [49], [50] Zhang et al. managed to capture and confine condensed water in small hydrophilic square areas and attract nearby water to that region. At a specific size, the condensed droplets roll off the surface and can be collected. The superhydrophobic surface was a semi-fluorinated calcinated glass and the hydrophilic islands were created by inkjet printing dopamine. [51] A similar method was used by Lee et al. to create a hydrophobic surface with hydrophilic spots. In their experiments an apRFp fluorinating plasma treatment process made the surface superhydrophobic, and an electrohydrodynamic jet printing process was used to print alcohol drops which chemically reacted with the surface to form hydrophilic spots. [52] Kirillova et al. used hydrophilic-hydrophobic 'janus' microparticles that self-assemble into hydrophilic-hydrophobic surfaces and showed that this surface architecture can be used for anti-icing or passive de-icing. The base of the ice crystals growing on this surface was confined to the hydrophilic sites, which reduced the adhesion of the crystals to the surface. The crystals also produced dry bands around them, feeding on unfrozen condensed droplets in their vicinity [14], [53]. This method will only become feasible when the ice adhesion strength on surfaces is decreased. Using a back-of-the-envelope calculation one can estimate at which velocity, the dynamic pressure p_d of the air flowing around the ice crystal base would match the cohesive strength of ice. The cohesive strength of ice is about 100 kPa, which is lower than the adhesion strength of ice to most materials, so therefore it is more realistic to brake the mechanically unstable ice crystals, instead of detaching them

from the hydrophilic sites. the local velocity of air has to be $404\ m/s$, if $p_d = \frac{1}{2}\rho v^2$. Airspeeds greater than the speed of sound are not to be counted on for passive de-icing in the current mission profile, definitely not within the boundary layer.

1.1.4 Scope

Many forms of ice, like rime ice, ground ice and frost form on aerodynamic surface during the mission profile of an aircraft. However, it is clear from literature for the instruction of aircraft pilots, that clear ice is the form of icing that incurs the highest risk to safety and the most severe risk of economic losses.

To understand the formation of clear ice, a better understanding of impacting subcooled droplets with the surface is required. Firstly, it has been shown that a molecular liquid layer of water covers materials, and the continuity of this MLL depends on humidity [22] Experiments performed at room temperature and $RH = 55\%$ show the presence of the molecular liquid layer (MLL) on most materials and the growth of the liquid layer with time. [23] This MLL could impact ice nucleation freezing front propagation mechanisms. Secondly, high-speed infrared observations of freezing have been performed with great success, using the latent heat escaping when the liquid crystallizes to observe the freezing of sessile and impacting droplets with high precision. [3] This method could be used for the observation of freezing of impacting droplets, as well as the freezing of the MLL. As the freezing of the thin MLL is expected to release much less latent heat than bulk freezing, new methods will have to be explored to observe the proposed MLL freezing front propagation.

To connect any nucleation or freezing front propagation mechanism to clear ice formation, impacting droplets will have to be used. If small droplets indeed freeze in tens or hundreds of microseconds, this prevents the observation of their nucleation mechanism with the available IR observation technique, which is limited to a framerate of $50\ Hz$ (sampling time interval of $20\ ms$). Therefore large droplets will be used to study freezing upon impaction.

For each test, specific test surfaces will be selected. For the characterization of the observation methods, a test surface is needed on which a continuous MLL forms, so that a freezing front propagation can be expected. To identify the effect of the governing parameters on nucleation time delay and freezing front propagation, test surfaces have to be selected.

Hydrophilic – hydrophobic patterns, which have shown to create dry bands around droplets or crystals [14], [53], could influence the continuity of the MLL and thus the icing mechanism. As the contact angle is a material property, this allows for the production of smooth, durable coatings. These aspects motivate the production of test surfaces with patterns of different contact angles and the observation of their impact on ice nucleation and freezing front propagation.

1.2 Research questions and outline

1.2.1 Research framework

Many different approaches have been taken in the last decade to study ice formation. Icing research is considered a difficult field, due to the many parameters that have to be accurately controlled to be able to compare test results between different research groups. Icing wind tunnels and actual aircraft, are the most relevant test environments for icing research for aeronautic applications. Also in these environments, the relative humidity, temperature of the environment, droplets and surface, droplet size and impact velocity, etc. should be accurately controlled and icing should be observed with high spatial and temporal resolution. These demands are impractical, which makes it hard for icing research to produce relevant results.

For cooling of a surface, usually a Peltier element is used [54]. Alternatively, a surface can be cooled by liquid hydrogen running through channels that are in thermal contact with the surface. [55] On this surface, sessile water droplets are deposited for the observation of static nucleation. To better approximate the real situation of freezing rain, small droplets (Fraunhofer) or a trickle of water are dropped on the inclined surface subcooled surface. The experiments performed in this thesis use a stack of two Peltier element, connected to a heat sink and cooling fan that is able to cool substrates to $-15°C$ in a lab environment with $T_{env} = 22°C$ and to $-35°C$ in a climate chamber with $T_{env} = 10°C$.

To follow ice nucleation in situ, infrared microscopy has been used [21], [56]. In a more complex method a laser has been employed to melt a thin nanoscale layer of ice and observing the refreezing through the change in infrared absorption spectrum between water and ice. [57] The experiments using visible light microscopy to identify ice nucleation usually base the observation on the change in transparency between ice and water. [16], [17], [37], [58] However, Tanaka et al. have added 7-amino-4-methylcoumarin and the temperature sensitive rhodamine-B to water to make it photoluminescent and capture changes in temperature with a high-speed color camera. [35] Another way to couple temperatures to visible light measurements, is the use of ultra-sensitive thermocouples. [38]

For freezing front propagation between droplets, visible microscopy has been used to identify the growth of dendrites between small sessile droplets on a surface. [59], [60], [61] To the author's knowledge, the identification of a freezing front through a molecular liquid layer (MLL) has not occurred in previous research. This demands the development of new observation methods. Infrared imaging should be able to observe this freezing front and couple the released latent heat to the thickness of the freezing MLL. For this thesis, a FLIR A315/A615 thermal camera has been made available by the department of Novel Aerospace Materials (NovAM) at the TU Delft, including a lens for increased spatial resolution and software for capturing at higher frame rates. A new method, recently employed to register changes in molecular activity in drying paints by Kooij et al., [62] is made available by NovAM, to determine its effectiveness in registering the MLL freezing front for MLLs too thin for observation with IRI.

To follow the freezing process of impacting droplets, high temporal resolution is required. Mostly microscopy in the visible spectrum has been employed, looking at droplets from the side. [16], [27], [35], [63] Observing bouncing droplets from the top with visible light microscopy allows for a better view of droplet contraction and pinning upon freezing. [27] In research for industrial applications, for example icing on airfoils, the nucleation of droplets is rarely followed real-time. Usually ice accretion is followed visually with low special and temporal resolution. This limits the ability to learn anything about the icing mechanisms at play in the experiments. However, the shape of the ice accretion over time and its impact on the airflow around the realistic objects is usually the focus of this industrial research, not the understanding. [14], [55], [64], [65] For this thesis, the initial understanding of ice nucleation in droplets and freezing front propagation was obtained from tests with sessile droplets. The tests that are done with impacting droplets,

use low impaction speeds, below $1.7\ m/s$ and large droplet diameters of 2 mm. This method is not expected to produce rime ice under any circumstance, which is not necessary for the studying of clear ice.

To test ice adhesion, test setups are usually built inhouse, due to a lack of standardized dedicated ice adhesion measurement equipment. A common method is the freezing of ice cubes to a surface, using a mold for the water and hitting it with a pendulum. The minimum height from which the pendulum has to be dropped, in order to detach the ice cube from the surface under consideration, can be related to the ice adhesion strength through the pendulum momentum. A slightly more controlled experiment attaches the ice cube to a rotating arm. The centrifugal force exerted on the ice cube can similarly be computed using the rotational rate and the distance of the ice cube to the center of rotation. [11], [14] Another method attaches the ice cube to the surface and pushes it off with an indenter, registering the applied shear force with high temporal accuracy. [29] If the ice adhesion is exceptionally low, this can be qualitatively demonstrated by tilting the surface on which an ice cube is adhered and measuring the tilt angle at which the ice cube starts sliding under its own weight. [46] The ice adhesion of droplets is much harder to determine than that of molded ice cubes. Mishchenko et al. succeeded in freezing a spring into sessile droplets. Then maximum elongation of the spring before failure of the frozen droplet in adhesion was taken as the ice adhesion strength. However, the adhesion of droplets to non-superhydrophobic surfaces was so high, that the frozen droplet failed in cohesion. [16]

The contact angles of surfaces can be measured with goniometers, available in most labs. Cryo-SEM has been used to study the increase in contact angle of micron sized droplets. To observe the contact angle of the droplets with $d_{drop} < 100\mu m$, Park et al. used FIB to make a cut in frozen droplets during observation with cryo-SEM [24]

The number of surfaces that has been tested for anti-icing in research is very large. The focus of this thesis will be on flat materials, to exclude the effect of roughness, as much as possible. Almost exclusively, materials with high contact angles contain fluorinated groups. To test the effect of material properties like contact angle and conductivity, simple materials like metal, glass, permanent marker ink, epoxy and olive oil are used in this thesis. The ionomer Surlyn 9520, PVDF and alginate were more complex materials, but available inhouse.

It should be clear from the discussion on the influence of relative humidity on ice adhesion strength on superhydrophobic surfaces in 1.1.3, that an environment with controlled humidity and temperature is very desirable, to determine or exclude the influence of these parameters on ice nucleation and freezing front propagation. Due to the limited availability of a climate chamber, many freezing tests were conducted under controlled lab environment, which is, although undesirable, similar to most experimental environments in literature.

In Figure 1.3, the different systems in the freezing setup are sketched, as used in this thesis. The first system is a test surface and substrate (red), including any condensed or deposited sessile droplets. The substrate was in thermal contact with the cooling system (grey), consisting of two 40x40 mm Peltier elements, a heat sink and a fan. The cooling system was powered by a manually controlled voltage source, connecting negative electrodes of both Peltier elements and fan, as well as all positive electrodes. This resulted in a controllable surface temperature of $-15°C < T_{surf} < 65°C$. To measure the temperature in realtime on every location on the surface, infrared imaging (IRI) was used (green). A FLIR A315/A615 thermal camera was employed together with a lens for higher spatial resolution. The collected temperature data, in the form of .seq files were stored on an external hard drive. Using FLIR software and ImageJ, the nucleation temperatures, nucleation time delays, temperature differences due to latent heat escape, freezing front propagation velocities, melting temperatures, etc. could be extracted and investigated. To study the effect of surface freezing on the freezing of impacting droplets, a subcooled droplet impaction system was

employed (yellow). Using a micro extruder, demineralized water was pushed through a plastic tube into a needle with $60\ mm$ length and $400\ \mu m$ outer diameter. This needle was rolled up into a spiral and attached to a small 20x20 mm Peltier element, which was itself in contact with a heat sink and a small fan. The negative and positive electrodes were directly connected to a separate voltage source, that provided a maximum of $3.5V$, to avoid damaging the small Peltier element. In this way, the needle had the ability to controllably deposit cooled droplets of between $0°C < T_{drop} < T_{env}$ with sizes of $d_{drop} = 2\ mm$ in freefall from a height of $140\ mm$.

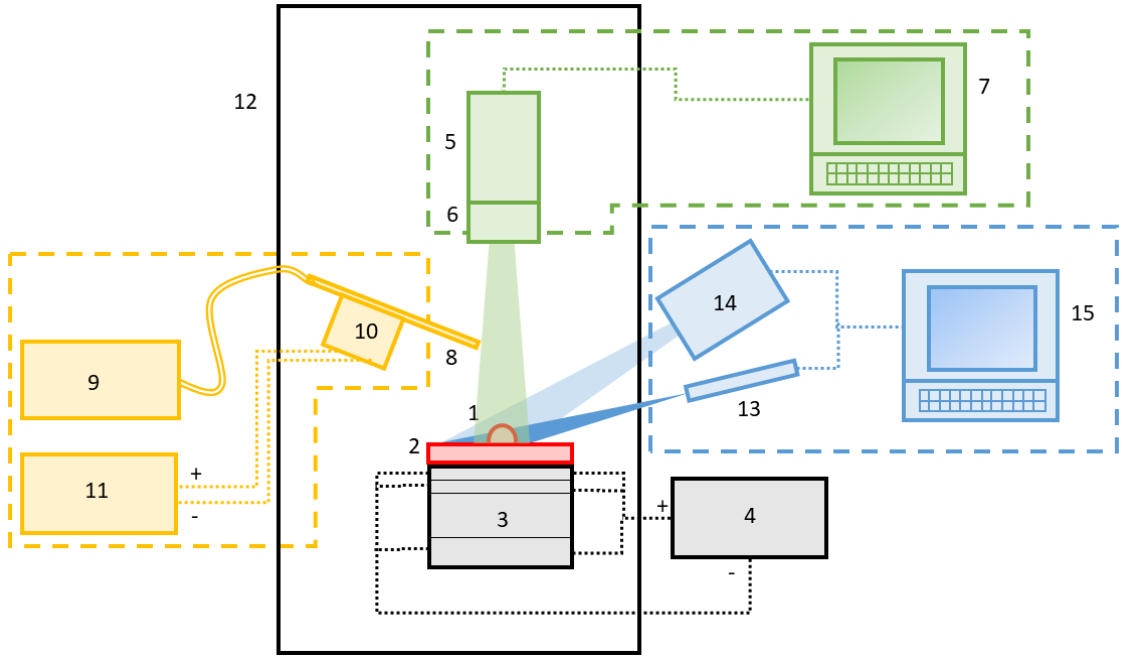

Figure 1.3: Schematic drawings of a self-built setup to observe nucleation and freezing front propagation, including systems for cooling (grey), Infrared Imaging (IRI) observation (green), droplet impaction (yellow) and laser speckle imaging (LSI) observation (blue) of the water-surface interaction during freezing (red). A droplet (1) is deposited on the test surface (2). The surface is cooled by two 40x40 mm Peltier elements attached to a heat sink with thermally conductive paste, which was cooled by a fan (3). The Peltier elements and fan are powered up to $11.5V$ DC by a voltage source (4). In all freezing experiments, freezing droplets on the test surface were observed from the top with a FLIR A315/A615 thermal camera (5) through a lens (6). Using an HDMI connection, the IRI data was collected on a laptop (7) and converted with the FLIR software into formats that were useful for data analysis with ImageJ. In the experiments with impacting droplets, water was fed through a plastic tube into a needle (8) by a microextruder (9). To cool down the droplets before extrusion, the needle was wound into a spiral and connected by thermal paste with a 20x20 mm Peltier element, small heat sink and fan (10), powered by a separate voltage source up to $3.5V$ DC (11). When using droplet impaction, the test surface was tilted, to allow for droplets to roll off. Whenever required, the test surface was placed in a climate chamber (12), necessarily containing part of the cooling, droplet impaction and IR observation setups. In a few tests, LSI observation of freezing front propagation was performed, either from the side, the top or slightly inclined, avoiding interference with the IR observation system. A blue laser (13) was aimed at sessile droplets on the test surface and the resulting speckle pattern reflecting from the surface and droplets registered with a camera at a framerate of $60\ Hz$ (14). The captured LSI frames were saved on a server and processed with inhouse software to show the local change in speckle pattern (15) [62]

1.2.2 Research questions

The thesis goal is to understand and prevent clear ice formation. To guide the research in this thesis through the complex field of icing, four main research questions can be formulated. They represent four logical steps from the observation of the freezing molecular layer of water towards methods that might help prevent clear ice on aircraft surfaces. Apart from the introduction, each research question corresponds to a chapter in this thesis.

1. What is the effect on the ice nucleation of sessile water droplets of the conversion of the molecular liquid layer (MLL) into a frozen layer?

    1.1. What experimental techniques can be used for the qualitative and quantitative observation of the freezing of the MLL?

    1.2. Which mechanisms of the freezing front propagation mechanism can be determined with the available observation methods?

2. How does the presence or absence of a frozen layer affect the ice nucleation temperature and time of an impacting droplet?

3. What is the influence of surface, material and environment on the ice nucleation mechanism of sessile droplets on smooth surfaces?

    3.1. What is the influence of identified relevant governing parameters on the nucleation temperature and nucleation time delay?

    3.2. What is the influence of the identified relevant governing parameters on the freezing front propagation velocity?

4. How can the identified relevant governing parameters of the nucleation temperature, nucleation time delay and freezing front propagation velocity be employed to create novel smooth, durable and non-toxic surfaces that prevent ice nucleation or growth of the frozen area?

The answer to these four main research questions and their subquestions is given per relevant chapter 2 to 5. The approaches, results, analysis and recommendations linked to the research questions are summarized again in chapter 6.

2. Experimental techniques for analysis of heterogeneous ice nucleation and freezing front propagation.

Research question 1:	What is the effect on the ice nucleation of sessile water droplets of the conversion of the molecular liquid layer (MLL) into a frozen layer?
Research question 1.1:	What experimental techniques can be used for the qualitative and quantitative observation of the freezing of the MLL?
Research question 1.2:	Which mechanisms of the freezing front propagation mechanism can be determined with the available observation methods?

2.1 Observing and analyzing ice nucleation by infrared imaging

Methodology

As briefly introduced in section 1.2.1, in order to study freezing of water on specific surfaces, a table top cooling system is required. Two Peltier elements of 40x40 mm are connected in parallel and mounted on a heat sink, connected to a small fan. The fan is separated from the table top by four metal feet, giving the fan the ability to pull air from the environment into the cooling fins of the heat sink. On top of the Peltier elements, substrates of glass, metal or Teflon of between 20x20 mm and 40x40 mm could be placed. To ensure cooling of the test surface, thermal paste was used between the substrate and the Peltier elements. The badly thermally conducting glass and Teflon substrates were chosen as thin and small as possible, to allow for the surface to be cooled down to at least $-15°C$.

The temperature of the surface was monitored with a FLIR A315/A615. Initial observations of ice nucleation were made with the standard lens. To allow for more spatial resolution, a lens was installed with higher magnification. The lens with higher magnification was used for all IRI reported in this thesis, unless mentioned otherwise, which allowed for a relatively high resolution of $31.25\ \mu m/px$, compared to, for example, Alizadeh et al., which used an IR camera with $100\ \mu m/px$ resolution. [33] The properties of the camera and lens assemblies are described in Table 2.1.

Camera properties	
Image resolution	$640\ x\ 480\ px$
Frame rate	$50\ Hz$ (up to 200 Hz with window reduction)
Lens field of view	$25°$
Focus length from lens	$100\ -\ 500\ mm$
Extra lens properties	
Lens field of view	$14 - 19°\ (20x15\ mm)$
Focus length for lens	$60\ mm$

Table 2.1: Properties of the FLIR A315/615 thermal camera and extra lens

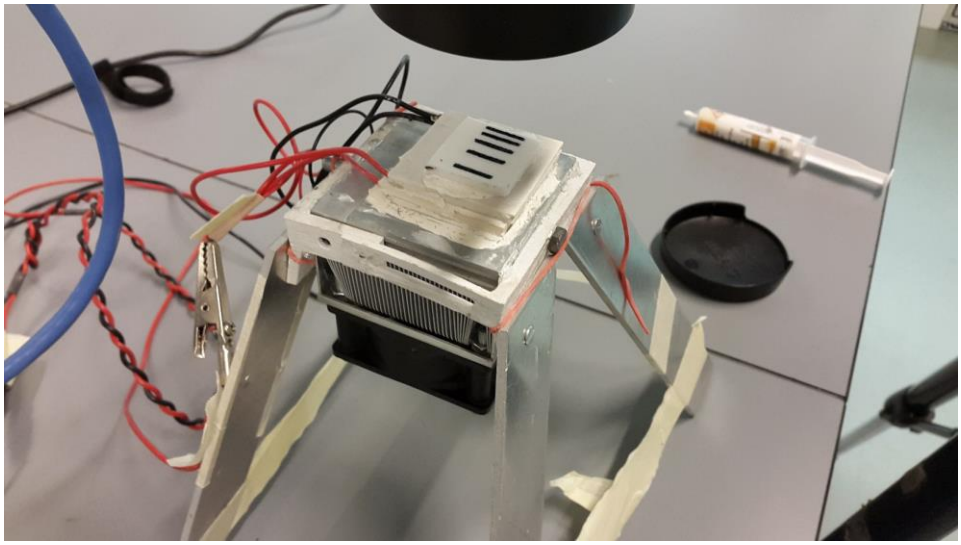

Figure 2.1: This picture of the cooling system shows how two Peltier elements are joined with thermal paste and electrically connected in parallel. These are attached to a heat sink, with a fan blowing air into the fins of the heat sink, to extract the heat coming from the hot side of the two Peltier elements. In this picture, a hydrophobic-hydrophilic surface (Teflon with permanent marker ink lines at variable distance from each other) is installed on the top Peltier element and is observed with the IR camera in a freezing experiment.

To evaporate condensed water droplets, the temperature of the surface was elevated to $50°C$ before every freezing test. The evaporation of droplets was followed with the IR camera, while keeping the Peltier elements at a voltage of between $1.5\ V$ and $3.5\ V$. After the condensation had disappeared, the polarity of the DC input to the Peltier elements and fan was inverted and set to the desired freezing voltage between $4\ V$ (minimum for fan operation) and $12\ V$ (maximum for Peltier elements).

The surface cools to the desired test temperature with a certain cooling rate. This cooling rate depends on the conductivity of the substrate and the set voltage. For a stable surface temperature in lab environment, the maximum set voltage was about $10\ V$. Above this voltage, the cooling system could not conduct enough heat away from the heat sink and the surface would slowly start heating up. In most experiments, the surface temperature was monitored real-time by setting 5 points in the observation window, one in the middle and one in every corner. The voltage of the cooling system was manually adjusted, according to the observed cooling rate and equilibrium temperature, which required constant re-evaluation.

Irrespective of the desired surface temperature and the cooling rate, the recording of every test was started in the FLIR software when a surface temperature of $-5°C$ was reached. This consistent recording allowed for the identification of the nucleation time delay and nucleation temperature in post-processing.

Demineralized water was deposited on the surfaces in two ways. Large droplets, with $0.5\ mm < d_{drop} < 5\ mm$ were deposited by needle on 'interesting' locations. To observe the transmission of ice nucleation between droplets, they were deposited in a grid or a cross configuration, as illustrated in Figure 2.2. The second way to deposit droplets was through condensation. This process consisted of $2-5$ cycles of freezing (at about $-15°C$) and melting (at $0°C$), until individual droplets could be observed with the IR camera. This allowed for the estimation of the droplet size around $0.1\ mm$.

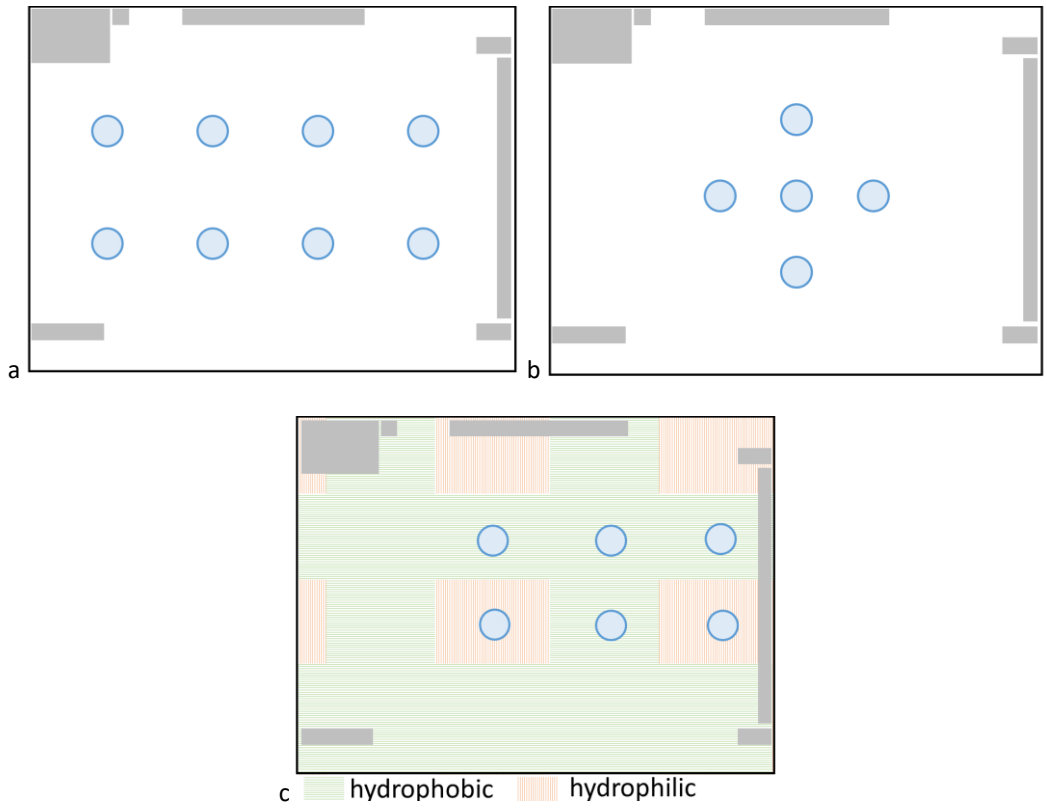

Figure 2.2: (a) droplets were deposited in a grid or (b) in a cross configuration to observe ice nucleation transmission between them or (c) on locations with different material properties. The grey areas would contain temperature and labeling data in the IR images and videos, as recorded with the FLIR software.

If nucleation is observed, the voltage on the cooling system is set to 0V. After melting, the recording with FLIR software is ended. The registering of melting can help to confirm that freezing occurred. If no freezing has occurred on the test surface, the surface will not show any sudden droplet coagulation or significant change in reflectivity when passing the transition temperature of $0°C$. This method works well for low humidities, where freezing fronts can be too weak to observe, but crystals do grow due to direct desublimation of water vapor, [66] After melting has been confirmed, the substrate can be exchanged for another substrate or the test can be performed again, to confirm the found nucleation temperatures or nucleation time delays.

The registration of the nucleation temperature has to be done with care, to avoid bias in the reported results. In postprocessing, temperature measurement points, indicated as 'spots' (Sp) in figures, are placed an their temperatures listed in a table. In the last frame before the latent heat escaping from ice nucleation, the temperature and time are registered and listed as 'nucleation temperature' T_n and nucleation time delay t_n. As a temperature measurement point is placed on every drop, as well as in representative locations for small condensed drops, several values are registered for T_n and t_n. These values are averaged, taking the highest and lowest values for T_n and t_n as the error margin of the freezing experiment. To allow for a realistic determination of T_n and t_n and their scatter, many experiments are conducted on the exact same surface in the same environment, as well as on surfaces made with the same production process. In every freezing experiment, the maximum temperature after ice nucleation is also registered, usually two frames or $40\ ms$ after the first significant increase in temperature from the escape of latent heat.

If after 3.5 minutes, no nucleation had occurred, the recording of the freezing experiment is stopped, to save on storage space for the video files. The experiment itself continues and the researcher looks

attentively at the real-time thermal imaging of the surface for about 5 more minutes. If after these 500 seconds, no nucleation has been observed, the experiment is ended. In this case, the average surface temperature is logged as the nucleation temperature, with a nucleation time delay of $t_n = \infty$.

Any material with sufficient thermal conductivity can be selected can be used as a substrate. In this thesis, glass, an aluminum alloy AA6082 and Teflon have been used as substrates. Any material can also be used as surface material, as long as it's not soluble in water and adheres well to the substrate. For the initial investigation towards the effectiveness of IRI to determine the nucleation temperature, PVDF thin films were spincoated on glass substrates of 1x40x50 mm at 2500 RPM for 30 seconds from a PVDF/DMF (5w%/95w%) solution. The coated glass plates were partially covered with Teflon tape and treated with an inhouse atmospheric arc plasma actuator. As the CNC controlled plasma actuator head scanned over the surface, the uncovered squares of PVDF were exposed to 5 – 10 seconds of atmospheric plasma.

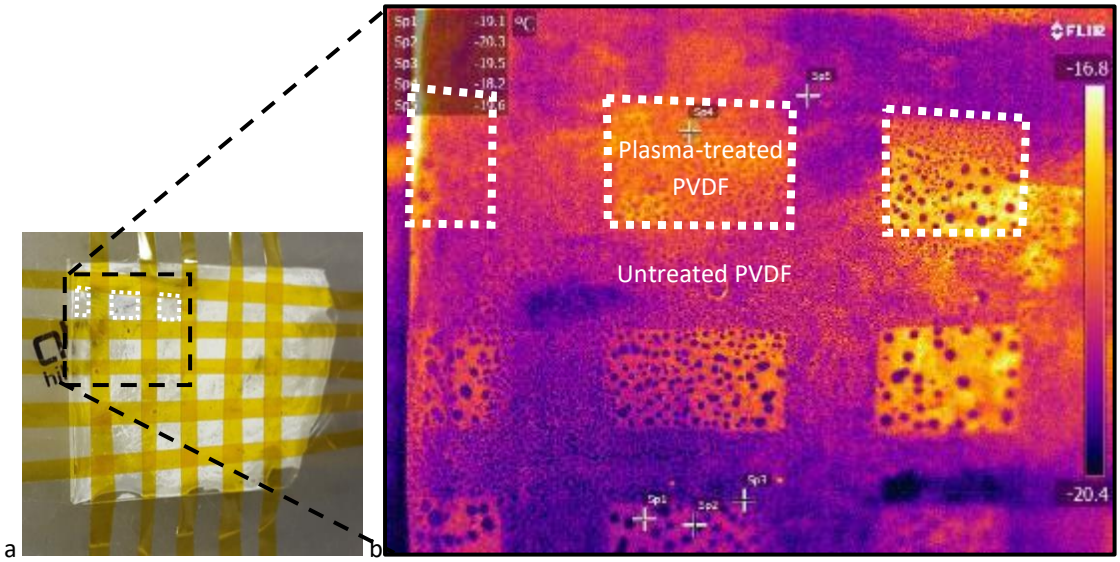

Figure 2.3: (a) A PVDF thin film on glass substrate, as prepared for treatment with atmospheric arc plasma actuator. (b) IR image illustrating difference between measured temperature on untreated hydrophobic bands and plasma treated hydrophilic square areas on the PVDF thin film (white dashed squares) on a glass substrate.

The initial freezing tests were performed in a climate controlled lab environment with $T_{env} = 22 \pm 1°C$ and $RH = 55\%$.

Results and discussion

Before evaluating the observation of nucleation with IRI, the difference in droplet formation between plasma treated and untreated areas of the PVDF thin film under IRI in Figure 2.3b must be addressed. The plasma treatment measurably decreases the contact angle. The literature on the growth of the molecular liquid layer on surfaces suggests that the decrease in contact angle will increase the thickness and continuity of a liquid layer between the droplets, as illustrated in Figure 2.4. [23] (hu1995) If on a (more hydrophilic) plasma treated area of the PVDF film water can flow between the droplets, it is expected that all the water will accumulate in a few larger droplets. In the (more hydrophobic) untreated PVDF, the droplets grow in isolation.

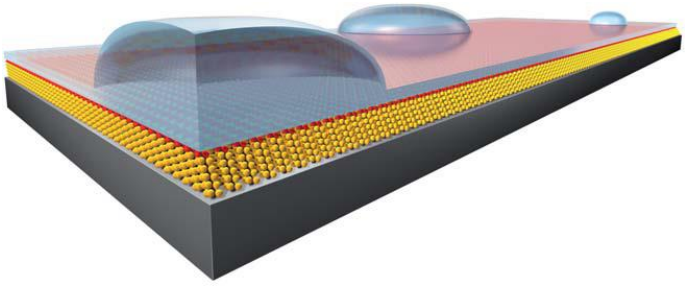

Figure 2.4: Illustration of the Molecular Liquid Layer, connecting nanoscale droplets on a COOH-terminated monolayer [23]

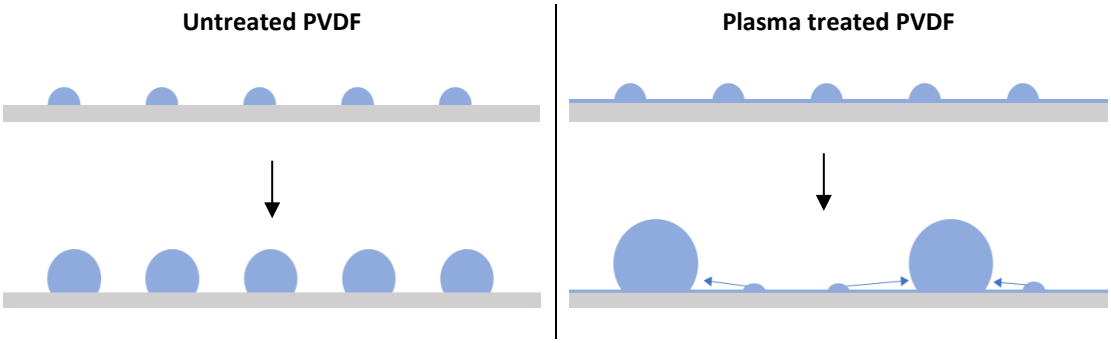

Figure 2.5: Droplets grow to a different size and at different distance from each other on untreated or plasma treated PVDF. (a) On untreated (more hydrophobic) PVDF, droplets grow in isolation. (b) On (more hydrophilic) plasma treated PVDF, water can be transported through a liquid layer between the droplets towards a few large droplets. The smaller droplets dissappear, which increases the average distance between droplets.

It should be noted here, that Guadarrama-Cetina et al. states that the distance between droplets on a surface should decrease for if the surface becomes more hydrophilic. [59] However, this statement is based on an experiment by Zhao et al. in 1995, who do not reach explicitly reach this conclusion in their publication. [67] The hypothesis that water is transported from smaller droplets to larger droplets through a thin layer of water on the (more hydrophilic) plasma treated PVDF, is further strengthened by the difference in observed temperature between hydrophilic and hydrophobic areas in Figure 2.3b. As water reflects infrared radiation, the same way clouds keep heat inside the lower atmosphere at night, the infrared signature of a layer of water is expected to reflect the environmental temperature. The shininess of a surface, caused by increased reflectivity in the visible spectrum, is how most would observe wetness. The same mechanism should hold true for the infrared spectrum. Although the difference in droplet size, inter-droplet distance and apparent surface temperature is not the central issue in this section, it already suggests that a liquid water layer might be present in between droplets, of which the freezing will be observed with IRI in section 2.2.

Figure 2.6 shows the frame just after nucleation of one of the recorded freezing experiments, as observed with IRI. Instead of condensed droplets, large droplets were deposited on a plasma patterned PVDF thin film on glass (sample illustrated in Figure 2.3). Freezing events can clearly be observed with the cooling setup, confirming the suitability of IRI to observe ice nucleation in droplets and bulk freezing front propagation, as used before by several researchers. [21], [3] The temperature can accurately be registered with high spatial ($31.25\ \mu m$) and temporal ($20\ ms$) resolution.

One important remark is the difference in temperature between droplets and within the same droplet, apparent from Figure 2.6. There is a consistent difference of $0.5°C$ between temperatures measured in the

center and the edge of large droplets, as observed with the IR camera. This difference decreases with droplet size until it is not visible anymore for droplets smaller than $1\ mm$.

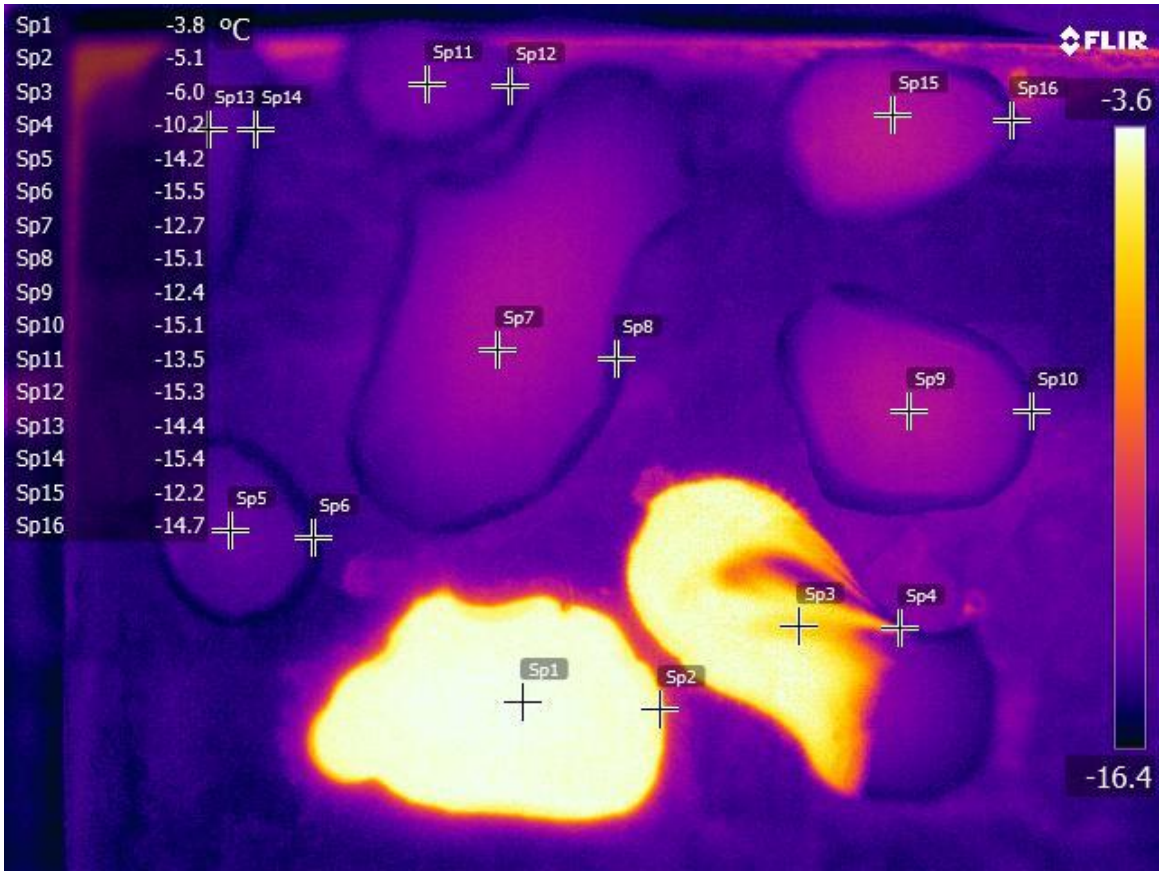

Figure 2.6 This frame is captured (at $t = t_n + 0.04s$) and illustrates the difference in temperature between droplet the droplet center and edge on square plasma patterned PVDF on a glass substrate at room humidity and temperature. The captured frame also shows the escape of latent heat in the infrared spectrum during nucleation, with the bottom droplet nucleating first at a temperature of $T_n = -13°C$ and increasing the temperature to $T_n = -3.8°C$. A bulk freezing front can be observed to travel through a second droplet from left to right.

The droplet is expected to be in a thermal equilibrium as a steady state. However, as this temperature difference between edge and center remains constant over time, the droplet must be losing heat to its surroundings through evaporation or radiation. Alternatively, the temperature difference is an artefact of the IR measurement technique and could be explained as the lack of transparency to IR of liquid water. In this case, the whole interface between the droplet and the surface is at a low temperature, but only at the edges, the layer of water is thin enough to see the interfacial temperature through the droplet. Another artefact could be increased reflection of environmental radiation towards the camera from the center of the droplet. However, as smaller droplets assume the lower edge temperature at the center, this is less likely to be the case. For the remainder of this study, the nucleation temperature is taken at the center of the droplet. The error of max. $0.5°C$ is small enough, as compared to the spread in nucleation temperatures.

Frosting, a different form of ice formation that does not involve ice nucleation from liquid to solid can also be observed with IRI, as illustrated in appendix D. The local difference in apparent temperature between different parts of the frost crystals do not provide much extra information about the ice nucleation process. At lower temperatures and low humidities, the frost might become a useful indicator that no transition from liquid water to ice should be expected.

When studying the frames after nucleation of the first droplet in Figure 2.6, all neighboring droplets nucleate in a very short time interval. Several frames of the recorded video are included in appendix C. This freezing front propagation between droplets is much faster than would be predicted by a dendrite growth front propagation or 'percolation-induced frost formation' mechanism, in which dendrites grow at velocities below 2 $\mu m/s$ according to Guadarrama-Cetina et al. [59] However, it is slower than bulk front propagation mechanism, around $350\ mm/s$ as found by Pasieka et al. and extrapolated to relevant subcooling temperature of $-12.5°C$. [21] Therefore, it can be concluded that the observed transmission of nucleation between droplets is either a new freezing front propagation mechanism, a variation of dendrite or bulk freezing front propagation or a mix between the two. The working hypothesis in this thesis is that the ice crystal is transferred between droplets through a molecular liquid layer (MLL) of water, as proven to be present on most surfaces by James et al., forming a layer of ice. [23]

The IRI setup used for the measurement of nucleation temperature and nucleation time delay, can apparently also be used for the observation of a new front propagation mechanism. During the freezing of the thin layer of water on the surface, latent heat is released, which is recorded by the IRI setup, as mentioned before. The difference in temperature before and after nucleation, can now be considered to represent the 'freezing front intensity' ΔT_n. Although clearly visible in some cases, as illustrated in appendix C, the freezing front propagation can be hard to register with IRI. In quantitative terms, the MLL freezing front propagation has been observed in a wide range of intensities, from very strong ($\Delta T_n > 9°C$) to very weak ($\Delta T_n \approx 0.1°C$). The IRI method can't capture temperature differences of $\Delta T_n < 0.1°C$. Simultaneous droplet nucleation has also been observed without a visible frontline, but in a spatially sequential manner. This prevents the reliable calculation of the freezing front propagation velocities. Therefore, a second technique is employed to register freezing, namely laser speckle imaging (LSI).

2.2 Analysis of MLL freezing with Laser Speckle Imaging and Infrared imaging

Laser speckle imaging (LSI) uses a laser to illuminate a surface and registers the reflected speckle pattern. The rate of change in this speckle pattern represent the activity of the molecules on the observed surface. In this thesis, ice nucleation or freezing front propagation will be performed for the first time with LSI. [62], [68]

Methodology

The LSI setup depicted in Figure 2.9 was used at the department of Novel Aerospace Materials (TU Delft), but originates from the department of Physical Chemistry and Soft Matter (University of Wageningen & Research). The setup, designed and built by van der Kooij and Fokkink, is schematically given in Figure 2.7. During the experiments, the same guidelines and processes are employed as described by van der Kooij et al. and Rabal and Braga to follow molecular movement in polymers. [62], [68] The setup uses a 532 nm laser to illuminate a sample and captures the backscattered light with a camera. This reflected light contains a speckle pattern, but does not immediately show any information regarding the shape or material of the studied sample. It is only when the speckle patterns of subsequent frames are correlated, using a certain correlating function that structure can be made to appear in the images. The mechanisms that can be observed are, among others, fluid flow and Brownian motion. One example, as given by van der Kooij et al., is the drying of paint, were the change in molecular mobility can visualize the paint drying process. The function used to correlate the speckle patterns between frames and create contrast in the output images in this thesis, is the intensity structure function, as shown in Equation 1.

$$d_2(t,x,y,\tau) = \frac{\langle [I(t,x,y) - I(t+\tau,x,y,)]^2 \rangle}{\langle I(t,x,y) \rangle \langle I(t+\tau,x,y) \rangle}$$ **Equation 1**

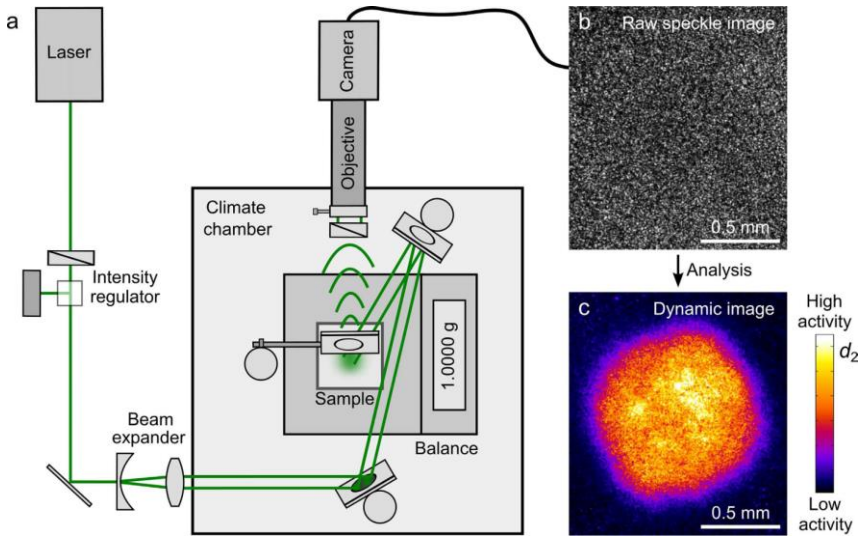

Figure 2.7: (a) A schematic overview of the Laser Speckle Imaging setup, as created by van der Kooij et al. A 532 nm blue laser illuminates the sample, a drop of paint on a piece of paper, in this figure. (b) The backscattered light coming from the sample is captured by a camera and contains an apparently random speckle pattern, giving no insight into the structure of the observed object. (c) The fluctuations in the backscattered speckle patterns between subsequent frames can reveal a local change in molecular activity, using the intensity structure function to obtain d_2 in Equation 1. [62]

The melting and freezing of droplets was observed on a vertical surface and a surface at an angle. These inclinations of $90°$ and $35°$ were necessary to fit the freezing setup into the LSI setup. The observation of a droplet on the vertical test surface, gave images that looked like a tilted sideview of a sessile droplet. As the camera looks down on the droplet from above, the droplet is slanted away from the camera, which makes it appear symmetrical. As can be seen in Figure 2.9, the environment of the LSI setup was uncontrolled, because the setup could not be placed inside a climate chamber. In the first test, droplets of water with 1 w% TiO_2 nanoparticles were deposited directly onto the top Peltier element of the cooling system. The droplet was deposited against a Teflon plate, so that it froze into a quarter of a ball configuration. This exposed one flat surface which could subsequently be observed with LSI.

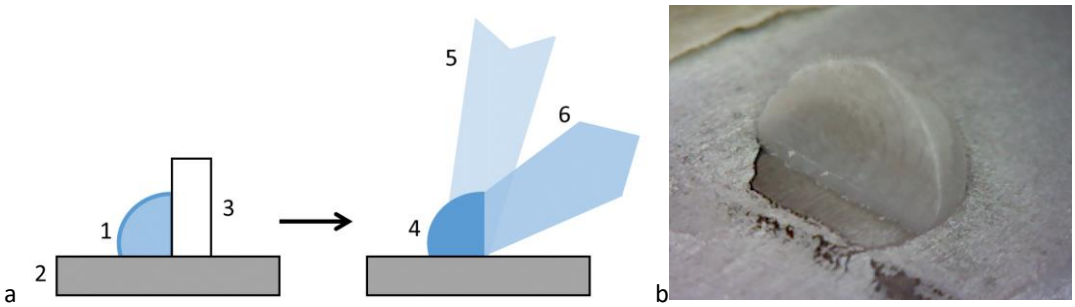

Figure 2.8: Illustration of a quarter droplet being created. In the sketch (a) a droplet (1) is deposited on a substrate (2) against a Teflon plate (3). After cooling down, the Teflon plate is removed and a frozen quarter droplet (4) is left. The flat surface of the frozen droplet is illuminated with a coherent expanded light bundle (5) and the backscattered light bundle (6) can be registered with the camera.

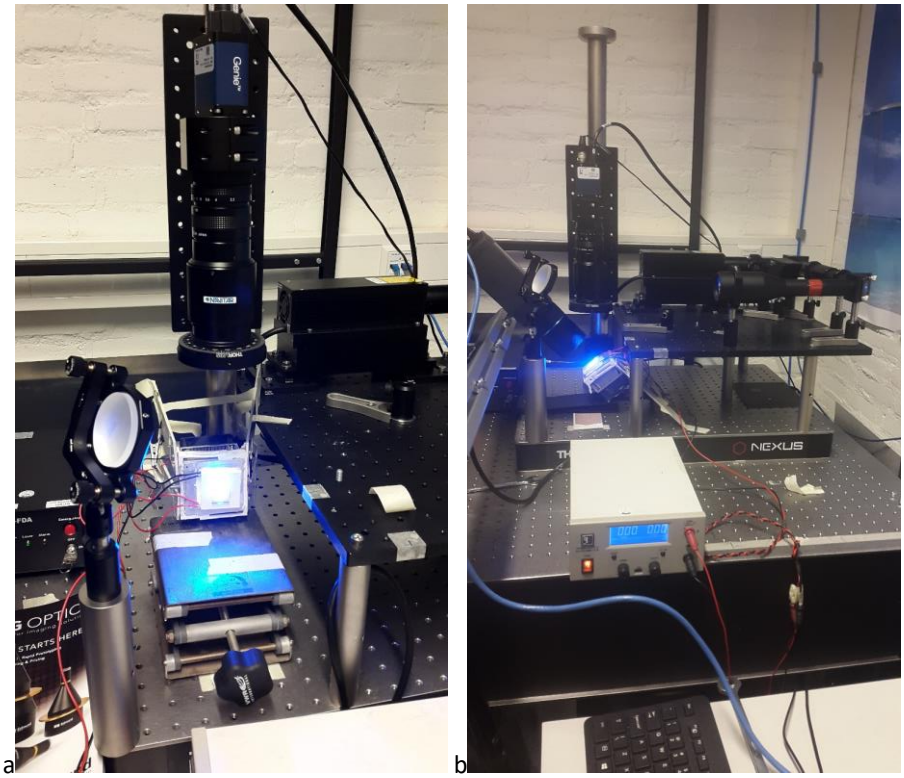

Figure 2.9: (a) The setup for initial observations of melting and freezing of sessile droplets by Laser Speckle Imaging (LSI), studied a droplet hanging on a vertical substrate. A mirror aims the coherent expanded light source, a 532 nm blue laser at test the surface. (b) By integrating the IRI setup into the LSI setup, simultaneous imaging of freezing droplets by IRI and LSI was made possible. This setup was built to extend the range of observation of the MLL freezing front propagation below the minimum intensity ΔT_n featured by the IRI setup. To fit the cooling system in the depicted setups, it had to be inclined to $90°$ and $35°$ in (a) and (b), resp.

Results and discussion

Figure 2.10a – d shows that the melting of a water droplet can be observed by LSI. Firstly an increased activity on solid-air interfaces of the droplet and the substrate is observed, as shown by the red regions. This phenomenon is linked to the melting of a frost layer that has formed from environmental humidity. Bulk melting starts at the droplet-substrate interface. A piece of ice floats on top of the droplet, until it has completely melted. Just after melting, moving regions of increased activity (red) can be seen. These are considered to be vortices due to convection of liquid that has been heated by the substrate into the colder freshly melted liquid near the top of the droplet. After these vortices die down, a fully red droplet is left. The increased activity of the liquid droplet at equilibrium temperature can be either due to Brownian motion of the TiO_2 nanoparticles in the water or a constant evaporation and condensation process that is known to take place at the water-air interface. [59]

In Figure 2.10e – h, the melting of a droplet can also be observed. During the cooling of the droplet down to $T_{surf} = 0°C$, no significant variation in activity is seen. Also, no significant effect of the latent heat during ice nucleation is observed, which occurs on the liquid-substrate interface. These two observations suggest that small changes in temperature can't be observed with LSI. However, a reduction in activity can clearly be observed, when a bulk freezing front slowly propagates from the substrate towards the top of the droplet. After the passing of this front, the activity stays high in the newly frozen ice. As this increased activity disappears after full droplet freezing, it is a transient phenomenon. One explanation would be that an unfrozen liquid layer remains for a few seconds on the ice-air interface, before becoming too thin to observe. It is known from literature that ice is covered with a thin liquid water layer, of which the thickness depends on temperature. [11] Another explanation could be that the remaining increased activity is an

artefact of the correlation between the LSI frames. A last observation that can be made, is the angle at which the layer of ice grows through the droplet. This creates a flat tabletop shape of the frozen. This phenomenon has not been observed in literature. [16], [17], [37], [58] Slowly freezing droplets have been widely reported to freeze into pointy shapes, with a sharp singularity at the tip of droplets. [24], [69], [70], [71] The table-top shape could be due to an unknown effect of the TiO_2 nanoparticles, dissolved in the liquid. It is expected that these nanoparticles are not easily integrated into the ice crystal, so their concentration in the unfrozen part of droplet is expected to increase until the limit of solubility is reached.

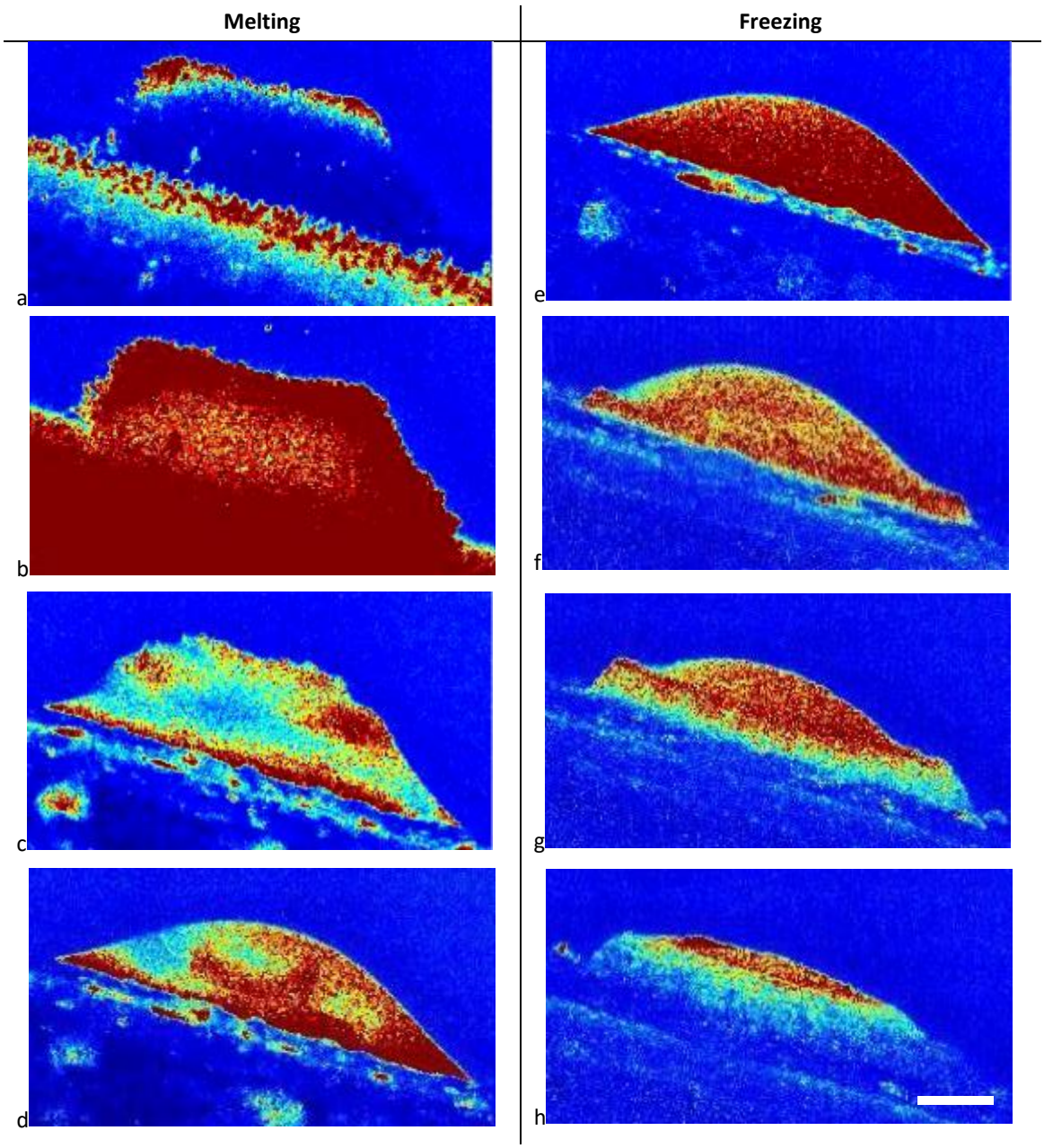

Figure 2.10: Topview of a frozen water droplet that melts and freezes again. The substrate is installed on a cooling system tilted by $90°$, as illustrated in Figure 2.9a. (a – b). Melting of the frozen droplet starts by the melting of frost that has grown on the substrate and the droplet. Melting of the bulk ice starts at the droplet-substrate interface, while a piece of ice floats in the molten droplet for some time until full melting. Just after melting of the ice, some vorticity due to convection can be observed in the liquid droplet. (e – h) The molten liquid droplet colors fully red, due to evaporation of water at its surface or Brownian motion within the droplet. Freezing starts at the droplet-substrate interface and progresses towards the top of the droplet. Due to a larger contact angle of the ice or an effect. The scalebar is $500\ \mu m$.

To investigate whether LSI is suitable for the observation of the MLL freezing front, LSI and IRI are employed simultaneously. The setup combined setup is shown in Figure 2.9b. The IR camera had to be aimed perpendicular with respect to the test surface, to keep the whole observation window in focus, while the LSI camera was aimed towards to the same part of the test surface at a small angle.

	IR	LSI
a	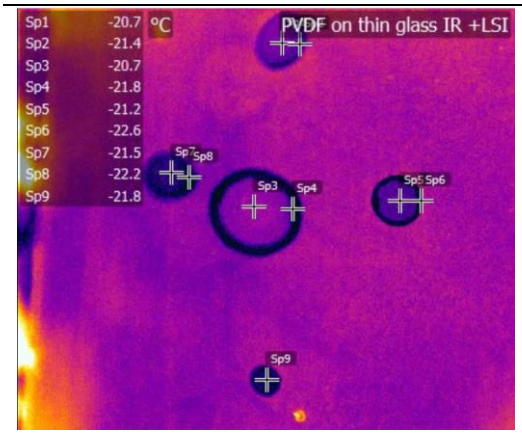	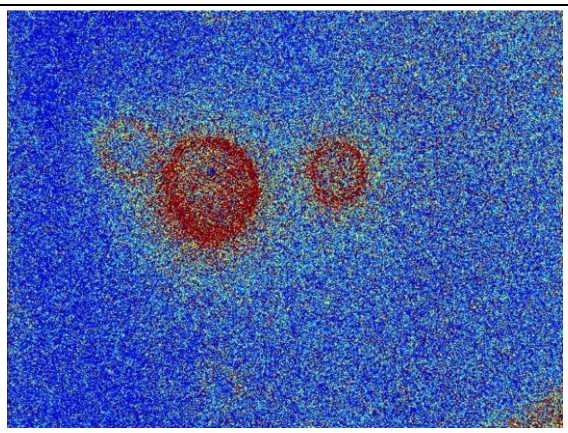
b	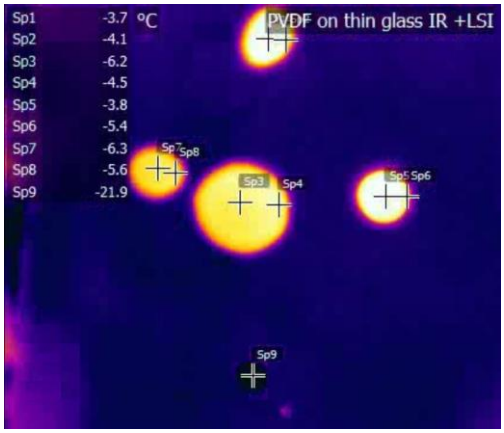	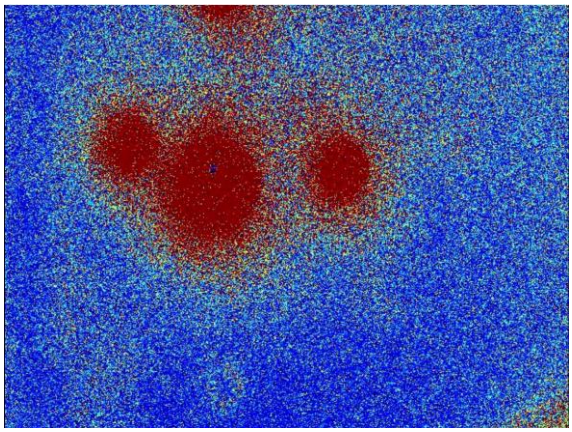
c	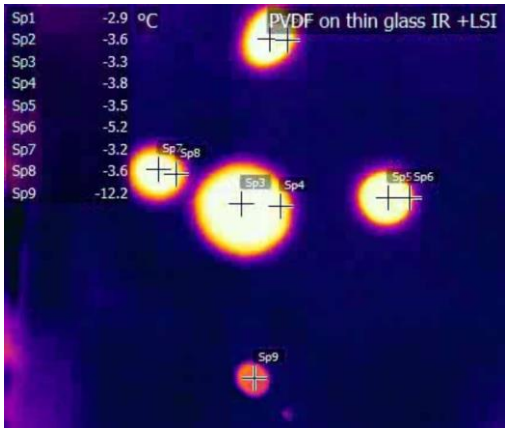	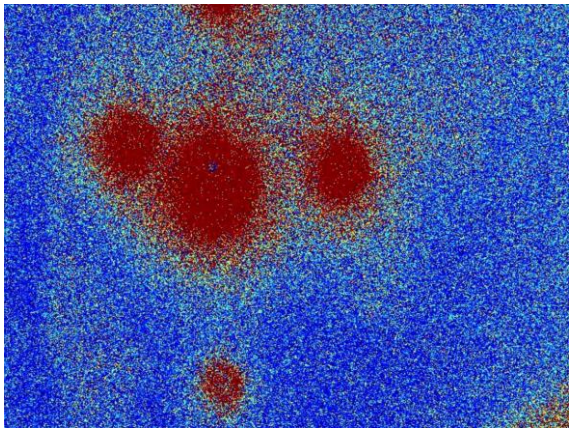

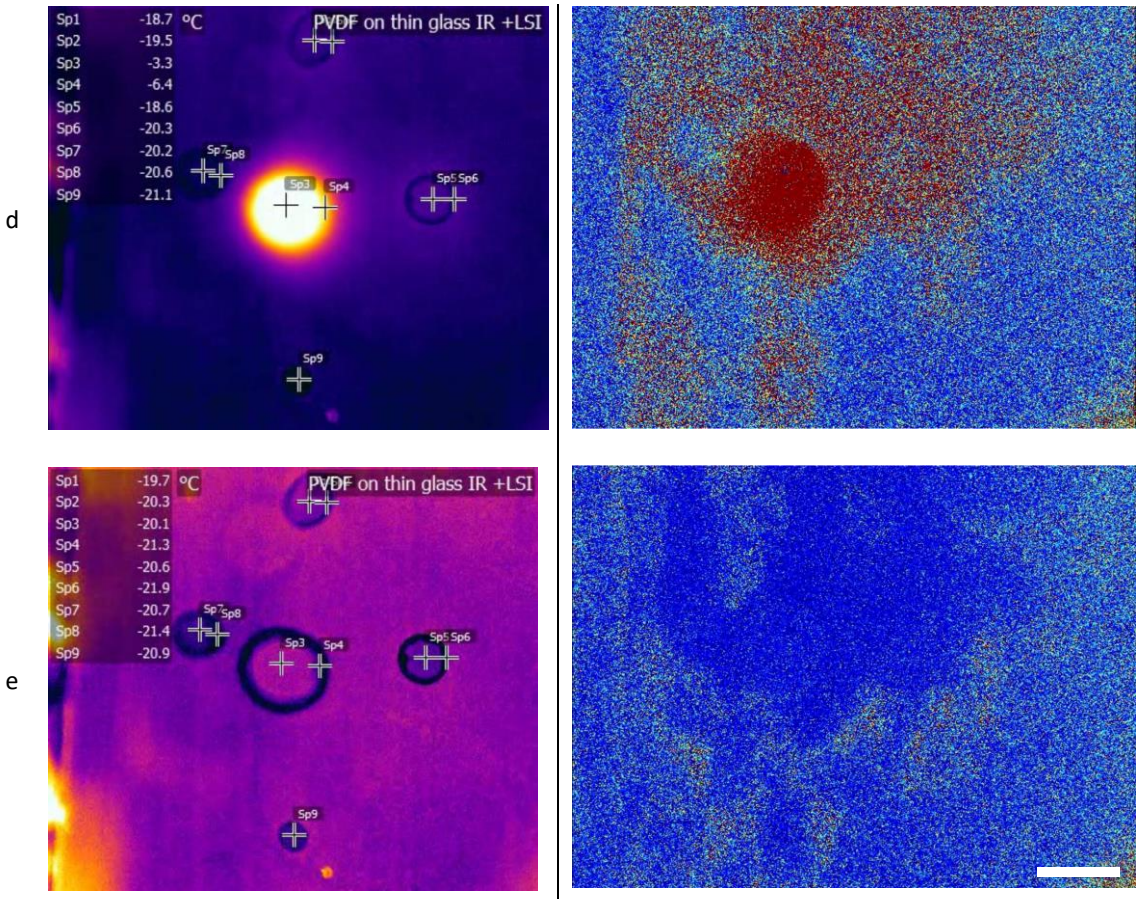

Figure 2.11 Nucleation of droplets on plasma treated PVDF observed with LSI. (a) A front spreads from the top right and (b) triggers nucleation in four of the sessile droplets. (c) The nucleation of the fifth droplet takes place $40\ ms$ after the nucleation of the largest droplet. (d) In the largest center droplet the molecular activity remains high. (e) After freezing of the droplet, the areas with frozen droplets become fully inactive, indicated by a blue area in the LSI image. The scalebar is 4 mm

The increase in activity in the subcooled water, as indicated by the red areas in the LSI frames in Figure 2.11, is linked to the process of constant heterogenous crystal formation and disruption at the solid-liquid interface. The edges of subcooled droplets are more active, also before nucleation. As mentioned in section 2.1, the temperature at the droplet edge appears to be lower than at the droplet center. The observation of higher activity at the droplet edges with simultaneous LSI, shows that this difference in temperature is not an artefact of the IRI technique. The increase in activity near the colder droplet edges supports the idea that a change in temperature, as observed with IRI, is not correlated with a significant change in molecular activity, as observed with LSI. This is also a strong indicator that latent heat from freezing is not (solely) responsible for the increase in molecular activity during freezing as deduced from the LSI frames in Figure 2.10e – h.

Freezing can clearly be observed by both IR and LSI. However, the weak freezing front propagating between droplets that could not be observed by IRI in Figure 2.11, could also not be observed with high temporal resolution with the LSI technique. Therefore, measurements of the freezing front propagation velocity will be performed using the IRI technique.

2.3 Measurement of dendrite, bulk or MLL freezing front propagation velocity

Within a certain range of freezing front intensities, given by the temperature difference before and after freezing (ΔT_n), the MLL freezing front propagation can be observed with IRI. To extract information from this data that could characterize the front propagation mechanism, an analysis method was developed. A consistent method allows for the characterization of the effect of different environmental, material and surface properties on the mechanism.

Methodology

A manual freezing front tracing method using ImageJ was developed. The frozen area in each frame was traced and its area and perimeter registered. As illustrated in Figure 2.13, the area growth rate G of the freezing front propagation is the difference of the total frozen area ΔA between two subsequent frames, separated by timestep Δt.

$$G = \frac{\Delta A}{\Delta t}$$

The area growth rate is expressed in units of mm^2/s and depends on the size of the observation window. To be able to physically connect it to the mechanism of freezing front propagation, it has to be normalized to a length. The most straightforward way to proceed, is by assuming an ideal situation, where the observation window is considered to be a unit cell, as depicted in Figure 2.12. When a straight front propagates along this unit cell, the newly frozen area ΔA can be obtained from the frontline length $L_{frontline}$ and the distance traveled at velocity $G^*_{frontline}$, within the timestep Δt, which yields the equation for the newly frozen area $\Delta A = L_{frontline} \cdot (\Delta t \cdot G^*_{frontline})$. As $G = \Delta A/\Delta t$, it suffices to divide the area growth rate G by the length of the frontline $L_{frontline}$, to obtain $G^*_{frontline}$.

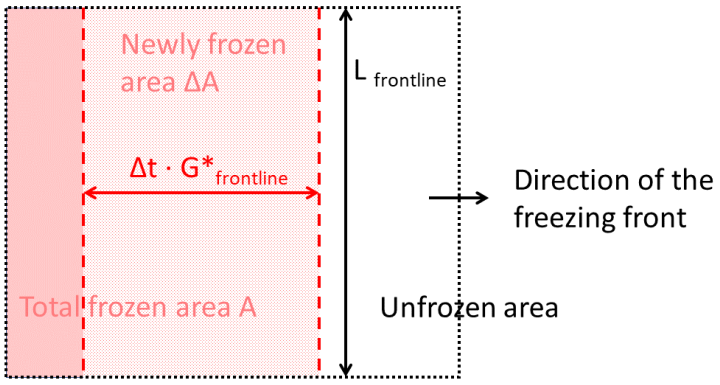

Figure 2.12: Sketch of the normalization of area growth rate G (mm^2/s) to front velocity G^* (mm/s), when the observation window (dotted line) is a unit cell of a straight propagating front. The unit cell is divided into the total frozen area A (red + pink area) and unfrozen area (white area within unit cell) by the frontline (red dashed line). The newly frozen area ΔA (pink area) is the area that has just frozen between time t and $t - \Delta t$. The distance Δx between the current frontline position at time t and the previous frontline position at time $t - \Delta t$ is $\Delta x = \Delta t \cdot G^*_{frontline}$. This yields $\Delta A = L_{frontline} \cdot (\Delta t \cdot G^*_{frontline})$

As illustrated in Figure 2.14, the approximation of the straight frontline is not realistic for small samples. Due to the proximity of the nucleation site, possibly within the observation frame, the frontline will be curved and its length will change from frame to frame. To be able to extract a normalized area growth rate G^* in this situation, the previous method is adapted. For this method, the 'passive frontline' is defined as the boundary length $L_{boundary}$ representing overlapping length of the circumference C of the frozen area

A and the boundary of the observation window. The part of the circumference of the frozen area A that is not in contact with the boundary of the observation window is called the 'active frontline'. As illustrated in Figure 2.13a, the active frontline can advance, whereas the passive frontline can't, making this the only part of the front that will contribute to the area growth rate. The length of the active frontline $L_{frontline}$ can now be obtained by subtracting the passive frontline $L_{boundary}$ from the circumference C. As shown in Figure 2.13b, the active frontline velocity $G^*_{frontline}$ is calculated by dividing the difference in frozen area ΔA. by the time Δt by the length of the active front line of the previous frame $L_{frontline\ n-1}$. Ideally, the average frontline between two frames should be chosen to determine the actual front velocity between those frames. The choice for the use of the active frontline length of the previous frame is made to simplify calculations. A choice for the active frontline length of the current frame would effectively be the same simplification.

$$G^*_{frontline} = \frac{\Delta A}{\Delta t \cdot (C_{n-1} - L_{boundary\ n-1})}$$

The front propagation can be too complex for tracking of the active frontline length. Therefore, a second normalization is proposed, using the circumference of the frozen area of the previous frame C_{n-1}. This parameter, $G^*_{perimeter}$ averages the velocity over the whole frozen area that lies within the observation window and is much simpler to compute.

$$G^*_{perimeter} = \frac{\Delta A}{\Delta t \cdot C_{n-1}}$$

Ideally, the surface does not contain any large liquid water droplets. Some of the tested surfaces did have deposited or condensed water droplets, either to benchmark the propagation of a freezing front through a molecular liquid layer or to observe their impact on the front nucleation. The freezing front propagation through droplets occurs with the higher bulk freezing velocities, increasing the measured velocities of other freezing front propagation measurements, as illustrated in Figure 2.13c. To be able to compare the growth rates of the freezing MLL on all tested surfaces, the frozen area A could be corrected with the area of large droplets within the observation window, yielding A_{-d}. Using this corrected area, a third parameter, $G^*_{-d\ frontline}$ could be computed.

$$G^*_{-d\ frontline} = \frac{\Delta A_{-d}}{\Delta t \cdot (C_{n-1} - L_{boundary\ n-1})}$$

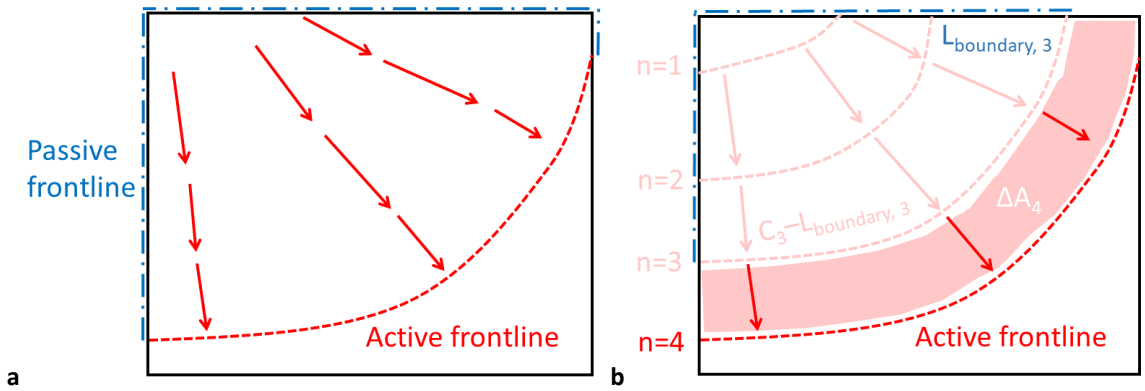

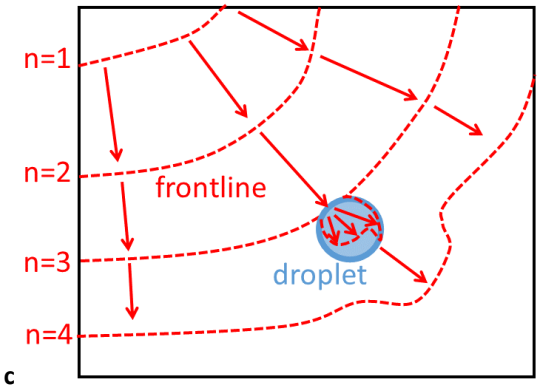

Figure 2.13: Illustration of front propagation through observation frame. (b) The frame edge is Part of the registered perimeter and acts like a passive frontline. (c) The encounter of a liquid droplet by the freezing front significantly increases its velocity. This increase in velocity can be taken into account, by subtracting the area of the frozen part of a droplet from the total frozen area ΔA, yielding ΔA_{-d}

This method assumes a frontline that is constantly propagating. If a part of the active frontline does not move from one frame to the next, it is considered to be 'passivated'. The length of the passivated frontline can be measured with the ImageJ tracing tool and is subtracted from the active frontline, along with the passive frontline already being subtracted to obtain $G^*_{frontline}$. When the passivated part of the frontline starts moving again, it is 'activated' and its length is not subtracted from the active frontline length anymore.

Results and discussion

To see if the previously described method to analyze the freezing front propagation velocity works, two tests are performed. The first test surface is a PVDF thin film on a glass substrate with a condensed molecular liquid layer (MLL). To achieve the condensed MLL, the sample was held at $T_{surf} = 10°C$ (named T_h, for 'holding temperature') for $5s$ (named t_h, for 'holding time'), before the surface was cooled down towards $T_{surf} = -20°C$. The test is performed in a controlled lab environment with $RH = 55\%$ and $T_{env} = 22°C$. Figure 2.14 shows the wide range of area growth rates G, between 175 and $545\ mm^2/s$ and active frontline velocities $G^*_{frontline}$, between 26 and $64\ mm/s$. In appendix E, some representative frames are shown of the freezing front propagation over the sample. Nucleation occurred within the observation window and the freezing front did not propagate outside of this window. The values for G, $G^*_{frontline}$ and $G^*_{perimeter}$ are plotted against the time after nucleation and always start two frames of timestep $2 \cdot \Delta t = 0.04s$ after the nucleation time delay t_n.

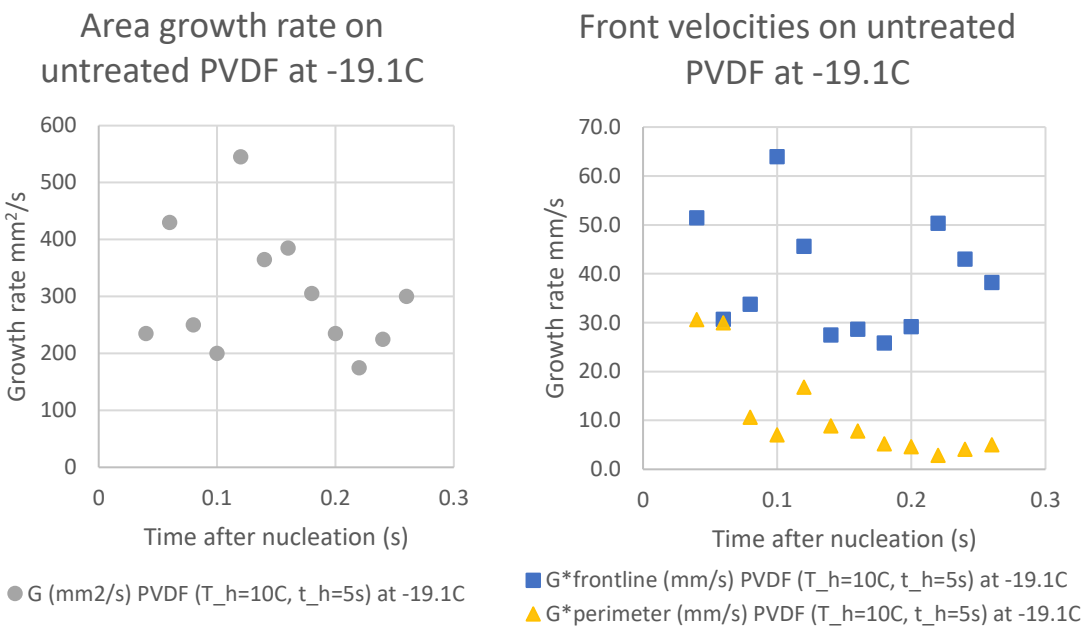

Figure 2.14: Results of a freezing experiment with condensed MLL on a PVDF thin film with $T_n = -19.1°C$ and $t_n = 47.12s$, using the ImageJ tracing method to obtain the (a) area growth rate G and (b) the active frontline velocity $G^*_{frontline}$ and average front velocity $G^*_{perimeter}$. Freezing front propagation on PVDF, with condensed MLL and with large droplets

In the graph in Figure 2.14b, two main observations can be made. Firstly, the large spread in $G^*_{frontline}$, due to the frontline switching from active to passive and being activated again, within the observation window. This conclusions was drawn by comparing the graphs at the original IR images (Freezing front propagation on PVDF, with condensed MLL and with large droplets) Apparently, $G^*_{frontline}$ is suitable to determine the activation and passivation of the frontline. Secondly, the difference between $G^*_{frontline}$ and $G^*_{perimeter}$ is very apparent. $G^*_{perimeter}$ does not show the bursts, especially towards the end of the front propagation and decreases to values well below the values of $G^*_{frontline}$. Therefore, $G^*_{perimeter}$ is considered to represent an average freezing front velocity of the total frozen area, decreasing when part of the frontline is passivated. As the calculation of $G^*_{perimeter}$ did not involved manual tracing of the passivated frontline, it was less labor intensive and less prone to human error or bias.

The second freezing test was performed to evaluate the effectiveness of eliminating the effect of large droplets during the freezing front propagation analysis, as well as the effect of small condensed droplets on the front velocities. Figure 2.15a-b illustrates the elimination of bulk freezing in droplets, transforming G to G_{-d}, $G^*_{frontline}$ to $G^*_{frontline-d}$ and $G^*_{perimeter}$ to $G^*_{perimeter-d}$.

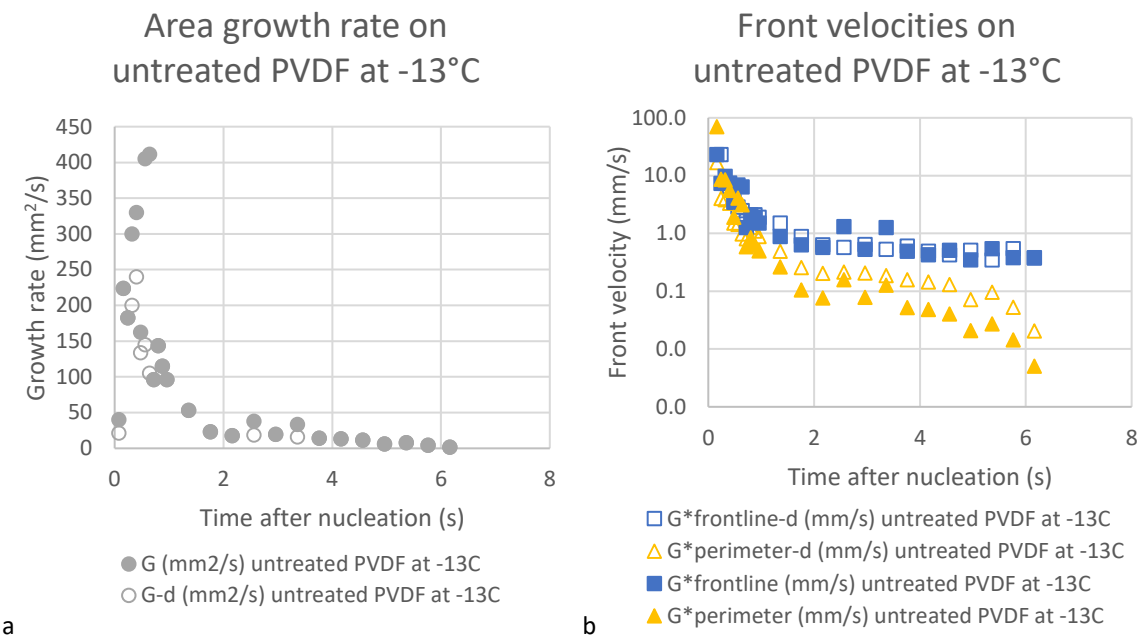

a b

Figure 2.15: (a) Uncorrected area growth rate (full circles) and area growth rates without the large bulk freezing velocities of large droplets (empty circles) (b) Uncorrected freezing front propagation velocities (full indicators), as well as front velocities where the fast bulk freezing droplets have been eliminated (empty indicators). The average freezing front propagation velocity $G^*_{perimeter}$ (yellow triangles) decreases in value with time and the active frontline velocity $G^*_{frontline}$ (blue squares) remains constant over time. Several IRI frames of the corresponding freezing experiment are given in appendix E.

In Figure 2.15a-b the normalization of the area growth rate G to obtain $G^*_{frontline}$ clearly yields a constant value for the front velocity. The initial decrease of $G^*_{frontline}$ corresponds to an actual slowing down of the front, visible in the IR images in appendix E. The front can also be observed to stabilize at a lower front propagation velocity through the small condensed droplets in these IR images, at velocities below $1\ mm/s$, corresponding to dendrite growth mechanism reported by Guadarrama-Cetina et al. [59] The area growth rate G and average frontline velocity $G^*_{perimeter}$ show a linear decrease due to the increase in total frozen area A and circumference C, resp.

Using $G^*_{frontline}$ and $G^*_{perimeter}$ and the difference between the two, different phases in MLL propagation can be identified. A first phase features very fast local growth. After $15-20\%$ of the time it takes to fully freeze the sample, the growth stabilizes on a lower level. The growth then gradually decreases and drops towards 0 mm/s towards the end. This behavior can be seen on all surfaces for very different timescales, hinting towards a geometrical effect. The effect could be due to the change in radius of curvature of the frontline. This radius is very small (convex) at nucleation, goes to infinity during normal freezing (straight) and becomes negative (concave) when the front fills up the last unfrozen areas. In the last phase the front is therefore hindered by areas that are already frozen.

To summarize the results of the first two initial tests, the calculation and newly understood physical interpretations of the parameters G, G_{-d}, $G^*_{frontline}$ and $G^*_{perimeter}$ are given in Table 2.2.

Symbol	Unit	Meaning	Calculation
G	mm²/s	Area growth rate	$G = \Delta A/\Delta t$
G_{-d}	mm²/s	Area growth rate with droplets subtracted	$G_{-d} = \Delta A_{-d}/\Delta t$
$G^*_{perimeter}$	mm/s	Front propagation velocity averaged over the whole liquid-solid boundary, limited by the frame boundary length	$G^*_{perimeter} = \Delta A/(\Delta t \cdot C_{n-1})$
$G^*_{frontline}$	mm/s	Front propagation velocity averaged over the active frontline, not limited by the frame boundary length	$G^*_{perimeter} = \Delta A/(\Delta t \cdot (C_{n-1} - L_{boundary\ n-1})$

Table 2.2: Growth rates and velocities that describe front propagation

Apart from the shape of the front, the shape of the observation window is also expected to influence the area growth rates and front velocities in Figure 2.15. To understand this influence, three simple cases are simulated, as depicted in Figure 2.16. In each case, a straight front propagates at a constant velocity of $56.5\ mm/s$ over a surface. The first case has a front that travels straight from the top of the observation window to the bottom. In the second and third case, the front is tilted $15°$ and $45°$, resp. These fronts are 'captured' with a time resolution $\Delta t = 0.02s$, just like in the actual IRI process.

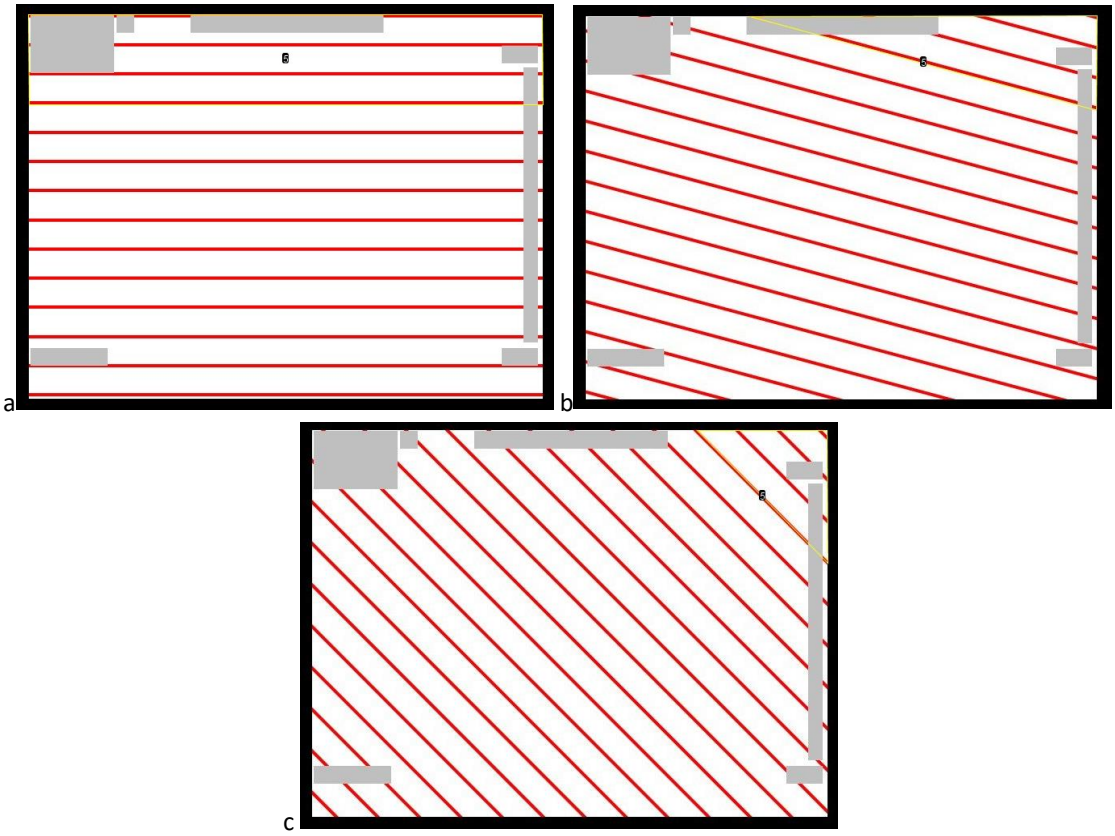

Figure 2.16: The fifth frame of each of the three cases, where a straight front is simulated that propagates over the surface at 56.5 mm/s. The front position (yellow line) is measured in time steps of 0.02s (red lines). The front propagates at different angles in each case, namely (a) $0°$ (b) $15°$ and (c) $45°$, for which the resulting area growth rates, average and active front velocities are given in Figure 2.17. Each of the image sequences for the three cases was generated with MS PowerPoint©, including placeholders (grey areas) for the areas that are obscured by the IRI FLIR software for reporting of the image title, time and temperature.

In each of the three cases, the sequence of 'captured' frames is analyzed with ImageJ and the resulting area growth rates and front velocities are plotted in Figure 2.17.

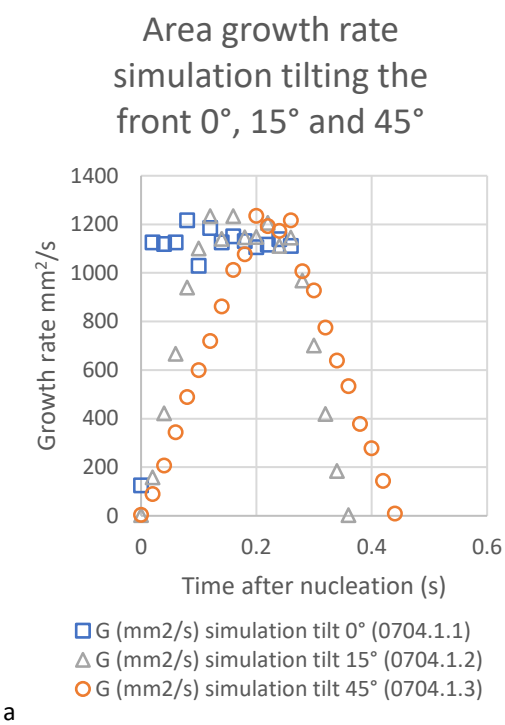

a

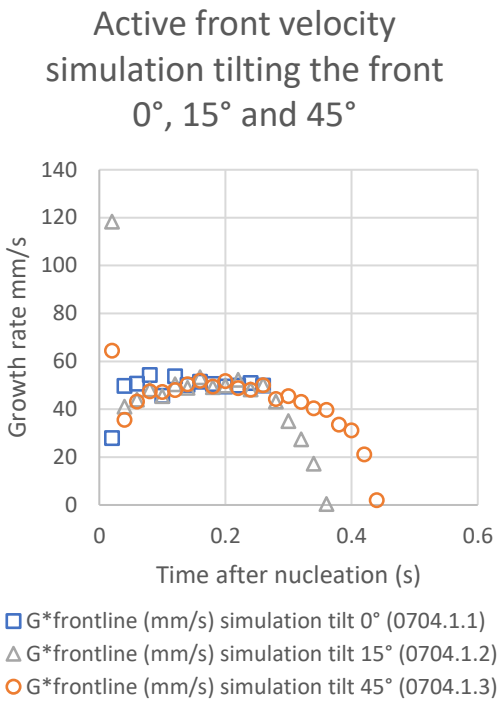

b

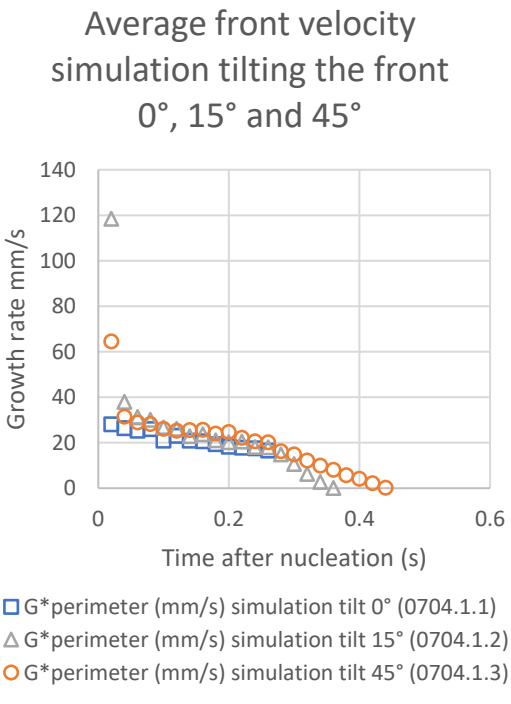

c

Figure 2.17: A simulation of a straight frontline passing over the surface reveals that its orientation w.r.t. the observation window influences (a) the area growth rate G, (b) the active front velocity $G^*_{frontline}$ and (c) the average front velocity $G^*_{perimeter}$. The area growth rate has a limited time window of accurate growth rate, the average front velocity decreases linearly as the front fills the fram, but the active front velocity remains approximately constant around the simulated front velocity of 56.5 mm/s.

The first thing that can be observed for the area growth rate G, shown in Figure 2.17a, is the decrease in initial slope of the graphs at higher angles of tilt of the simulated fronts. This happens when the front enters the frame from a corner and more and more of the active front will become visible until one vertex of the observation window is fully passed by the front. Until the front has covered a second vertex, the amount of visible area that is frozen every timestep is constant. This results in a plateau of the area growth rate. The width of this plateau decreases with increasing tilting of the front, at least up to $45°$. The height of the plateau increases with higher angles of tilt up to $45°$, by a maximum factor of $\sqrt{2}$ for a square observation window. It is surprising how much the area growth rate G oscillates around this plateau value, even for the simple simulations of an idealized situation, with a straight front line. This suggests an uncertainty of about $200\ mm^2/s$, intrinsic to the method of manual front tracing. It seems like there is an infliction point around $0.26s$ for all tilt angles. Here, the plateau ends and values for the area growth rate (and also front velocities) start to decrease. The coincidence of these points is just that, a coincidence. Namely for tilt angles of 0°, 15°, 30°, 60°, 75° and 90°, the times at which these infliction points are expected to occur, are respectively 0.26s, 0.26s, 0.24s, 0.26s, 0.32s, 0.34s and 0.36s. After this infliction point, where the front has also covered a second vertex of the observation window, the value for the area growth rate decreases with a constant slope, opposite to the initial slope. This decrease is therefore also slower for higher angles of tilt up until $45°$. The total freezing time is obviously longer for tilted fronts in Figure 2.17, as more sequential frontlines become visible when they travel at a tilt angle. For the current aspect ratio of the observation window, there is a maximum number of frames to be observed between a tilt of $45°$ and 60°.

In Figure 2.17b, the average front velocity $G^*_{perimeter}$ is plotted over time. As mentioned earlier, the first measurement point is at the second frame. The first measurement point is very inaccurate for tilted straight fronts, due to the magnification of small human error in the measured total frozen area A and circumference C. This infers that small front propagations at the edge, which occur frequently in the IRI process, are hard to characterize accurately. From the second measurement point, measured values are consistent. Unfortunately, the $G^*_{perimeter}$ values consistently underestimate the actual front velocity value of $56.5\ mm/s$ for all tilt angles. There is no plateau, but a steady decrease in value. This decrease corresponds to the area growth rate A divided by an increasing circumference C. The slope of the linear decrease in average front velocity changes twice for the tilted fronts. Each of the two infliction points occurs when the front has completely covered a vertex of the observation window. They are located symmetrically around the time it takes the freezing front to cover half of the sample. A last observation is the more gentle change in slope for angles of tilt closer to $45°$.

The active front velocity $G^*_{frontline}$, as plotted in Figure 2.17c, has some features similar to the average front velocity. The first measurement point is also located at second frame. The first measurement point is inaccurate as well, meaning it will be impossible to measure small bursts of MFL propagation accurately, if they are not sustained over several frames. From the second measurement onwards, the values of the active frontline velocity are more accurate than those of the average frontline velocity. The active front velocity stabilizes around a value of $50\ mm/s$, while the actual value is $56.5\ mm/s$. $G^*_{frontline}$ is expected to be more sensitive to human errors in the manual tracing method, compared to $G^*_{perimeter}$. An error in the measurement of the length of the active frontline will be magnified more, as it is larger with respect to the active frontline than with respect to the circumference C of the total frozen area.

It is clear that the active frontline velocity $G^*_{frontline}$ is the most reliable parameter to determine the value of the front velocity for a straight front propagating at constant velocity over the whole surface. The front can only be observed within the observation window, so the freezing is not analyzed on the basis of a representative unit cell. A solution would be higher temporal and special resolution of the front. A second solution would be to automate the tracing for scalability, reproducibility and error estimation. Combining these two solutions would allow for local front calculation, for example with small square observation

windows, tilted in the direction of the front velocity, as illustrated in Figure 2.18. The implementation of both solutions is absolutely necessary, as straight fronts rarely occur and the measurement of the active frontline is impractical for small, concave or convex fronts and frontlines that are locally or temporarily deactivated.

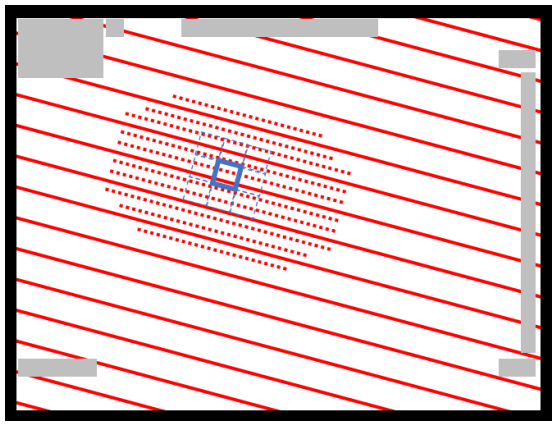

Figure 2.18: Unit cell method, using small unit cells (blue full and dashed squares)to make the computation of the local front velocity more reproducible than the manual method as used in this thesis. This method needs higher spacial and temporal accuracy (red dashed lines) than is currently available in the IRI setup described in section 2.1.

2.4 Conclusion

To answer research subquestion 1.1 (“What experimental techniques can be used for the qualitative and quantitative observation of the freezing of the MLL?”) was addressed by building a cooling system was constructed that could cool samples to $-15°C$. An infrared camera and an a laser speckle interferometry (LSI) setup were employed to observe nucleation qualitatively. The IRI setup could also identify regions with different reflectivity to the local contact angle. This was attributed to the presence of a molecular liquid layer of water (MLL), causing a difference in droplet growth mechanism. The infrared imaging (IRI) technique and test process registered the nucleation time delay t_n and nucleation temperature T_n, allowing for quantitative analysis of freezing events in sessile and impacting droplets, as well as in the MLL. By combining the IRI technique and LSI, a novel freezing front mechanism could be observed to transmit nucleation between droplets. The freezing mechanism seemed to be retarded by regions with higher contact angles. When the freezing volume becomes too small, the latent heat released by the MLL freezing front propagation can become too little to observe with IRI. The IRI data of the freezing front propagation could be converted into the frozen area growth rate G, the average front velocity $G^*_{perimeter}$ and the active frontline velocity $G^*_{frontline}$. This involved a manual process, prone to human error and judgement. The influence of the orientation of the observation window on the measured front velocities is large for G and small for $G^*_{frontline}$, both featuring a plateau around the predicted value. $G^*_{perimeter}$ features a constant decrease, but is much easier to measure with the manual front tracing process. An automated tracing process using small unit cells would make the process faster and more repeatable.

As an answer to research subquestion 1.2 (“Which mechanisms of the freezing front propagation mechanism can be determined with the available observation methods?”), four freezing mechanisms could be clearly distinguished with IRI. Frost growth, dendrite, MLL and bulk freezing can be separated by their front velocities, which are < 0.01, 0.1, 10 and $100\ mm/s$, resp. The LSI technique allows for the following of frost formation and bulk freezing. It also showed increased molecular activity on the droplet-coating interface just before nucleation, which was ascribed to seed crystal formation and breakup. It is expected that this technique, employed for the first time to research on freezing water, could register dendrite and

MLL freezing front propagations as well. However, the spatial and temporal resolution of the camera would have to be improved.

3. Influence of MLL freezing on the formation of clear ice

Research question 2: How does the presence or absence of a frozen layer affect the ice nucleation temperature and time of an impacting droplet?

3.1 State-of-the-art of impacting droplet freezing

As described in Table 1.1, clear ice and rime ice both grow due to subcooled droplets impacting on a cold surface with $T_{surf} < 0°C$, with clear ice featuring fast-growing, transparent ice that is hard to remove. The first factor differentiating clear ice from rime ice, is the higher surface temperature at which impacting droplets nucleate, implying a higher nucleation temperature, with $-6°C < T_n < 0°C$. The second factor differentiating clear ice, is the large droplet size, with $40\ \mu m < d_{drop} < 5000\ \mu m$. These larger droplets freeze slower which allows them to smear out and form transparent, dense ice. In literature, it has not been unambiguously been proven that the difference in droplet size is the reason why large 'freezing rain' droplets, creating clear ice, are able to nucleate at higher temperatures than smaller 'cloud' droplets, creating rime ice. A reason to be skeptical of the assumption that droplet size differentiates between the formation of clear or rime ice, is that it does not explain the much higher adhesion strength of clear ice. In Table 3.1, all parameters are listed that might affect nucleation temperature, nucleation time delay and adhesion strength of ice created by impacting droplets, along with the publications on freezing of sessile and impacting droplets in the past decade.

	Parameter	**References in literature**
Environmental properties	Relative humidity	[3], [16], [17], [29], [37], [38], [39], [40]
	Environmental temperature	[16], [21]
	Droplet size	[24], [59], [61]
Material properties	Contact angle	[3], [14], [16], [17], [25], [26], [28], [53], [72], [73]
	Conductivity	[3], [16], [32], [35], [74]
	Elasticity	[29]
Surface properties	Surface temperature	[2], [17], [31], [74]
	Roughness	[16], [34], [41], [60]
	Frequency	[75], [76], [77], [78], [79], [80]

Table 3.1: All parameters affecting the nucleation temperature, nucleation time delay and adhesion strength of impacting droplets, with the most recent relevant research

In the literature listed in Table 3.1, the nucleation temperature and nucleation time delay are also used frequently for the evaluation of anti-icing performance. A low nucleation temperature and high nucleation time delay are considered to be good for anti-icing.

Antonini et al. used increased temperature to reduce icing. They studied the formation of ice on wing sections by impacting supercooled droplets. By using a heated superhydrophobic coating, they were able to keep the surface permanently ice-free, while saving 80% in the amount of energy used. On a hydrophilic surface, impacting droplets did not freeze if the surface temperature remained above 0°C. With water running over the surface from a leading edge at 40°C, towards the trailing edge of the wing section, freezing

occurred as soon as the droplets touched the area below 0°C and 'runback icing' was created. [2] This research indicates that a surface that is exposed to high humidities only triggers nucleation in flowing droplets in the areas where $T_{surf} = 0°C$. In lower humidities and possibly shorter testing times, freezing of impacting droplets occurs only when T_{surf} is well below $0°C$. However, the contact angle seems to have an effect on this nucleation temperature. Wang et al. reported a decrease in nucleation temperature with increasing contact angle. In their experiments, $10\ \mu l$ droplets didn't freeze on superhydrophobic surfaces at $T_{surf} = -10°C$ and $RH = 45\% - 55\%$, whereas they did freeze on superhydrophilic samples. The superhydrophobic surfaces also featured a 13% reduction in ice adhesion strength, as compared to the superhydrophilic surfaces. [63] At low humidities of $RH = 5\%$, freezing of impacting droplets can be fully prevented, as shown in research by Mishchenko et al., where ice did not form by impacting droplets on superhydrophobic surfaces with $T_{surf} < -25°C$. [16]

Decreasing the nucleation temperature is mainly positive for anti-icing, because droplets can be repelled by the surface before they have been able to cool down to the nucleation temperature. Eventually all droplets of water will nucleate at $T_{surf} < 0°C$, given enough time, as nucleation is a stochastic process. [17] Therefore increasing the nucleation time delay or reducing the contact time is effectively using the same strategy as reducing the nucleation temperature. The repulsion of droplets with superhydrophobic surfaces has been shown by Mishchenko et al. to prevent nucleation. Using a heat transfer model, with variable T_{surf} and a bouncing droplet model, droplet pinning could be accurately predicted at a critical T_{surf}, suggesting that heat conduction through the water-solid interface determines the nucleation time. [16] This research indicates that the nucleation time delay is critical to the freezing and suggests that it is solely determined by heat conduction. This is confirmed by Alizadeh et al. who used IRI of impacting droplets to register nucleation time delay, as they state that the increased nucleation time delay of superhydrophobic surfaces is due to lower heat conduction and lower amount of available area for heterogeneous nucleation. [3] However, both Alizadeh et al. and Mishchenko et al. worked at very low relative humidities, around $RH = 5\%$. This is in contrast with the research by Wang et al., that investigated impacting droplets with a high speed camera in the visible spectrum. At high humidities of 85 – 90% the lowest environmental temperature at which droplets rebounded or rolled of a tilted surface without freezing was $-10°C$. [63]

A factor that is important for the freezing of impacting droplets and will not be considered in this thesis, is the effect of impaction speed. Impaction speed remains hard to increase into a regime that is realistic for transonic aeronautics, while controlling relative humidity and observing freezing with high spatial and temporal accuracy. Limited progress is being made through simulation tools. Blake et al. present a 2D simulation technique for large impacting droplets at low speed, where the contact angle of the surface could be varied. Although no relevant conclusions were made yet, the goal of their line of research is specifically aeronautics and the stated goal for future research was droplets impacting at high speed. (Blake2015)

This chapter will study the difference in nucleation temperature T_n and nucleation time delay t_n of droplets landing on frozen and unfrozen surfaces, using IRI. With the same observation technique, a new freezing front has been observed in section 2, that travels faster than would be expected from a dendrite growth mechanism [59] and slower than would be expected from a bulk freezing mechanism. [21] None of the authors listed in Table 3.1, reported the control of surface freezing or the effect this might have on the obtained results for the nucleation temperature, nucleation time delay or ice adhesion strength of impacting droplets. This freezing front is only visible with IRI and Laser Speckle Imaging at high temporal and spatial resolution. The lack of public reporting on this freezing front propagation mechanism motivates the investigation of its effect on the nucleation of impacting droplets. As stated by the research question under consideration, it is hypothesized that large droplets impacting on a frozen surface will nucleate at higher T_n and shorter t_n, compared to droplets landing on a surface where no freezing front has propagated.

3.2 Effect of frozen/unfrozen surface on the freezing of impacting droplets

Methodology

To see if the nucleation temperature increases or nucleation time delay decreases when water droplets land on a frozen surface, some droplets were deposited on an unfrozen surface and some after the passing of an MLL freezing front. The test surface was a PVDF film on AA6082 aluminum substrate, which was locally plasma treated. During arc plasma treatment in atmospheric conditions, a mask of Kapton tape covered parts of the PVDF thin film, so as to preserve it in the untreated state. The local plasma treatment was not required to be able to test the current hypothesis, however it did not prevent testing and could produce initial insight. Because of the high conductivity of the metal substrate, the PVDF thin film was locally carbonated by the plasma treatment, as shown in Figure 3.1a.

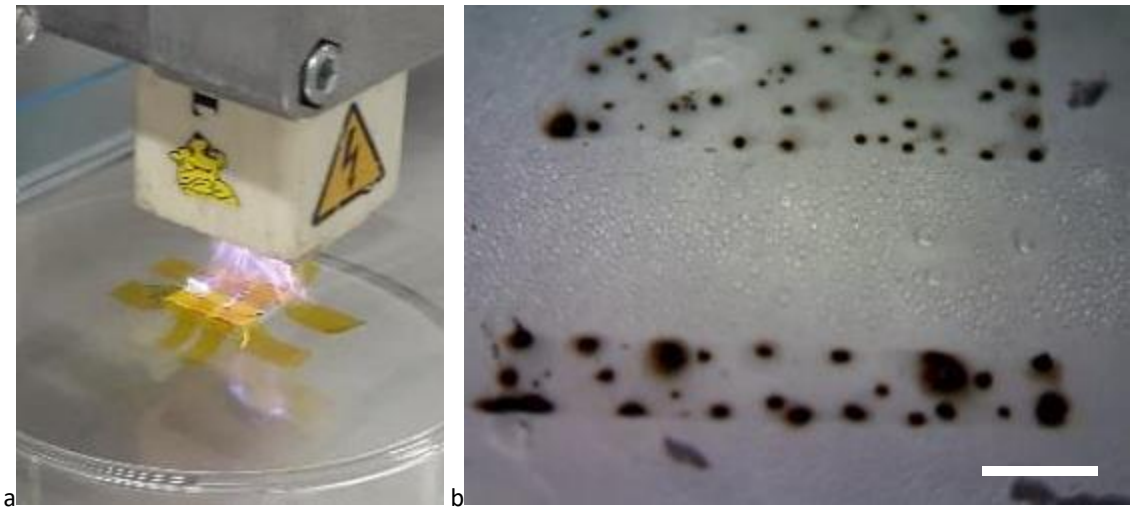

Figure 3.1: For the initial insight into the effect of surface freezing on impacting droplets, a locally plasma treated PVDF thin film on a AA6082 aluminum substrate was used. (a) The plasma treatment process exposed some areas of the film to atmospheric plasma for about $10\ s$. To preserve some of the PVDF film in its original state, some areas were covered with Kapton tape. (b) Due to the high conductivity of the metal substrate, carbonated spots appeared in the plasma treated areas. The length of the scalebar is $2\ mm$.

The test described in Figure 3.1 and Figure 3.3 inspired a more systematic test, which could observe the freezing behavior of impacting droplets on unfrozen surfaces and surfaces with a frozen layer of water. As a hypothesis, the nucleation front 'primes' the surface for freezing of impacting droplets at higher nucleation temperatures, when it propagates over the surfaces. This hypothesis was tested in a climate chamber under a relative humidity (RH) of 60% and an environmental temperature (T_{env}) $20°C$, with subcooled droplets impacting on an epoxy coating on an AA6082 aluminum substrate and on a square pattern of permanent marker ink on a Teflon substrate, as shown in Figure 3.2. The impacting droplets have a diameter of $2\ mm$. As measured by Gunn et al., the terminal velocity of these droplets is $6.5\ m/s$. [81] However, the droplets can't reach this velocity and impact below $1.7\ m/s$, the theoretical limit of a droplet in free fall from a height of $14\ cm$.

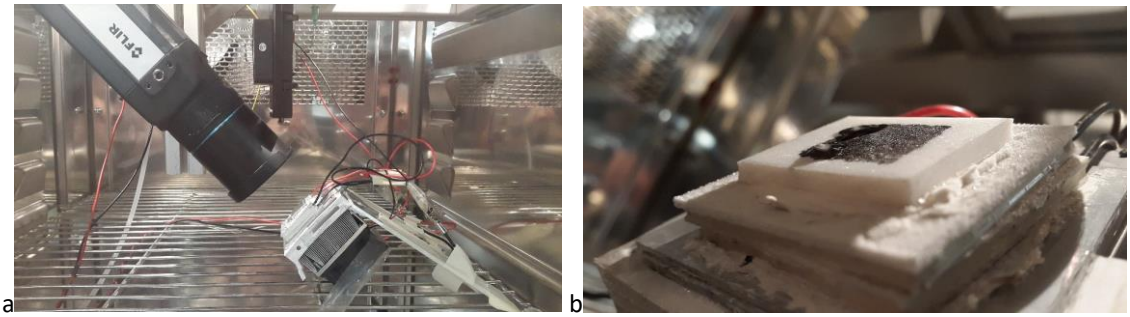

Figure 3.2: (a) Climate chamber test setup for the observation of cooled impacting droplets on epoxy on a metal substrate. The surface is tilted to allow for droplets to flow off. (b) Impacted droplets froze in a transparent form of ice. The shown sample is a square pattern of permanent marker ink on a Teflon substrate, not the epoxy film reported in the second test and only serves as an illustration of the sample placement and the formation of transparent frozen droplets.

As explained in section 1.1.3, the performance of superhydrophobic coatings for anti-icing is disputed. Results reported in the past two decades show both increase and decrease in adhesion strength, depending on the specific test circumstances. As Alizadeh et al. states, the resulting adhesion reduction force (ARF) seems to be heavily influenced by the relative humidity, with high relative humidities featuring low ARF and low relative humidities featuring very high ARF. [3] Therefore, as a third test, impacting of subcooled water droplets on a subcooled superhydrophobic surface is studied with IRI.

Results and discussion

In the first test, nine droplets at room temperature were deposited on the PVDF film in a sequence depicted in Figure 3.3. Three droplets were placed on the hydrophobic area. After nucleation of two nearby droplets that were deposited on a hydrophilic area near the bottom of the sample, they nucleate one by one. In the hydrophilic area near the top of the sample, this nucleation front also swoops over the surface, without encountering any droplets. Two drops are now deposited in this hydrophilic area where the freezing front has just passed by, with the use of a needle. They nucleate immediately, without any freezing delay. The immediate nucleation is not visible, but is inferred from the lack of a clear freezing event, while the droplets are cooling down. They have clearly been frozen, as evidenced from a later melting cycle, but no peak in latent heat is observed.

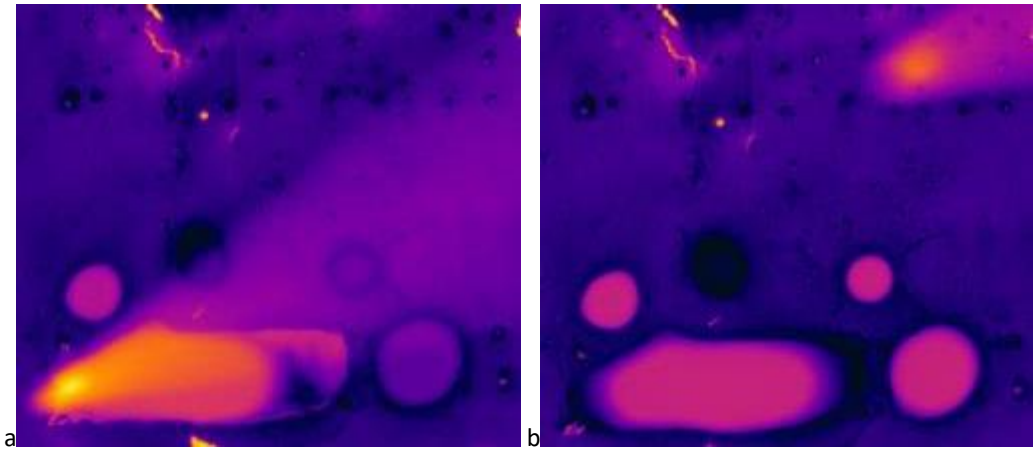

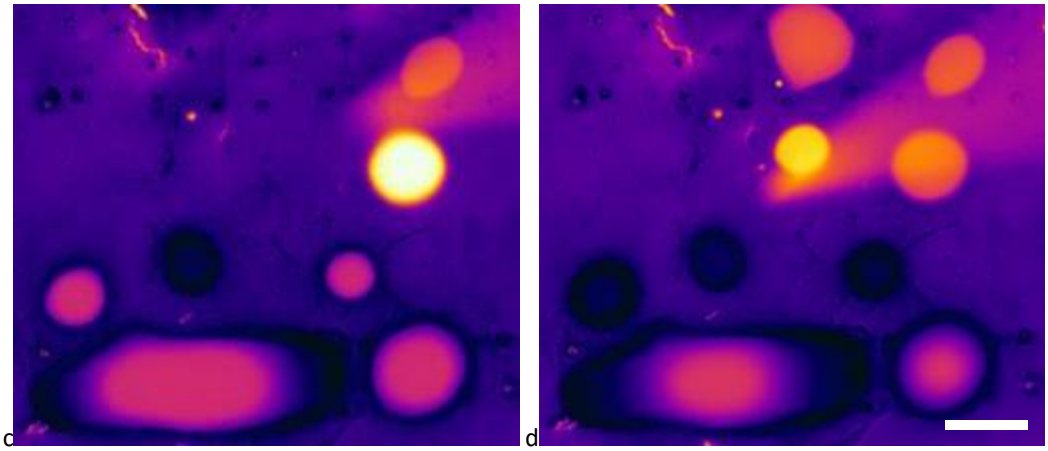

Figure 3.3: Nine droplets are deposited on a PVDF thin film on a AA6082 substrate. A strip of PVDF near the bottom of the IR image and a (partially visible square at the top of the image have been plasma treated, resulting in a hydrophilic surface with carbonated spots. in the depicted chronological sequence one can observe (a) Nucleation of liquid sessile bottom droplets after touch with a needle (b) MLL front propagation over the plasma treated areas (only visible in video) (c, d) Top droplets are deposited and freeze upon contact with surface. The scalebar is $5\ mm$

In the first run of the second freezing test, illustrated in Figure 3.2a, cooled droplets that were impacted on an unfrozen surface did not get pinned and stayed liquid as long as the surrounding surface remained liquid. This is illustrated by one of the frames taken from an image sequence in Figure 3.4. The other frames showing the first run, are included in appendix F. A droplet of $11.5°C$ impacts an unfrozen surface at $-12°C < T_{surf} < -10°C$. The three-phase boundary line is not pinned and slowly retracts until the surface tension reaches an equilibrium. The droplet cools down to $-10.0°C$ within $5\ s$.

In the second run of the second freezing test, cooled droplets were impacted on a surface that was in the process of freezing. In the test depicted in Figure 3.4, the droplet could be observed to nucleate after $t_n = 0.4\ s$ after impacting on the surface. More frames of this freezing process are included in appendix F. The temperature of the droplet was $11.5°C$ and the temperature of the surface was $-12°C < T_{surf} < -10°C$. Due to the high temperature of the droplet, the latent heat due to freezing could not be observed as clearly as with sessile droplets, so the nucleation time delay might be shorter than $0.4\ s$. It took $12\ s$ for the frozen droplet to cool down to $-10.0°C$. The nucleation temperature of $T_n = 11.5°C$ is unexpectedly high and it can be assumed that the measured droplet temperature at freezing is not representative of the temperature at the droplet-solid interface. The actual temperature on this interface should be below $0°C$, but could not be measured with the current 'topview setup'. A third run in exactly the same circumstances and using the same methodology as the second run, gave exactly the same result, namely immediate freezing of the droplet after impact.

Out of the three runs of the second test, one can conclude that large droplets freeze at high nucleation temperatures, when impacting on an epoxy surface with freezing condensed droplets at $-12°C < T_{surf} < -10°C$. The nucleation time delay is below $0.4\ s$, but should be observed with colder droplets. On an unfrozen epoxy surface at the same surface temperature, an impacting droplet does not freeze.

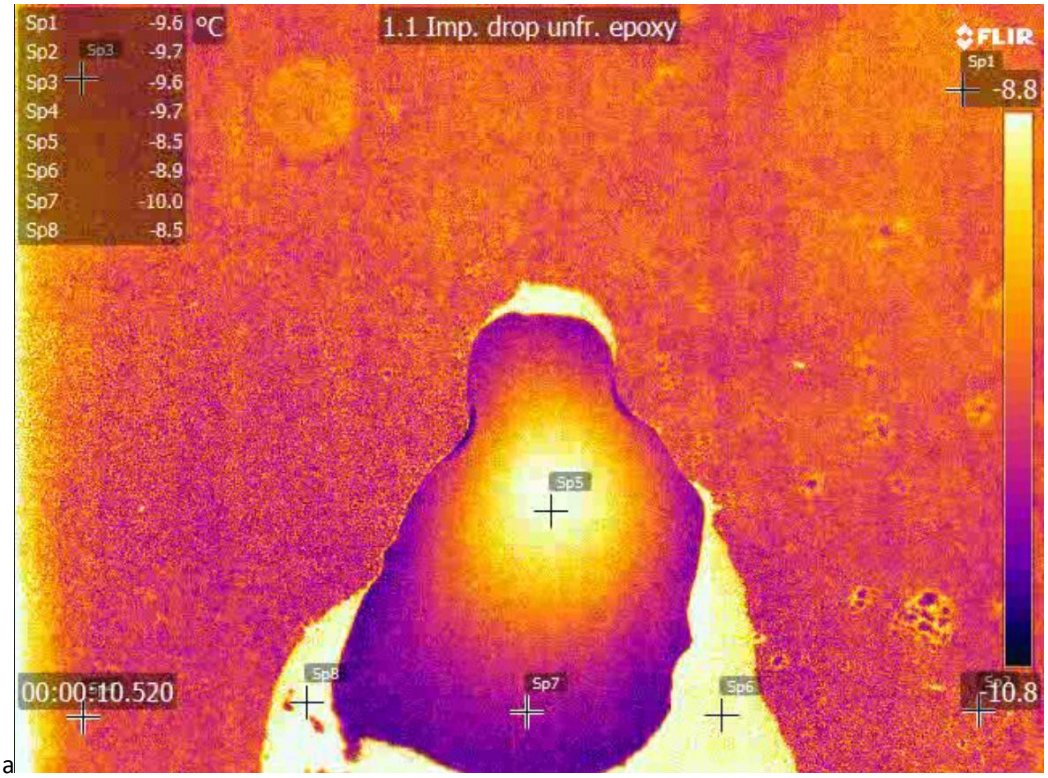

a

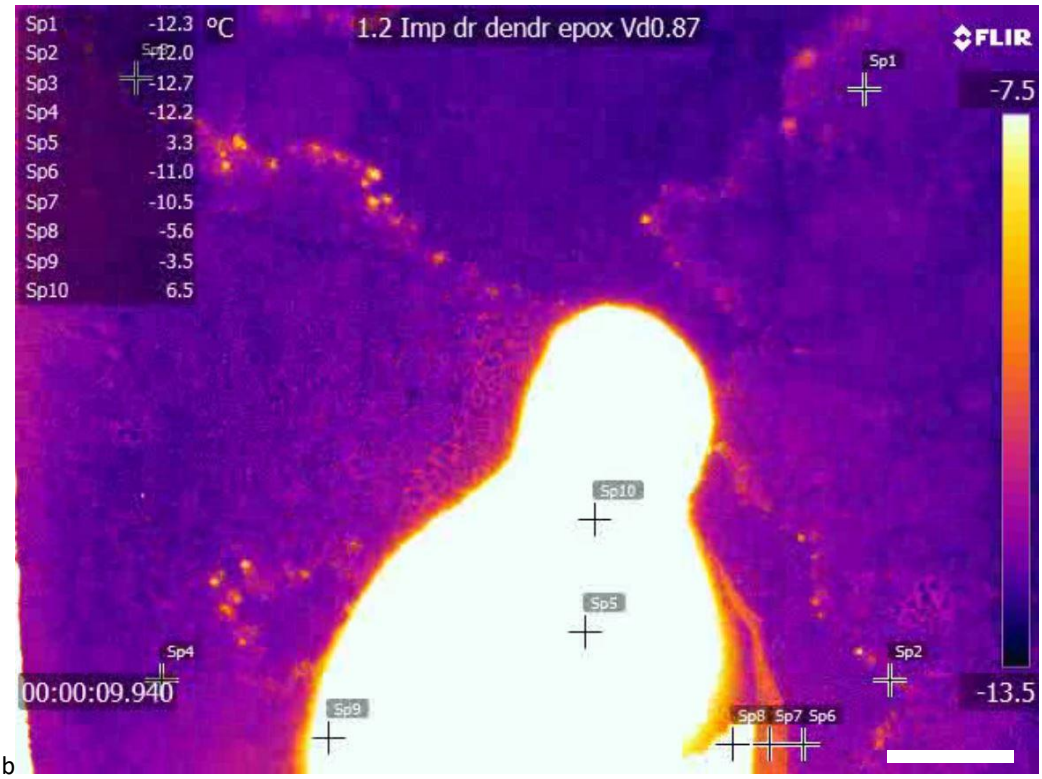

b

Figure 3.4: (a) A droplet with $T_{drop} = 11.5°C$ impacting on an unfrozen epoxy surface did not freeze and cooled down to $-10°C$ in $5\ s$, without droplet pinning. (b) A droplet with $T_{drop} = 11.5°C$ impacting on a freezing epoxy surface, froze after a short time of $t_n < 0.4\ s$. The exact location of nucleation could not be identified due to the high temperature of the impacting droplet covering the escape of latent heat. The scalebar is $2\ mm$

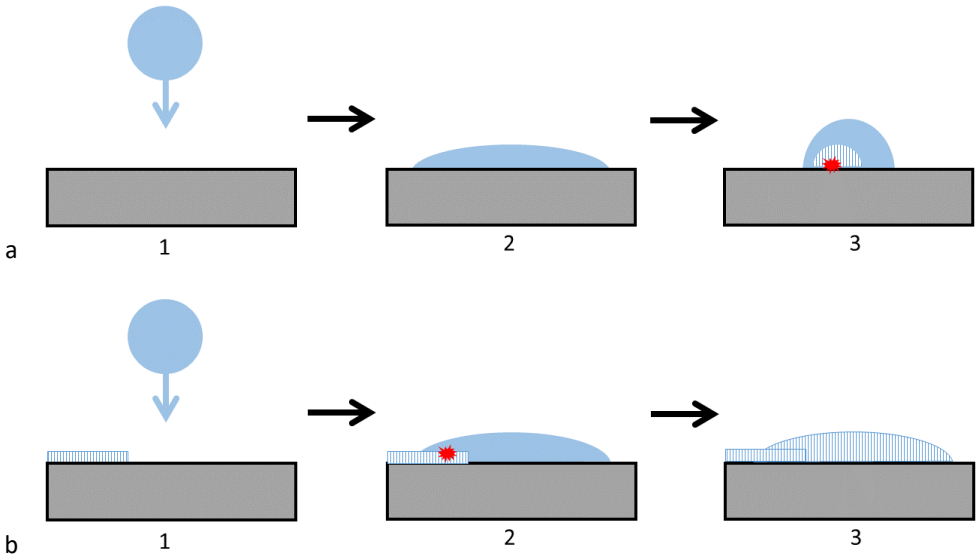

Figure 3.5: Illustration a water droplet impacting on a surface at $T_{surf} < 0°C$. (a) When a droplet impacts on a surface were no ice crystal is present, it will have time to contract. After cooling down to T_{surf}, the droplet will freeze after some time delay t_n. (b) If a droplet lands on a surface with frozen condensed droplets or a frozen MLL, the impacting droplet will nucleate immediately at high temperature. The droplet can't retract due to the pinned water-surface-air three phase boundary line and freezes slowly in a 'smeared out' shape.

The nucleation of impacting droplets on frozen surfaces and the difference with freezing on unfrozen surfaces is illustrated in Figure 3.5. This hypothesis, now supported by freezing experiments, concurs with recent research performed by Schremb et al. They observed immediate nucleation of impacting droplets on frozen surfaces with high temporal and spatial resolution in the visual spectrum.

The results of the third test are of limited use. The droplets impacting on an unfrozen superhydrophobic surface, did not nucleate and were immediately repelled by the surface. As can be seen in Figure 3.6, the large impacting droplets cleaned the superhydrophobic surface of any condensed droplet, exposing the bar metal surface. Due to the uncontrollable relative humidity at $RH = 44\%$, a lot of condensation formed on the surface. The sliding of small droplets over the surface could not be distinguished from potentially nucleating droplets, so no judgement could be made on whether the surface was freezing. Therefore it can not be concluded whether a freezing or frozen superhydrophobic surface can or can't pin impacting droplets.

Due to the uncontrollable environmental temperature at $T_{env} = 22°C$, the surface could not also be cooled below $T_{surf} < -12°C$. As reported by Wang et al., impacting droplets don't induce icing at $T_{surf} \geq -10°C$. [63]

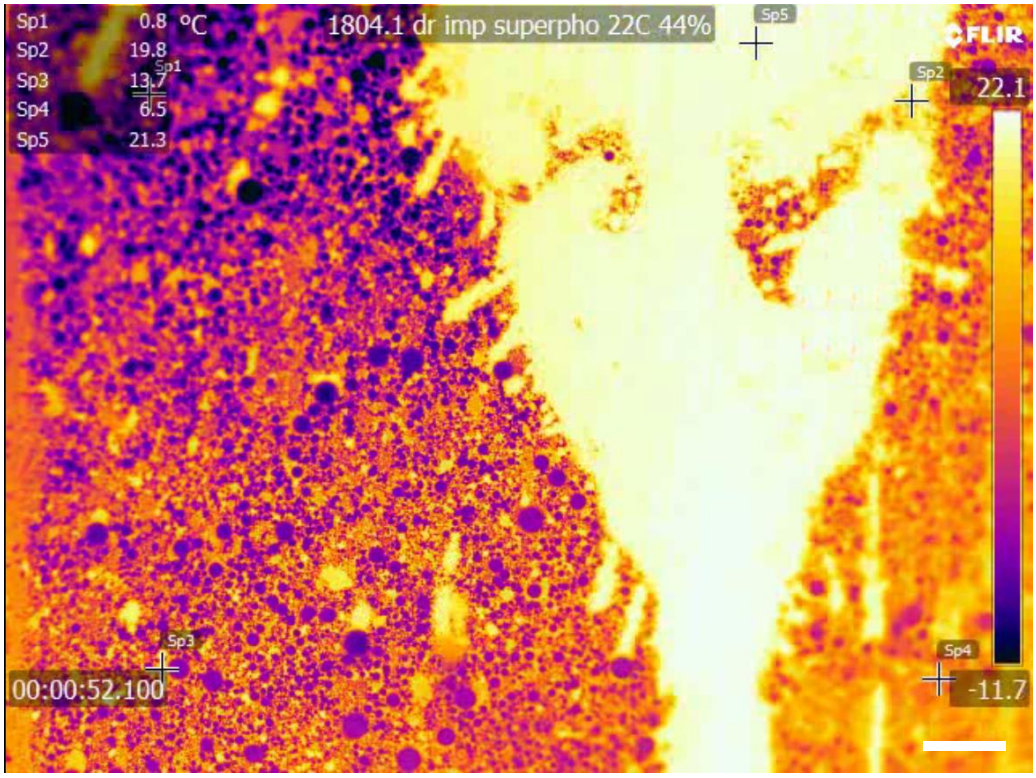

Figure 3.6: A droplet that impacts on a superhydrophobic surface at $T_{surf} \approx -10°C$ rebounds immediately before freezing. Due to the high relative humidity of $RH = 44\%$, condensed droplets are formed. When these droplets are removed by the bouncing impacting droplet, the highly reflective superhydrophobic metal surface is exposed, creating the illusion of the escape of latent heat. The white scalebar is 2 mm

The observations of the superhydrophobic surface could not resolve the conflict in literature on case-dependent increased or decreased ice adhesion strength. More systematic testing in an environment with controllable relative humidity and temperature is required to support the hypothesis that high ice adhesion on some hydrophobic samples is due to "priming" of the surface by a frozen layer on the surface, created by an MLL or dendrite freezing front propagation.

The appearance of runback icing on aircraft wings, as mentioned earlier, connects well with the observation of a droplets nucleation upon contact with ice and the hypothesis of a freezing MLL. When droplets roll over a wing after being melted at the leading edge, they nucleate at a very specific boundary. This location has been connected to the very specific temperature of $0°C$. For Antonini et al. ice formed between a leading edge temperature of $40°C$ and a trailing edge environmental temperature of $-17°C$, starting at the line of constant $0°C$ temperature. [2] The surface near the trailing edge below the critical nucleation temperature of $-10°C$ is expected to have a nucleation event in the MLL which would propagate over the whole subzero part of the surface. When a liquid water droplet runs over the surface, it is expected to nucleate as soon as it touches the frozen MLL. This process is illustrated in Figure 3.7, using the research by Antonini et al as illustration.

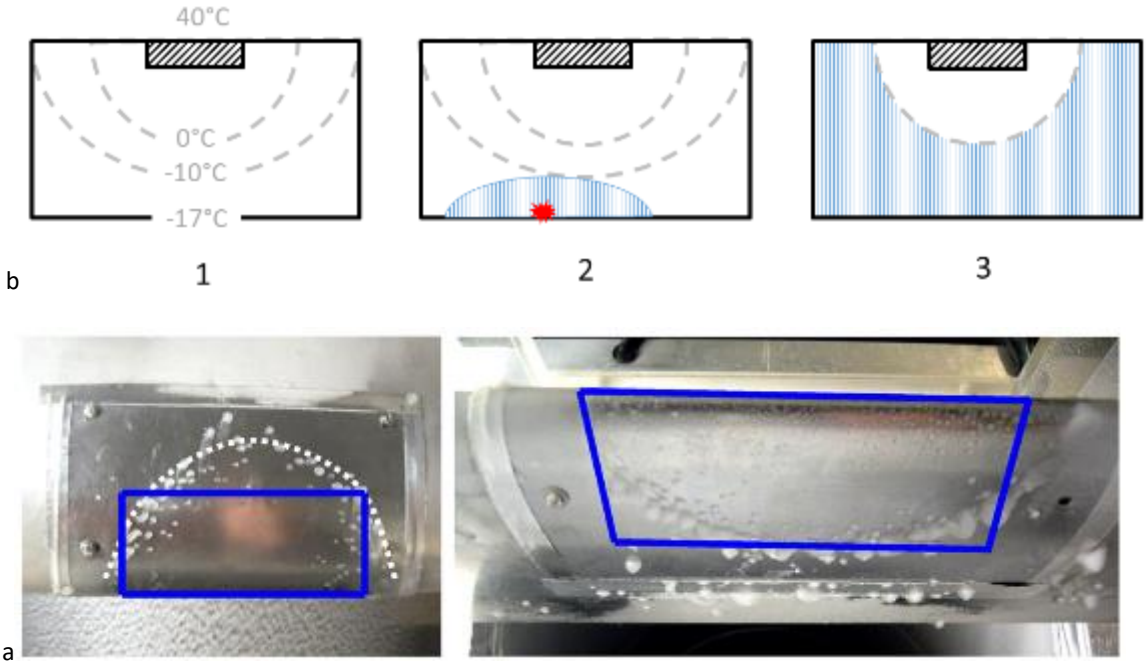

Figure 3.7: (a) When a heating element (dashed rectangle) is installed on the leading edge of an airfoil, it heats up the airfoil unevenly (interrupted grey lines). This creates a region where $T_{surf} > 0°C$ close to the heating element and a region where $T_{surf} < 0°C$ towards the trailing edge. When a nucleation event happens somewhere on the subzero region of the airfoil, the MLL will freeze up until the $0°C$ isotherm. (b) Droplets flowing over the surface after being molten by the heating element will freeze at high droplet temperatures, allowing for slow freezing and thus observable 'smearing'. [2]

Droplets freeze at relatively high nucleation temperatures when they impact on an epoxy surface that is frozen by a mixed MLL/dendrite freezing front. This is in accordance with the recent results obtained by Schremb et al. on high-speed light microscopy of impacting droplets in topview. They were not able specific as to the origin of the nucleation mechanism [61] Although an indication was given with the first test on plasma treated PVDF, it remains to be systematically proven that the same pinning and freezing process would also happen for impacted cooled droplets on a surface with a frozen layer created by a purely MLL freezing front. The observed increased nucleation temperatures are also a feature of clear ice, which motivates a further investigation of the parameters that govern the freezing front propagation. By controlling this process, nucleation of impacting droplets at high nucleation temperatures, and perhaps clear ice, could be prevented.

3.3 Conclusion

Research question 2 ("How does the presence or absence of a frozen layer affect the ice nucleation temperature and time of an impacting droplet?") was answered by impacting cooled droplets on frozen and unfrozen surfaces, while observing the droplet freezing with IRI. Short nucleation times were observed of $t_n < 0.4\ s$ for droplets impacting on frozen surfaces, which confirms the results published recently by Schremb et al. [61] As these droplets had temperatures around $11.5°C$ when impacting on the surface, high nucleation temperatures are suggested. This could explain the origin of clear ice, where slow freezing at a high subzero nucleation temperature allows for transparent ice growth and smearing out of impacting droplets. The droplets impacting on unfrozen surfaces for reference, didn't freeze upon impact. The transmission of nucleation through an MLL also explains the phenomenon of runback icing, as observed by Antonini et al. [2]

4. Governing parameters for freezing on surfaces

Research question 3: What is the influence of surface, material and environment on the ice nucleation mechanism of sessile droplets on smooth surfaces?

Now that the relevancy of a freezing front for the formation of clear ice has been established, the governing parameters of its nucleation and propagation velocity should be evaluated. If either nucleation could be delayed or propagation velocity retarded using one or more of these governing parameters, surface architectures could be designed that prevent or retard clear ice formation. A better understanding of the effect of surface, material and environmental properties on the freezing process could also help engineers, decision makers and professionals in the aeronautics industry to make better assessments of the icing risk, increasing flight safety and reducing financial risk.

4.1 Properties affecting heterogeneous ice nucleation time delay

In literature, the ice nucleation time delay is used as one of the strategies to avoid freezing of impacting droplets. Delaying nucleation of a freezing front propagation, uses the same logic and makes sure that droplets do not come in contact with the frozen layer. The first reason to avoid contact between impacting droplets and the frozen surface, is that impacting droplets might be able to bounce and leave the surface before nucleation can occur. The second reason for avoiding contact with the frozen area, is that this allows droplets to cool down and freeze at lower nucleation temperatures. In this circumstance, they might freeze faster, smear out less and reduce ice adhesion.

To increase the nucleation time delay of the freezing front, one strategy is to influence properties of the environment. Although the environmental properties are impractical to influence, the problem of icing is so urgent, that adjustment to mission profiles to ensure safety are not farfetched. Three of these environmental governing parameters are environmental temperature, relative humidity and the size of droplets in clouds or rain that impact the aircraft surface. A second strategy is to select the right materials to cover aerodynamically critical surfaces. Although many more material properties exist, only two are expected to have a significant influence on the nucleation time delay, namely the contact angle and conductivity. As a third strategy, the surface properties could be altered without changing the material. Although the selected surface properties of surface temperature, roughness, vibration and electrical charge can only be controlled with certain materials, their effects on nucleation time delay are not exclusively linked to their material.

	Parameter	Test surface
Surface properties	Surface temperature	Untreated PVDF
	Roughness	*Out of scope*
	Frequency	Top electrode of piezo element
	Electrical charge	*Out of scope*
Material properties	Contact angle	Plasma treated PVDF, epoxy, metal
	Conductivity	PVDF, epoxy, metal, Teflon
Environmental properties	Relative humidity	Epoxy, plasma treated PVDF
	Environmental temperature	*Out of scope*
	Droplet size	Teflon

Table 4.1: Properties that might govern nucleation time delay can be labeled as environmental, material or surface properties. The effect of environmental temperature, roughness and electrical charge were considered out of the

scope of the current research (grey). After a first round of sensitivity tests, the effect of droplet size, conductivity and frequency was unclear or negligible (orange), so only the effects of relative humidity, contact angle and surface temperature were studied systematically (green).

The environmental temperature could influence freezing by cooling droplets to lower temperatures before impact. Secondly, the air might extract more or less latent heat out of a freezing impacted droplet through conduction or convection at a different temperature. Mishchenko et al. states that the influence of the droplet temperature does not seem to influence the freezing process. [16] As the scope of the current thesis is to understand the freezing process and develop a coating solution, the environmental temperature is kept constant, but its influence on freezing is not characterized. Although an important property for ice nucleation, roughness is not selected either. As the scope limits the resulting coatings to non-toxic, durable and smooth, the effect of roughness is of less interest in this thesis. Roughness as a surface property is also very hard to control systematically and observe accurately, as it spans over several orders of magnitude in scale, from nm to mm. As water is a polar molecule and the interactions on the water-surface interface are basically due to the local electromagnetic fields, the electrical charge is a potential governing parameter. However, it is hard to control as a surface property. On top of that, it is hard to measure or work with the combination of small currents and voltages, definitely in the presence of humidity.

The environmental humidity and droplet size were selected candidate governing parameters for a first sensitivity study, as they are of interest to the nucleation process and relatively easy to control. The contact angle and conductivity were selected for testing as well, because material properties have the potential to be easily integrated in current aircraft coatings. They fit well within the thesis scope to investigate a non-toxic, durable and smooth solution for anti-icing on aircraft. The effect of the surface temperature as a governing parameter was studied as it is necessary to control this surface property anyway, to be able to induce freezing with the current cooling system. It is also well reported on in literature. Surface vibration was selected for an initial study, due to its novelty and inspiration from literature. The available expertise and general direction of research in the department of Novel Aerospace Materials at the TU Delft towards piezoelectric coatings also motivated the selection of this surface property.

4.1.1 Surface temperature

The property of surface temperature is used to induce freezing in every test in the current chapter and has to be wisely chosen for freezing to occur. Therefore, the nucleation temperature is a relevant parameter in every test. To be able to assess the effect of any other surface, material or environmental property, the nucleation temperature must be identical.

Methodology

As a first sensitivity test, the previously described cooling system was used, using two Peltier elements on top of a heat sink, with a fan to cool down the heat sink, as shown in Figure 2.1. The environment was a lab environment with $45\% < RH < 65\%$ and $20°C < T_{env} < 25°C$. At least 15 tests were performed, where surfaces with and without droplets were cooled down to surface temperatures between $-11°C$ and $-27°C$. After cooling to these subzero temperatures, nucleation of either large deposited drops, condensed drops or the MLL was observed through an infrared spike, as detailed in section 2.1.

Figure 4.1a shows the average nucleation time delay on the horizontal axis, for every freezing event on samples with a thin film of PVDF on a glass substrate. On the vertical axis, the average temperature is given for each freezing event. The error bars indicate the spread in nucleation temperature T_n and nucleation time t_n of droplets on the test surface. The data obtained from measurement points inside droplets is indicated with full triangles. Freezing that occurred outside droplets are represented by empty triangles.

In Figure 4.1b, the averages are split up into their constituent nucleation time delays and nucleation temperatures. Each point represents a measurement point on the surface or on a droplet. Each symbol represents a different test. Some of the tests are performed on the same PVDF thin film on glass and only the time is varied at which the sample is allowed to rest at a positive temperature before freezing (holding temperature T_h) for a certain time (holding time t_h).

Results and discussion

A shown in Figure 4.1, the first sensitivity tests demonstrated an expected sharp increase in nucleation time delay t_n at a critical nucleation temperature T_n of $-11°C$ to $-14°C$. This area of sharp increase in nucleation time, is indicated by the blue dashed area in Figure 4.1a and Figure 4.1b.

It was also expected that the nucleation time delay t_n would clearly decrease with decreasing nucleation temperature T_n. The number of water molecules required to form a stable nucleus decreases exponentially with temperature. [18] However, this was not observed. Instead, a plateau is observed in between $-27°C$ and $-14°C$, where $5s < t_n < 30s$ and T_n is independent of t_n. In this area, indicated by an orange checker pattern in Figure 4.1a and Figure 4.1b, the nucleation time delay seems to be invariant with the nucleation temperature. The first sensitivity test was not systematic enough to be able to register subtle changes, like a linear or exponential decrease in t_n.

The overlap in $t_n(T_n)$ measurements inside drops (full triangles) and on the surface outside drops (empty triangles) in Figure 4.1a suggests that there is no difference in nucleation mechanism between the two. In Figure 4.1a can be seen how the average nucleation time delay per nucleation event decreases with the average nucleation temperature for that event. By recording these events with high time and spatial resolution, the freezing of the surface and drops could be linked visually. When nucleation occurred somewhere on the surface, the crystal was unambiguously observed to travel over the surface from drop to drop. This crystal transmission is also strongly illustrated by Figure 4.1b, where nucleation time delays of drops are almost identical for all measurement points on the surface, resulting in very small (mostly invisible) horizontal error bars in Figure 4.1a. Once nucleation has taken place somewhere on the surface, nucleation time delay does not depend on nucleation temperature anymore.

This strongly supports the hypothesis that a freezing molecular liquid layer (MLL) transfers water crystallization between droplets, as discussed in detail in section 4.2. The observation that nucleation outside droplets occurred at slightly higher nucleation temperatures could be an artifact of the IRI technique or an indication that nucleation takes place in the MLL at slightly higher T_n and therefore shorter t_n. This could be a logical consequence of the stochastic nature of heterogeneous nucleation, as more solid-liquid interface is available to the MLL than to the droplets.

Figure 4.1a seems to indicate that MLL freezing occurs in narrow time bands of $5\,s < t_n < 25\,s$ and $-20°C < T_n < -14°C$, whereas droplet nucleation features a wider spread of $10\,s < t_n < 80\,s$ and $-12°C < T_n < -27°C$. As the observation of the MLL freezing mechanism has not been studied before, some caution is advisable here. It is possible that the current observation technique or test setup does not allow detection of the MLL below certain values for the front intensity ΔT. The influence of the MLL thickness on the front intensity is illustrated in Figure 4.27, in section 4.2.3 explaining the effect of relative humidity.

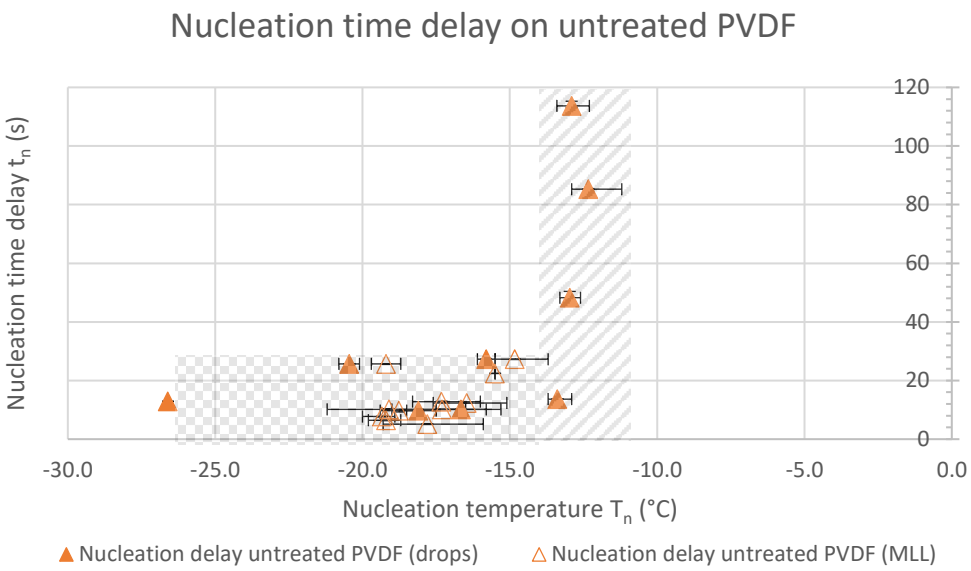

a

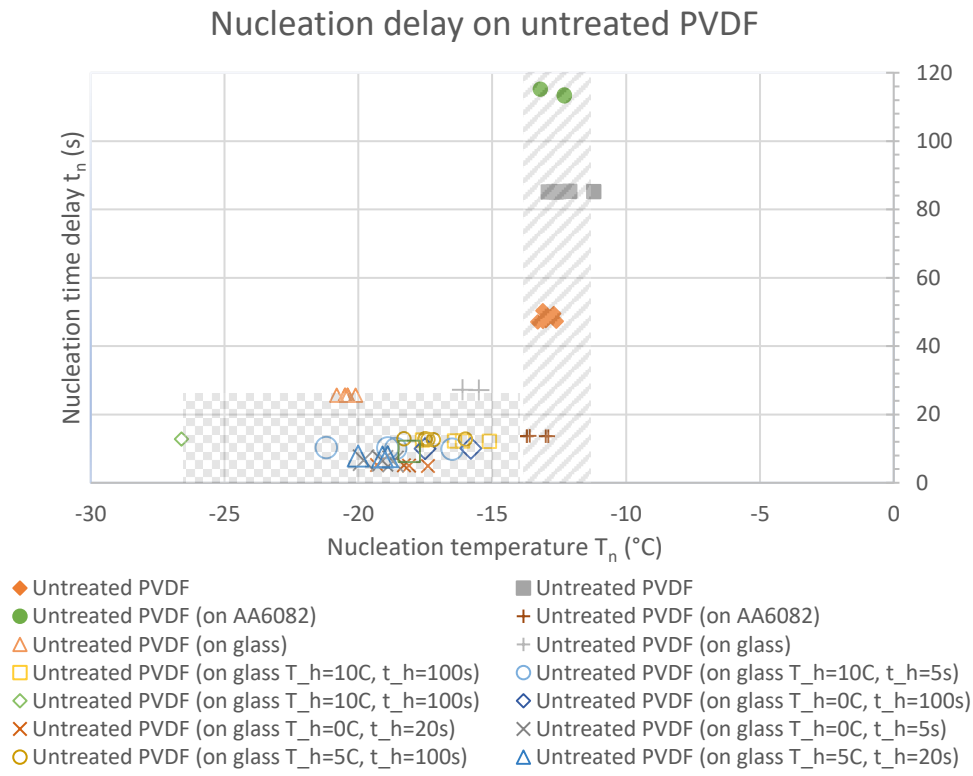

b

Figure 4.1: Effect of Nucleation temperature on nucleation time delay on untreated PVDF in room humidity and temperature, showing (a) averages per freezing cycle and spread of nucleation temperature of the MLL (empty orange triangles) and droplets (full orange triangles) (b) the different nucleation temperatures and time delays within every test run, with small spreads in nucleation time delay inferring simultaneous nucleation of condensed or deposited droplets. From -11°C to -14°C a critical nucleation temperature is indicated (hatched area) and from -14°C to -27°C a range of temperature invariance is indicated (checkerboard area). In the graph labels, 'T_h' stands for the holding temperature T_h in $[°C]$ at which the surface is kept prior to the freezing experiment. Similarly, 't_h' stands for the holding time t_h in $[s]$ for which the surface was held at T_h.

The clearest nucleation freezing event to observe, is nucleation of the deposited (large) and condensed (small) droplets, due to the large amount of latent heat infrared radiation released with freezing. The MLL mechanism was often less clear to observe. As discussed in section 4.2, the time and temperature at which the MLL is allowed to grow in thickness before the freezing experiment starts, correlates with the IR intensity during MLL nucleation. The nature of lowering intensity with decreasing holding time and increasing holding temperature from 'clear' to 'barely visible' to 'invisible' adds credence to the criticisism that the MLL also occurs outside the range of $5\ s < t_n < 25\ s$ and $-20°C < T_n < -14°C$, but is just not observable with the current IRI technique.

There are valid outliers, with significantly lower nucleation temperature or higher nucleation time. They are interpreted as outliers inherent to the stochastic nature of ice nucleation. This conclusion is acceptable, as freezing is observed to become more intense for these outliers.

The $t_n(T_n)$ curve gives nucleation time as a function of nucleation temperature. The exact temperature is hard to control with the cooling system during the sensitivity analysis of the effect of the other environmental, material and surface governing parameters. However, as the temperature is easy to observe with IRI, a $t_n(T_n)$ curve can be created for every variation of these governing parameters, while keeping the other parameters the same. A change to the curve due to a change in one of the properties will show the effect of that property on the nucleation behavior of sessile droplets or the MLL.

4.1.2 Frequency

Ultrasonic vibrations are being used in the food industry for fast and controllable freeze drying. [75] Already in a patent application in 1992, Acton and Morris proposed to use vibrations of $16–100\ kHz$ for the crystallization of water. The optimal frequency should be in the range of $20–40\ kHz$. In the process of freeze drying a few large ice crystals are desired. Using only up to $5\ s$ and preferably below $1\ s$ of ultrasound irradiation at a temperature close to the freezing point, results in formation of large ice crystals. [75]

Methodology

To assess the effect of vibration on nucleation time delay and nucleation temperature, a piezo-electric element was attached with thermal paste on top of a Peltier element. Sessile droplets were deposited on top of the top metal electrode, with droplet diameters of $2\ mm < d_{drop} < 5\ mm$. A frequency sweep was performed from $5\ Hz$ to $5\ MHz$. At every frequency, the surface temperature was gradually decreased at the same rate until freezing was observed. Every sixth measurement was done without surface vibration (frequency of $0\ Hz$), to benchmark the effect of vibration on the freezing behavior.

a 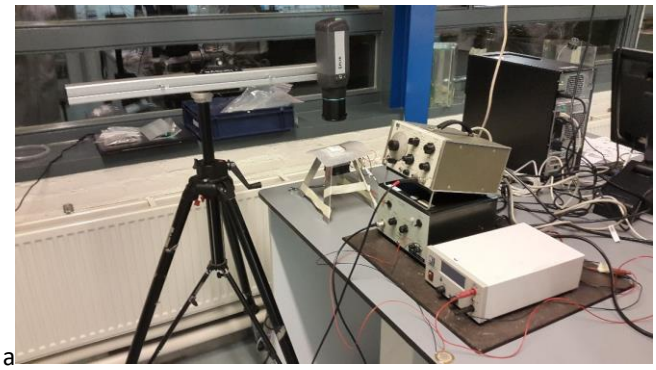 b 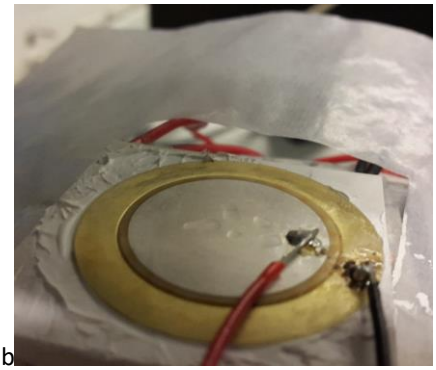

Figure 4.2: (a) The setup that measured the effect of vibration at room temperature and humidity. An IR camera looked perpendicularly on the top electrode of a piezoelectric element that received a signal from a source and signal

amplifier. The frequency of vibration was varied between $5\ Hz$ and $5\ MHz$. (b) Sessile droplets were manually deposited on the top electrode of a piezoelectric element with a syringe, that was installed on the cooling system.

The resulting relationship between frequency and the nucleation temperature T_n is given in Figure 4.3. The error bars indicate that several experiments have taken place at that frequency and give the maximum and minimum values measured for the nucleation temperature. The nucleation temperatures at $1\ Hz$ represent the values measured without vibration, as $0\ Hz$ can't be shown on a logarithmic scale.

The nucleation time delay t_n is not registered. Although its dependency on surface vibration might be interesting, the cooling at constant cooling rate does not allow for registration of a representative and reproducible nucleation time delay.

Results and discussion

As can be seen in Figure 4.3, the vibrations of a metal surface with sessile droplets had no significant effect on their nucleation temperature. The increase in the average nucleation temperature with $1.5°C$ around $1\ kHz$, from $-15°C$ to $-13.5°C$, lies within the error margin and was verified to be insignificant using the nucleation temperatures at $0\ Hz$ as a benchmark. It might be an artefact of the testing method or the environment. The frequency sweep was interupted at this point for some time. When continuing the test, the benchmark $0\ Hz$ nucleation temperatures increased with the same amount as the average increase of T_n observed for the frequencies above $1\ kHz$ in Figure 4.3.

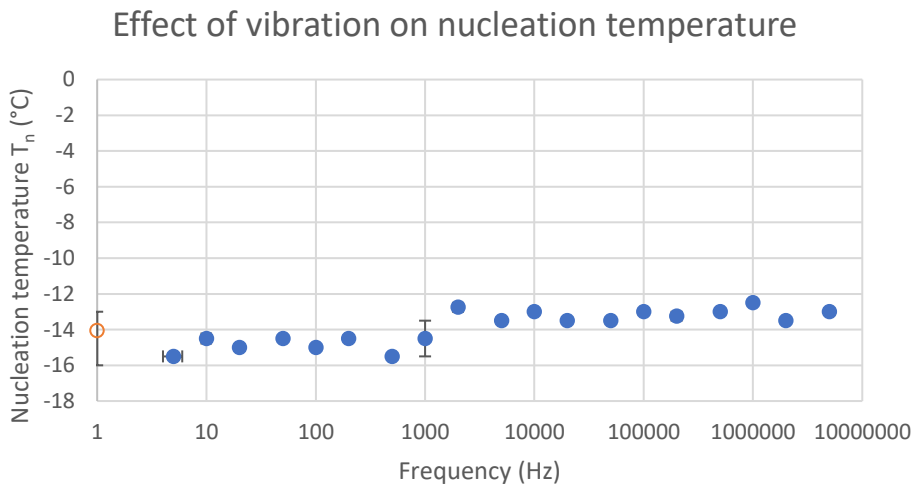

Figure 4.3: Effect of surface vibration between $5\ Hz$ and $5\ MHz$ on the nucleation temperature (full blue circles). The nucleation temperatures measured at $0\ Hz$ (empty orange circle) are placed at $1\ Hz$, to be able to use a logarithmic scale.

In an environment with uncontrolled relative humidity, the nucleation of droplets does not take place on the interface of the droplet with the surface. The crystal is transferred by a MLL freezing front from a nucleation site elsewhere on the sample. This front always came from the center of the piezo-electric element, where it was coldest. This is illustrated in Figure 4.4, where the front line is indicated by an interrupted white line. In appendix G, a series of three frames is included, to illustrate the freezing front propagation.

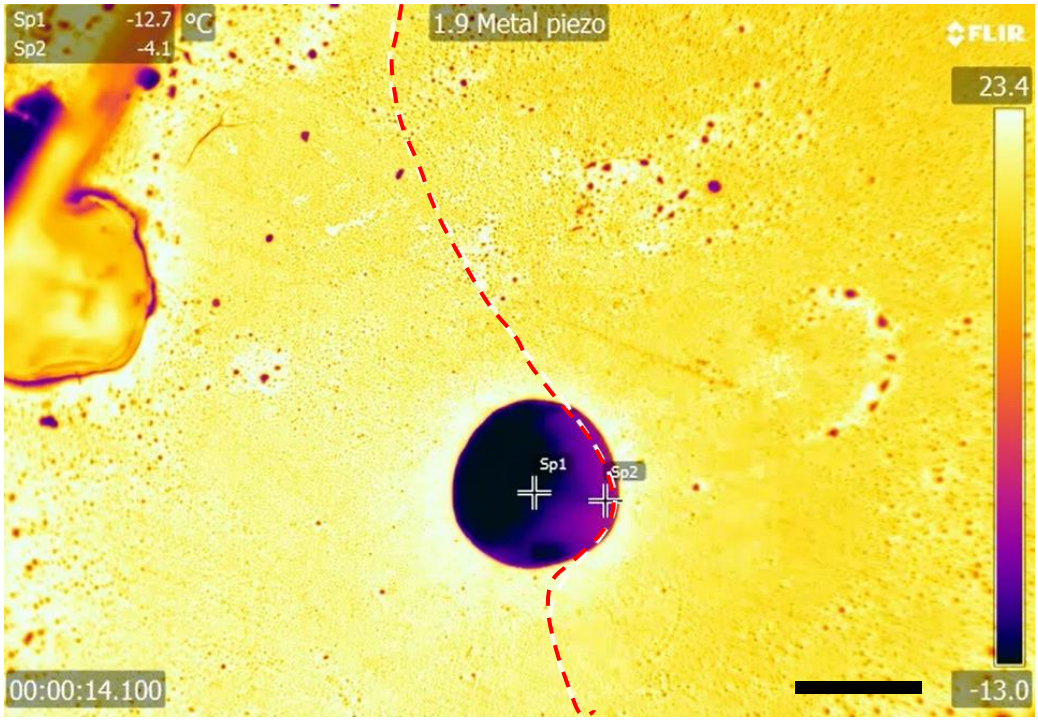

Figure 4.4: A faint MLL freezing front can be observed to propagate over the metal top electrode of the piezo electric element. The freezing front (red dashed line, separating dark yellow from light yellow area) appears in the top right corner, reaches the droplet and covers the whole surface in a short time of under $0.1\ s$. The black scale bar is $2\ mm$. More frames of the MLL freezing front propagation can be found in appendix G

Surface vibration with a piezoelectric element did not induce nucleation, although controllable nucleation was expected between $16\ kHz$ and $100\ kHz$ [75]. The increase in nucleation temperature with $1.5°C$ at $1\ kHz$ was not significant. The lack of influence from surface vibration could be due to a lack of power of the applied signal or bad transmission of the vibration through the water-electrode interface. The transducers that induce ice nucleation in the food industry are much more powerful. Another possibility is that the cold temperatures influence the effectiveness of the piezoelectric element to produce or transmit vibration into the water droplet. As nucleation never happened inside the observation window of the IRI method, interesting effects might be observable near the point of nucleation in the MLL elsewhere on the surface.

4.1.3 Contact angle

Increasing the contact angle has been regarded as a good strategy to decrease ice adhesion and has been shown to reduce the ice nucleation rate. [3], [29] For flat surfaces, the contact angle is a material property that emerges from the bonding strength between water molecules, as illustrated in Figure 4.5. Generally, polar molecules on the solid surface, like OH groups, yield attraction with the OH groups of water, through hydrogen bonds. [25] Through Monte Carlo simulations, it has recently been shown by Li et al. that this bonding strength plays a major role in nucleation. [18]

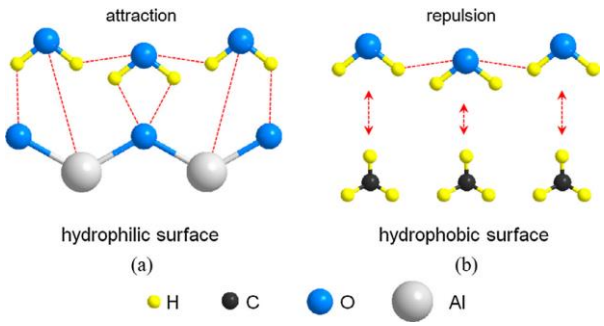

Figure 4.5: The origin of the contact angle of a flat surface lies in the interactions between surface and water molecules, making surfaces hydrophilic or hydrophobic. [86]

In literature, increasing the contact angle of coatings has been suggested as a design parameter for passive anti-icing. Most of these coatings are modified with silicone or fluorine functional groups. Ice adhesion formed from sessile or impacting droplets has been measured to be proportional to the surface free energy of materials. For example, Saito et al. dispersed PTFE particles in polyvinylidene fluoride matrix with mass concentrations between $30\ m\%$ and $95\ m\%$ to achieve contact angles of $105° < \theta < 150°$. Decreasing the surface free energy resulted in a threefold decrease of ice adhesions strength F_a. [82] Next to decreasing ice adhesion, nucleation time delay has been shown to be affected by the contact angle, depending on the kind of icing that is studied. The formation of clear ice in freezing rain can be reduced by decreasing the contact angle, although rime ice couldn't prevented. [14] A reduction in wetting of the hydrophobic surface explains the increase in nucleation time delay through heat conduction. [16] However, the surface wetting alone does not convincingly explain the reduction in clear ice formation, while rime ice formation remains unaffected. This different behavior could originate in a limited understanding of the formation mechanism of clear ice. As hypothesized in this thesis, a frozen layer of water on the surface might be needed to create clear ice, while not being necessary to form rime ice. Apart from clear ice and rime ice formation, frost formation is also affected by the contact angle. Wang et al. measured frost thickness growth over time and noticed a delay in growth initiation of 60 minutes on hydrophobic surfaces, as compared to hydrophilic bare aluminum. [25]

It is important to note that the surface free energy of a material is not the only parameter influencing the contact angle of water droplets. Also roughness [82], surface temperature [17] and droplet size [24] strongly influence the contact angle. This makes the contact angle a complex and ambiguous governing parameter.

Methodology

For the initial sensitivity analysis of the effect of contact angle on the freezing behavior, a PVDF thin film is spincoated on glass. Using arc plasma treatment, the contact angle of this material could be reduced without changing any other material or surface property, which enabled systematic testing.

The measurement points plotted in the $t_n(T_n)$ graph in Figure 4.6 include the previously obtained values for the temperature dependency of the nucleation time delay from Figure 4.1a (orange triangles). The surfaces used for the testing of this temperature dependence were made of thin films of untreated PVDF. The new measurement points for t_n and T_n are obtained from plasma-treated PVDF films and are added to this graph (blue squares) to observe any horizontal or vertical shift due to the decreased contact angle. Just as in Figure 4.1a in section 4.1.1, some of the nucleation events were observed outside of deposited droplets. Their values for t_n and T_n are also included in Figure 4.6 for untreated PVDF (empty orange triangles) and plasma-treated PVDF (empty blue squares).

To check the validity of the nucleation temperature increase with decreasing contact angle on untreated and plasma-treated PVDF, other materials were used for testing. The contact angles of all surfaces that were produced for testing, are given in Table 4.2.

Surface material	**Contact angle**
Anodized aluminium (50 µm pore size)	$113°$
Teflon	$101° \pm 7°$
Untreated PVDF	$95° \pm 5°$
Anodized aluminium filled with PVDF	$95°$
Plasma treated PVDF	$85° \pm 5°$
Top electrode piezo element	$83°$
Epoxy (Epikote)	$76°$
Ink on Teflon	$63° \pm 10°$
Glass substrate	$63° \pm 2°$
Alginate film	$10°$

Table 4.2: Contact angles of tested surface materials

As it is inherently impossible to select a different material which only differs in surface energy from the PVDF thin film, a material with a much higher contact angle was selected. Droplets of between $2\ mm$ and $5\ mm$ were deposited on top of a Teflon plate, which was installed on the Peltier setup in a standard controlled lab environment. The resulting data point of nucleation time delay at a specific nucleation temperature of the droplets on Teflon is shown in Figure 4.7a. (full blue circle) The error bars indicate the different values for nucleation time delay and nucleation temperature within the same test. Nucleation also occurred outside of the deposited droplets in condensed water (empty orange circle) After testing one Teflon plate, a pattern of lines was added with permanent marker ink and the same test was repeated several times (full blue diamonds), registering nucleation of outside of deposited droplets as well (empty orange diamonds). The lines of marker ink did not touch each other. To illustrate the difference in values obtained for the nucleation temperature and nucleation time delay within the same test, all obtained values are shown in Figure 4.7b.

To validate the effect of contact angle on other materials, three materials were tested at higher relative humidity of $RH = 80\%$. Tests on epoxy, plasma patterned PVDF and metal were performed in a climate chamber, to achieve controlled and reproducible environmental properties. The increased humidity and relevant materials should be more representative for the aircraft mission profile under consideration. The production of the metal surfaces with empty and oil-filled holes is explained in detail in section 5.1. Every test consisted of three different surface temperatures, namely $T_{surf} = [-10°C;\ -15°C;\ -25°C]$, that were achieved at high cooling rate. However, as can be seen in Figure 4.8, the nucleation temperatures do not align nicely around these three values for T_{surf}, due to several complications with the test procedure. To be able to observe the critical nucleation temperature for the plasma treated PVDF, an extra test at $T_{surf} = -12°C$ was performed, next to the one at $T_{surf} = -10°C$. The nucleation temperatures on metal were limited to temperatures above $T_{surf} = -14°C$. Nucleation occurred without exception when reaching this surface temperature while trying to cool down the samples to $T_{surf} = -15°C$ or $T_{surf} = -25°C$.

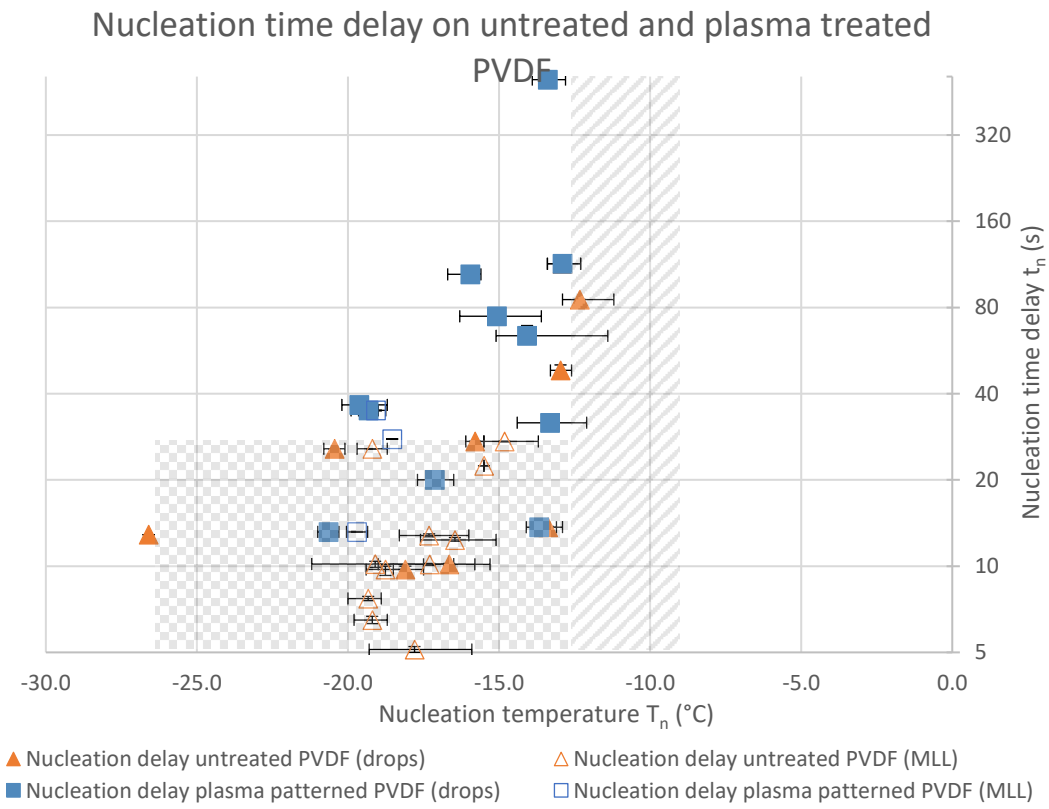

Figure 4.6: Effect of decreasing the contact angle on Nucleation delay and nucleation temperature from hydrophobic untreated PVDF (orange triangles) to hydrophilic plasma treated PVDF (blue squares). The registration of temperature and time of nucleation in the Molecular liquid layer (empty indicators) and droplets (filled indicators), are separately indicated. The critical nucleation temperature range (hatched area) and temperature invariant delay range (checker pattern area) are indicated for freezing on the untreated PVDF films. Note the logarithmic vertical axis for the nucleation time delay.

A slight, but insignificant increase in average nucleation time delay t_n can be observed in Figure 4.6, when comparing the measurements the new plasma-treated PVDF (blue squares) to the previously obtained untreated (orange triangles). An increase in t_n with the contact angle would be unexpected. The contact angle decrease of $10°$ from untreated PVDF to plasma treated PVDF is considered to be too small to affect the nucleation delay significantly.

In the PVDF thin films, plasma treatment was done on squares, surrounded by untreated PVDF, as shown in Figure 2.3, the MLL propagation was not able to propagate over parts of the hydrophobic areas separating the hydrophilic squares. The MLL propagation could even be seen to nucleate in, but be confined to the hydrophilic, plasma-treated areas in some cases. This means that although the small decrease in contact angle didn't significantly change the nucleation time delay, it did affect the freezing front propagation mechanism. More analysis is done on the effect of the contact angle on the freezing front propagation mechanism in section 4.2.2.

Considering the last test on a Teflon surface, the effect of hydrophobicity on nucleation time delay on Teflon should be explained by the reduction in contact area. This factor is itself explained by a reduction in heat conduction through the water-Teflon interface, which is influenced by the contact area and material conductivity. If less heat can escape into to the coating through the droplet-solid interface, the latent heat

from the droplet can't escape, which is needed to allow nucleation. [3][16] This explanation seems to be supported by the large increase in nucleation time delay on Teflon.

As can be seen in Figure 4.7, the nucleation temperatures of $-20°C < T_n < -11°C$, seem unaffected by the increase in contact angle in the test with Teflon as a surface. This confirms the invariance with the contact angle observed in the initial sensitivity tests, were the contact angle of PVDF thin films was decreased by plasma treatment.

The most remarkable result is the increase in spread of the values for the nucleation time delay in Figure 4.7, by one to three orders of magnitude, compared to the values for untreated and plasma-treated PVDF in Figure 4.6. There are many more seemingly independent nucleation events on Teflon within the same test run, which can easily be visually confirmed by studying IR images of freezing deposited and condensed droplets on Teflon. The increased contact angle clearly does not prevent nucleation, but does seem to induce a much slower form of front propagation. This slower front might use the dendrite freezing front propagation mechanism, featuring small branches of ice that grow from frozen droplets to unfrozen droplets. [59] Surfaces with lower contact angles than Teflon, like the PVDF thin films, are suspected to freeze with the MLL freezing front propagation mechanism, which is several orders of magnitude faster. These surfaces only need one nucleation event to occur stochastically, to have nucleation of every droplet or liquid layer on the whole surface, resulting in identical values for t_n per test run as shown by the vertical error bars in Figure 4.6.

The effect of the contact angle on the freezing front propagation mechanism is confirmed by adding permanent marker ink lines on Teflon and performing the experiments again. The droplets on marker ink showed similar nucleation time delays as the 'untreated' Teflon, but featured a very different nucleation mechanism. As illustrated in Figure 4.21 and discussed in detail in section 4.2.2, the fast freezing front propagation through the MLL was confined to the surfaces covered with ink. Nucleation on the edge of the marker ink pattern on the Teflon substrate induced nucleation over the whole surface of permanent marker ink. This can be observed as slightly reduced spread in nucleation time delays in Figure 4.7. However, as can be seen in the same graph, the nucleation of the permanent marker areas showed surprisingly similar nucleation time delays t_n and nucleation temperatures T_n, as compared to the clean Teflon samples. Due to the hydrophobic Teflon boundaries, t_n remains high on the permanent marker areas, as compared to values for t_n on the untreated or plasma patterned PVDF. As an unexpected result, the average values for t_n measured for the permanent marker ink patterned Teflon are higher than the 'clean' Teflon. However, the increase in t_n for the Teflon with ink pattern are well within the error margin of the 'clean' Teflon results.

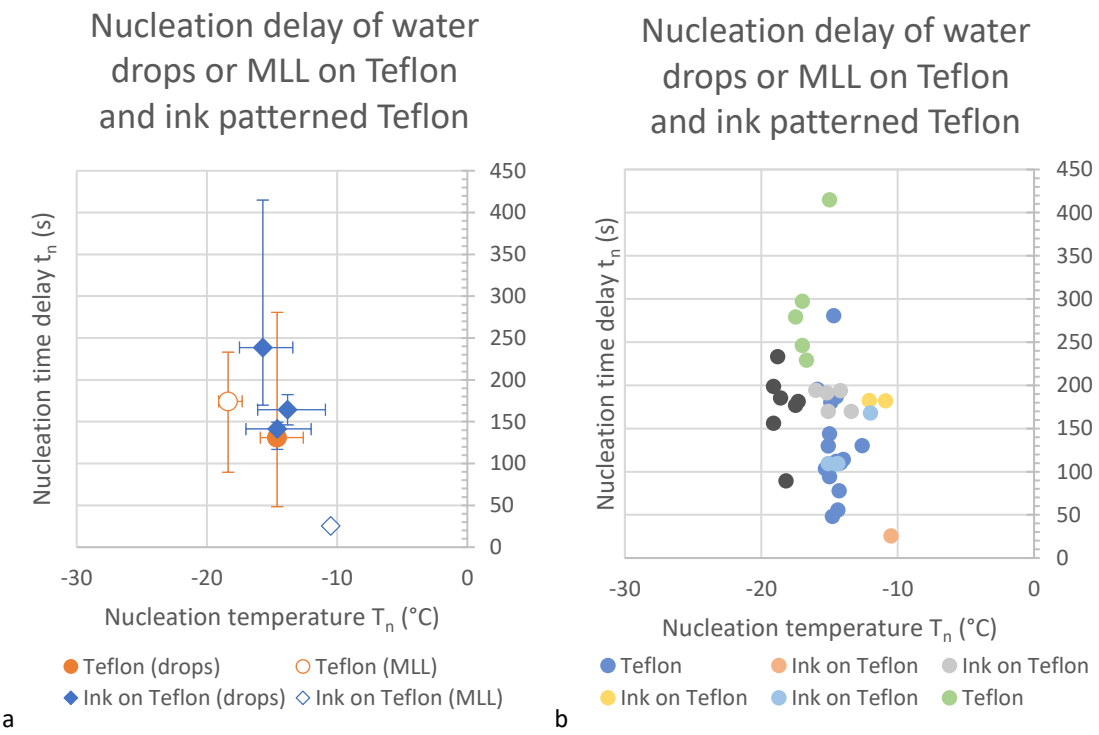

Figure 4.7: Graphs showing the effect of increasing the contact angle on nucleation temperature and nucleation time delay. The surfaces of permanent ink patterns on a Teflon substrate are tested at room humidity and temperature. (a) The graph shows average values for t_n and T_n per freezing test run and their respective spreads as error bars. (b) The large difference in nucleation time delays within each test run is illustrated, inferring isolated nucleation or dendrite growth of condensed or deposited droplets. A very slow front, nucleating droplet by droplet is observed with IRI.

Figure 4.8 gives the resulting relationships between t_n and T_n for the four tested surfaces in the last validation test. The values for t_n around $500s$ represent the test runs where no freezing occurred and are indicated with arrows.

The more hydrophilic metal surfaces seem to nucleate at lower nucleation time delays and higher nucleation temperatures than the polymer surfaces, featuring higher contact angles. It seems from Figure 4.8 that the critical nucleation temperature, above which no nucleation occurs, is located at $T_{surf} > -10°C$.

The unavoidable nucleation of the MLL on all metal samples within a narrow band between $-14°C < T_{surf} < -10°C$ concurs with the consistent nucleation temperatures of droplets on the top electrode of the piezo element in Figure 4.3 in section 4.1.2. For the metal surfaces, the nucleation time delay is too short to be observed in sessile droplets on a very cold surface. The time to cool down to a surface temperature of $-25°C$ with the cooling system was much larger than t_n.

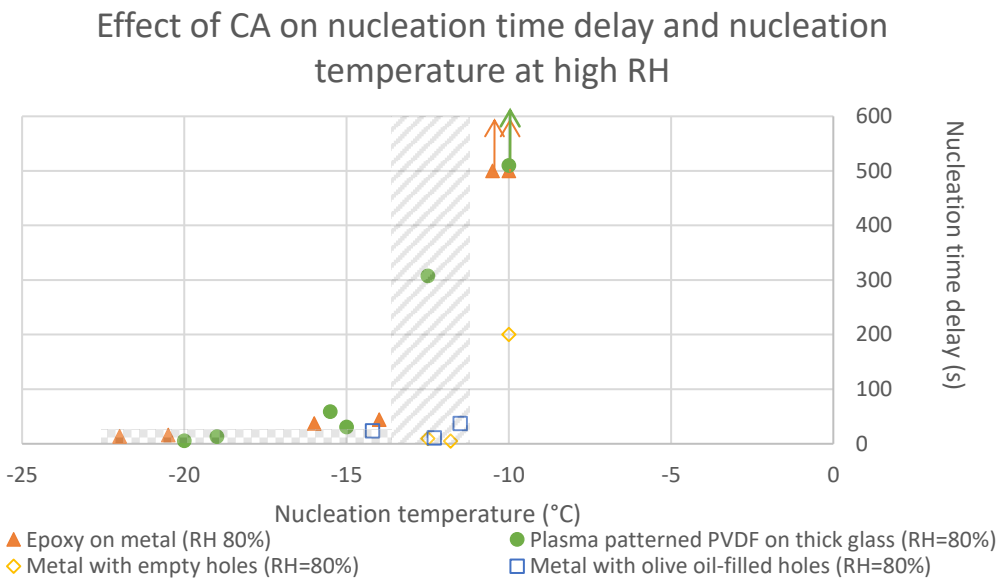

Figure 4.8: Effect of contact angle on nucleation time delay t_n and nucleation temperature T_n in high relative humidity. The critical nucleation temperature (hatched) and the temperature invariant area (checker pattern) for epoxy are indicated. The contact angle of epoxy and plasma treated PVDF is higher than the contact angle of the metal substrates.

The short nucleation time delays for metal surfaces confirm that either their low contact angle or high thermal conductivity induces fast nucleation at relatively high temperatures. The third test does not separate the two candidate governing parameters in a satisfactory way, as most easily available high contact angle materials feature low thermal conductivity. If the contact angle is a dominant factor, it might be the higher continuity of the MLL. This would yield a larger water-substrate interface, increasing the probability of a nucleation event occurring. The continuity of the MLL on the metal samples can clearly be observed with IRI, as the freezing events feature a steady MLL freezing front propagating over the surface. This will be shown in Figure 5.6, when discussion the freezing front propagation.

An unfortunate consequence of the continuity of the MLL, is that the actual site of nucleation lies outside of the observation window. This fact implies that the point of nucleation might even be at the colder interface between the metal substrate and the Peltier element, travelling over the sides of the substrate to reach the top surface. This effect could be the cause of the short nucleation time delays on metal surfaces and the narrow range of nucleation temperature, as compared to the more hydrophobic PVDF and epoxy surfaces in the graph in Figure 4.8. However, also the plasma patterned PVDF surfaces have an MLL freezing front propagating over the surface, with the nucleation site outside of the observation window. In this case no shorter t_n or more narrow range of higher values for T_n is observed. It should be noted that he MLL freezing front only travels over the plasma treated bands, and nucleation of the edge of the substrate can be observed after the MLL freezing front reaches the edge. This can be seen in the frames included in appendix H and supports the suggestion that nucleation on the side, interface or Peltier element causes the reduction in t_n and increase in values for T_n. During the freezing of the epoxy coating, small bursts of MLL freezing can be observed, seemingly originating inside the observation window. The values for t_n and T_n are very similar for the PVDF and epoxy coatings.

Although the contact angle is widely reported in literature as a governing parameter for freezing of impacting and sessile droplets [17,16,3,28,53,25,72,26,14,73], it is not a governing parameter that reflects a deep understanding of the nucleation mechanism of ice. More specifically, the contact angle is itself an aggregate of the surface energy, roughness and contact angle heterogeneity (at scales differing with at least

6 orders of magnitude), humidity and surface temperature. [83]This has created conflicts in literature. One example is the direct linking of contact angle hysteresis (CAH) to ice adhesion strength by Kulinich et al., expanding on the direct relationship of contact angle to ice adhesion strength on surfaces with low CAH by Saito et al. The increase of ice adhesion strength with the CAH is suggested to be due to an increase in contact area, but is not quantitatively linked to the origin of the CAH, namely roughness or contact angle heterogeneity. [72,82]

4.1.4 Conductivity

In the second test in section 4.1.3, patterns of permanent marker ink on Teflon were tested. As can be seen in table Table 4.3, the conductivities of the ceramic particles in the ink and the Teflon are similar, corresponding to similar nucleation time delays in Figure 4.7. These results concur with the independence of t_n and T_n on the decrease in contact angle from untreated PVDF to plasma treated PVDF, where the conductivity remains the same after the plasma treatment process. In the third test in section 4.1.3, metal surfaces with high thermal conductivities are compared to epoxy and PVDF surfaces with low conductivities. Here, a clear decrease in t_n can be observed, as well as a more narrow and higher range of values for T_n. These three experiments strongly suggest that the nucleation of the MLL might depend on the surface conductivity more than on the contact angle. This hypothesis concurs with tests and models in literature. For example, Mishchenko et al. used classical heterogeneous nucleation theory and dynamic wetting behavior to predict at which contact time enough heat would be conducted out of the droplet, to allow freezing. [16]

Methodology

To determine the sensitivity of nucleation time delay and nucleation temperature to changes in conductivity in the current section, no new tests were performed. Instead, all values for t_n and T_n that were measured in previous tests were used to construct their dependency on the conductivity and effusivity in Figure 4.10 and Figure 4.11, respectively. The conductivity k is expressed in W/mK and represents the rate at which heat can be transported over a length and is generally used as an anisotropic material property. The effusivity e represents the ability of a material to exchange heat with its surroundings and is expressed in $Ws^{0.5}/m^2K$. The effusivity is registered, as it might represent the ability of the material to accept latent heat that escapes from nucleating droplets and the MLL can be computed as:

$$e = \sqrt{k\rho c_p}$$

The coating thickness of the PVDF films was measured with the PosiTector 6000 (*DeFelsko*) at 5 spots on each sample. The results showed consistent PVDF film thicknesses between 15 and 30 μm on metal. The thickness of thin films on glass could not directly be tested on the glass substrates, as the PosiTector requires conductive substrates. The glass substrates did not have homogeneous thickness, so they couldn't be placed on a conductive substrate with their respective thickness being subtracted. Therefore, the PVDF film thickness on the glass substrates was checked by delaminating two thin films and placing them on a conductive surface. This showed film thicknesses within the range of 15 and 30 μm mentioned before.

The conductivity and effusivity of tested surfaces were determined with a TCi Thermal Conductivity Analyzer (*C-Therm Technologies*). The setup involves a heating element on which samples are placed face-down. For good thermal conductivity between the heating element and the tested surfaces, a small quantity of water was deposited on the TCi before placing the samples. This process is illustrated for a thin film of PVDF on thin glass in appendix J. Each material was tested for 10 heating and cooling cycles, discarding the first

result. To accurately determine the conductivity of permanent marker ink on Teflon, the previously frozen lines of ink on Teflon couldn't be used. A square was drawn on Teflon with a different black permanent marker ink, as illustrated in appendix J, so that the complete heating element could be covered. This different ink was assumed to give representative results for the conductivity of permanent marker ink, used for example in Figure 4.21.

As can be seen in Table 4.3, the thickness and material of the substrates had a large influence on the conductivity. The measured conductivity can therefore not just be considered as a material property of the applied thin films. As an example of the influence of the substrate material, an untreated PVDF thin film on metal would have $2.5 < k < 11\ W/mK$, closer to $k = 27\ W/mK$ of the bare metal substrate, whereas an untreated PVDF thin film on thin glass demonstrated $k = 5\ W/mK$. As an example of the influence of substrate thickness made from the same material, plasma treated PVDF on thin glass featured $k = 5\ W/mK$, whereas plasma treated PVDF on thick glass had $k = 1\ W/mK$.

Surface material	Conductivity (W/mK)	Effusivity ($Ws^{0.5}/m^2K$)
Bare AA6082	27.3 ± 0.6	9900 ± 100
Untreated PVDF (on metal)	6.67 ± 4.2	-
Plasma treated PVDF (on metal)	5.73 ± 0.03	3677 ± 11
Plasma treated PVDF (on glass)	4.94 ± 0.2	3360 ± 80
Untreated PVDF (on glass)	4.88 ± 0.08	3330 ± 33
PVDF + alginate (on glass)	1.96 ± 0.02	1948 ± 13
Epoxy (Epikote) (on metal)	1.57 ± 0.02	1720 ± 14
Plasma treated PVDF (on thick glass)	0.93 ± 0.02	1360 ± 12
Teflon	0.42 ± 0.01	776 ± 10
Permanent marker ink (on Teflon)	0.21 ± 0.03	896 ± 22
Alginate (on metal)	20.6 ± 0.3	8561 ± 72

Table 4.3: Conductivity and effusivity of tested surface materials

Results and discussion

The adhesion of the coating to the substrate also had an effect on the conductivity, with badly adhered plasma treated PVDF having a conductivity of $k = 1.91 \pm 0.03\ W/mK$ and effusivity of $e = 1920 \pm 18\ Ws^{0.5}/m^2K$. It means that bad adhesion increased the amount of energy that could be transported through the coating and is suspected to be due to water adsorption on the film-substrate interface or water absorption in porous PVDF. In initial tests of the plasma treatment process, the removal of a well adhered mask of Kapton tape delaminated the PVDF thin film. In initial freezing tests using these thin films as surfaces, a MLL freezing front was observed to travel equally easily over plasma treated and untreated areas in initial tests of the plasma treatment process. It is expected that a freezing front can travel in between the PVDF thin film and metal or glass substrates, also inducing crystallization on the top surface of the thin films through pores in the film. The effect of thin film delamination on ice nucleation on the surface was most clearly illustrated in tests that were performed on PVDF thin films with holes scratched in the surface. In Figure 4.9, one of the frames of a freezing experiment on these samples illustrates how the freezing front seems to 'pop up' out of the coating, especially around the holes. More frames can be found in appendix I. Note the areas with seemingly higher temperatures connecting the holes, through which the freezing front propagates fast. If these areas are where the thin film of PVDF has delaminated, the temperature difference and freezing front propagation might be caused by water absorption, yielding higher reflectivity and a continuous water layer.

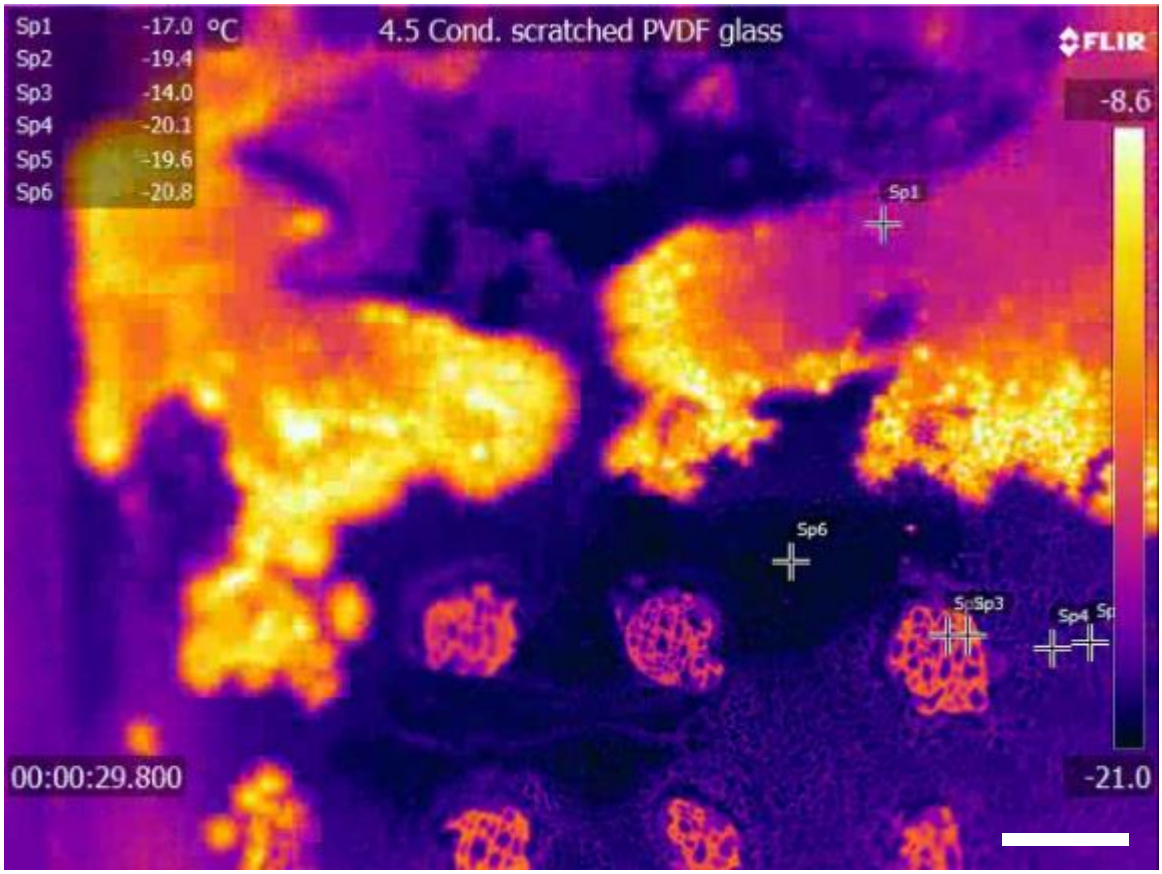

Figure 4.9: Nucleation and front propagation over a PVDF thin film with holes in a grid on a glass substrate at $t = t_n + 0.12s$. The white scalebar is $2\ mm$

In Figure 4.10a and Figure 4.11a, the values for t_n of nucleation in droplets and in the MLL seem to reduce by an order of magnitude, by increasing the conductivity and effusivity by two orders of magnitude. This fits the hypothesis that freezing occurs sooner if there is more capacity for the material to absorb and conduct heat. In Figure 4.10b and Figure 4.11b, the nucleation temperature seems to decrease slightly with increased effusivity and conductivity, which would be opposite to the expected trend. However, this decrease of the nucleation temperature does not seem significant and is within the spread of the data in both.

The large spread in values for $t_n(k)$ or $t_n(e)$, might be partially due to the large spread in values for $T_n(k)$ and $T_n(e)$ in the selected tests. As seen in section 4.1.1, t_n was found to be largely independent of T_n on PVDF thin films on glass. However, this behavior might be different for other materials and even a small dependence of $t_n(T_n)$, could result in a spread in the graph of $t_n(k)$ or $t_n(e)$, as the temperatures vary between $-27°C < T < -10.5°C$.

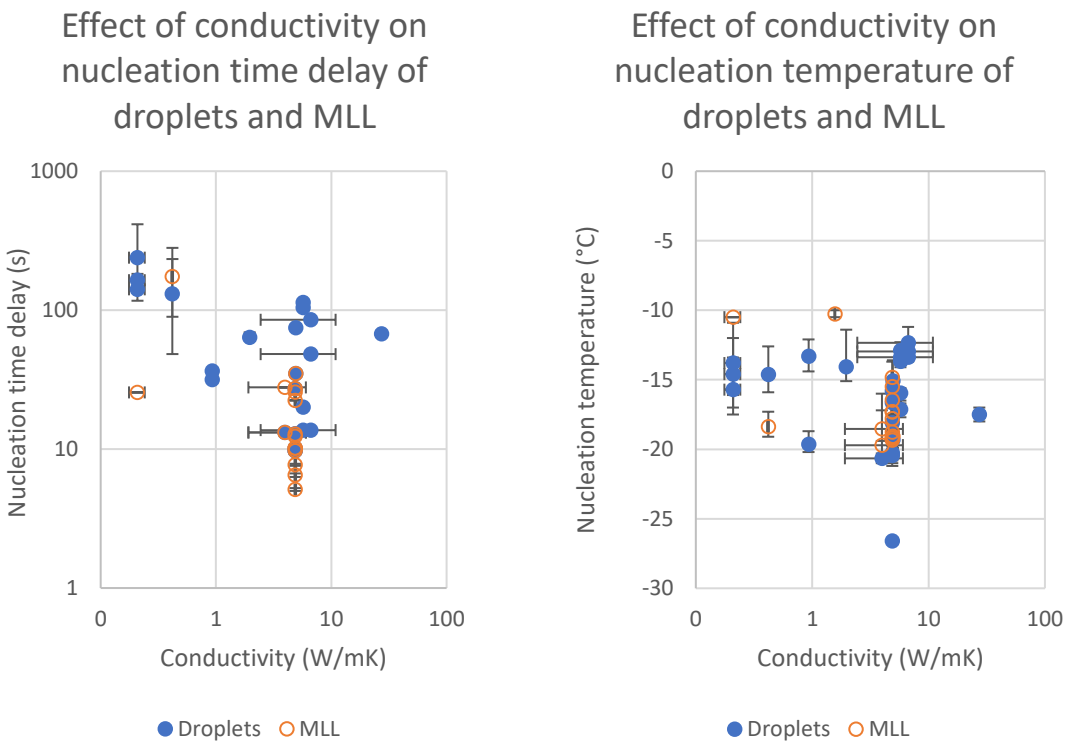

a b

Figure 4.10: Effect of conductivity on (a) nucleation time delay and (b) nucleation temperature for droplets and the MLL on glass, plasma treated and untreated PVDF (on metal and glass), permanent marker ink (on Teflon), bar Teflon, Epoxy on metal and bare aluminum.

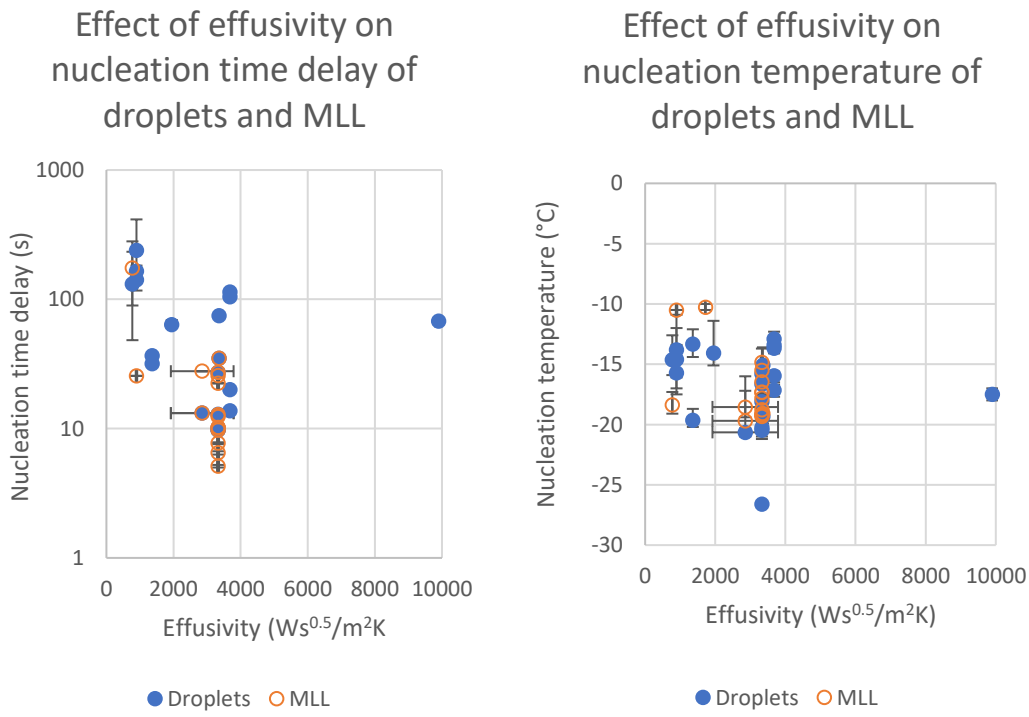

a **b**

Figure 4.11: Effect of effusivity on (a) nucleation time delay and (b) nucleation temperature for droplets and the MLL on PVDF (on glass), PVDF (on metal), permanent marker ink (on Teflon), epoxy (on metal) and bare aluminum.

Although the spread of measured values for t_n and T_n is very large, the results seem to confirm the conclusions in literature, where the effect of higher conductivity is a decrease in nucleation time delays of droplets. [16] A more in-depth and systematic investigation into the effect of conductivity on nucleation time delay and nucleation temperature was considered to be out of the scope of the current research, due to limited time available.

4.1.5 Relative humidity

As mentioned before, relative humidity (RH) has a large effect on the adhesion strength of ice, as well as the nucleation time delay [40]. The hypothesis tested in this section, is whether this might be due to a freezing layer of water on the surface. There exists a molecular liquid layer (MLL) of water on all surfaces, which needs time to grow in thickness. [23] Below $RH = 25\%$, 2D clusters of water molecules with thickness of a few Angstrom remain unconnected, with clusters of sizes less than a few 1000 Angstrom. With $25\% < RH < 40\%$, these clusters merge into 2D islands, with complete coverage of the surface above $RH = 40\%$ (hu1995).

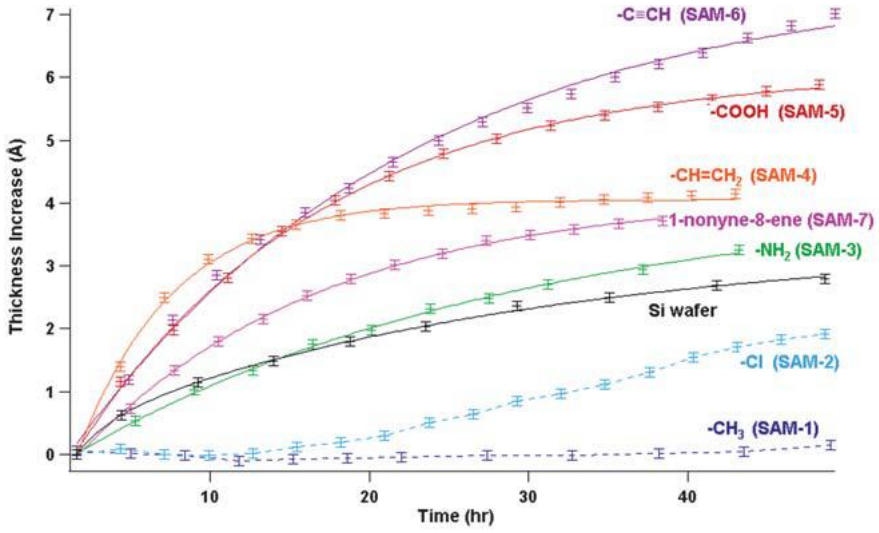

a

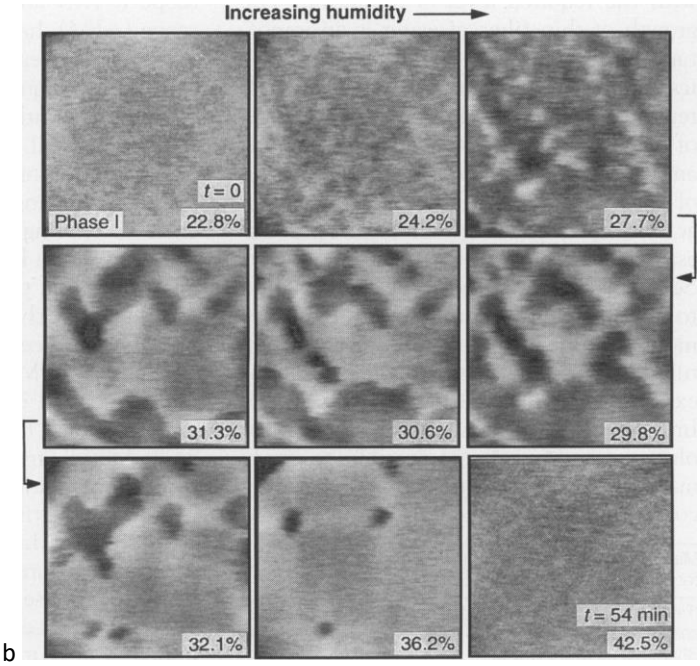

b

Figure 4.12: Growth of the molecular liquid layer (MLL), as observed with atomic force microscopy (AFM). (a) The growth of a liquid layer of water of average thickness between $\mathbf{0.1}$ Å and $\mathbf{7}$ Å has been observed by James et al. on both hydrophilic and hydrophobic surfaces. [23] (b) A change in MLL continuity with relative humidity has been observed by Hu et al. on Mica, with water clusters of several $\mathbf{1000}$ Å diameter and heights of $\mathbf{2}$ Å at $\boldsymbol{RH} < \mathbf{25}\%$, islands at $\mathbf{25}\% < \boldsymbol{RH} < \mathbf{40}\%$ and a continuous MLL at $\boldsymbol{RH} > \mathbf{40}\%$ (Hu1995)

An effect that might be related to the existence of an MLL at high relative humidities, is the decrease of the contact angle of water droplets on superhydrophobic surfaces with temperature. This effect is accredited by Heydari et al. to an increase in water condensation and consequent transition from a Cassie-Baxter to a Wenzel state. Within the same research, this decrease in contact angle with temperature is linked to a reduction in nucleation time delay t_n. Whereas, Mischenko et al. and Alizadeh et al. show a significant increase in nucleation time delay at $RH = 2 - 5\%$, Heydari et al. showed no such effect at $RH = 40\%$. [16,3] This was confirmed by Jung et al. on surfaces of different chemical composition and Yin et al., both at $RH = 80\%$. [37,38] In the tests by Heydari et al., the cooling rate was varied below $5.5\ °C/min$, which would be more than enough to form a molecular liquid water layer. [17] Although the transition from Cassie-Baxter to Wenzel state could eliminate the effect of low contact area that gives anti-icing properties to superhydrophobic surfaces, this does not explain the simultaneous freezing of several droplets at the same time. Nor does it explain immediate freezing of drops upon impact on a subcooled surface, as reported by Varanasi et al. [40] and illustrated in Figure 4.13. Also, the immediate continuity of clear ice on large wings hints to another cause for the decreased anti-icing performance with increased humidity. At the nucleation rates of impacting droplets determined experimentally, it would need a long time for a continuous layer to form on aircraft wings if the droplets are assumed to freeze independently. In other words, there needs to be propagation of nucleation between droplets, with the MLL as obvious candidate for the transmission of crystallization.

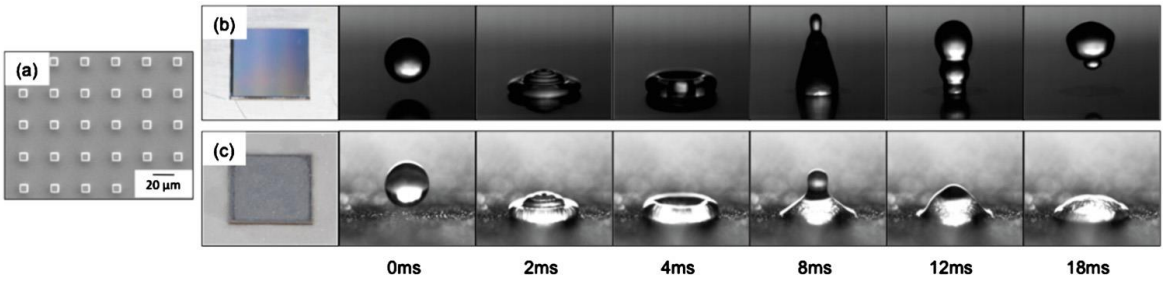

Figure 4.13: (b) Impacting droplets bounce on a superhydrophobic surface at $\boldsymbol{T_{surf}} = \mathbf{18}°\boldsymbol{C}$ and $\boldsymbol{RH} = \mathbf{70}\%$. (c) Impacting droplets are pinned on the same frosted superhydrophobic surface, according to Varanasi et al. due to a Cassie-Wenzel transition because of hydrophilic ice growth on the hydrophobic pillars. [40]

Methodology

The effect of humidity on the nucleation time delay and temperature was tested in a systematic manner. By placing the freezing setup in the climate chamber, as schematically shown in Figure 1.3, the relative humidity could be accurately adjusted. Two materials were used, namely an Epikote epoxy coating, as a realistic aircraft coating material, and plasma treated PVDF for its well characterized critical temperature at uncontrolled relative humidity in previous sections. The tested surface temperatures for the epoxy coating were $T_{surf} = [-25°C;\ -15°C; -10°C]$. For low relative humidities, nucleation didn't occur at $-15°C$, so an extra test at -20°C was performed on epoxy. The plasma-treated PVDF surfaces were cooled down to $-25°C$, $-15°C$ and $-10°C$ as well. Similarly to the freezing tests on epoxy, nucleation didn't occur at $T_{surf} = -15°C$ for low humidities, so extra tests were performed at $T_{surf} = -30°C$.

Results and discussion

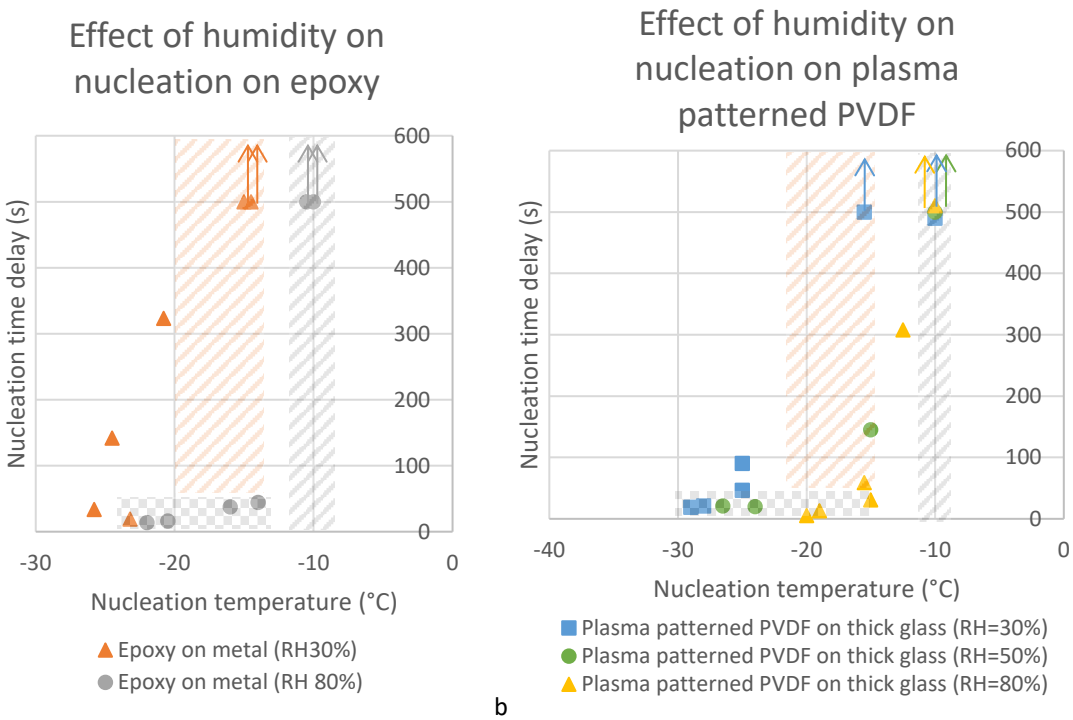

a b

Figure 4.14: Effect of humidity on nucleation time delay on (a) epoxy on metal substrate and (b) on plasma treated PVDF

Figure 4.14a shows a clear dependency of the $t_n(T_n)$ graph on relative humidity for the epoxy coating. The critical nucleation temperature decreases with a few degrees, when going from $RH = 80\%$ to $RH = 30\%$. The explanation is twofold. Firstly, less area is expected to be covered by the MLL, as it consists of unconnected water islands below $RH = 40\%$, as shown in Figure 4.12. This offers less surface-water interface for heterogeneous nucleation to occur. Secondly, if nucleation does occur on the epoxy surface somewhere outside of the observation window, it can't propagate over the whole sample.

Figure 4.14b shows the same dependency of the $t_n(T_n)$ graph for plasma treated PVDF, but for $RH = 30\%, 50\%$ and 80%. The overlap of the graphs with $RH = 50\%$ and $RH = 80\%$ suggests that the continuity of the MLL above $RH = 40\%$ is indeed critical for freezing.

Due to the limited time available for testing in a climate chamber, a limited number of datapoints was collected on both the epoxy and plasma patterned PVDF. To obtain error bars on the graphs in Figure 4.14, more tests should be performed around the critical nucleation temperatures of $-20°C < T_{surf} < -10°C$ and critical humidity of $RH = 40\%$. This could conclusively link the continuity of the MLL to nucleation time delay. It can however be conclusively stated that the relative humidity is a governing factor in the nucleation of a frozen water layer on the surface of epoxy and a PVDF thin film. The current IRI and droplet impaction setup in the climate chamber can be used in future research to link nucleation of an MLL to the droplet pinning and increased ice adhesion of impacting droplets on superhydrophobic surfaces in high humidity, as reported by Varanasi.

4.1.6 Droplet size

As introduced in Table 1.1, in section 1.1.1, the differentiation of clear ice and rime ice is mainly done through the droplet size. In general, at a droplet size of $40\mu m < d_{drop} < 2000\ \mu m$, clear ice can be expected to form and for $5\ \mu m < d_{drop} < 40\ \mu m$, rime ice forms. As an alternative explanation, this thesis has proposed to differentiate on the state of the surface, which may either be in a frozen or an unfrozen state when a droplet impacts. Complete freezing of small droplets take less time than complete freezing of large droplets, but they would feature the same nucleation time delay and nucleation temperature. In this case, the droplet size is not expected to be a governing parameter for droplet nucleation.

This simple hypothesis is expected to be complicated by two factors. Firstly, the amount of water-coating surface area available for latent heat conduction and heterogeneous nucleation is much larger for large droplets. Secondly, the sharp increase in contact angle of small droplets (as Park et al. found from $d_{drop} = 40\ \mu m$ ($\theta = 100°$) to $d_{drop} = 5\ \mu m$ ($\theta = 160°$) on a surface with a contact angle $\theta = 90°$) will further decrease the available area latent heat conduction and heterogeneous nucleation of small droplets. [24] Even without a frozen surface, this lower heat conduction, lower availability of nucleation sites and higher contact angle might make sure that the contact time during harmonic bouncing of a small droplet on an aircraft surface is lower than the nucleation time delay. For large droplets, this contact time could become larger than the nucleation time delay, resulting in droplet nucleation, pinning and smearing out until freezing has completed. [16]

If the influence of the surface state dominates the nucleation process, droplet size should not be a significant factor in determining the nucleation time delay. As shown in chapter 3, this is the case for large droplets that impact at high temperature, but this independence of t_n and T_n on the droplet size remains to be proven for lower T_{surf} and smaller droplet sizes.

Methodology

Similarly to the study of the effect of conductivity, a first sensitivity test of the effect of sessile droplet size on nucleation time delay and nucleation temperature analyzes the freezing data gathered on many different surfaces. The freezing data is mainly composed of droplet sizes and $t_n(T_n)$ datapoints on PVDF on glass and metal substrates, but also on Teflon, permanent marker ink on Teflon, bare aluminum and a Surlyn thick film on metal. Large droplets ($d_{drop} > 1\ mm$) were deposited with a needle. Small droplets ($d_{drop} < 0.4\ mm$) could be obtained on the surface by condensation at surface temperatures above the nucleation temperature.

In Figure 4.16a, the nucleation temperature is plotted for different droplet areas. In Figure 4.16b, the nucleation time delay is given for the different droplet areas. In Figure 4.15, these plots are combined into a single $t_n(T_n)$ graph. The grouping of data points at small droplet sizes is due to the inability to create droplets larger than 0.4 mm with condensation.

Results and discussion

No significant effect of droplet size on t_n or T_n can be derived from the graphs in Figure 4.16. An increase in T_n with increasing droplet size was expected in Figure 4.16a. This increase could be observed very weakly in the graph most clearly in the droplets on PVDF on glass (dark blue) with $0.1\ mm < d_{drop} < 2.5\ mm$. However, this increase is much smaller than the vertical spread of measured temperature values. A decrease in t_n was expected with increased droplet size. Possibly also due to the large vertical spread, such an increase can't be observed in Figure 4.16b. Although the first sensitivity test is only indicative for the dependency of nucleation temperature on droplet size, it does illustrate the limited influence of the droplet size on t_n and T_n.

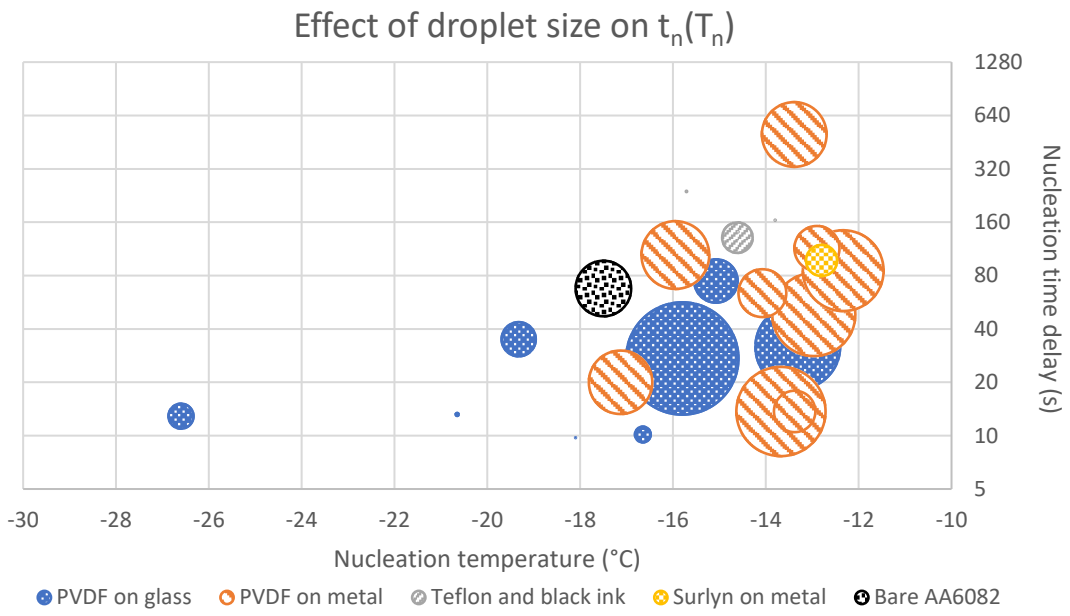

Figure 4.15: No immediate effect of sessile droplet size on the $t_n(T_n)$ datapoints is visible. The droplets are deposited or condensed in an lab environment with $55\% < RH < 65\%$ and at $T_{env} = 22°C$ on PVDF on glass, PVDF on metal, permanent marker ink on Teflon, epoxy on metal and bare aluminium.

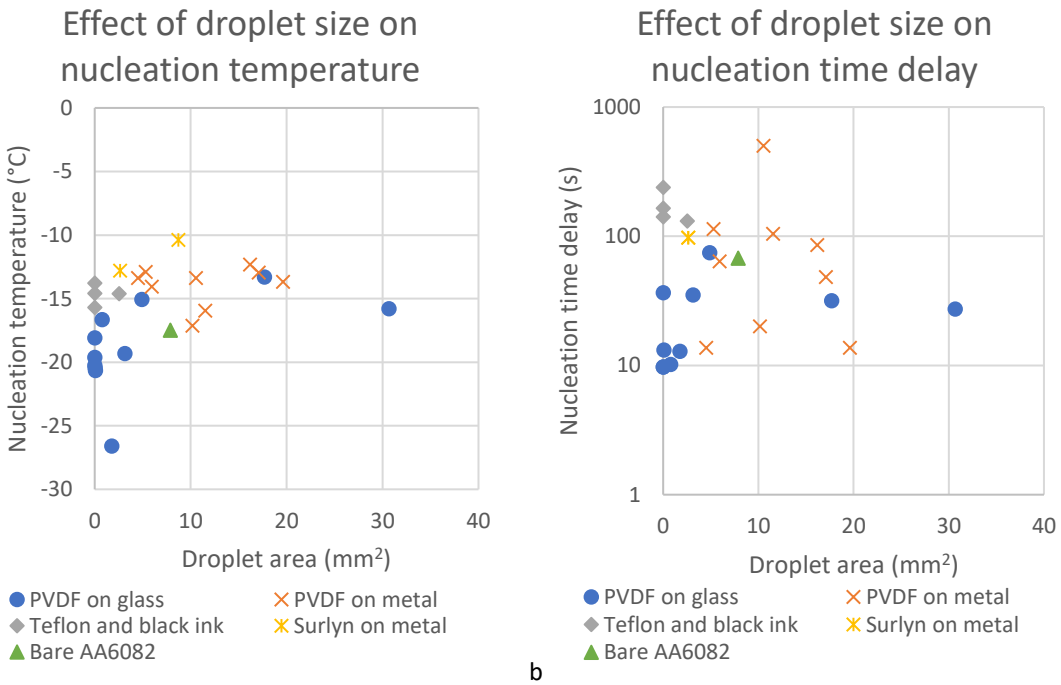

a b

Figure 4.16: Effect of sessile droplet size on (a) nucleation temperature and (b) nucleation time delay. The droplets are deposited or condensed on PVDF on glass, PVDF on metal, permanent marker ink on Teflon, epoxy on metal and bare aluminium.

If an MLL does indeed cover most of the surfaces and heterogeneous ice nucleation only occurs at the surface-water interface, an independency of nucleation behavior on droplet size was expected. A change in droplet size would in this case not affect the amount of interfacial area available for nucleation. In Figure 4.16b, the nucleation time delay seems to be invariant with increasing droplet size.

4.2 Factors affecting heterogeneous nucleation front propagation

It seems from section 4.1, that at surface temperatures below a critical temperature, nucleation of the MLL can't be prevented. Therefore, the slowing down or halting of its expansion over the complete aircraft surface could prevent impacting droplets touching a frozen layer upon impact. The parameters that are expected to govern the freezing front propagation, are listed in Table 4.4.

	Parameter	Material
Surface properties	Surface temperature	Epoxy
	Roughness	*Out of scope*
	Frequency	*Out of scope*
	Electrical charge	*Out of scope*
Material properties	Contact angle	Epoxy, plasma treated PVDF
	Conductivity + contact area	*Out of scope*
Environmental properties	Relative humidity	Epoxy, plasma treated PVDF
	Environmental temperature	*Out of scope*

Table 4.4: Environmental, material and surface properties that affect front propagation velocity. Out of each category, the governing parameter is tested that looked most promising during previous tests for ice nucleation. (green)

Research has recently been done in the last 5 years by Pasieka et al. and Xu et al. on crystallization front propagation in bulk water [21,57], and percolation-induced frost formation [59]. These freezing mechanisms are named 'bulk freezing front propagation' and 'dendrite freezing front propagation' in this thesis. In this framework, the front velocity of the novel freezing mechanism 'MLL freezing front propagation' lies in between these two mechanisms, possibly as a transition region between the two. This chapter will attempt to determine the governing parameters of the new freezing mechanism. As indicated in Table 4.4, only the effect of surface temperature, contact angle and relative humidity are assessed. Due to the limited time available, the other parameters, like frequency, electrical charge, conductivity and environmental temperature are considered out of the scope of this thesis. The roughness is not selected for testing due its potentially complex influence on the MLL freezing front propagation mechanism and the desire to create smooth, durable and manufacturable coatings to slow down the freezing front.

4.2.1 Surface temperature

The dependency of freezing front propagation velocity on temperature is small for bulk freezing in the temperature range relevant for the mission profiles of aircraft or wind turbines. This is according to Xu et al., who measured the bulk freezing front velocity to be around $100\ mm/s$. Below $T = -25°C$, the growth rate does decrease significantly with temperature. After a fragile-to-strong cross-over at $T = -50°C$ the growth rate decays exponentially, which is well approximated by the Wilson-Frenkel model. (Xu 2016) However, the freezing front propagation velocity is greatly dependent on temperature for $-7°C < T < -2°C$, according to Pasieka et al., who showed linear variation of between $60\ mm/s$ and $350\ mm/s$. [21]

Methodology

To test the effect of surface temperature on the MLL front velocity, untreated PVDF on glass is tested in a lab environment. The methods used for this test are similar to the previously described freezing tests.

Figure 4.17a shows the average front velocity at $T_{surf} = [-13°C; -16.5°C; -19°C]$ and Figure 4.17b shows the frontline velocity at these same temperatures. Concurring with the analysis method in section 2.2, the

first datapoint is considered unreliable, so it is omitted in these graphs. With this datapoint included, the curves would start at the same point in time. The discrepancy in starting time is exaggerated by the log-log scales used in both graphs and by the fact that the sampling rate was lower for the test runs in which the freezing fronts propagated slower.

After this initial sensitivity test, a more controlled test was done in a climate chamber on a more representative aircraft coating, namely epoxy (Epikote). Due to the erratic movement of the front, the frontline velocity could not be used, the area growth rate and average front velocity were registered and shown in Figure 4.19.

Results and discussion

The temperature independence of $G(t)$ can be observed in Figure 4.17a and b. As both the growth rate and time measurements span over three orders of magnitude, the curves have to be plotted on a log-log scale. A master curve that seems to appear for both $G^*_{frontline}$ and $G^*_{perimeter}$ hints towards a steady decay of growth rate with time, independent of timescale and thus independent of the front propagation mechanism. The apparent exponential decay of the sample with the highest surface temperature of -13°C in Figure 4.17 is not reproduced in the other samples at lower surface temperatures. No master curve was expected in the $G^*_{perimeter}(t)$ or $G^*_{frontline}(t)$ graphs. Although it is probably an artefact of the log-log scaling, the appearance of master curve might show that areas with fast MLL freezing front propagation ($G^* > 1\ mm/s$) freeze first and independently from other areas with slow dendrite freezing front propagation ($G^* < 1\ mm/s$). The master curve thus illustrates how parts of the surface are quickly frozen by MLL freezing front propagation and later the remaining surface is frozen by the well-known dendrite freezing front propagation mechanism and eventually, even later by frosting.

A higher nucleation temperature does seem to yield longer freezing times at lower growth rates. The order of magnitude difference between the analyzed samples suggests a different, (partially) temperature-dependent propagation mechanism for the sample frozen at $T_{surf} = -13°C$.

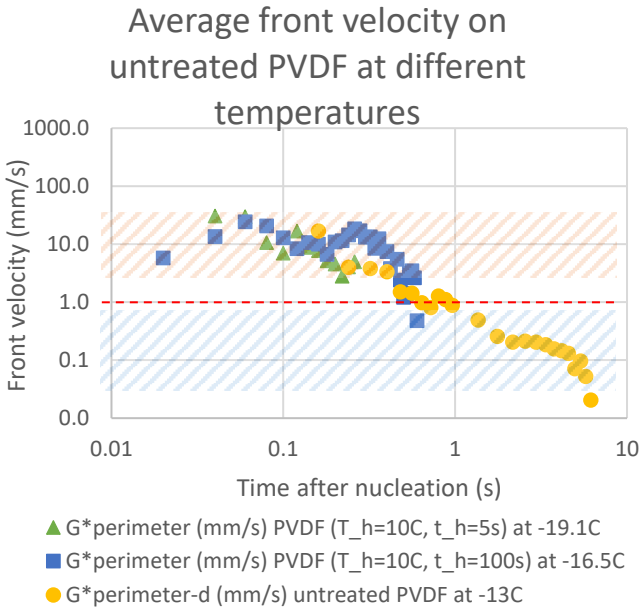

a

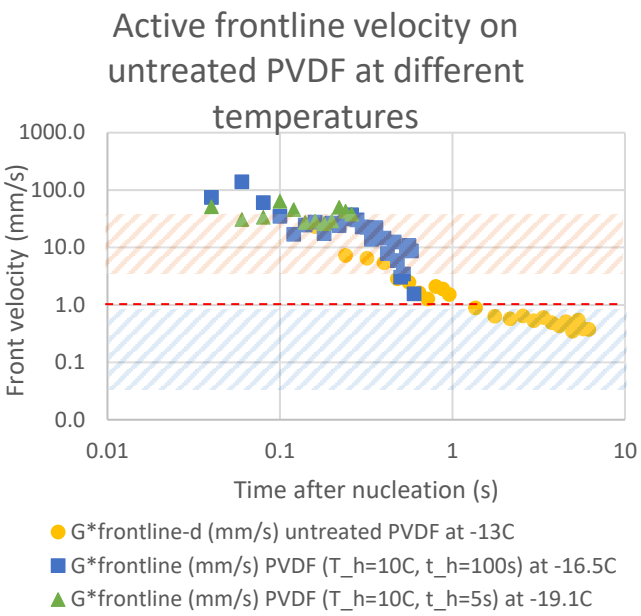

b

Figure 4.17: front velocities on an untreated PVDF film for different surface temperatures of $T_{surf} = [-13°C; -16.5°C; -19.1°C]$. (a) normalized using the perimeter of the frozen area. (b) Normalized using the length of the active frontline. Different freezing front propagation mechanisms are indicated as hatched areas, namely MLL (orange) and dendrite growth (blue), separated by the rough boundary of 1 mm/s (dashed red line).

It seems like the front velocity decreases over time and different phases can be identified within the freezing front propagation. In Figure 4.18, an attempt is made at identifying two phases for each nucleation temperature. In the graph, one can see that the $G^*_{perimeter}$ is lower in the $20\% - 100\%$ part of the front propagation. However, the uncertainties in front velocity between the so-called phases of the front propagation overlap too much for a conclusive phase identification. Visually, different front propagation mechanisms appear to occur, with very different front velocities. This difference is attributed to the presence or absence of an MLL. Non-continuous MLLs might cause a hybrid mechanism, between MLL and dendrite freezing front propagation. As indicated in Figure 4.18, MLL freezing is observed around $G^*_{perimeter} = 10\ mm/s$ and dendrite freezing around $G^*_{perimeter} = 0.1\ mm/s$. For this reason a boundary is defined at $G^*_{perimeter} = 1\ mm/s$, to be able to identify the front propagation mechanism from front velocity graphs.

For lower temperatures, the front velocities are higher on average. This is in accordance with the results published by Pasieka et al. as mentioned earlier, although their results are limited to supercooled temperatures between $-2°C$ and $-7°C$. [21]

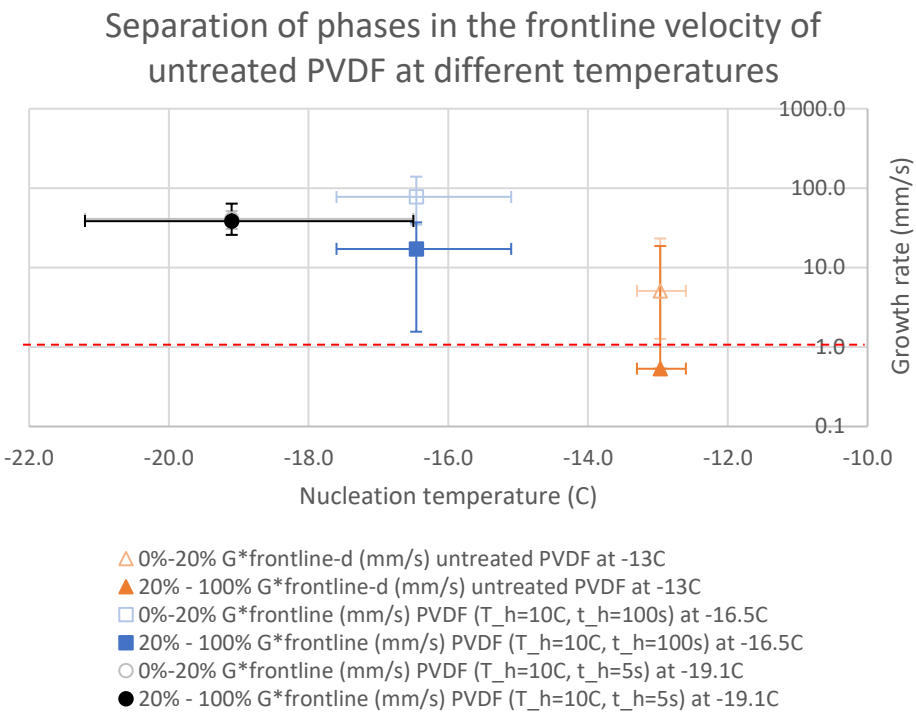

Figure 4.18: Average velocities and frontline velocities for different stages in the front propagation process. The dashed red line indicates the transition from a dendrite to a MLL freezing front propagation mechanism

The test results shown in Figure 4.19 show that the front velocity is slightly higher for higher surface temperatures. This is counter to the expected result, as the driving force for freezing is higher at lower temperatures. Lower temperatures might actually make it harder for the crystal to grow, as shown by the Monte-Carlo simulations by Li et al. explained in section 1.1.2. [18] However, the apparent difference in freezing front velocity is well within the error margin. Therefore, for all further purposes in this thesis, the freezing front propagation velocity is considered invariant with temperature, below the critical nucleation temperature of $-14°C < T_{surf} < -11°C$. This allows comparison of front propagation velocities on surfaces with different surface temperatures in the range of $-22°C < T\_surf < -14°C$.

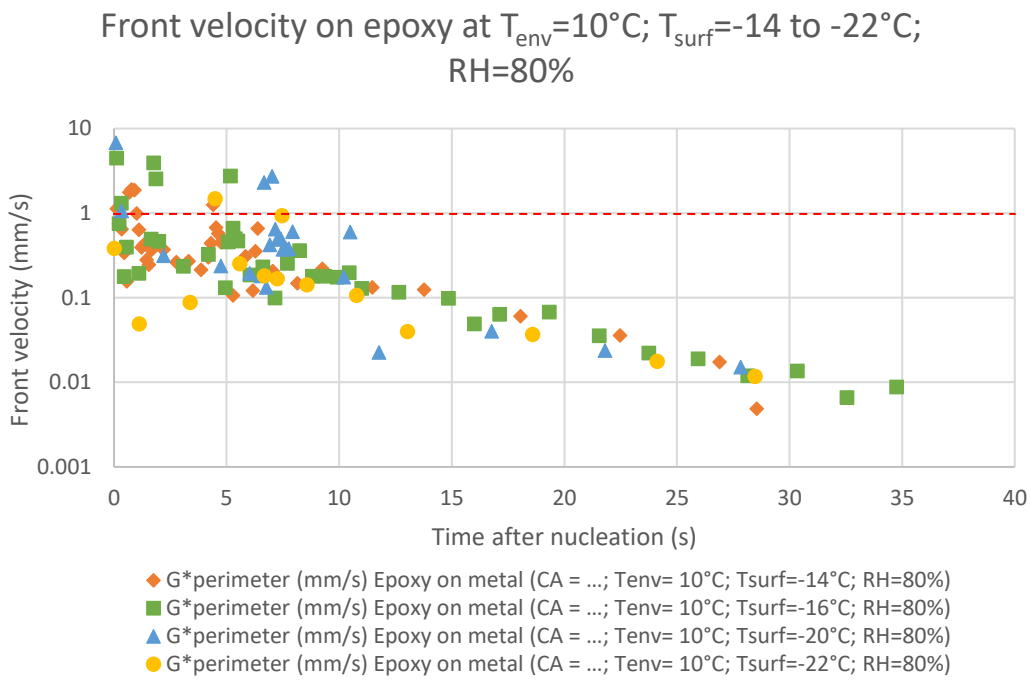

Figure 4.19: Frontline velocity $G^*_{perimeter}$ on epoxy at different surface temperatures. Two tests at $T_{surf} = -10°C$ and $T_{surf} = -10.5°C$ are not shown in the figure, as no freezing occurred. The dashed red line indicates the boundary between dendrite and MLL freezing front propagation mechanisms. It should be noted that the decrease of front velocity with time is an artefact of the method of observation and analysis, as explained in section 2.2.

The bursts of MLL freezing ($G^*_{perimeter} > 1\ mm/s$) might be caused by previously impacted droplets. This is strongly hinted by the shape and location of the areas that freeze with this mechanism, of which an example is shown in Figure 4.20. These areas are located exactly where previous droplets were deposited in previous test runs. The freezing by MLL of these areas can be caused by absorption of water into the Epikote epoxy coating or the remainder of a thicker MLL. Epoxy is known to be able to absorb small quantities of water. Although all surfaces were heated between test runs to $45°C < T_{surf} < 55°C$ to remove any trace of condensed droplets, impacted droplets or MLL, the MLL has been shown to grow in thickness at $T_{surf} = 50°C$. [23] Alternatively, the dried droplets could have left behind hydrophilic ions that had been dissolved before drying. These ions would be hygroscopic and locally increase the thickness of the MLL, effectively creating hydrophilic regions on the coating. As deionized water was used for the impacting droplets some contamination of the used deionized water should have occurred, if ions are left after drying.

Whatever the actual cause of the MLL freezing front propagation bursts, they definitely travel through the specific areas were droplets had been impacted before. This implies that the MLL freezing front propagation is sensitive to the history of impacted droplets. For the study of clear ice formation on aircraft surfaces, the presence of areas with dried droplets or deposition of aerosol ionic particles might determine whether an MLL propagation front will occur or not. Further research might result in the advice to aircraft operators to heat up surfaces to at least $T_{surf} > 65°C$ and make sure critical surfaces are cleaned regularly.

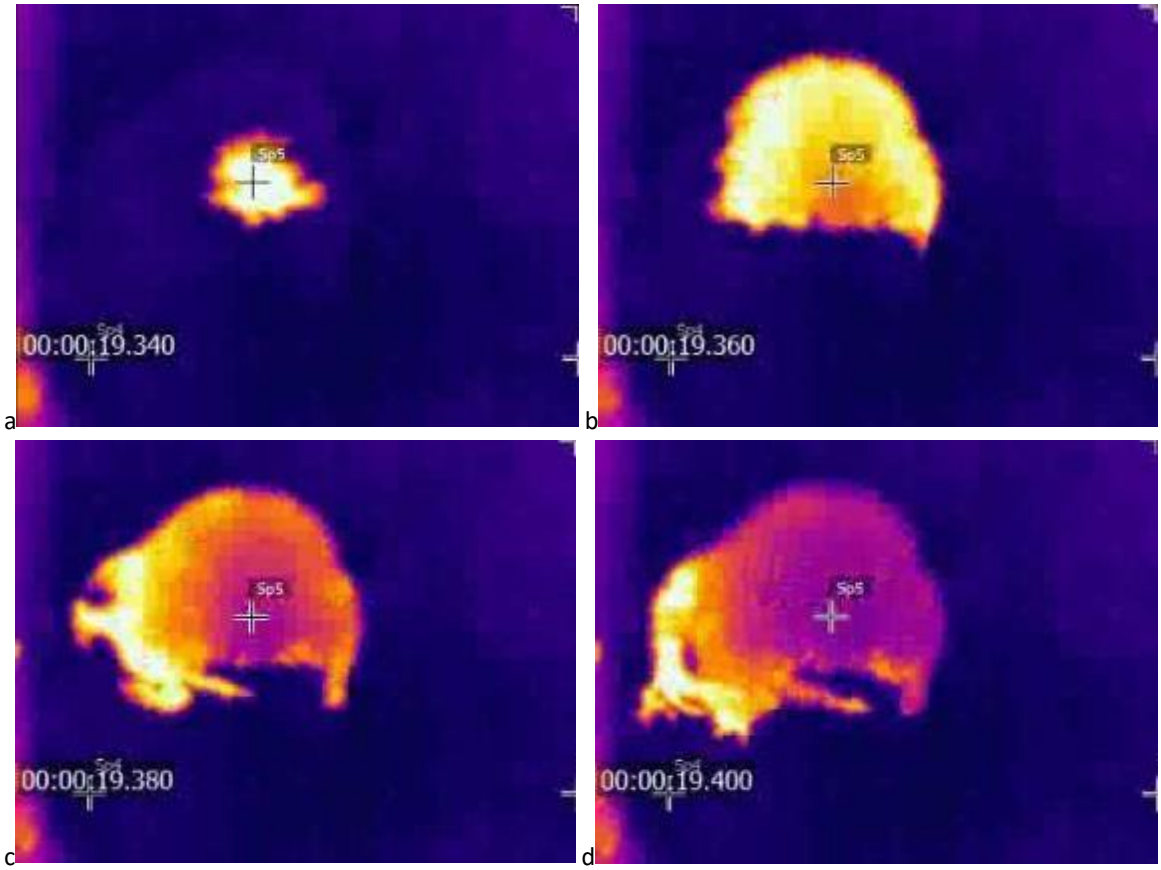

Figure 4.20: Four Frames of an MLL freezing burst on epoxy with $T_{env} = 10°C$, $T_{surf} = -24.5°C$, $RH = 80\%$. The MLL freezing front takes the shape of a previously impacted droplet. For scale, the width of the figures is $8\ mm$.

As mentioned earlier, James et al. concluded that the MLL grew on an alkyne terminated polymer at temperatures below $T_{surf} = 50°C$. Above $T_{surf} = 65\ °C$, the MLL shrunk with 1 Å per hour initially. After 12 hours at $T_{surf} = 100°C$, the MLL thickness had only been reduced by 10 Å. [23] As between each cycle of freezing, the surface was only heated to $45°C < T_{surf} < 55°C$ for between 2 and 20 minutes, the MLL would be expected not to be fully evaporated. Another explanation could be the absorption of water from the droplet into the epoxy coating, which created a locally hydrophilic site. The effect of a lower contact angle is investigated in section 4.2.2.

4.2.2 Contact angle

A second candidate governing parameter for the freezing front propagation velocity is the contact angle. If effective in slowing down or terminating the freezing front, this material property has the potential for the design of smooth, durable and manufacturable coatings for aircraft.

Haifeng-Zhang showed that continuously increasing the contact angle from $30°$ to $150°$ continuously increased the nucleation time delay of $25\ \mu l$ droplets, although only by seconds. More importantly, the rate of freezing increased continuously as well. [26]

Ice adhesion strength on rough surfaces might not be strongly correlated with the contact angle, but correlates well with the contact angle hysteresis (CAH), according to Kulinich et al. Lower ice adhesion for higher contact angles is only valid for low hysteresis. [72]The connection of the influence of CAH with the molecular liquid layer, as introduced in section 2.2, is hard to hypothesize. If the MLL would play a role in

reduction of ice adhesion strength, it could be argued that ice adhesion should decrease with increasing contact angle hysteresis. The MLL could be interrupted by the same chemical heterogeneity or roughness that causes CAH. This could prevent a continuous, homogeneously crystalline molecular layer of ice to form fast on surfaces with high contact hysteresis, which would in turn reduce the 'priming' of the surface. Also, the discontinuity of the MLL, if this is the case on surfaces with high contact angle hysteresis, would decrease the contact area between water and surface. This should decrease the nucleation time delay. However, it could also be argued that CAH should decrease the nucleation time delay under the influence of the MLL, as measured by Kulinich et al. If the hysteresis is caused by metallic ions in the material, these could serve as hydrophilic sites for nucleation of the MLL. The chemical heterogeneity or roughness of the surface, creating the CAH might also keep water adsorbed to the surface, making the MLL thicker and more continuous.

Methodology

The first material that was used, is permanent marker ink on Teflon in a standard controlled lab environment. The difference in conductivity is small between the two materials, but the difference in contact angle large.

The second test of the effect of the contact angle is identical to the test described in section 4.1.5, where the effect of humidity is measured. Two metal surfaces, an epoxy surface and a plasma treated PVDF thin film are employed in a climate chamber and frozen under IRI. The contact angles of the metal, epoxy and PVDF surfaces are listed in Table 4.5. As previously described, the PVDF thin film on a glass substrate could be plasma treated to form hydrophilic squares. The MLL freezing front propagation was observed to be confined to these hydrophilic squares.

Material	**CA** $(°)$	$\boldsymbol{T_{surf}}$ $(°C)$	$\boldsymbol{G}$ (mm^2/s)	$\boldsymbol{G^*_{perimeter}}$ (mm/s)	$\boldsymbol{G^*_{frontline}}$ (mm/s)
Metal with oil-filled holes	90	-12.3	122.4	3.8	7.0
Metal with empty holes	90	-12.5	547.3	19.6	45.8
Epoxy on metal	75	-16	22.5	0.6	0.9
Epoxy on metal	75	-14	24.0	0.5	0.8
Plasma treated PVDF	85 ± 5	-15	28.2	1.3	2.5
Plasma treated PVDF	85 ± 5	-15.5	115.5	4.6	18.3

Table 4.5: Effect of contact angle on front propagation (CA to be added) at $\boldsymbol{RH = 80\%}$ and $\boldsymbol{T_{env} = 10°C}$

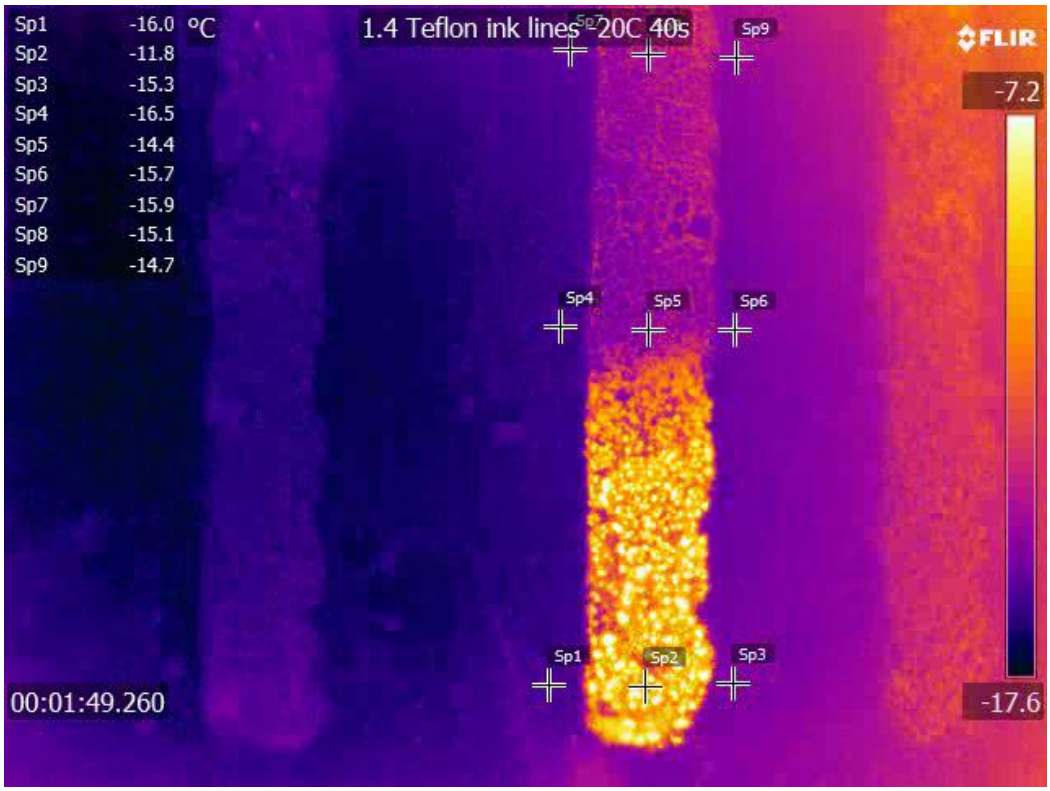

Figure 4.21: Freezing front propagation on Permanent marker ink on Teflon

As described in section 4.1.3, the droplets on Teflon have long nucleation time delays. On large timescales they do appear to feature a freezing front propagation. Due to the individual droplets being visible under IR and the low velocity, it could be concluded that the front propagation on Teflon was dendrite growth.

However, when this dendrite front reached the surface of the permanent marker ink, as illustrated in Figure 4.21, the whole ink-covered area immediately froze, within $0.1\ s$. Frozen droplets can clearly transmit nucleation to unfrozen neighboring droplets, with a front velocity much higher than that of dendrite freezing. This is an example of MLL freezing front propagation. After full freezing of the ink-covered area, the freezing front transitioned back to the Teflon freezing front propagation mechanism, namely dendrite growth. In this manner, the freezing front slowly transmitted nucleation from one ink-covered area to another

In Figure 4.22, an image is shown of Teflon with ink lines after melting. The places that have not been frozen do not show any droplet coagulation. This is seen as a strong indication that the nucleation propagation mechanism is dendrite growth and not MLL front propagation. During so-called 'percolation induced frost formation', as described by Guadarrama-Cetina et al. [59], frozen droplets grow crystals on their surface, sucking water from neighboring droplets through evaporation and condensation. This happens due to an imbalance in vapor pressure between the surface of the liquid droplets and ice crystal, preferentially condensing water vapor onto the second. It creates dry bands around the frozen droplets, as also demonstrated by Kirillova et al. [53] This same mechanism could 'dry up' the MLL connecting droplets. If that is the case, the darker areas in Figure 4.22 could be where the MLL is still present. When the dendrite propagation front approaches, the MLL could dry up just before the freezing front arrives. Guadarrama-Cetina et al. showed that the evaporation and condensation mechanism creating dry bands around frozen droplets acts on distances over $150\ \mu m$. [59]

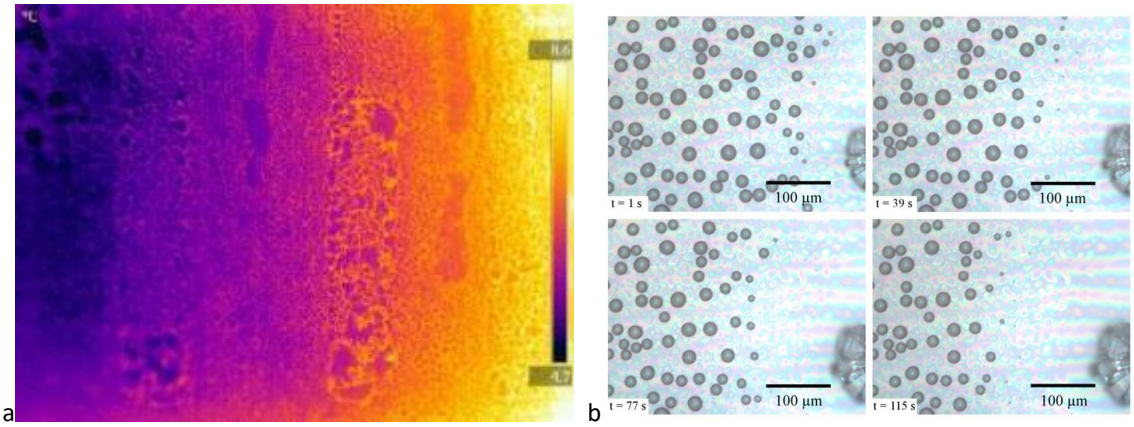

Figure 4.22: (a) Teflon with permanent marker ink lines, after a freezing and melting cycle (b) Creation of a dry band around frozen droplets [59]

Figure 4.23 shows front velocities on epoxy, plasma-treated PVDF and metal. It seems like the front velocity increases with the contact angle. This would be a very unexpected result, counter to the hypothesis that an increase in contact angle prevents a continuous MLL to form and transmit crystallization.

Within the test runs on PVDF, in the areas where the PVDF thin film was dark, the growth rate was drastically reduced and a much slower nucleation mechanism was observed. In the lighter areas, indicating the presence of absorbed or adsorbed water, the freezing front was not affected by the hydrophobic-hydrophilic boundary.

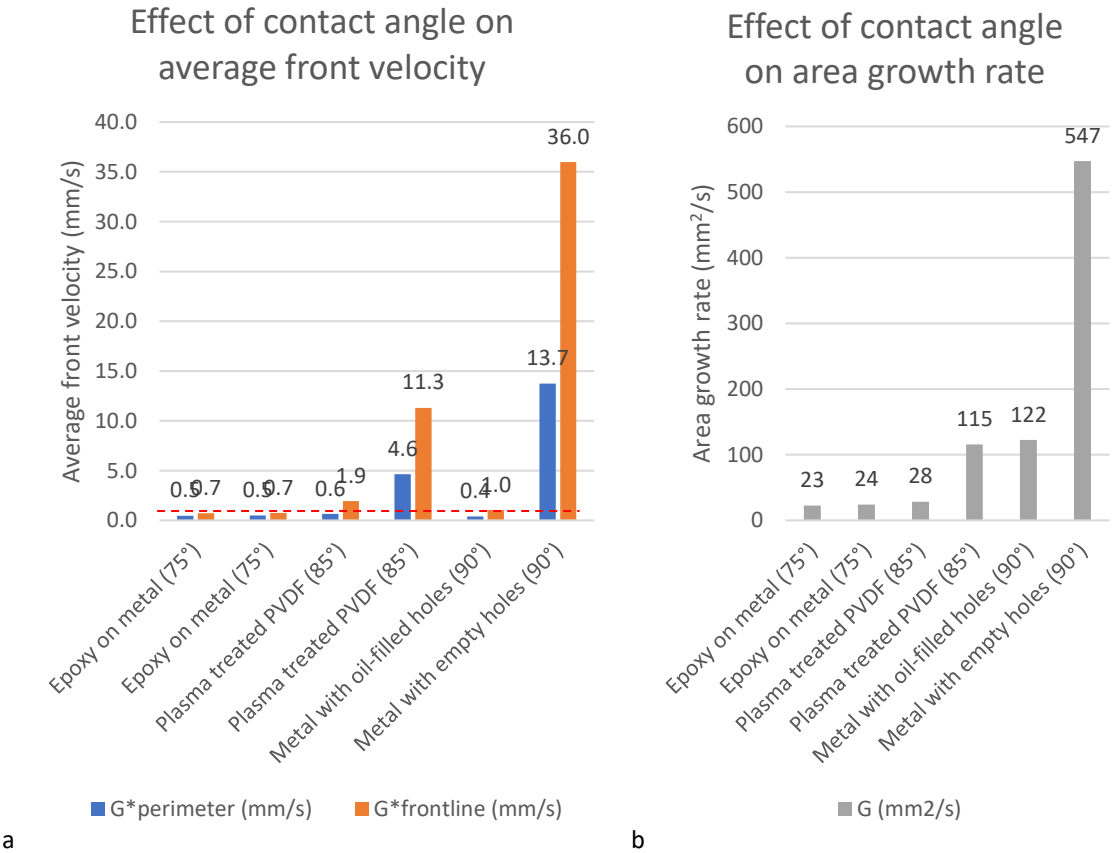

Figure 4.23: (a) Active and Average Front velocities and (b) area growth rates on epoxy, plasma treated PVDF and metal at $T_{env} = 10℃$, $T_{surf} = -12.5℃ > T\_surf > -16℃$ and $RH = 80\%$.

The large difference in active frontline velocity between metal with empty and oil-filled holes originates from the averaging process. Section 5.1 uses Figure 5.5b to clarify this difference in detail and to show that the initial MLL freezing front moves a lot faster than the low average velocity in Figure 4.23.

The surprising increase of the freezing front velocity with the contact angle might be explained by another parameter. As the metal is much more conductive than the polymer coatings, these surface might induce a higher freezing front propagation velocity. However, the conductivity is outside of the scope of this thesis.

4.2.3 Relative humidity

As discussed in section 4.1.5, the nucleation time and nucleation temperature of the MLL depend on humidity, when falling below $RH = 40\%$. Many publications mention the relative humidity as a relevant parameter for the nucleation delay and ice adhesion strength, especially for impacting droplets and/or superhydrophobic surfaces. [16,3,17,37,38,29,39,40] The consensus is that water vapor would penetrate in the micro- and nanopores and mechanically lock frozen droplets, increasing ice adhesion. As no analysis on the MLL freezing front propagation has been performed yet in literature, the effect of the relative humidity has to be evaluated. Although it is not a coating property that can be used for the design of an anti-icing coating, it might help in forming a better understanding of the new freezing mechanism.

Methodology

In a first test, to observe the effect of the relative humidity on the freezing front propagation velocity, thin films of plasma-treated PVDF were tested in a cold climate chamber at $T_{env} = 10°C$ at cold surface temperatures of $19°C < T_{surf} < -25°C$. Three relative humidities where tested, namely $RH = [30\%;\ 50\%;\ 80\%]$. The averages for the obtained front velocities in table (Figure 4.24) are computed according to the approach as concluded in section 2.3, which included removing the first datapoint.

As mentioned in section 2.2, the intensity of the front is not identical between tests, with weaker fronts being barely visibly with IRI. The change front intensity was linked to the thickness of the of the MLL. In an initial test, this assumption is tested on two surfaces of plasma-treated PVDF. Before the surface temperature decreases below $0°C$, one of the surfaces is held at $5°C$ for $20\ s$ and the other surface is held at $0°C$ for $315\ s$. The positive temperature at which the surface is held before the start of the test is named "holding temperature" or T_{hold}. The amount of time the surface is allowed to rest at T_{hold} is named the "holding time" or t_{hold}. During the subsequent freezing test, the front intensity is quantified as the difference between the nucleation temperature T_n, which is the surface temperature in the last frame before nucleation occurs, and the maximum surface temperature at the same location in the following frames. The temperature increase due to the escape of latent heat ΔT, usually reaches a maximum after two frames, at time $t = t_n + 0.04s$. To separate the effects of increasing T_{hold} and t_{hold}, a second test freezes a single surface of plasma-treated PVDF with 9 different combinations of holding temperature and holding time, with $T_{hold} = [0°C; 5°C; 10°C]$ and $t_{hold} = [5\ s; 20s; 100s]$. Between each test, any remnant surface water is evaporated at the usual heat $T_{surf} = 40°C$ for 10 minutes each. Some of the representative images are shown in a grid, to show the change in front intensity in Figure 4.27.

Results and discussion

As can be seen in Figure 4.24, a change in relative humidity does not seem to decrease the average values for the average front velocity $G^*_{perimeter}$ or the active frontline velocity $G^*_{frontline}$ significantly. The MLL is expected to be discontinuous a $RH = 30\%$, so at least the average front velocity was expected to decrease.

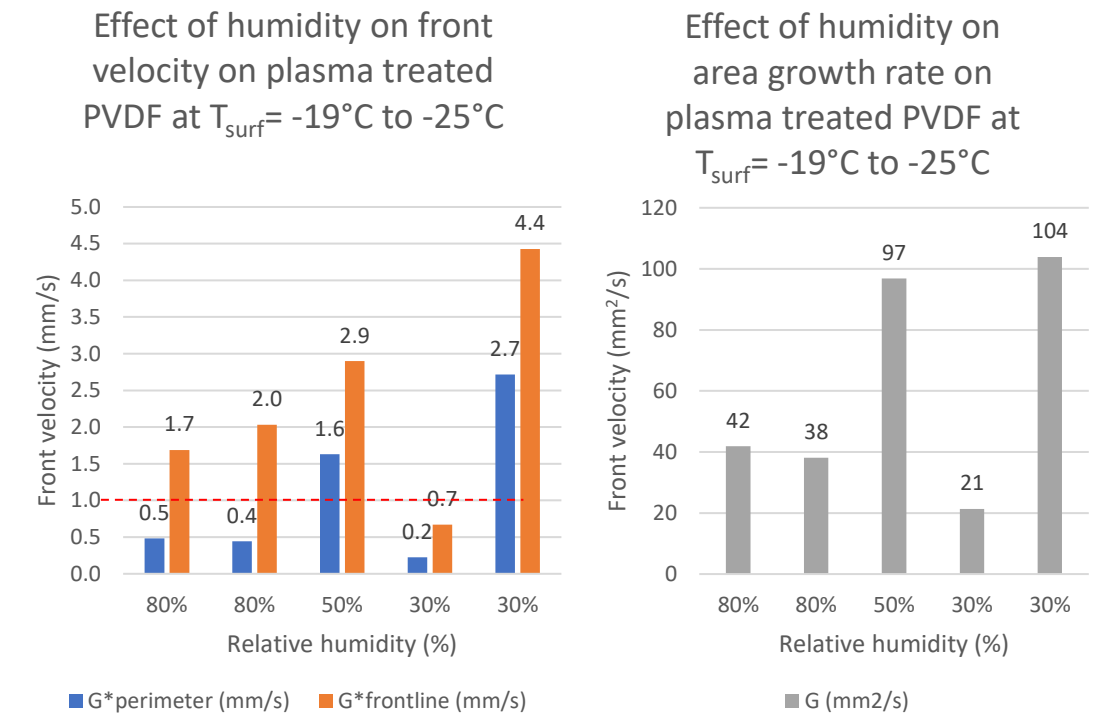

Figure 4.24: (a) Effect of relative humidity on the average MLL freezing front propagation velocity and (b) on the average area growth rate. The five experiments were conducted on and identical plasma treated PVDF at $-19℃ < T_{surf} < -25℃$, placed in a controlled environment with $T_{env} = 10℃$ and $RH = [30\%; 50\%; 80\%]$.

However, when plotting the measured values for $G^*_{frontline}$ over time, as shown in Figure 4.25, the origin of the surprising increase of average velocities with decreasing relative humidities becomes more clear. At relative humidities above 50%, a front propagates relatively continuously over the surface, as a mix between dendrite freezing ($G^*_{frontline} < 1mm/s$) and spikes of MLL freezing ($G^*_{frontline} > 1mm/s$). At relative humidities of 30%, the front propagation is terminated fast. The reactivation of the frontline takes much longer, indicating a lack of condensed water or MLL for nucleation transmission. Due to the lack of slow dendrite freezing regions, the average values of front velocity per humidity in Figure 4.24 are much higher.

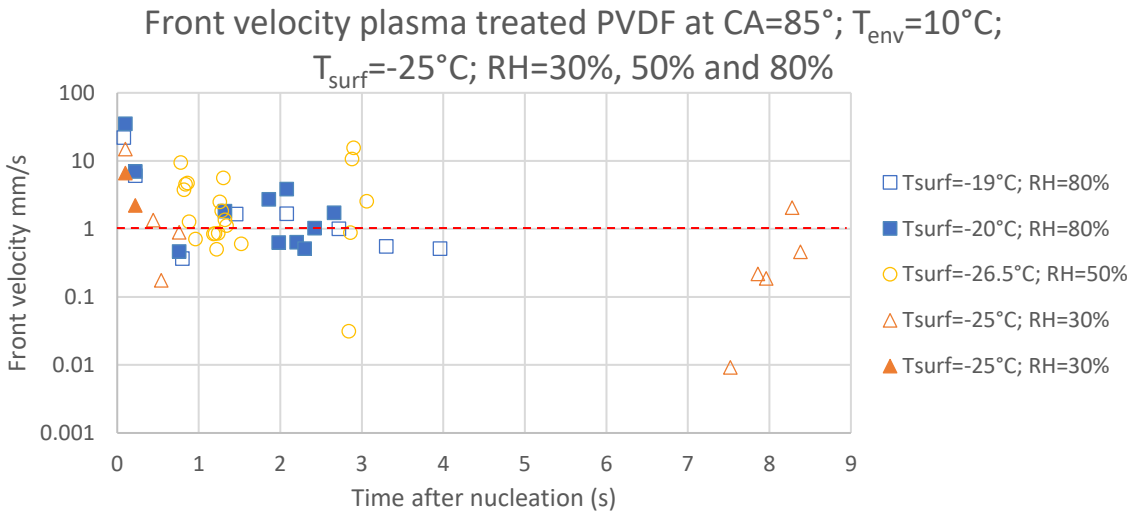

Figure 4.25: The active frontline velocity over time on plasma treated PVDF for 5 experiments with similar surface temperatures of $-25°C < T_{surf} < -19°C$ but at different relative humidities of $RH = [30\%; 50\%; 80\%]$. The red dashed line at $G^*_{frontline} = 1\ mm/s$ separates the low dendrite freezing front propagation velocities from the higher MLL freezing front propagation velocities.

In the second set of tests, the effect of the relative humidity on the front intensity ΔT is assessed. The blue triangles in Figure 4.26, show the results for the front intensity of an MLL front on the first plasma treated PVDF surface, which was held at $5°C$ for $20\ s$. During the subsequent freezing experiment, this surface nucleated at $T_{surf} = -18.5 \pm 1.3°C$ after $t_n = 28\ s$. The orange diamonds represent second test surface, where the plasma treated PVDF is frozen after extensive condensation of water and coagulation is allowed. This surface was held at $0°C$ for $315\ s$ and froze at $T_{surf} = -19.7 \pm 3.7°C$ after $t_n = 13\ s$, so similar to the first test surface. The graph in Figure 4.26 clearly shows an increase in the front intensity with longer exposure to condensation, so the thickness of the water layer clearly has an effect on the freezing front intensity ΔT the temperature difference before and after nucleation.

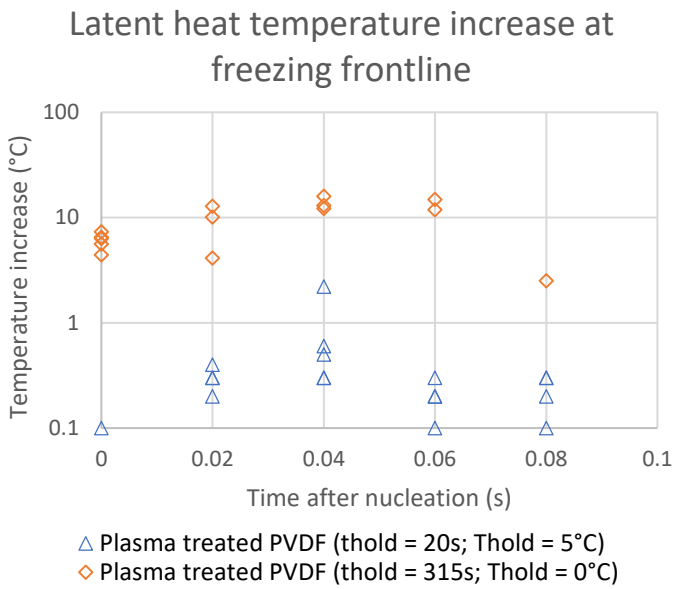

Figure 4.26: The freezing front intensity differs between a thick and thin freezing layer of water. In a thick layer of water, the freezing front is easily visible at low holding temperature (T_{hold}) and long holding time (t_{hold}) (orange diamonds), compared to the surface held at higher T_{hold} for shorter t_{hold} (blue triangles).

The time water is allowed to condense on the surface of the plasma-treated PVDF clearly has an effect on the nucleation front velocity. This can be explained to originate from a thicker MLL at longer condensation times (or t_{hold}, the 'holding time') at a certain temperature of the critical nucleation temperature (or T_{hold}, the 'holding temperature').

Figure 4.27 shows the test results for 9 combinations of different holding times ($t_{hold} = [5s;\ 20s;\ 100s]$) at different (positive) holding temperatures ($T_{hold} = [0°C;\ 5°C;\ 10°C]$). The surfaces freeze at similar nucleation temperatures of $16.7°C < T_n < 19.3°C$ and similar nucleation time delays of $5.8s < t_n < 12.9s$. Three categories can be identified, representing strong fronts (red background), weak fronts (yellow background) and no fronts (green background).

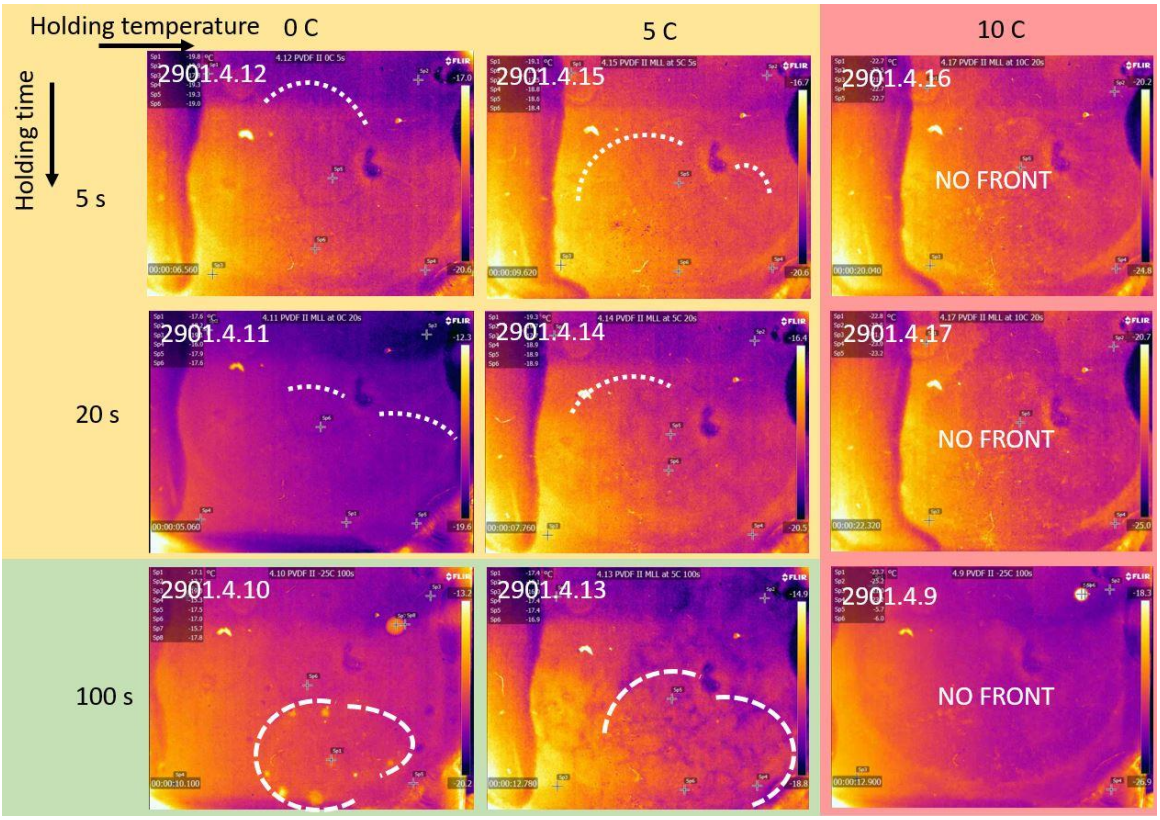

Figure 4.27: The MLL freezing front intensity registered with IRI can be increased by holding the surface at a lower (above 0℃) temperature (holding temperature) before the freezing experiment is started. The 9 experiments are performed on the same plasma treated PVDF thin film, cooling down the surface to $-19℃ < T_{surf} < -17℃$ under lab environmental conditions ($20℃ < Tenv < 24℃$ and $50\% < RH < 65\%$) . The MLL freezing front intensity is similarly increased by increasing the time (holding time, t_{hold}) that the surface is held at a positive temperature (holding temperature, T_{hold}), before the freezing experiment is executed. This results in clearly visible MLL freezing fronts at long holding times and low holding temperatures (red area); The set of experiments shows an intermediate region with a weakly visible MLL freezing front when short holding times and low holding temperatures are used (yellow area); No front is visible with IRI at high holding temperatures, irrespective of the holding time (green area).

In the strong fronts, where the surfaces rested at $t_{hold} = 100s$ and $T_{hold} = 0°C$ and $5°C$, the front intensity of the MLL outside of droplets is $0.0°C < \Delta T < 0.3°C$, whereas the average value for ΔT is $0.14°C$. In the freezing experiments with the same holding temperatures of $T_{hold} = 0°C$ and $5°C$ but with shorter holding times of $t_{hold} = 5s$ and $20s$, the freezing front is barely visible. However, in these experiments, the front intensity is measured to be in the same range as for the visible fronts, namely $0.0°C < \Delta T < 0.3°C$. The average front intensity is $0.08°C$, indicating that most measurement points registered $\Delta T = 0.0°C$. For the surfaces held at $T_{hold} = 10°C$, no freezing front could be observed with IRI, irrespective of t_{hold}.

The similar ranges of $0.0°C < \Delta T < 0.3°C$ for visible and hardly visible freezing fronts, is most likely due to an intrinsic bias to the freezing front identification process. If the freezing front is defined as an increase in temperature, the front intensity will be registered when a temperature increase is observed. This temperature increase might be a random fluctuation, up to the value of $0.3°C$, but is easily mistaken for a front intensity.

The lack of a freezing front propagation at $T_{hold} > 10°C$ and the weaker freezing fronts observed for indicates the growth of a layer of condensed water with time. As described in section 4.1.5, this layer could be a molecular layer of water. It also indicates that the freezing front intensity is hard to quantify with the current manual process. This could be fixed with an automated front propagation analysis method.

4.3 Conclusion

The influence of surface, material and environmental parameters on ice nucleation was assessed to answer research subquestion 3.1 ("What is the influence of identified relevant governing parameters on the nucleation temperature and nucleation time delay?"). Firstly, the surface temperature had a large effect on the nucleation time delay. Above a critical surface temperature of between $-11°C$ and $-14°C$, no nucleation took place. Below this temperature, the nucleation time delay remained between $5s$ and $30s$ on PVDF thin films. The small difference between values for t_n of separate droplets strongly supports the hypothesis that nucleation is transmitted between droplets, which is visually confirmed with IRI. The $t_n(T_n)$ curves can be used answer research subquestion 3.1. Secondly, the effect of surface vibration could not be observed by freezing droplets on a piezoelectric element, vibrating at $5\,Hz$ to $5\,MHz$. No significant decrease in the nucleation time or temperature was observed around the expected value of between $16\,kHz$ and $100\,kHz$. Thirdly, increasing the contact angle was found to increase the nucleation time delay significantly, while leaving the critical nucleation temperature unaffected. It was hard to separate the effect of contact angle from the effect of conductivity with the performed tests. This made it impossible to attribute an observed decrease in t_n and T_n on metal samples to a decrease in contact angle. The spread in values for t_n increased with one to three orders of magnitude, when switching from plasma-treated PVDF to the more hydrophobic Teflon. This was explained by nucleation transmission through the MLL. Also, hydrophilic lines of permanent marker ink featured high values for t_n, similar to the surrounding hydrophobic Teflon. Fourthly, by increasing the conductivity and effusivity by two orders of magnitude the nucleation time delay seemed to decrease by an order of magnitude, although a quantitatively reliable relationship could not be found. An insignificant decrease in nucleation temperature with increased conductivity and effusivity was observed, which would be opposite to the expected trend. Fifthly, decreasing the humidity from $RH = 50\%$ to $RH = 30\%$ increased values for t_n significantly and reduced the critical nucleation time delay by at least $5°C$. It is expected that the MLL forms unconnected islands around $RH = 40\%$, offering less interfacial area for heterogeneous nucleation. Sixthly, values for t_n and T_n were shown to be similar for different droplet sizes between $0.01\,mm^2$ and $30\,mm^2$. This supports the idea that the whole surface of the material serves as area for heterogeneous nucleation, irrespective of whether it is covered by a droplet or the MLL. Lastly, the effect of roughness, surface electrical charge and environmental temperature on ice nucleation were out of the scope of this thesis.

To answer research subquestion 3.2 ("What is the influence of the identified relevant governing parameters on the freezing front propagation velocity?"), the effect of the surface temperature, contact angle and relative humidity were chosen, based on their effect on ice nucleation. Firstly, the freezing front propagation velocity, represented by $G^*_{perimeter}$, was unaffected by the surface temperature in several experiments. Two phases in time could be identified on epoxy coatings at high relative humidities. In the first few seconds, small regions would freeze with spikes of $G^*_{perimeter} > 1\,mm/s$, stabilizing to constant values of $G^*_{perimeter} < 1\,mm/s$. These regions, freezing by MLL nucleation were at the exact location of previously deposited droplets, suggesting water penetration into the epoxy coating, a thick MLL stable up to $T_{surf} > 45°C$ or deposition of hygroscopic salt. Secondly, an local increase in contact angle on hydrophobic hydrophilic samples was observed to terminate the fast MLL freezing front propagation and switch to the slower dendrite freezing front propagation. Based on the average values for $G^*_{perimeter}$, an unexpected sharp increase in front propagation velocity with an increase in contact angle could be concluded for samples with high humidity. However, due to large error bars, this result was not significant. Thirdly, the relative humidity did not affect $G^*_{perimeter}$ much for $RH = 50\%$ and 80%. For $RH = 30\%$, a large difference between front propagation velocities and long times between MLL propagation events could be observed. This was assumed to be due to the effect of discontinuity of the MLL at $RH < 40\%$. In general, the use of average values for $G^*_{perimeter}$ was unsuccessful in identifying the effect of governing parameters on freezing front velocity. The error bars for $G^*_{perimeter}$ had ranges of over one to three orders of magnitude per freezing event and the length of freezing differed over two orders of magnitude between tests. This is intrinsic to the freezing process, certainly at low relative humidities, and is caused by the mixing of dendrite and MLL freezing front propagation. The increase in average values for $G^*_{perimeter}$ should be solved by sampling the velocity with high time resolution at equal timesteps, something that is prohibitively long with a manual front tracing method.

5. Anti-icing performance of hydrophobic-hydrophilic coatings

Research question 4: How can the identified relevant governing parameters of the nucleation temperature, nucleation time delay and freezing front propagation velocity be employed to create novel smooth, durable and non-toxic surfaces that prevent ice nucleation or growth of the frozen area?

The clear decrease in nucleation temperature of the surface with decrease of the environmental humidity in section 4.1.5, confirms the hypothesis that nucleation occurs in the molecular liquid layer. The observations, combined with literature suggest that at relative humidities above 40% nucleation is transmitted over the whole surface. The logical consequence is that a surface will be 'primed' for freezing of impacting droplets at the relative humidities and temperatures featured in the critical parts of the mission profile. The 'primed' surface allows impacting droplets to freeze at higher temperatures, compared to 'dry' surfaces. These higher nucleation temperatures could be the same as those that cause clear ice formation, for which the conditions of formation are given in Table 1.1. The reduction of bulk freezing velocity at higher nucleation temperatures, as reported by Pasieka et al. in 2014, allows 'smearing out' of supercooled large droplets.

In section 4.2.2 was concluded that the contact angle of a surface material can affect the front propagation velocity. Within the mechanisms of MLL freezing or dendrite freezing, no significant dependency on of nucleation delay on the contact angle was observed. However, the contact angle did affect which of the two mechanisms propagated over the surface. Using this knowledge, a new strategy is proposed in this chapter. Instead of preventing nucleation or reducing ice adhesion with microtopographies, both of which have not been adequately successful in the past decade to see industrial application, [30] it might be better to locally decrease the average front propagation velocity by several orders of magnitude. In this chapter, several designs are presented along with some initial test results, for the reduction of front propagation velocity by a local change in contact angle.

Antonini et al. proposed two options for icing mitigation, namely rebounding of impacting droplets or ice shedding after freezing. [2] The strategy in the current chapter would enable both of Antonini's strategies. To allow for droplet rebounding, edge pinning has to be avoided, which occurs soon after impact on surfaces 'primed' by a frozen MLL or condensed droplets. Ice shedding works best on surfaces with high contact angles, especially superhydrophobic surfaces. However, in high humidities superhydrophobic surfaces perform even worse, which has been ascribed to water penetrating all topographies above $60\ nm$. The effect on higher ice adhesion could be caused by the freezing of this adsorbed water layer, allowing for extra strong mechanical locking, which could be avoided as well by shielding it from a nucleation front.

Two architectures can be imagined to 'protect' regions of the surface from a propagating MLL freezing front, by forcing it to continue as a much slower dendrite freezing front. The first is to place hydrophobic spots in the path of the front. The second is to create hydrophilic spots that allow freezing, but in a controlled location, crystal orientation or shape.

5.1 Hydrophobic islands in a hydrophilic surface

The first strategy to avoid MLL freezing is to create hydrophobic islands, surrounded by the normal, more hydrophilic material. When these hydrophobic islands are placed close together to form a line, they can completely separate two parts of a surface. This would allow for the segmentation of wing or hull surfaces and might isolate the frozen area to a single segment, as sketched in Figure 5.1. If the surface segmentation of hydrophilic coatings by hydrophobic lines is effective in stopping the MLL freezing front propagation and if the frozen MLL can unambiguously be linked to the formation of clear ice, the size of areas with clear ice

could be controlled at every location on the aircraft. In critical regions, such as the leading edges, a higher density of hydrophobic lines could create smaller patches of clear ice that would be more easily removable.

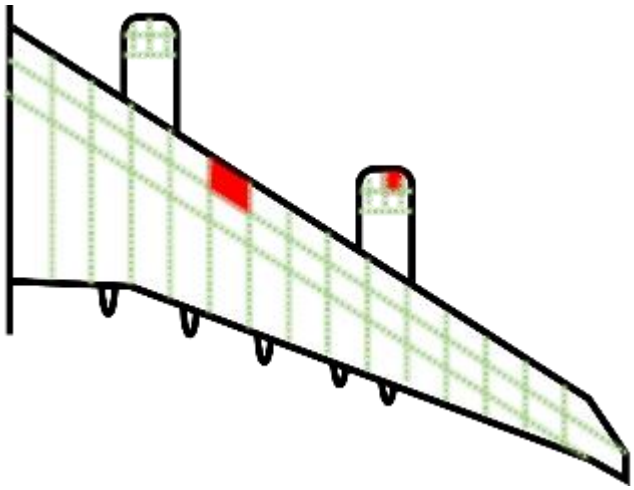

Figure 5.1: Segmentation of an aircraft wing using hydrophobic lines (green dashed) that inhibit the MLL freezing front propagation. These line could contain the area with a frozen water layer to individual segments (red areas), when a nucleation event occurs on e.g. the wing's leading edge or the turbine inlet. The discontinuity of the clear ice sheet could also make it easier for clear ice to be detached from a surface by heating or mechanical removal, as well as improving the visibility of clear ice.

If this method succeeds in making the sheet of clear ice discontinuous, the sheet could be easier to remove by heating or mechanical removal. It might also be easier for pilots to observe the growth of clear ice, if it grows in patches, instead of as a continuous sheet. The transparency of clear ice makes it hard for pilots to notice clear ice formation, while there is little time to activate anti-icing or de-icing systems, according to the interview with a professional pilot summarized in appendix A.

If the MLL freezing front could be detected in real-time, the de-icing systems could be activated on the location where clear ice will start to form. This could entail local release of liquid freeze point depressants or local heating up to $0°C$, to melt the frozen layer. Such a system with direct feedback could reduce the use of toxic fluids and reduce the energy required for de-icing. The design, construction and testing of such a system is out of the scope of this thesis. However, one could imagine sensitive integrated sensors registering the local escape of latent heat or change in coating stiffness due to the freezing MLL. Alternatively, an IRI or LSI tool could be aimed at some of the critical surfaces to observe the escape of latent heat.

Methodology

The effectiveness of such an architecture in terminating a front is expected to depend strongly on the distance between the hydrophobic islands. The observed nucleation fronts, for example on permanent marker ink on Teflon in Figure 4.21, hint at maximum distances under 100 µm.

By filling up the pores of an anodized metal with hydrophobic PVDF, an array of microscopic islands could be created. A solution of PVDF in DMF was applied to a plate of anodized aluminum with pore sizes of $60\ \mu m$. After a few minutes, the solution was wiped of and the plate shortly wiped with acetone on a paper towel. This process was repeated until a visual difference could be observed between untreated and treated part of the aluminum substrate.

The process produced a sample that showed structural coloring on half of the surface, as shown in Figure 5.2, indicating that some of the PVDF had been deposited on the surface or in the pores. This surface was not tested for freezing .

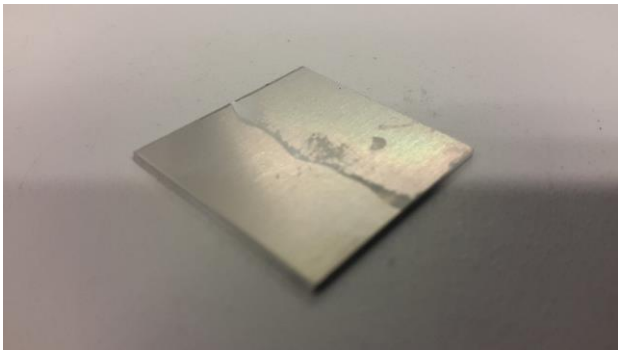

Figure 5.2: Anodized aluminium, where half of the pores is filled with PVDF

The surface coating could also (locally) be impregnated with oil, instead of PVDF. Slippery Liquid-Infused Porous Surfaces (SLIPSs) have been suggested as robust superhydrophobic coatings for easy de-icing. Wang et al. demonstrated lack of water droplet pinning of several tilted surfaces impregnated with a SiO_2-UHMWPE (ultra-high molecular weight polyethylene) suspension. The surfaces resisted 10m abrasion with sandpaper of grid 200, 40 cycles of tape peeling, long-term water dripping and placement in severely chemically corrosive environments. [45] In earlier research, Wang et al. had demonstrated pinning of water droplets on superhydrophobic surfaces at $T_{surf} = 0$°C, whereas the droplets would freely roll off tilted lyophobic surfaces at $T_{surf} < -20$°C. A suspension of SiO_2 was sprayed to create rough superhydrophobic surfaces, which were in turn infused with a perfluorinated lubricant. [32] The anti-icing capabilities of SLIPSs have been reported for the first time by Wong et al. in 2011, who showed reduced frosting and sliding of frozen droplets over epoxy nanostructures and membranes of Teflon nanofibers, both infused with a perfluorinated liquid. [46]

The effectiveness of perfluorinated liquids for anti-icing and easy de-icing seems obvious from literature. However, fluorinated polymers are generally avoided in application on aircraft for their toxicity when used on surfaces that interact with humans. Therefore, the first experiments with SLIPSs in this thesis were performed with standard olive oil, which is harmless in case of human contact.

Holes with a diameter of 400 µm were drilled in an aluminum plate with a thickness of $2\ mm$, shown in Figure 5.3, using the Sirius 1000 Laser. This $1\ kW$ excimer laser with wavelength of $308\ nm$ was provided by the Sirius Laser Facility at the TU Delft. If the laser drilled through the substrate, the exit holes were 200 ± 100 µm in diameter. Around the exit holes no heat-affected zone or burrs could be observed. Because of the clean surface and the smaller hole diameter on the bottom surface, this side of the drilled substrate was used for icing experiments.

a 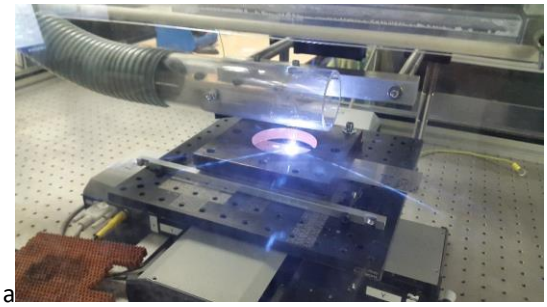 b 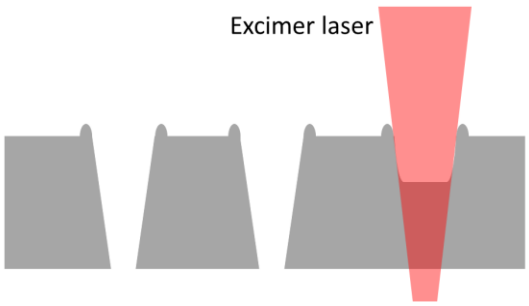

Figure 5.3: (a) Laser drilling of holes with Excimer UV laser at the Delft Sirius Laser Facility (b) Sketch of the conical laser beam drilling holes through an aluminum plate, creating larger holes on the top side and smaller holes on the bottom side. On the top side material builds up around the hole.

The holes in the aluminum substrate were filled with olive oil, by depositing the oil on the top side of the sample. The oil was forced into the holes and out from the bottom side with air pressure. The bottom side was cleaned with acetone, to mitigate the continuous pool of oil that formed, as shown in Figure 5.4b. A thin film of oil might have been left between the filled holes. The substrate was placed top-down on the Peltier, with conductive paste in between, to ensure heat conduction. The setup was placed in a climate chamber, as depicted in Figure 3.2.

a 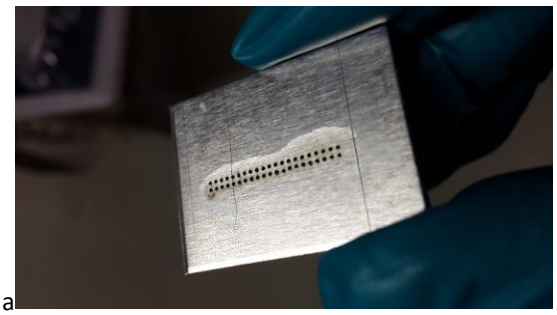 b 

Figure 5.4: (a) Top view and (b) bottom view of oil-filled conical holes, laser drilled in an Aluminum substrate. To make use of the small exit holes of the laser, the bottom surface of the sample was tested for anti-icing

As demonstrated by Figure 5.6, the surface temperature was hard to register with the IR camera, because of the reflective metal surface. Therefore, the temperature was measured with IR in one of the oil-filled or empty holes.

Both the nucleation time delay and nucleation temperature on the surface with oil-filled holes were observed and plotted in Figure 5.5 for humidities of $RH = [46\%; 56\%; 67\%; 80\%]$. A different sample, using the same production method as mentioned before, but with empty holes was also tested at relative humidities of $RH = 80\%$.

Results and discussion

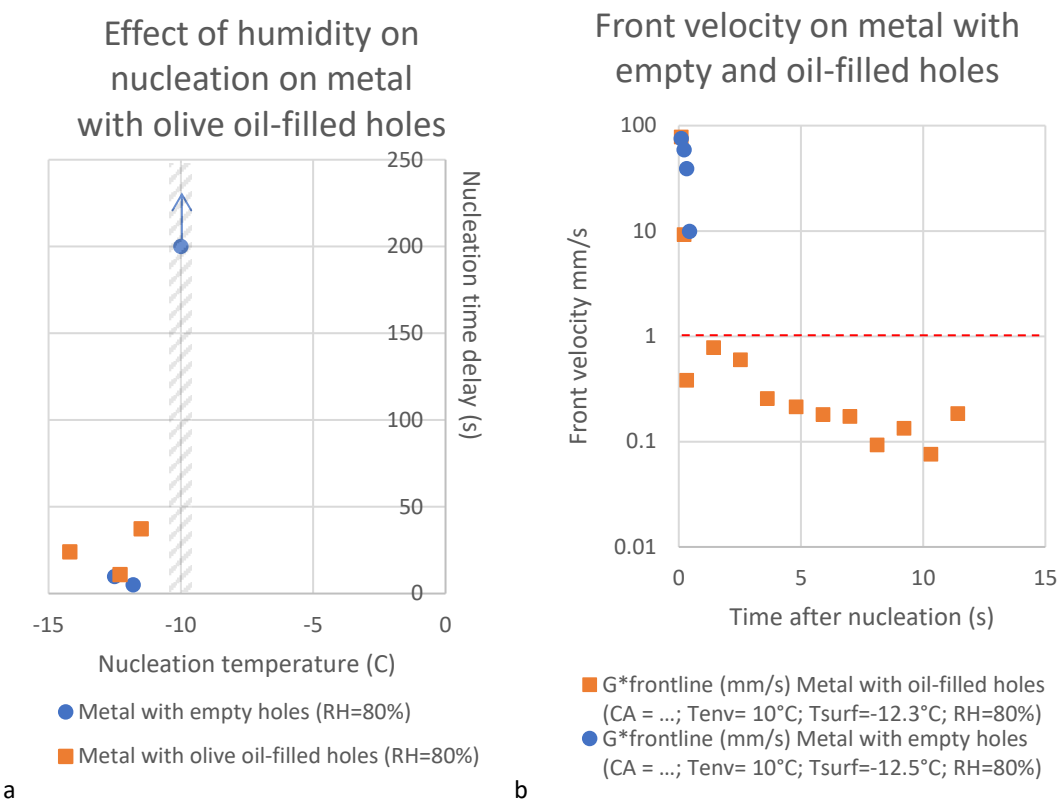

Figure 5.5: (a) Nucleation time delay, nucleation temperature and critical nucleation temperature (hatched area) for $RH = 80\%$. (b) Representative front velocity profiles of on metal with empty and oil-filled holes. The dashed red line at 1 mm/s indicates the boundary between dendrite and MLL freezing front propagation mechanisms

The intention was to perform tests at $T_{surf} = [-10℃; -15℃; -25℃]$ with a relative humidity of $RH = 80\%$ for both the surface with empty holes and the surface with oil-filled holes. However, the empty indicators in Figure 5.5a show that nucleation only occurred above $T_{surf} > -14.2℃$ for both surfaces. The hatched area in Figure 5.5a indicates the critical nucleation temperature of between $-13℃$ and $-11℃$, as observed during experiments.

The time it takes for the surfaces to freeze completely differs by two orders of magnitude between the surfaces with empty or oil-filled holes. The surface containing oil clearly features a transition from MLL freezing to dendrite freezing in Figure 5.5b. The initial freezing phase is shown as snapshots in the left column of Figure 5.6, which shows the first 0.2 seconds of front propagation at typical MLL freezing front velocities of $G^*_{frontline} > 10\, mm/s$. After this initial phase, the front continues, stabilizing around $G^*_{frontline} = 1\, mm/s$. The transition from MLL freezing to dendrite freezing is expected to be caused by a film of oil that remained on the surface when wiping the excess oil with acetone. As stated in section 4.2.2, a local contact angle increase can trigger a transition from MLL freezing front propagation to dendrite freezing front propagation.

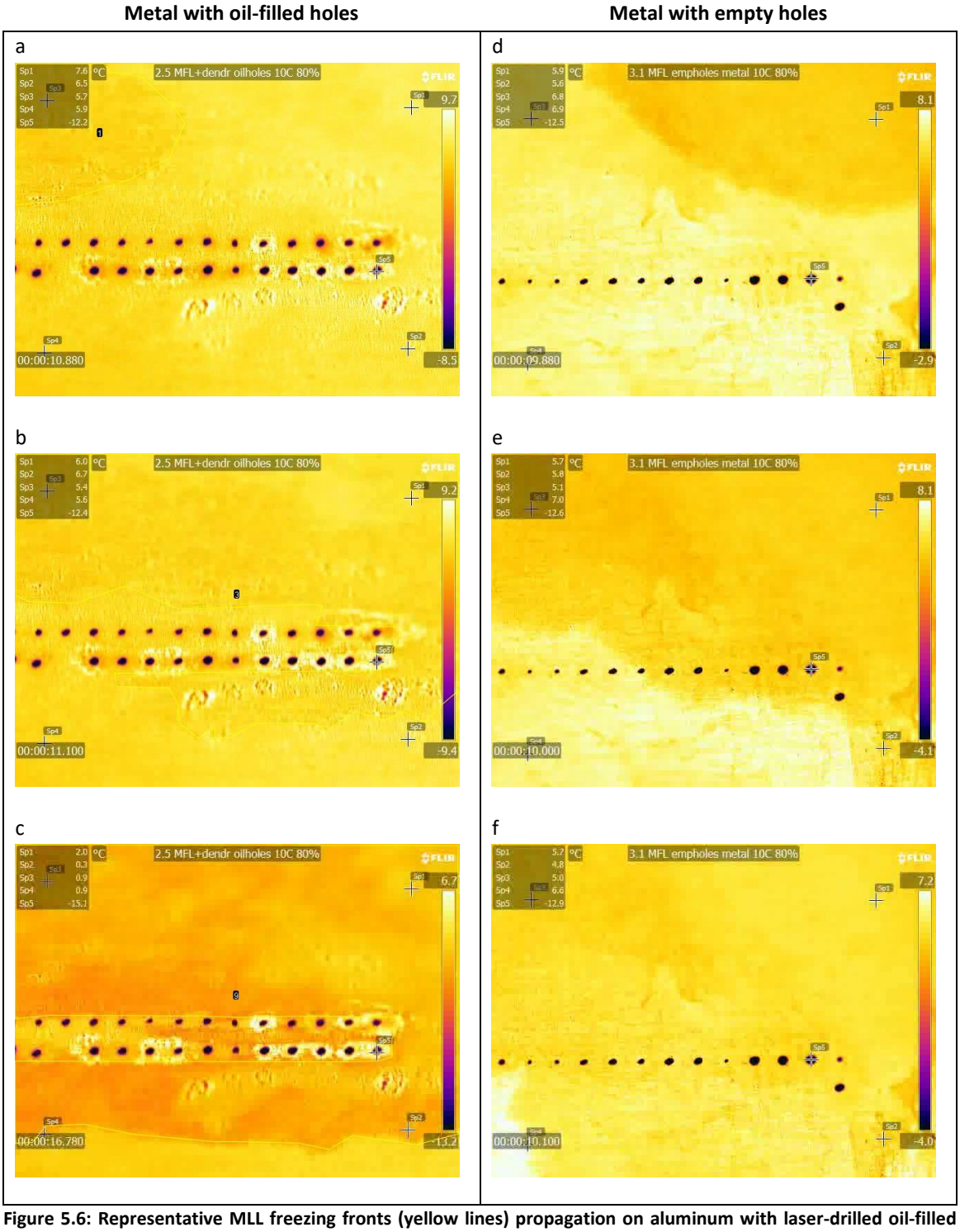

Figure 5.6: Representative MLL freezing fronts (yellow lines) propagation on aluminum with laser-drilled oil-filled (left a-c) and empty (right d-f) holes at around $T_{surf} = -12.5$℃. On the surface of the metal with oil-filled holes the MLL freezing front appears from (a) the top-left corner, (b) bypassing the oil-filled holes and (c) continuing to spread as slow dendrite growth. On the surface of the metal with empty holes, the MLL freezing front (a) appears from the top-right corner (b) going over the holes without slowing down and (c) completely covers the surface.

These results concur with LaForte et al., who researched 274 coatings produced between 2003 and 2014. One of their conclusions was the remarkable effectiveness of grease-type coatings. [30]

5.2 Hydrophilic islands in a hydrophobic surface

As mentioned in section 1.1.3, Kirillova et al. demonstrated the effect of contact angle on frost growth. Crystals of $50\ \mu m$ would grow on hydrophilic sites with an average length of $8\ \mu m$, surrounded by dry bands of about $100\ \mu m$. [53] Inspired by these results, several scalable production techniques were used to create hydrophilic islands on hydrophobic surfaces. Using one of these techniques, the effect of the distance between hydrophilic sites on front propagation could be observed in future research. The aim would be to determine the distance between sites, from which point the MLL freezing front velocity is significantly retarded.

It would also be interesting to control the shape of the ice that forms on an aerodynamic surface, to prevent the drag increase induced by icing. Droplet shapes can be controlled by inkjet printing of hydrophobic-hydrophilic patterns on a surface. [84]One suggestion could be the freezing of water into sharp riblets of ice extending in the direction of the flow. When sessile water droplets freeze, the top of the droplet becomes sharp, which has been named 'tip singularity'. [69]

The first samples were created with inkjet printing. Inkjet printing of hydrophilic islands has been performed before by Zhang et al. (zhang2015) In this thesis, a black model fluid, bought from Dimatix (product number: 2100201179 MFL-003), was deposited with a DMP 2850 inkjet printer. Droplets with a volume of $1\ pl$, or a diameter of 10 µm, were deposited on two substrates, namely a polyethylene (PE) plate and a spincoated, untreated PVDF thin film. These surfaces were attached to a Peltier element and placed in a climate chamber, identical to the setup shown in Figure 3.2a.

In Figure 5.7a, the polyethylene surface is shown before the freezing experiment took place. In Figure 5.7b, the PVDF surface is shown after the freezing experiment. In both experiments, the surfaces could only be tested once, as the ink dissolved in the condensed water.

a

b

c

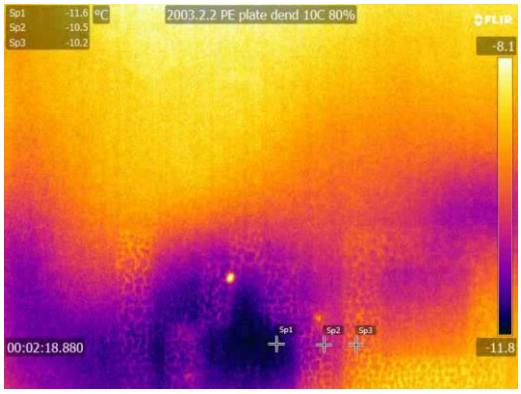

d

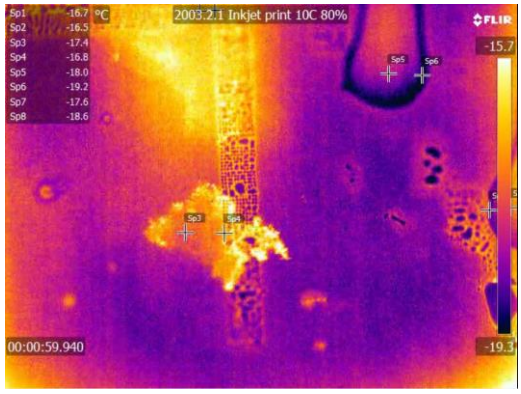

Figure 5.7: Inkjet printed pattern of hydrophilic sites on surfaces of (a) polyethylene (before freezing) and (b) PVDF (after freezing) and snapshots of (c) weak and slow dendrite freezing front propagation on PE at $T_{surf} = -11$℃ and (d) strong and fast MLL freezing front propagation on PVDF at $RH = 80\%$.

The dendrite freezing front propagation was unaffected by the ink pattern. The MLL freezing front propagation was momentarily retarded by the ink pattern, until it was able to break through the barrier, as illustrated in Figure 5.7d.

To avoid the hydrophilic-hydrophobic architecture disappearing, two more durable methods where developed and tested. The first method is drilling small holes in Teflon, the result of which is depicted in Figure 5.8a. These holes could be filled up with a hydrophilic material. For this purpose, an alginate (6w%) / water (94w%) was used.

The second method that was tried, was the deposition of droplets with diameters of between 0.5 and $1\ mm$ on a spincoated PVDF surface. This method is depicted in Figure 5.8. The alginate droplets were cured with a calcium chloride solution through ion exchange.

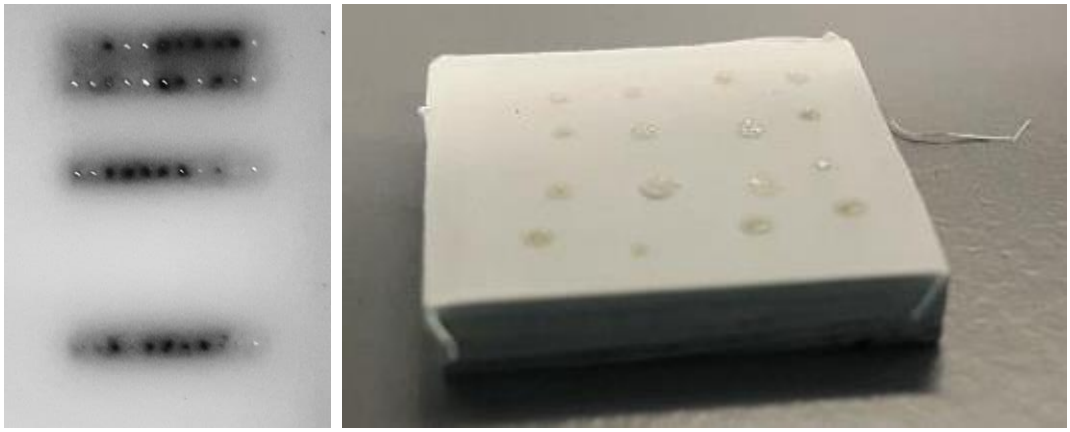

Figure 5.8: (a) Holes laser-drilled in Teflon (b) inkjet printed patterns and (c) hand-deposited droplets of hydrophilic alginate on a PVDF thin film

The creation of holes in Teflon, using the same Laser drilling method as described in section 5.1, was not successful. Although the holes were through holes, as proven with a needle, the Teflon was visibly carbonated at the edges of the holes. The heat affected zones around the holes are black spots in Figure 5.8a. This prevented further development of the Teflon laser drilling method.

The deposition of droplets on PVDF was unsuccessful in creating a durable hydrophobic-hydrophilic pattern. The PVDF thin film featured bad adhesion to the metal substrate, which possibly allowed for water to penetrate into the interface. Large, continuous regions of these samples that appeared darker (colder) under the IR microscope, also easily transmitted the MLL freezing front. Although the quality of these samples was unsatisfactory for any conclusive findings, the MLL front did seem to travel from alginate island to alginate island. Snapshots of this process are included in appendix D.

Although the exact mechanism remains unclear, several follow-up tests indicated the solution of DMF in the water. Through osmosis, the alginate/water was shown to deplete PVDF/DMF solutions of DMF until solidification, when the amount of added PVDF was close to its solubility limit in DMF. Vice versa, PVDF/DMF extracted water out of the alginate/water solution until solidification. No reaction could be observed between PVDF and alginate, PVDF and water or alginate and DMF. The production of microstructures by impressing liquid droplets into a liquid substrate and subsequent curing, is not new. The technique has been used to produced enclosed liquid capsules and hollow vein networks. Guo et al. created microchannels with

diameters of between 50 and $1000\ \mu m$ in PDMS, by inkjetting a low-density sacrificial ink into a PDMS prepolymer. Rayleigh breakup was prevented to be able to print continuous lines, by using an ink with temperature-sensitive viscosity. [85]

Other methods that were experimented with to easily create hydrophilic islands were unsuccessful. The ionomer Surlyn was dissolved in 2,2 dichloroethane and spincoated on aluminum substrates. The increase in nucleation time delay that was observed on these substrates was found to be due to the deposition of a dissolved polymer cap closing of the mixing bottles. Surlyn and Nucrel were also pressed with Kapton foil at 110℃ to form thin films on aluminum substrates. However, no significant effect on the nucleation time delay, nucleation temperature or MLL freezing front velocity was observed. The process is illustrated in appendix L.

5.3 Conclusion

The previously discovered ability of the contact angle to stop the MLL freezing front propagation, was used to address research question 4 ("How can the identified relevant governing parameters of the nucleation temperature, nucleation time delay and freezing front propagation velocity be employed to create novel smooth, durable and non-toxic surfaces that prevent ice nucleation or growth of the frozen area?"). Firstly, the ability of hydrophobic islands to stop MLL front propagation over a hydrophilic surface was assessed, by laser-drilling $200 \pm 100\ \mu m$ holes in an aluminum surface. The MLL freezing front was observed to travel around the holes when they were filled up with olive oil, but over the holes when they were empty. A fast initial front propagation transitioned to a much slower dendrite front propagation when in coming into contact with oil residue on the metal surface. Other strategies of filling up pores of anodized aluminum with PVDF and inkjet printing PVDF spots on glass were not assessed with freezing experiments due to time constraints. However, they are promising as production techniques for scalable, non-toxic, durable and smooth anti-icing surface architectures.

Secondly, hydrophilic islands in a hydrophobic surface were created by inkjet printing hydrophilic ink on surfaces, filling laser-drilled holes in Teflon with alginate and depositing alginate droplets on PVDF surfaces and locally plasma treating PVDF thin films. Only the plasma treatment of PVDF succeeded in creating a durable pattern of hydrophilic regions in a hydrophobic environment, clearly containing the MLL front propagation to the plasma treated areas. The other architectures that were conceived and produced to obtain hydrophilic-hydrophobic architectures at different length scales are listed in Table 5.1.

Pattern size	**Coating architecture and material**	**Results**
$1 - 10\ nm$	Surlyn ionomer, as compared to Nucrel	Negative initial
$10 - 100\ nm$	Copolymerization	Not tested
$100 - 1000\ nm$	Blending	Not tested
$10 - 100\ \mu m$	Anodization	Positive initial
$20 - 50\ \mu m$	Inkjet printing	Positive initial
$50 - 500\ \mu m$	Sirius laser drilling of aluminium/Teflon plates	Positive/negative
$1 - 2\ mm$	PVDF thin film with alginate islands	Negative initial
$1 - 4\ mm$	Permanent marker ink deposition	Positive
$2 - 5\ mm$	Scratching pattern in hydrophobic film on hydrophilic	Negative initial
$1 - 20\ mm$	Plasma treatment	Positive

Table 5.1: Different production methods can be employed to create hydrophilic-hydrophobic patterns. This table lists all scalable methods that were under consideration in this thesis and their respective results. The methods that were out of the scope of this thesis due to time constraints, are indicated as 'Not tested'. The methods that were not tested to their full potential, are indicated as positive or negative 'initial'.

6. Conclusions and recommendations

To study freezing of surfaces, several coatings were subjected to freezing conditions with an inhouse produced setup under observation of infrared imaging (IRI) and laser speckle imaging (LSI). This allowed for the qualitative and quantitative observation of ice nucleation and freezing front propagation. A novel combination of IRI and LSI was used to observe the freezing temperature, latent heat release and local molecular activity.

The detrimental effect of increased humidity on ice adhesion on superhydrophobic surfaces has been proven. However, humidity remained to be linked to the formation of clear ice on aircraft. Clear ice grows faster, with stronger adhesion and at higher temperatures and larger droplet sizes than rime ice. The second research question aimed at proving that clear ice occurs when droplets impact on a surface with a frozen molecular liquid layer (MLL) of water. The presence of a thin, continuous frozen MLL allows impacting droplets to freeze above the normal minimal temperature of $T_{surf} = -10°C$. The combination of high humidity and increased nucleation temperature allowing impacting droplets to smear out before freezing. Firstly, at the higher nucleation temperature, the bulk freezing front propagation or growth rate is slower. Secondly, a larger droplet size increases the time required for full droplet freezing. Any situation with high relative humidity and higher nucleation temperatures would therefore be expected to yield a form of ice that features fast and dense growth, with homogeneous crystallinity and high adhesion strength. This is exactly what differentiates clear ice from rime ice, as illustrated in Table 1.1. As nucleation of the MLL was observed between $-14℃$ and $-20℃$, within the expected surface temperatures of aircraft in the loiter or final approach phase of their mission profile, further research into the effect of a frozen MLL on clear ice is expected give pilots a better understanding of and perhaps control over clear ice formation. One step that should certainly be taken, is the observation of impacting droplets on superhydrophobic surfaces with IRI at high spatial and temporal resolution, combined with ice adhesion measurements. This could confirm the hypothesis that it is the frozen MLL that causes the conflict in literature on the anti-icing performance of superhydrophobic surfaces.

To prevent a freezing front propagating through over the complete surface, either nucleation or front propagation have to be reduced. The third research question aimed at determining the effect of surface, material and environmental properties on ice nucleation and freezing front propagation on surfaces. The results are summarized in Table 6.1.

Ice nucleation

Surface temperature	Temperature independence below a critical nucleation temperature of $-11°C$ to $-14°C$. Above this temperature range, no nucleation occurs.
Frequency	No effect observed in the expected range of between $16\ kHz$ $100\ kHz$.
Contact angle	Increasing the contact angle increases t_n and induces spread in the t_n values.
Conductivity	An increase in conductivity produced a reduction in t_n.
Relative humidity	Relative humidities of $RH < 40\%$ yield lower critical nucleation temperatures
Droplet size	No relationship between freezing behavior and droplet size.

Freezing front propagation

Surface temperature	No relationship between surface temperature and front velocity.
Contact angle	High contact angle can switch MLL freezing front into a dendrite freezing front.

Relative humidity	Relative humidities fo $RH < 40\%$ increase the initial freezing front intensity, but feature isolated MLL propagation.

Table 6.1: The effects of some of the surface, material and environmental parameters that govern heterogeneous freezing of aircraft surfaces on ice nucleation and freezing front propagation. The parameters indicated in green yielded unambiguous results. The parameters in orange had large error bars or an expected effect was not observed.

After studying effect of environmental, material and surface properties on icing, the most effective governing parameter, the contact angle, was used for the design of proof-of-concept smooth, non-toxic, durable and producible anti-icing coatings. The most successful architectures in containing the MLL freezing front, were an aluminum surface with small oil-filled holes, Teflon with permanent marker ink and locally plasma-treated PVDF.

The observations made with the IRI technique have to be better understood, to be able to conclude more about the heterogeneous freezing process of the MLL. As a first step when continuing with the materials used in this thesis, one should find out what causes 'darker areas' in hydrophilic (plasma treated) islands on hydrophobic (PVDF) surface under IRI. Suggestions for this effect are the MLL or micron sized droplets. To observe impacting droplets on frozen or unfrozen surfaces, an IR camera with a framerate of at least $500\ Hz$ is desirable. To be able to use the LSI technique for quantitative analysis of weak freezing fronts, a frame acquisition rate above $500\ Hz$ is required. This will enable the error reduction by averaging at least 2 frames while the MLL freezing front passes over the surface.

A better understanding of the MLL front propagation mechanism is needed for controlling ice nucleation. This can be achieved by developing a better method for analyzing front propagation velocity. As a first step, image recognition software is needed that can automatically identify the front line automatically, ideally in real-time. If further research on the freezing front is performed, the front velocities should be sampled at constant rate. This allows for a reliable values for the average front velocities.

Further research into separation of parameters affecting nucleation and front propagation would also be advisable. In this thesis, some of the governing parameters could not be separated in the tested samples. The nucleation time should for example be normalized with respect to humidity, heat conduction and surface energy. One approach would be to develop better production techniques for surface architectures, so only one surface or material variable, like roughness, contact angle and conductivity is changing between samples. Another approach would be to use an environment with controlled humidity and temperature at all times, to reduce the error bars in all for $t_n(T_n)$. The use of constant sample geometries and more stable coatings as surface would also be required, to have a more systematic approach and exclude issues of difference in heat conduction and water absorption.

Hydrophobic-hydrophilic coatings have the potential to be durable (flat) and easily applicable, as the contact angle is material property. Materials with higher contact angle could be integrated into existing coating systems with only small additional weight. Apart from the effect of contact angle, more coatings for anti-icing could be imagined using the local changes in temperature, vibration, electrical charge, conductivity or roughness, once more is understood about the MLL freezing front propagation and its influence on clear ice.

A. Summary pilot interview

Pilot experience with ice formation on aircraft

- Icing on the ground is a problem. Ice is removed mechanically and with anti-icing fluid.
- Ice grows in rain, snow and rime and is mainly formed on leading edge, stabilizer and rudder, front windows and antenna's.
- Jet engine inlets, stator vanes and propellers can freeze. Just at a moment in the mission profile when maximum performance and reliability is needed from the engines.
- Icing is a risk when flying under $10℃$ with visible moisture. Air cools down when it is accelerated over the upper side of the wing, so T_{surf} can reach subzero temperatures even when $T_{env} = 0°C$.
- Hail never forms a problem, as it doesn't stick to the wing.
- Ice doesn't occur during cruise of passenger aircraft, only in the tropics. There is a band of danger between $-20℃ < T_{env} < 0℃$, depending on the humidity, which forms an issue during landing and take-off.
- With a jet or turboprop engine, the pilot will try to ascent or descent to get out of the icing danger zone. For non-military aircraft, descending is usually the only option to react fast.

Problems caused by ice

- Ice disturbs the profile and increases the surface roughness, especially at higher angles of attack.
- Additional weight can make the aircraft harder to handle.
- It might become impossible to collect data with a pitot tube, when the entrance measure the total pressure freezes shut. This has been a problem for the AF447.
- For smaller airplanes, cables that are used to adjust the power can get stuck.
- Hinges can freeze due to ground ice or runback ice.

Current solutions used by pilots

- Bleed air: Hot air is taken from the turbine and redirected to the leading edge. This costs a lot of energy, but is very reliable. When aircraft will become electric, another option is needed. The CJ 1 or 2 type aircraft has a bleed air de-icing system. Smaller aircraft can't use bleed air, as they lack a turbine that can supply hot air.
- Electrical heating: Resistive heating costs a lot of electrical energy.
- Glycols: Freezing point depressant are used to prevent or detach ice. The DH 43 uses TKS panels, which are perforated titanium plates that 'sweat' out a freezing point depressant. During normal operations, the TKS tank takes 2.5 hours (normal), 1.5 hours (high) or 0.5 hours (max) to run out of liquid. This might not be enough in some situations.
- Boots: Mechanical removal, which works really effectively. As the boots are made from rubber, they wear. They can also break if used under the rubber's T_g.
- RainX: Hydrophilic coating that prevents water from freezing on the windows.
- De-icing: This costs several thousands of euro's. If ground ice has to be removed from a passenger airplane, the airliner will not make any profit on that flight.

B. Scopus search results for “anti-icing”

Search result from the platform *Scopus*, indicating the increase in the number of peer-reviewed publications mentioning anti-icing in the title. The graph was obtained by accessing the platform on 22-4-2018.

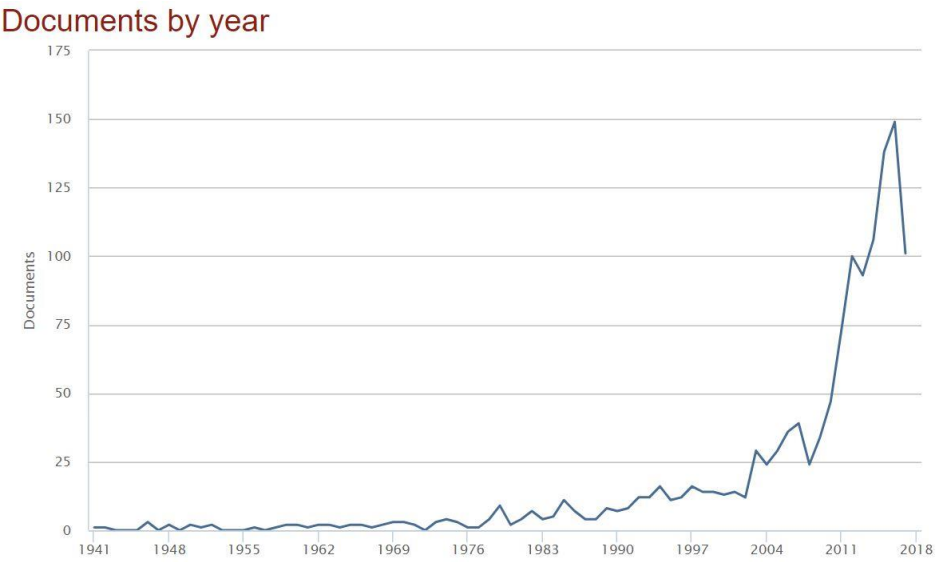

C. Plasma patterned PVDF thin film on glass with large droplets.

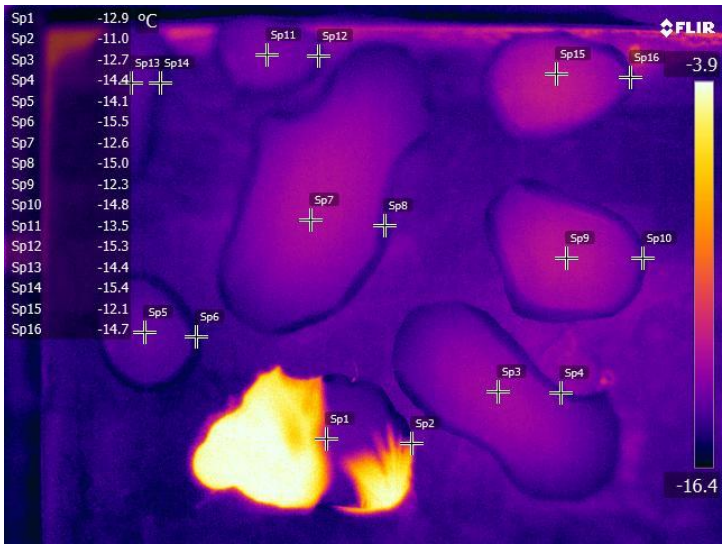

$t_n + 0.02s$

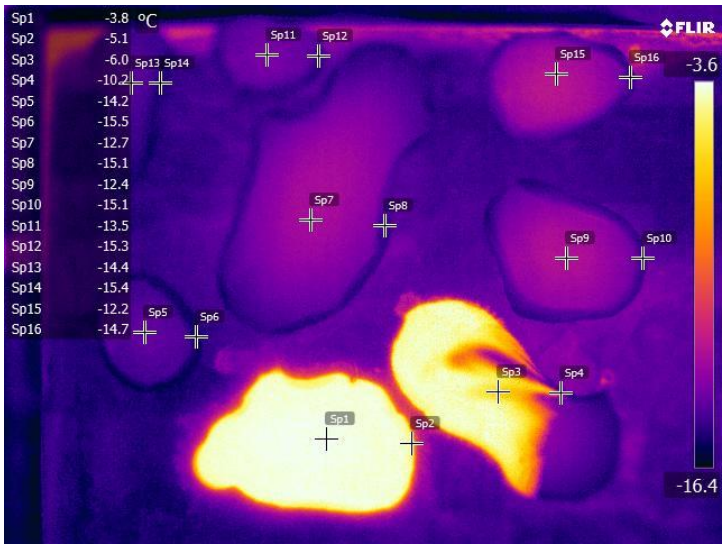

$t_n + 0.06s$

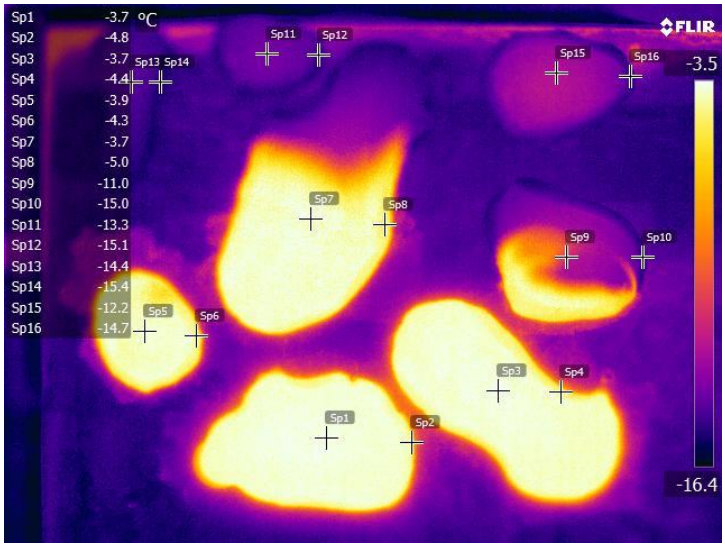

$t_n + 0.12s$

D. Frost growth on untreated PVDF on glass

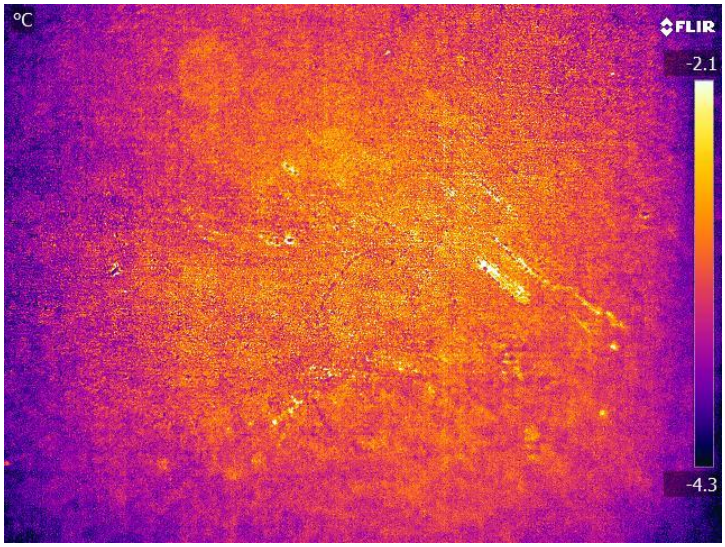

after 10 minutes

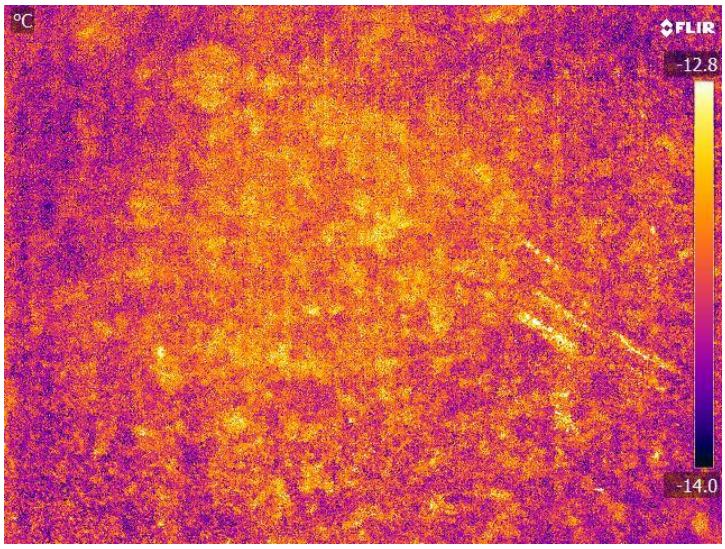

after 15 minutes

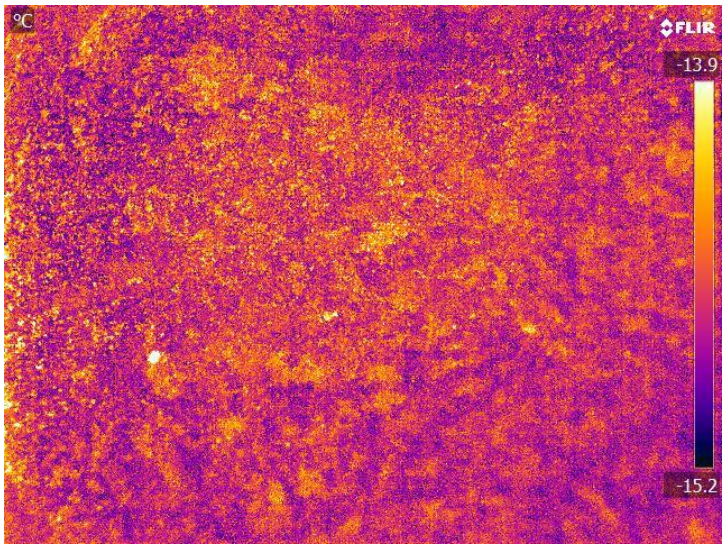

after 20 minutes

E. Freezing front propagation on PVDF, with condensed MLL and with large droplets

Test 1: without droplets

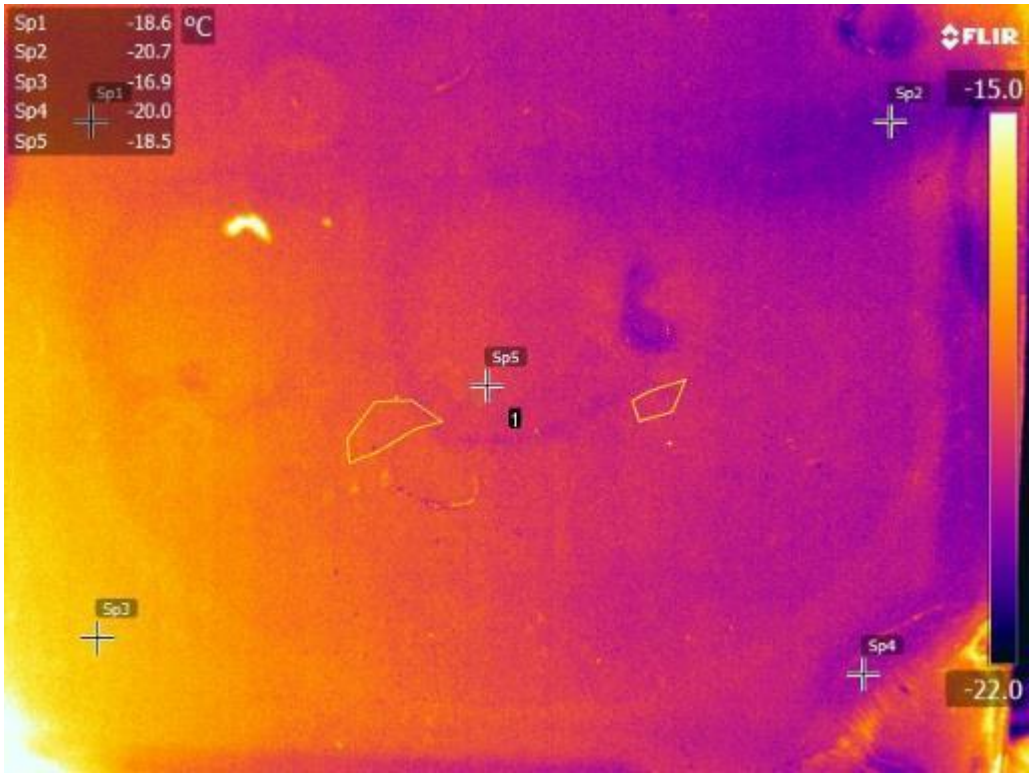

$t = t_n + 0.02s$

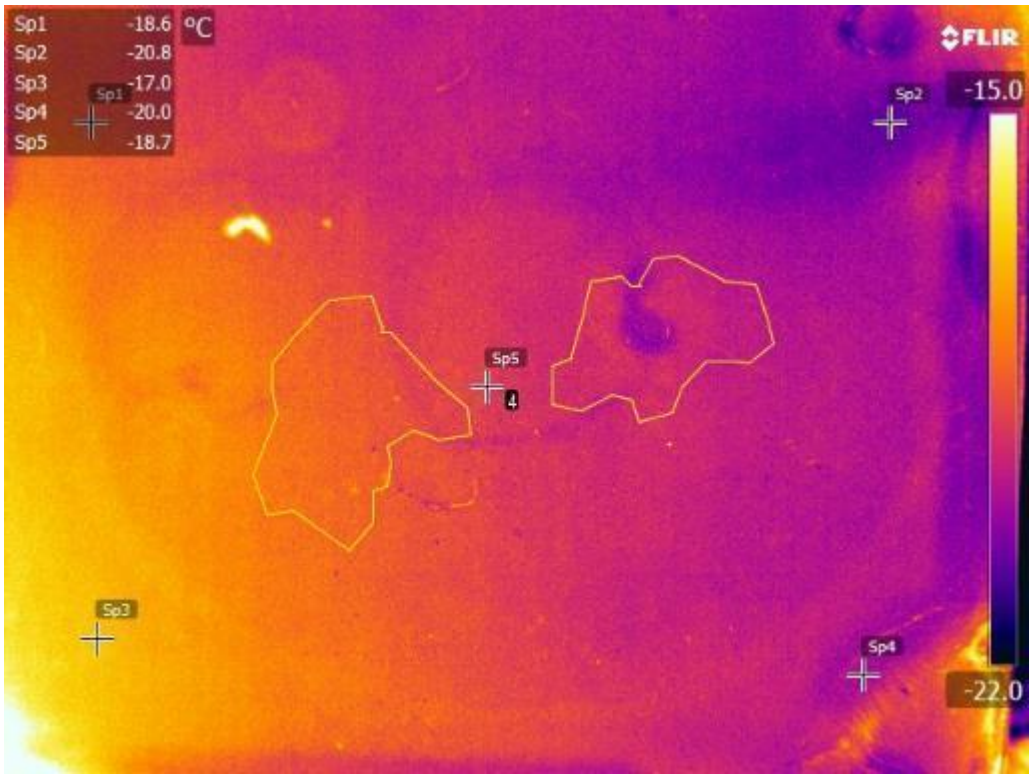

$t = t_n + 0.08s$

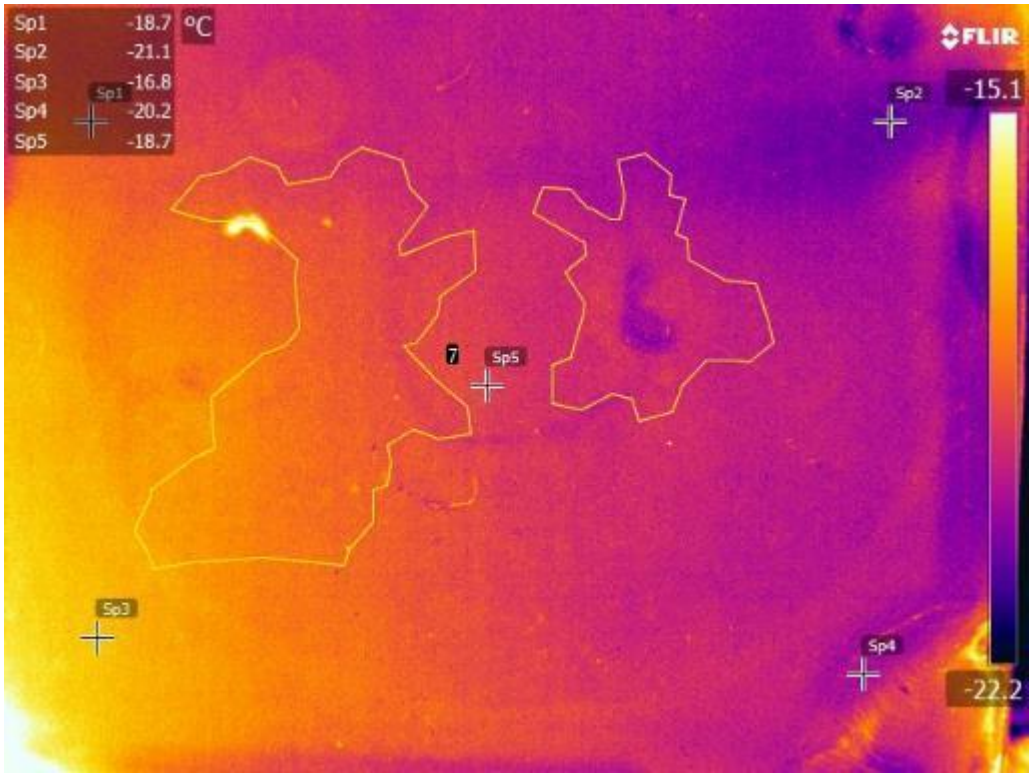

$t = t_n + 0.14s$

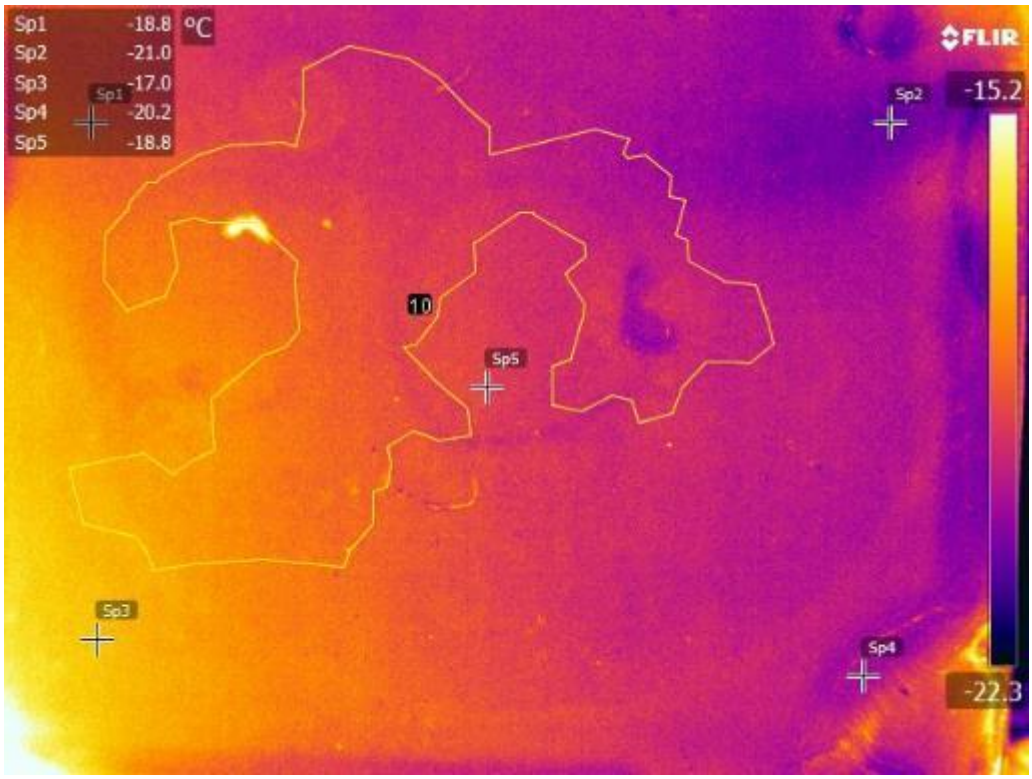

$t = t_n + 0.20s$

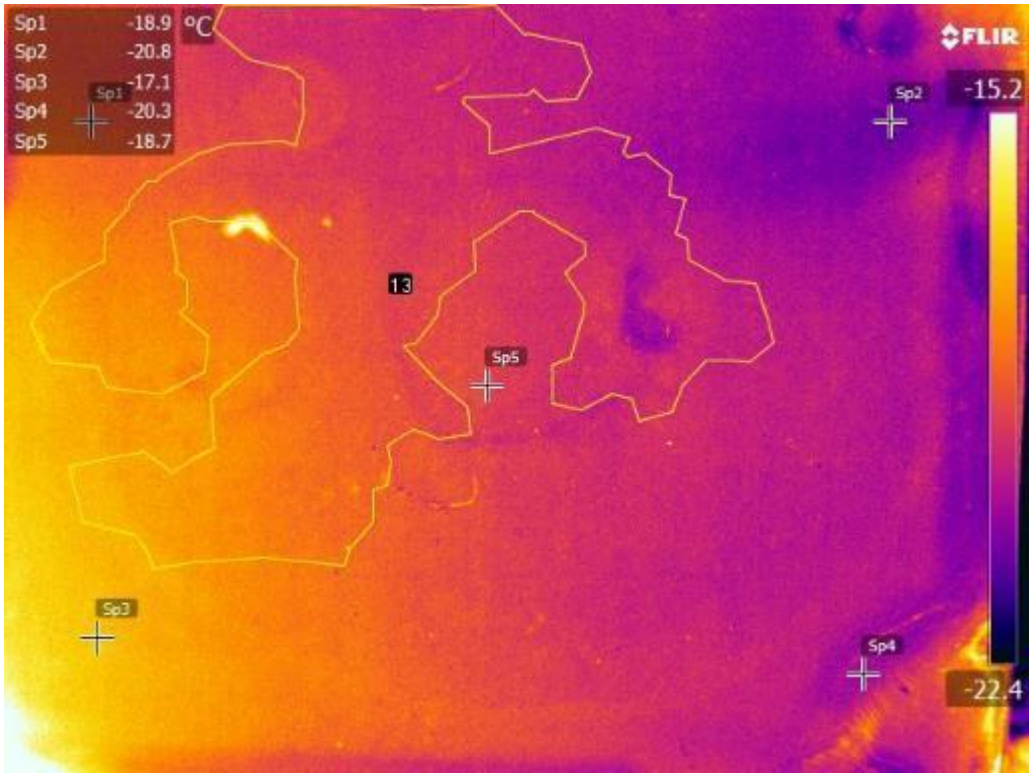

$t = t_n + 0.26s$

Test 2: with droplets

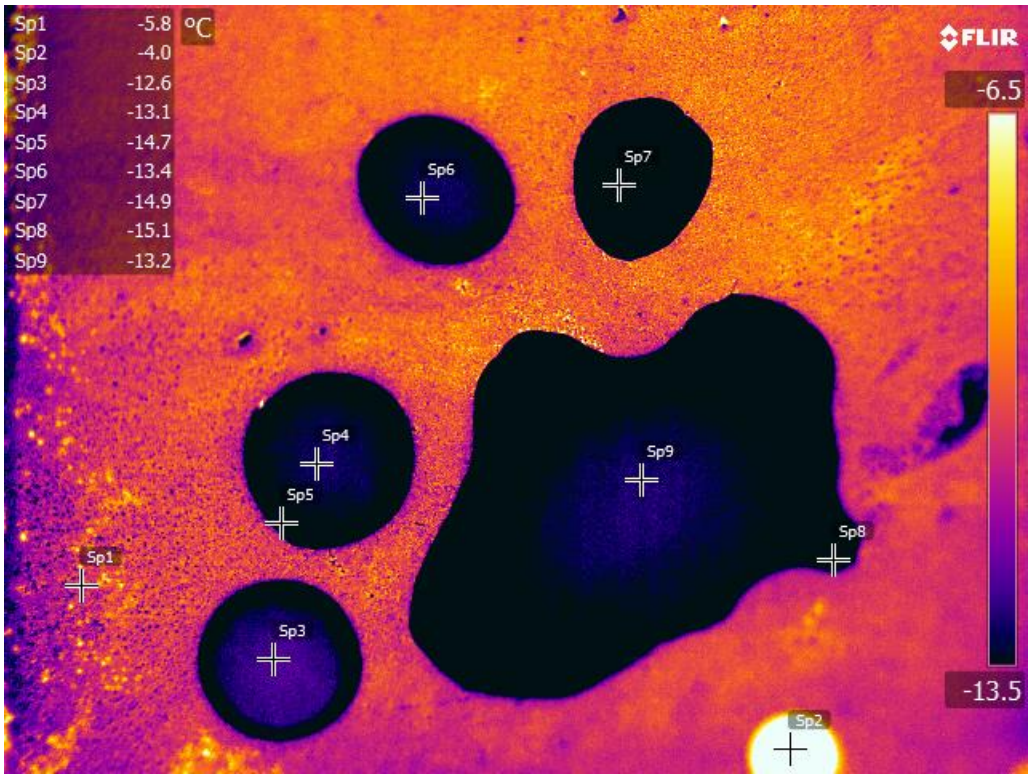

$t = t_n + 0.16s$

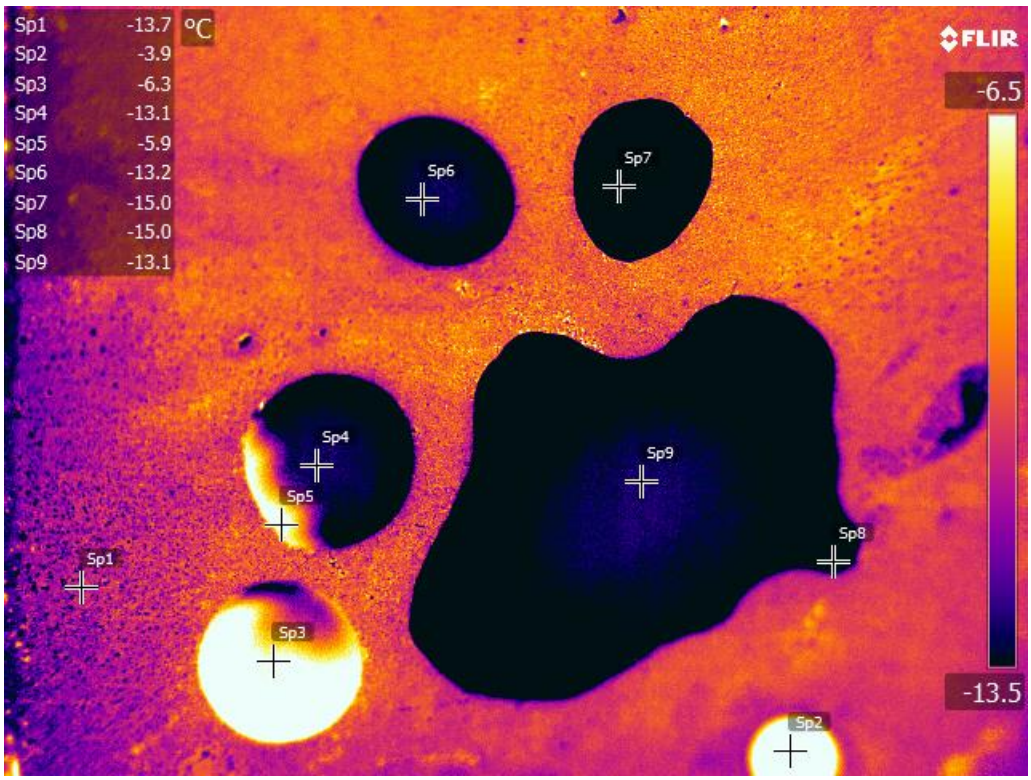

$t = t_n + 0.24s$

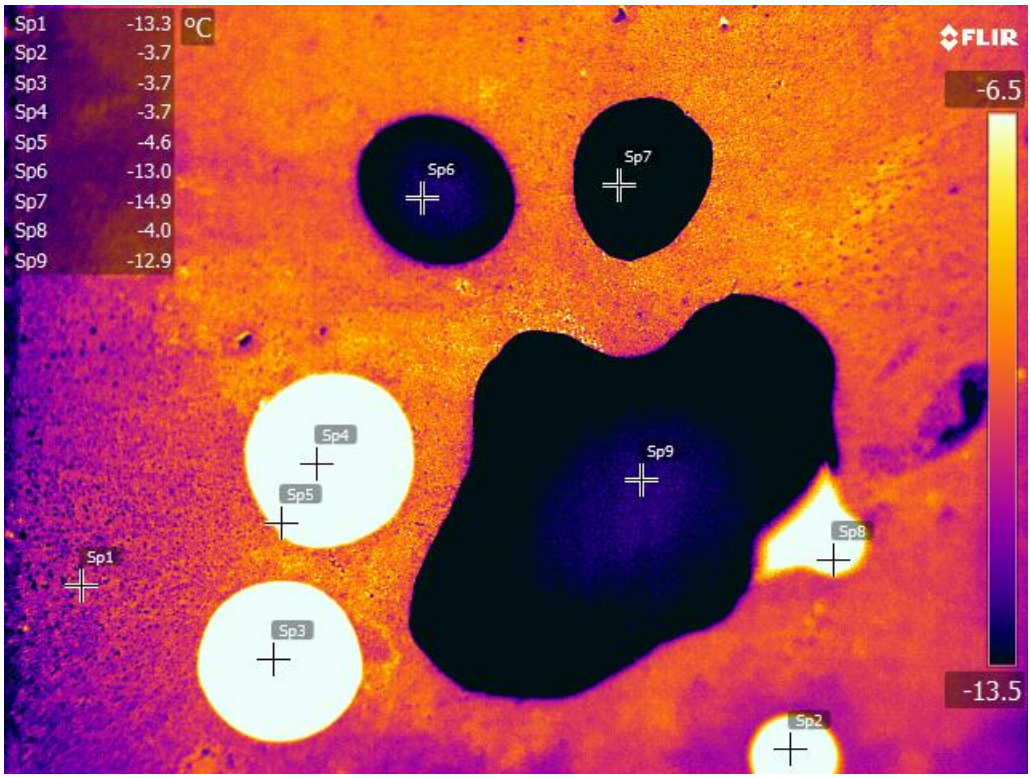

$t = t_n + 0.48s$

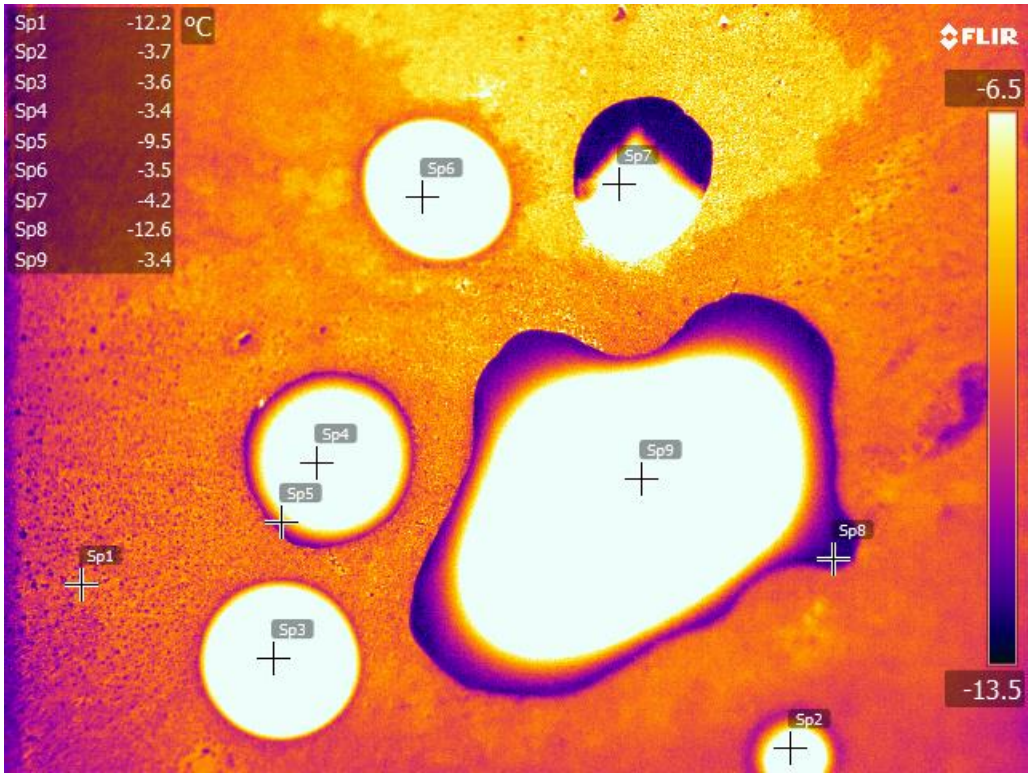

$t = t_n + 3.12s$

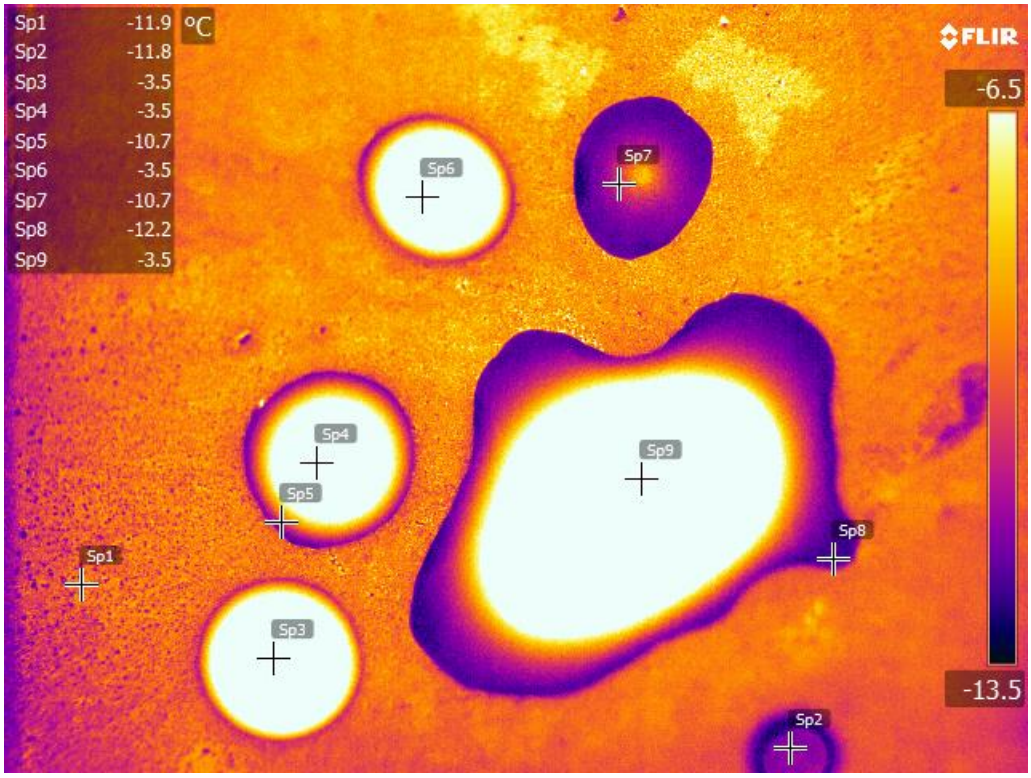
Sp1 -11.9 °C
Sp2 -11.8
Sp3 -3.5
Sp4 -3.5
Sp5 -10.7
Sp6 -3.5
Sp7 -10.7
Sp8 -12.2
Sp9 -3.5
FLIR
-6.5
-13.5
Sp1
Sp2
Sp3
Sp4
Sp5
Sp6
Sp7
Sp8
Sp9

$t = t_n + 4.96s$

F. Impacting droplets on frozen or unfrozen epoxy

IR observation of impacting droplet on cooled epoxy coating at $T_{env} = 20℃$ and $-10℃ > T_{surf} > -12℃$. In the row of images left to right (a) small, subcooled droplets condense on the epoxy, (b) a droplet with $T_{drop} = 11.5℃$ impacts the unfrozen surface, (c) after which the droplet gradually cools down to $T_{surf} = -10.0℃$ in 5 seconds, (d) without freezing, as shown by the mobile droplet edge three-phase boundary.

The sequence of images illustrate left to right (e) a dendrite front propagating over the surface, (f) which gets hit by a droplet at $T_{drop} = 11.5℃$. (g) The droplet nucleates after $0.4\ s$ on the side of the droplet in contact with the frozen surface. The front travels through point Sp8 in the figure. (h-i) The cooling of the droplet towards $T_{drop} = -10.0℃$ takes 12 seconds and the droplet edge does not retract more after freezing has taken place.

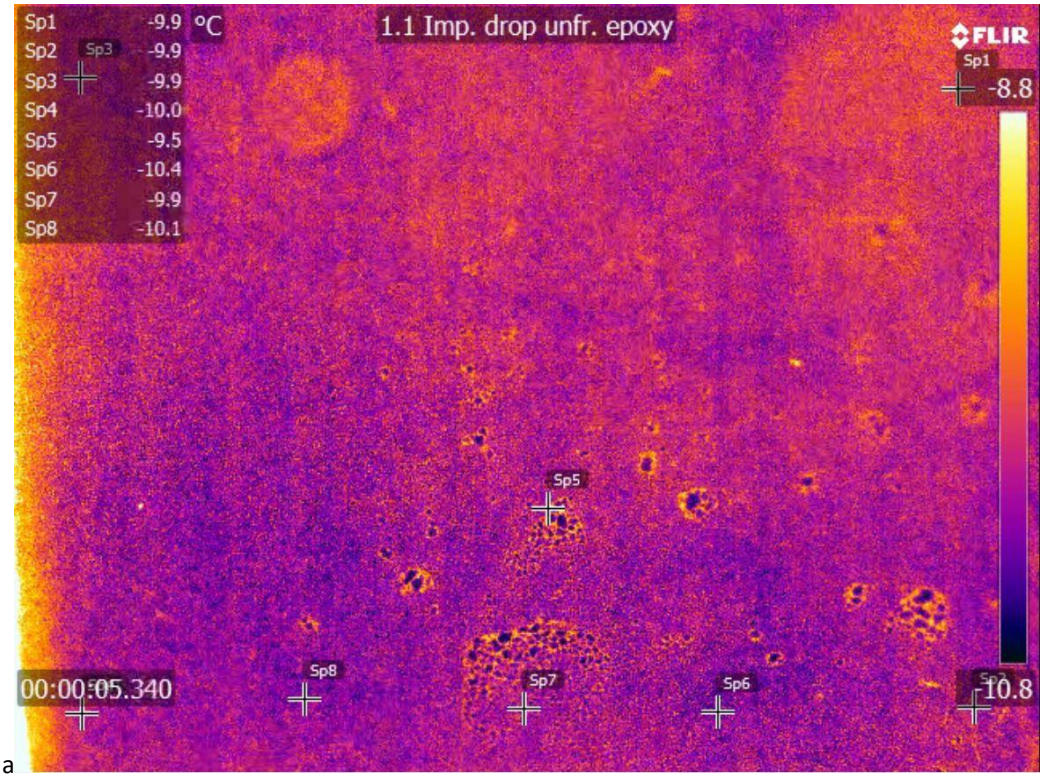

a

b

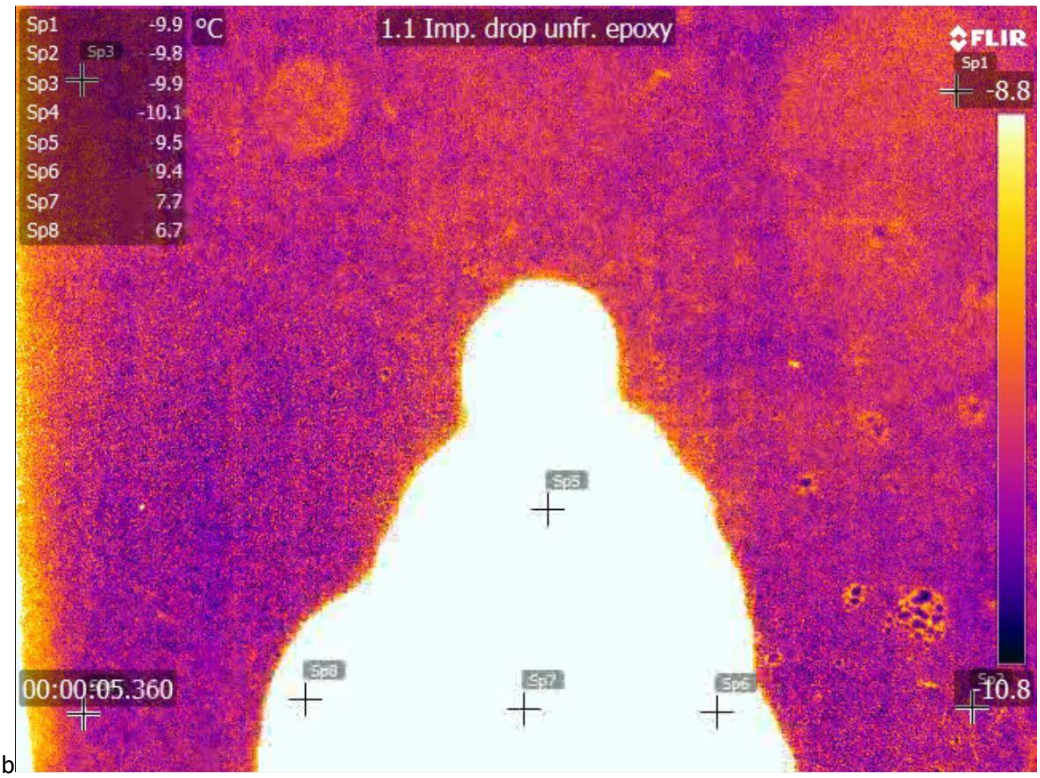
Sp1 -9.9 °C
Sp2 -9.8
Sp3 -9.9
Sp4 -10.1
Sp5 -9.5
Sp6 -9.4
Sp7 7.7
Sp8 6.7
1.1 Imp. drop unfr. epoxy
FLIR
Sp1
-8.8
Sp5
Sp8
Sp7
Sp6
00:00:05.360
10.8

c

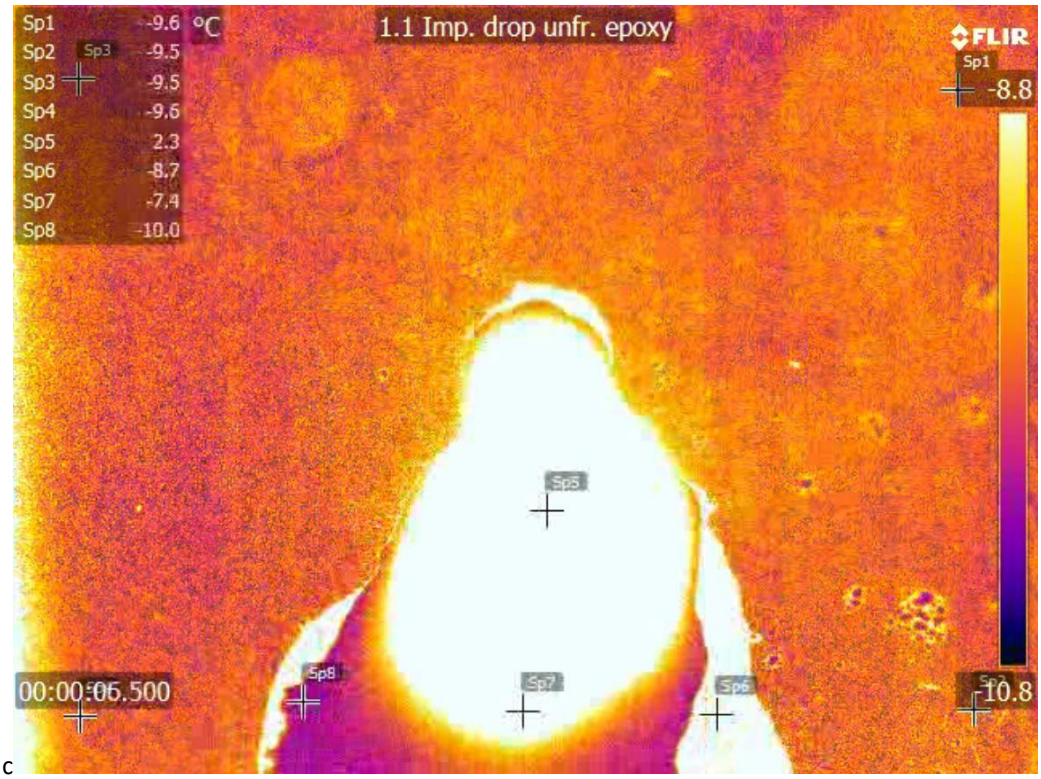
Sp1 -9.6 °C
Sp2 -9.5
Sp3 -9.5
Sp4 -9.6
Sp5 2.3
Sp6 -8.7
Sp7 -7.4
Sp8 -10.0
1.1 Imp. drop unfr. epoxy
FLIR
Sp1
-8.8
Sp5
Sp8
Sp7
Sp6
00:00:06.500
10.8

d

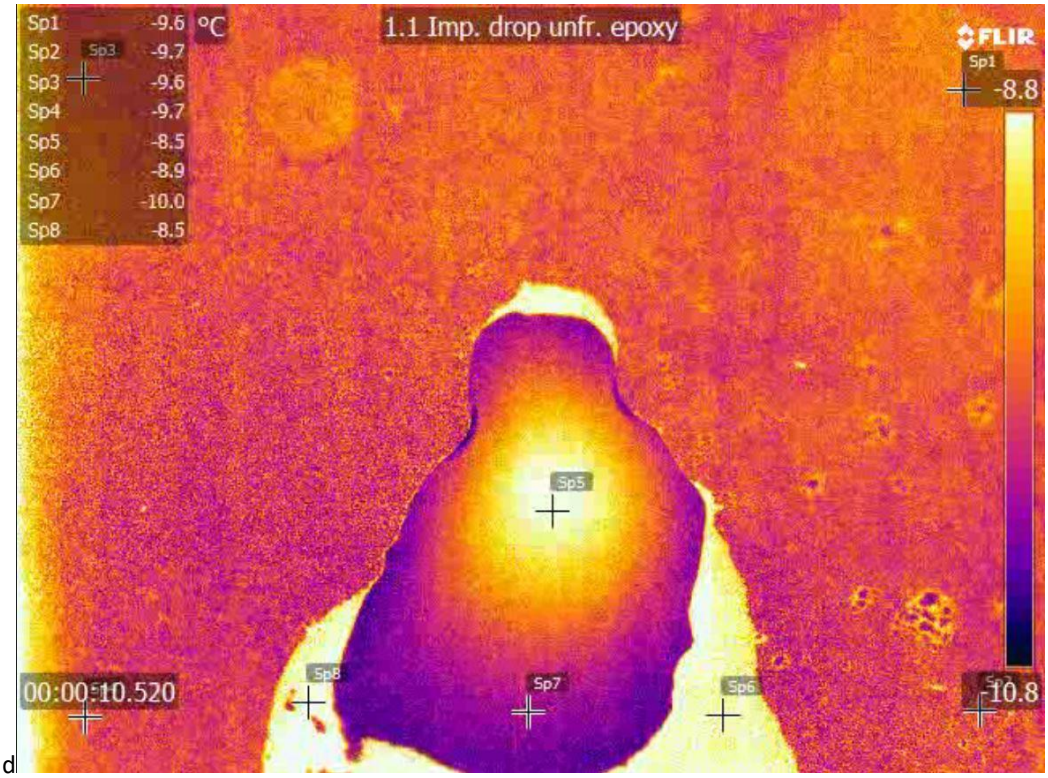
Sp1 -9.6 °C
Sp2 -9.7
Sp3 -9.6
Sp4 -9.7
Sp5 -8.5
Sp6 -8.9
Sp7 -10.0
Sp8 -8.5
1.1 Imp. drop unfr. epoxy
FLIR
Sp1
-8.8
Sp5
Sp8
Sp7
Sp6
00:00:10.520
10.8

e

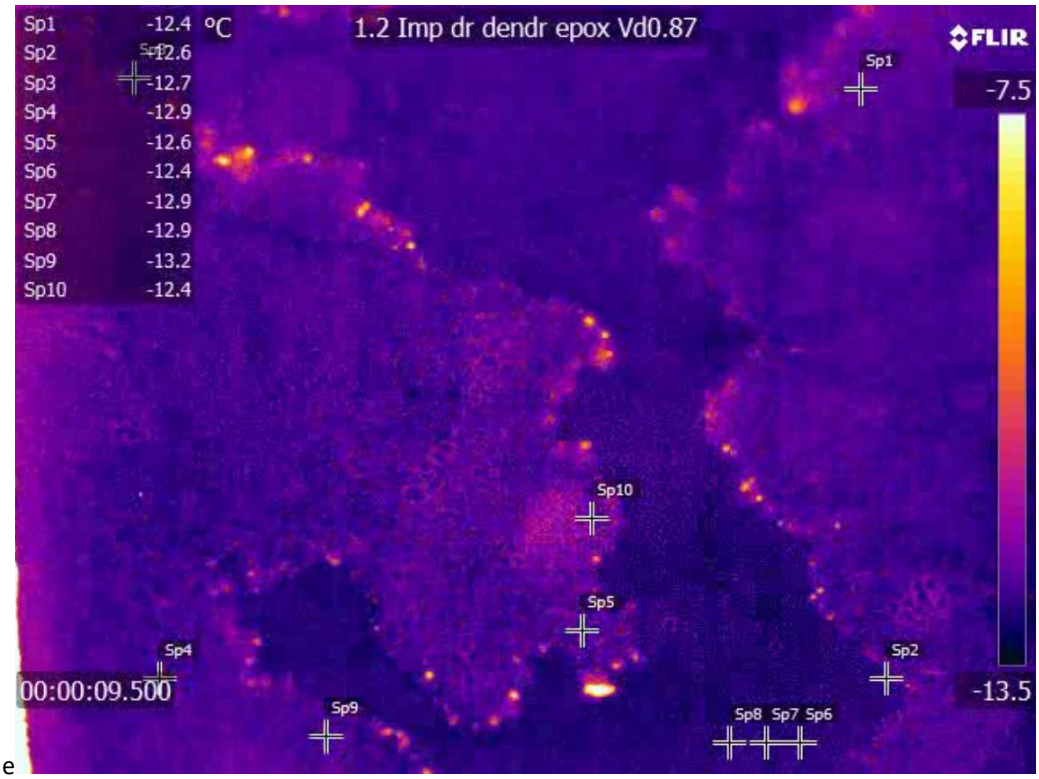
Sp1 -12.4 °C
Sp2 -12.6
Sp3 -12.7
Sp4 -12.9
Sp5 -12.6
Sp6 -12.4
Sp7 -12.9
Sp8 -12.9
Sp9 -13.2
Sp10 -12.4
1.2 Imp dr dendr epox Vd0.87
FLIR
Sp1
-7.5
Sp10
Sp5
Sp4
Sp2
00:00:09.500
Sp9
Sp8 Sp7 Sp6
-13.5

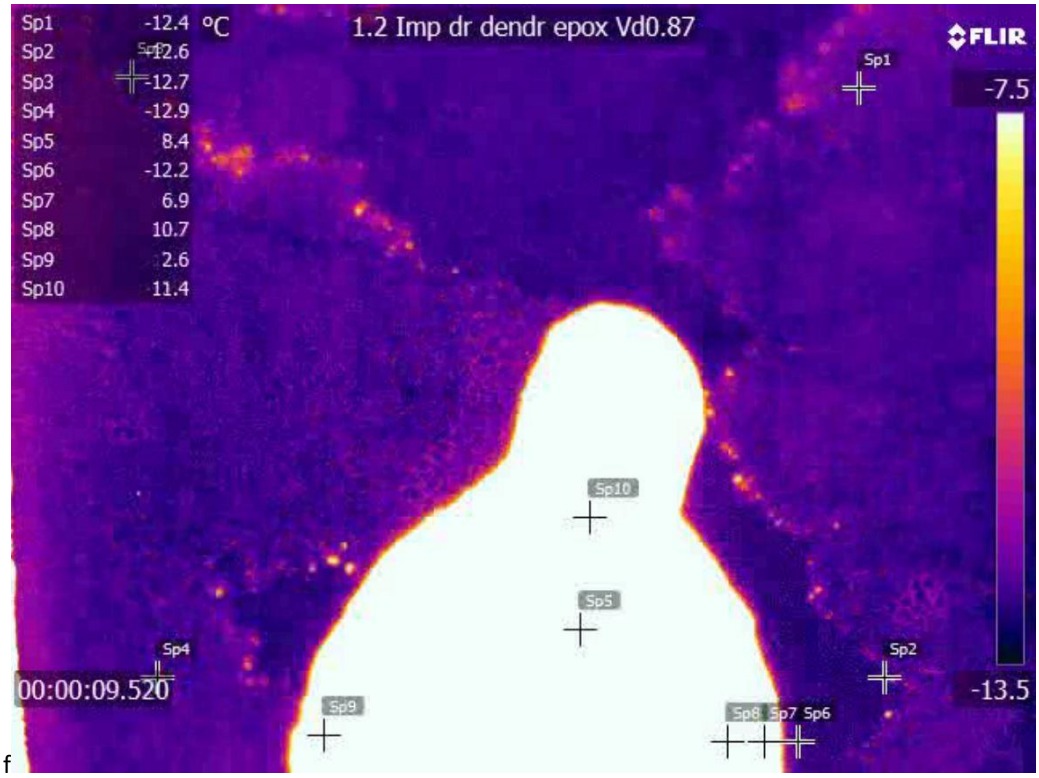
Sp1 -12.4 °C
Sp2 -12.6
Sp3 -12.7
Sp4 -12.9
Sp5 8.4
Sp6 -12.2
Sp7 6.9
Sp8 10.7
Sp9 2.6
Sp10 11.4
1.2 Imp dr dendr epox Vd0.87
FLIR
-7.5
-13.5
00:00:09.520

f

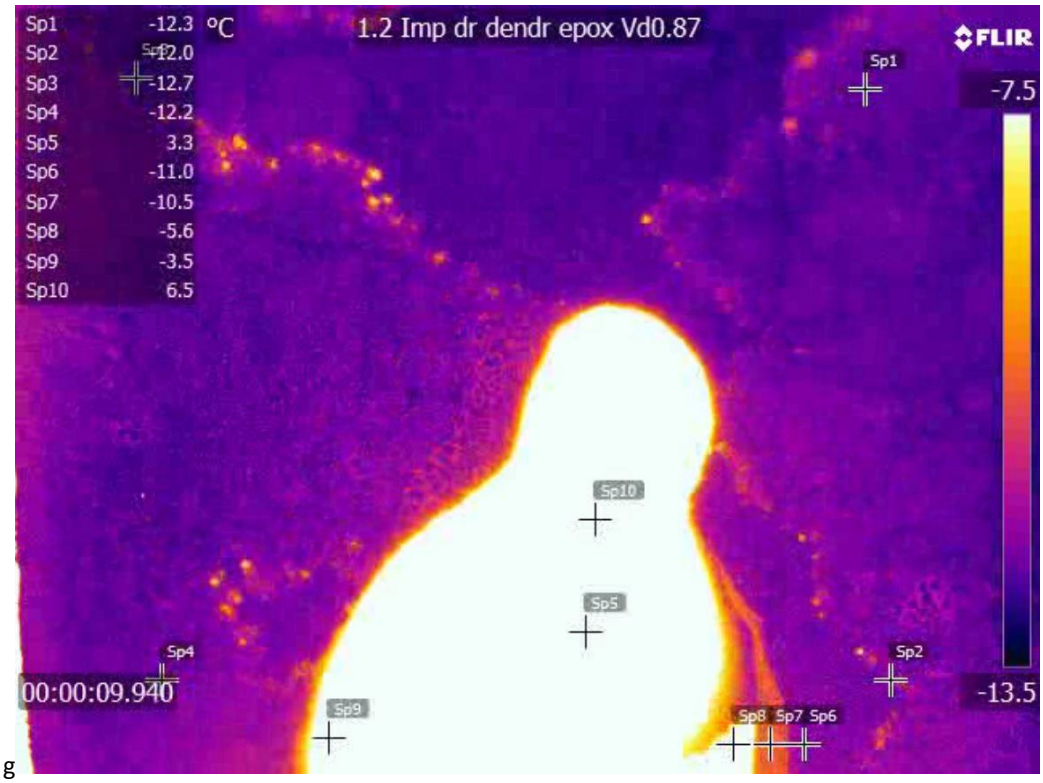
Sp1 -12.3 °C
Sp2 -12.0
Sp3 -12.7
Sp4 -12.2
Sp5 3.3
Sp6 -11.0
Sp7 -10.5
Sp8 -5.6
Sp9 -3.5
Sp10 6.5
1.2 Imp dr dendr epox Vd0.87
FLIR
-7.5
-13.5
00:00:09.940

g

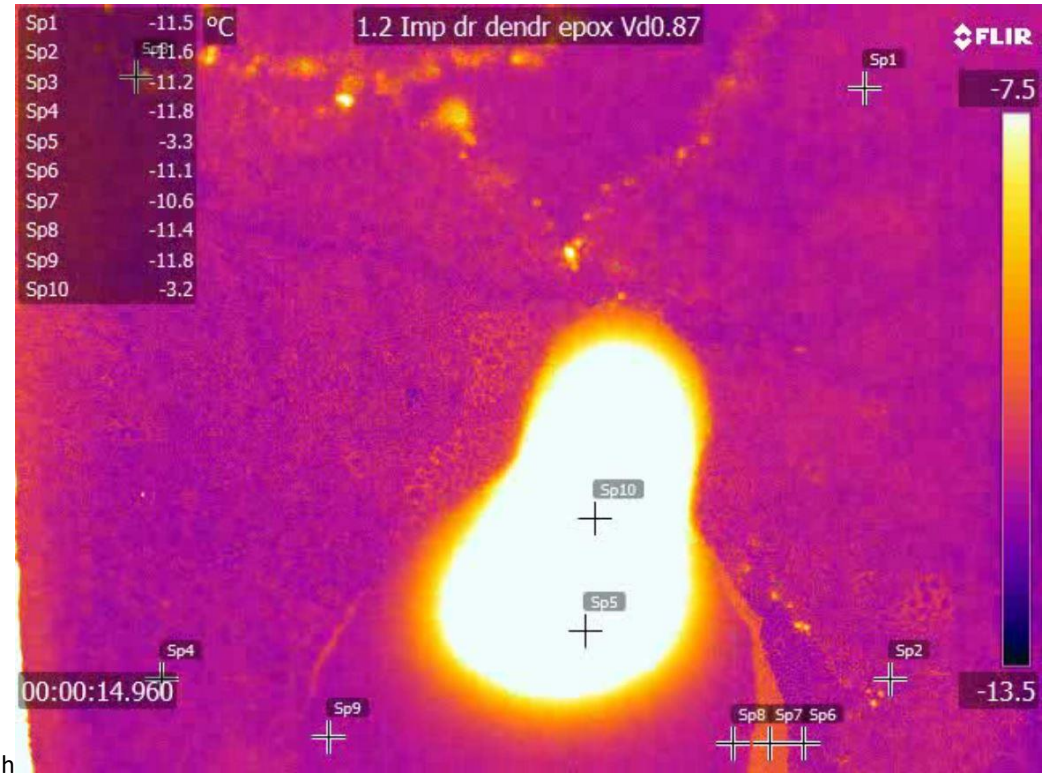
Sp1 -11.5 °C
Sp2 -11.6
Sp3 -11.2
Sp4 -11.8
Sp5 -3.3
Sp6 -11.1
Sp7 -10.6
Sp8 -11.4
Sp9 -11.8
Sp10 -3.2
1.2 Imp dr dendr epox Vd0.87
FLIR
-7.5
-13.5
00:00:14.960
Sp1
Sp2
Sp4
Sp5
Sp6
Sp7
Sp8
Sp9
Sp10

h

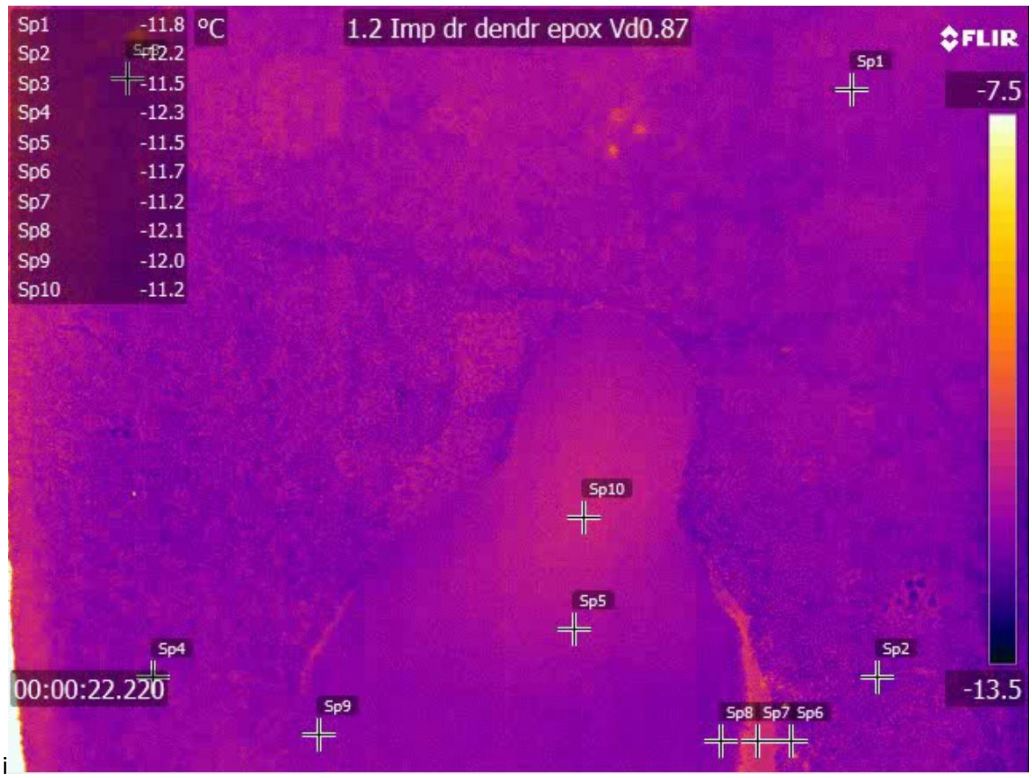
Sp1 -11.8 °C
Sp2 -12.2
Sp3 -11.5
Sp4 -12.3
Sp5 -11.5
Sp6 -11.7
Sp7 -11.2
Sp8 -12.1
Sp9 -12.0
Sp10 -11.2
1.2 Imp dr dendr epox Vd0.87
FLIR
-7.5
-13.5
00:00:22.220
Sp1
Sp2
Sp4
Sp5
Sp6
Sp7
Sp8
Sp9
Sp10

i

G. Freezing front propagation on piezo-electric element

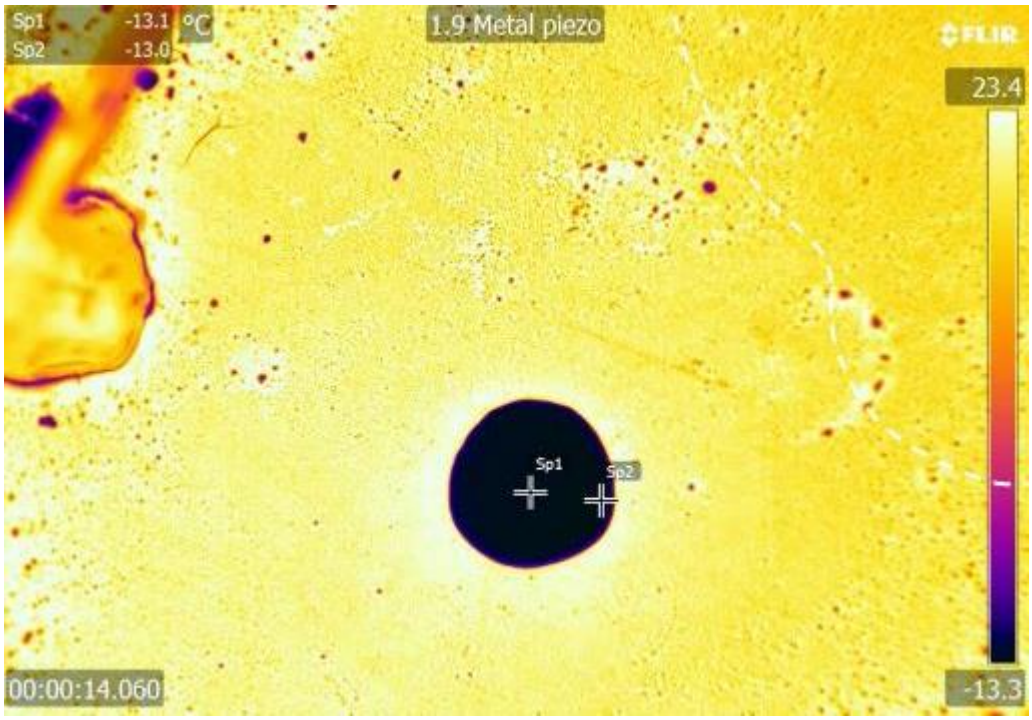

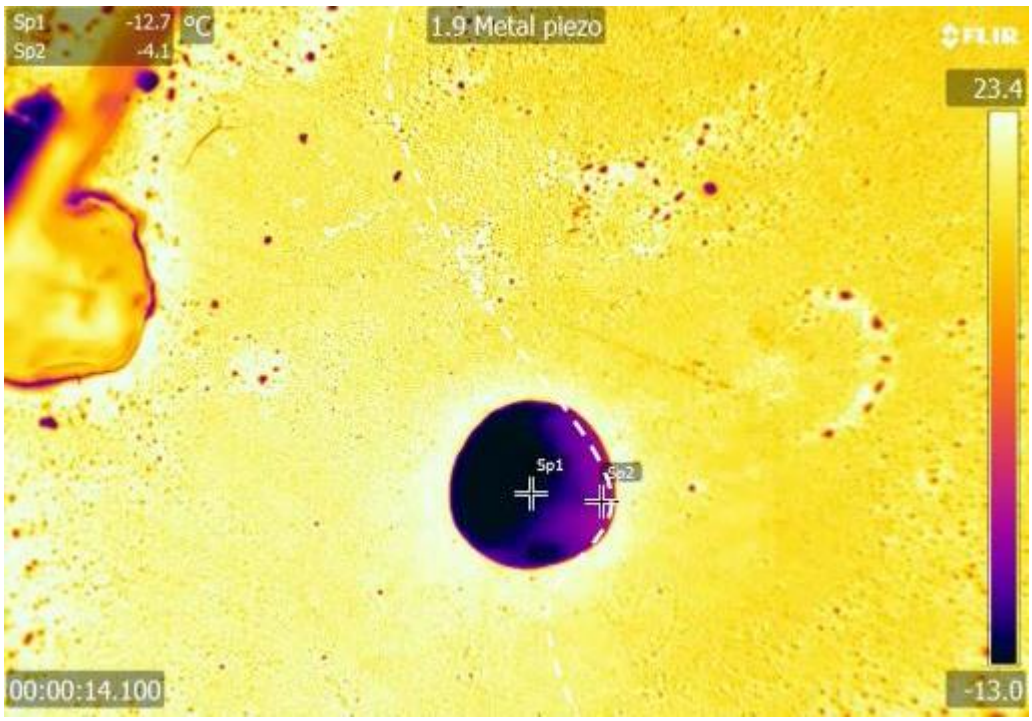

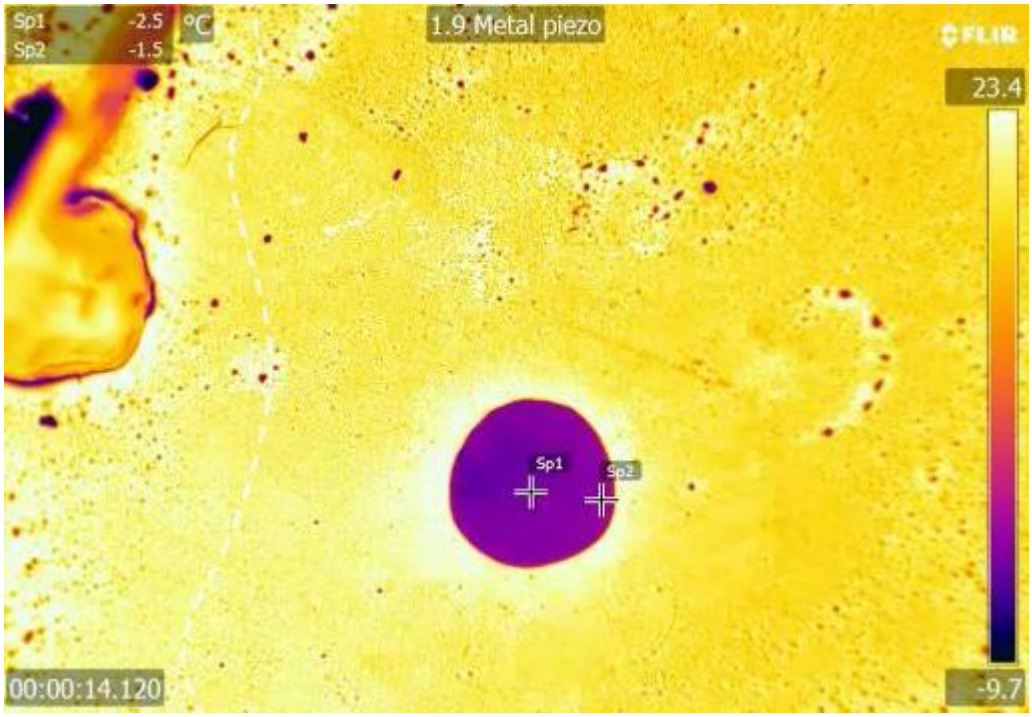
Sp1 -2.5 °C
Sp2 -1.5
1.9 Metal piezo
FLIR
23.4
Sp1
Sp2
00:00:14.120
-9.7

H. MLL Freezing front propagation on plasma patterned PVDF

Front propagation on plasma patterned PVDF with $T_{env} = 10°C$, $T_{surf} = -12°C$ and $RH = 80\%$

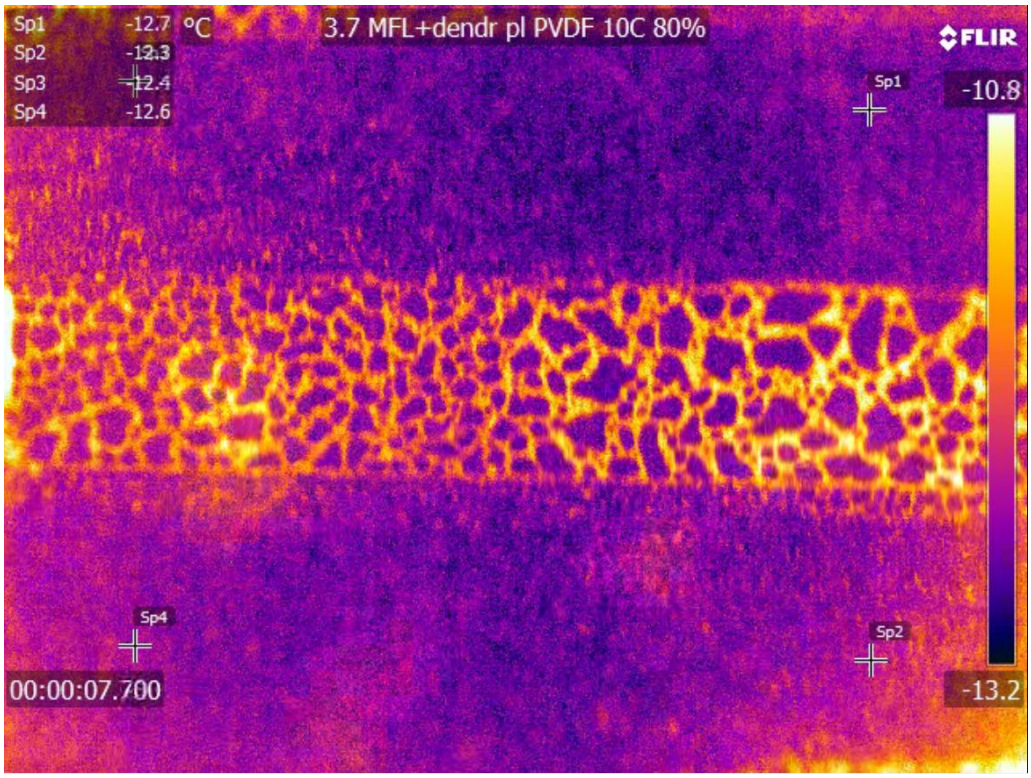

$t = t_n - 0.1s$

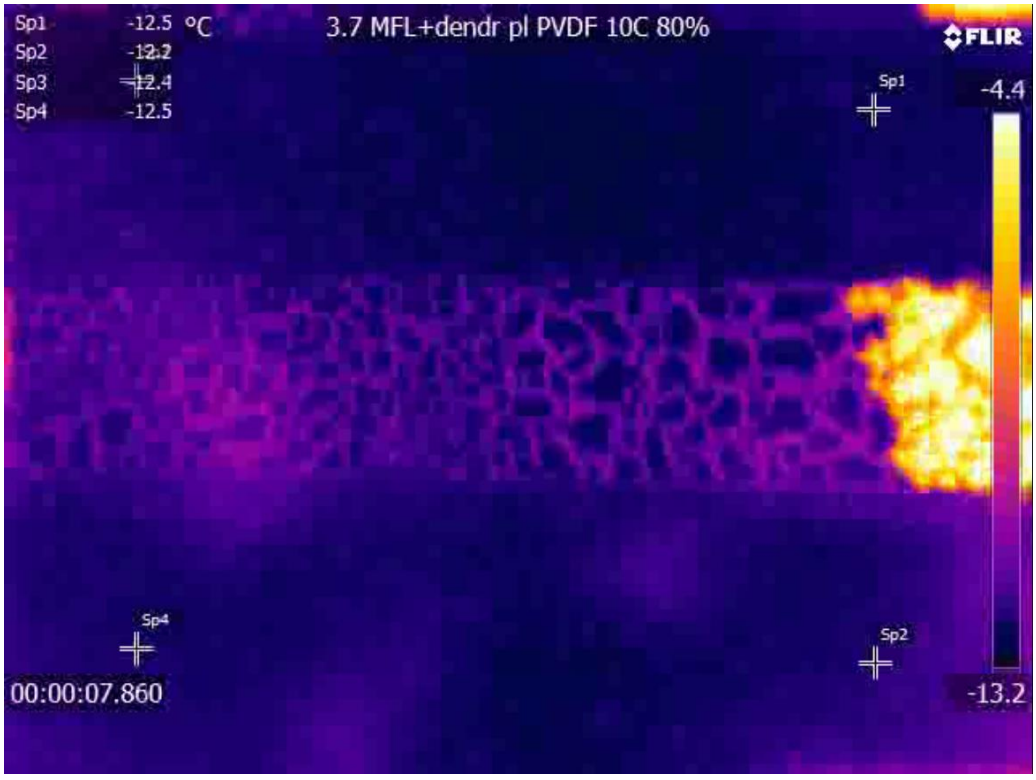

$t = t_n + 0.06s$

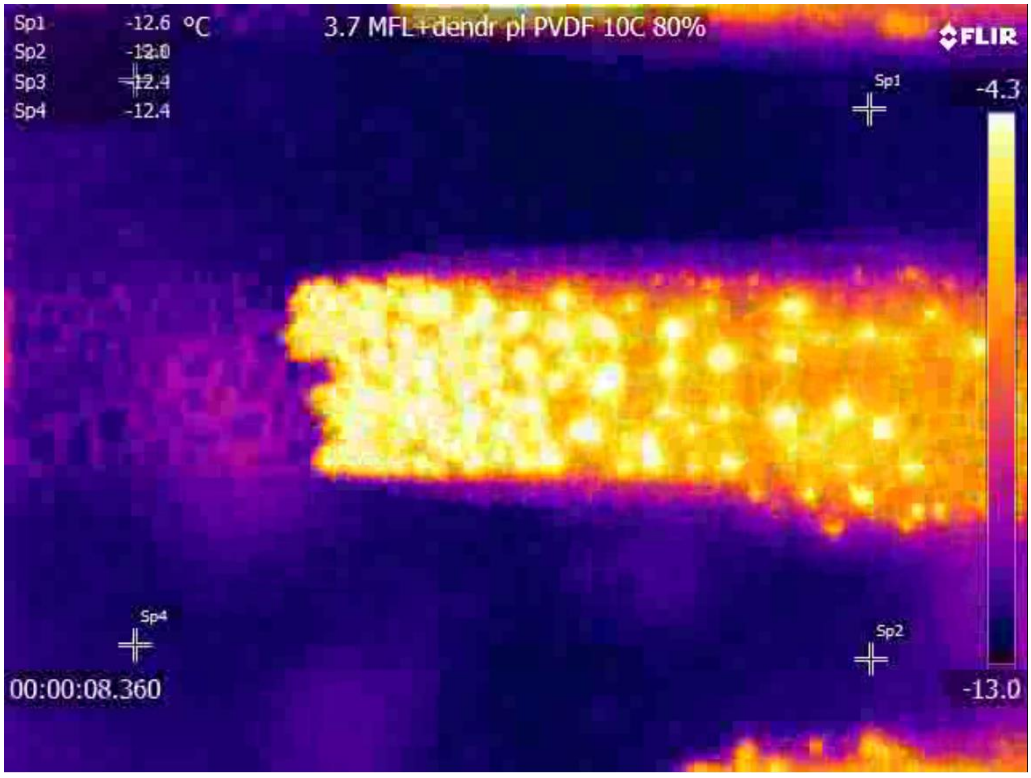

$t = t_n + 0.56s$

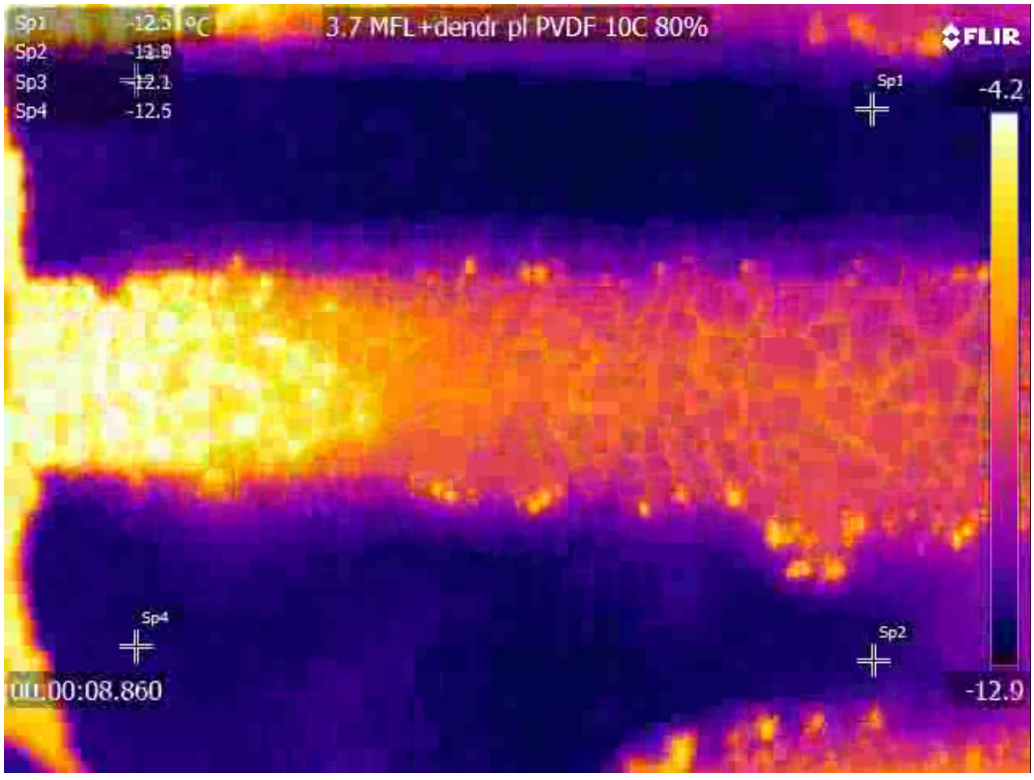

$t = t_n + 1.06s$

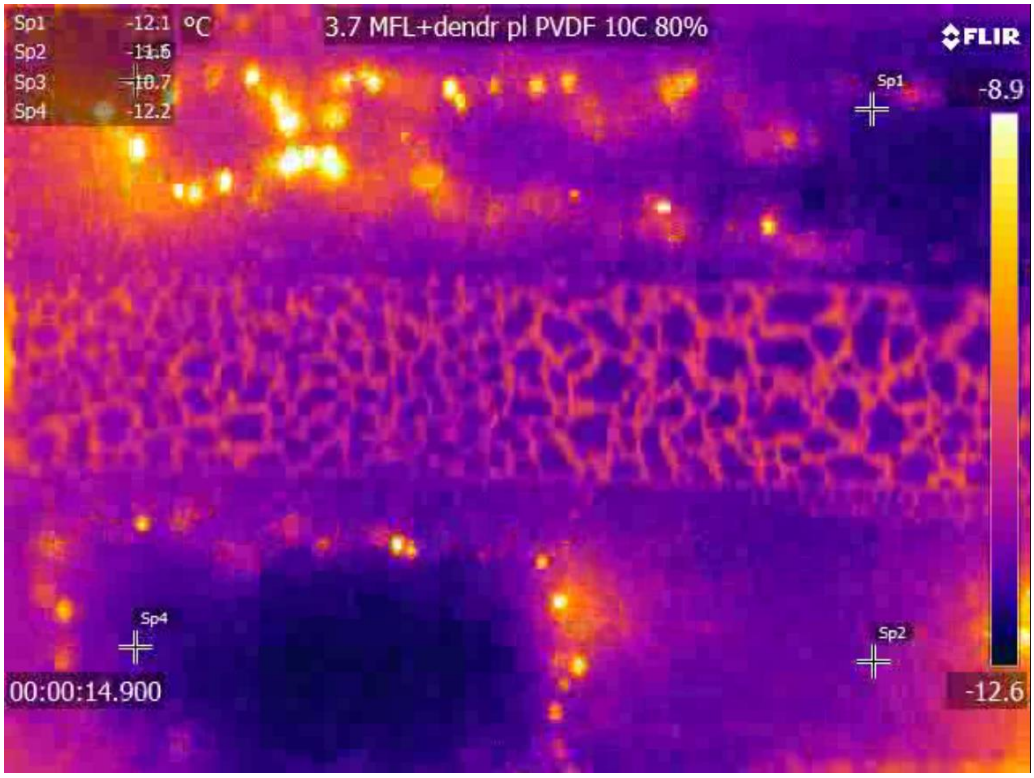

$t = t_n + 7.1s$

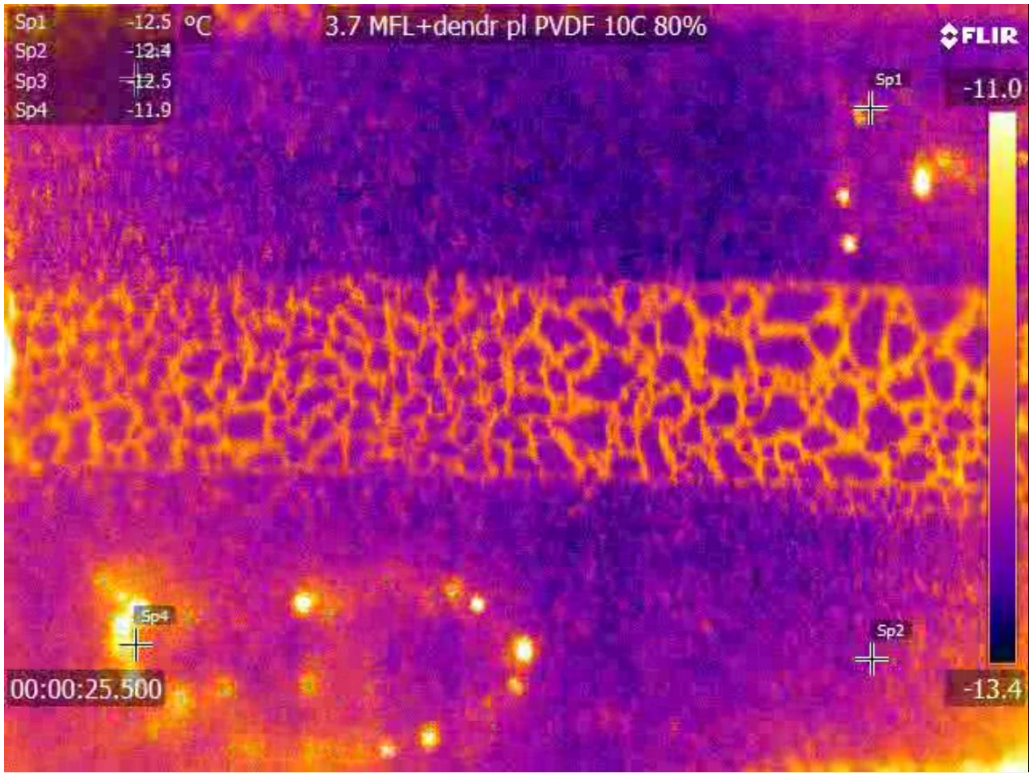

$t = t_n + 17.8s$

I. Front propagation over scratched PVDF

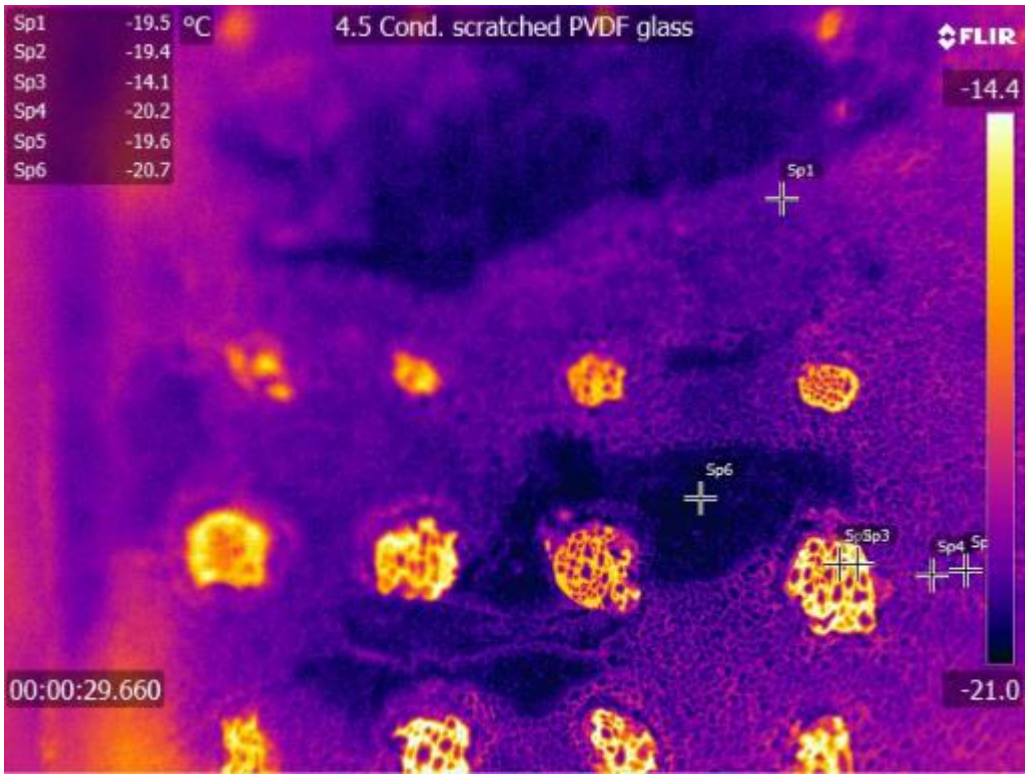

$t = t_n - 0.02s$

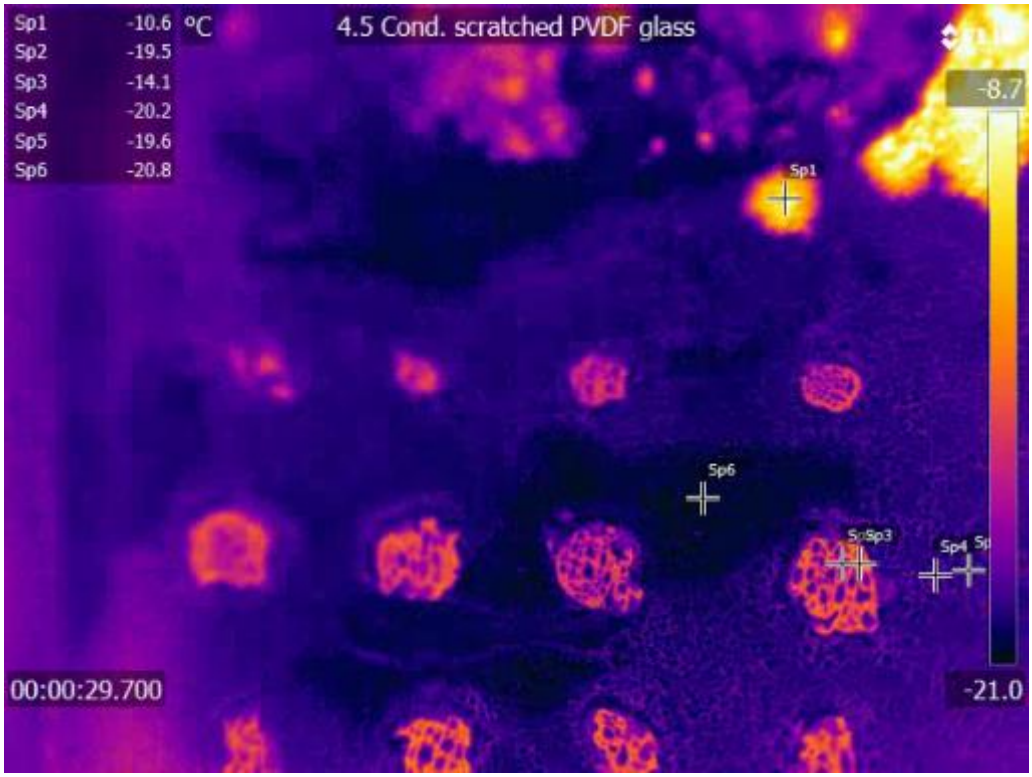

$t = t_n + 0.02s$

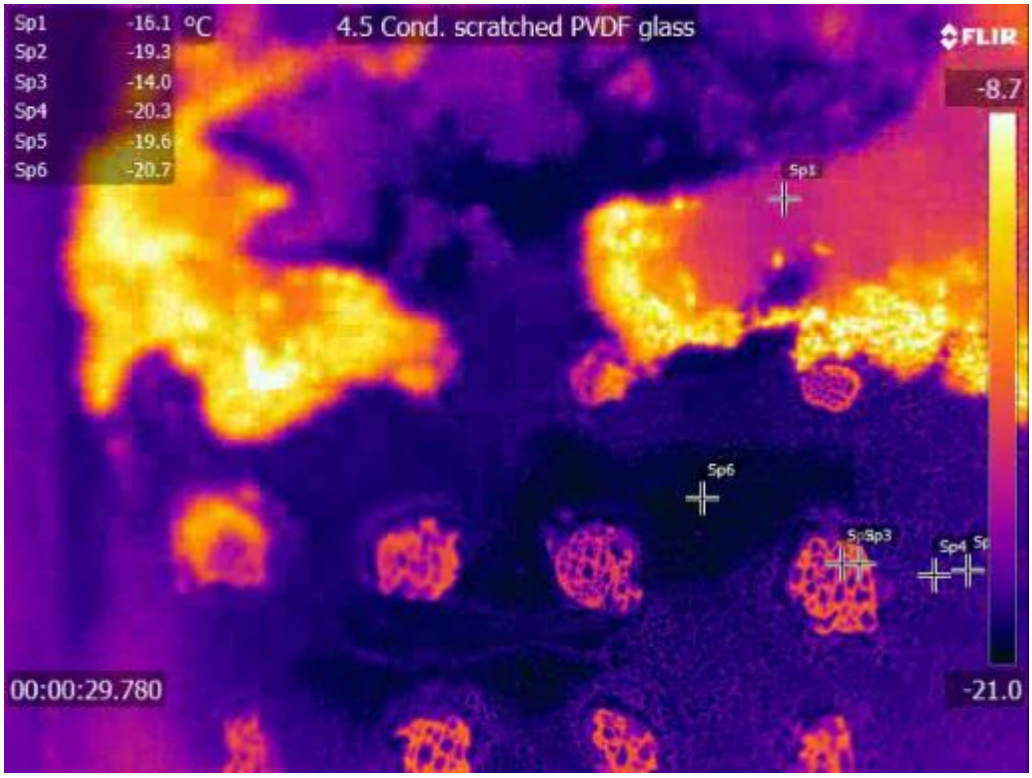

$t = t_n + 0.20s$

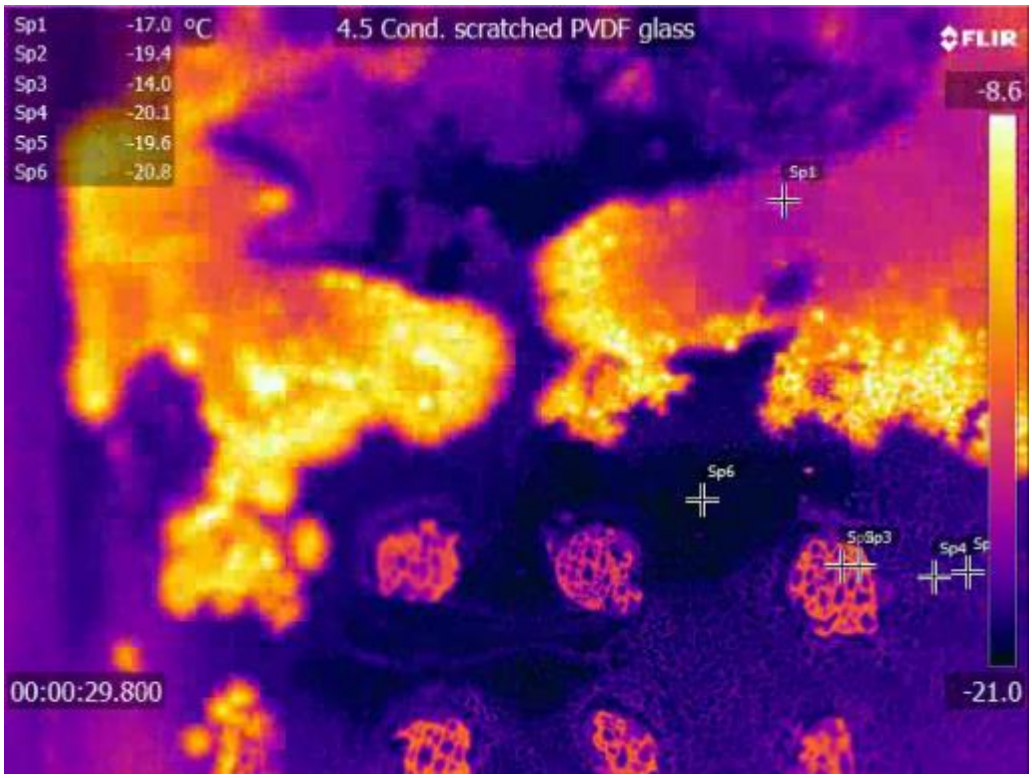

$t = t_n + 0.22s$

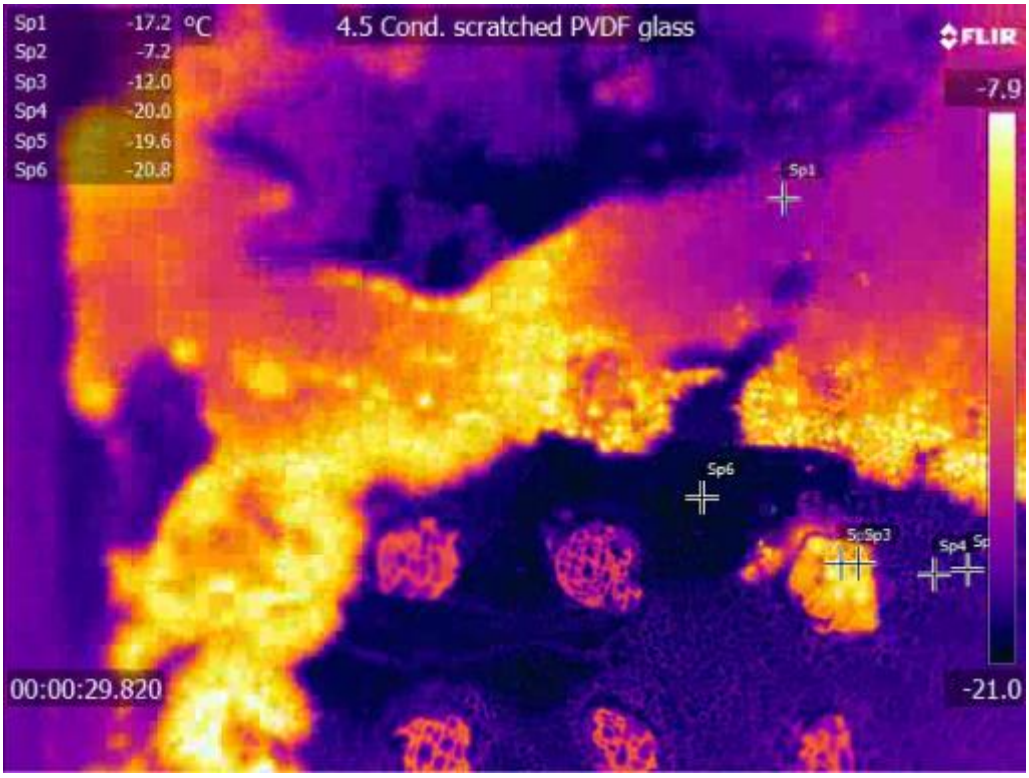

$t = t_n + 0.24s$

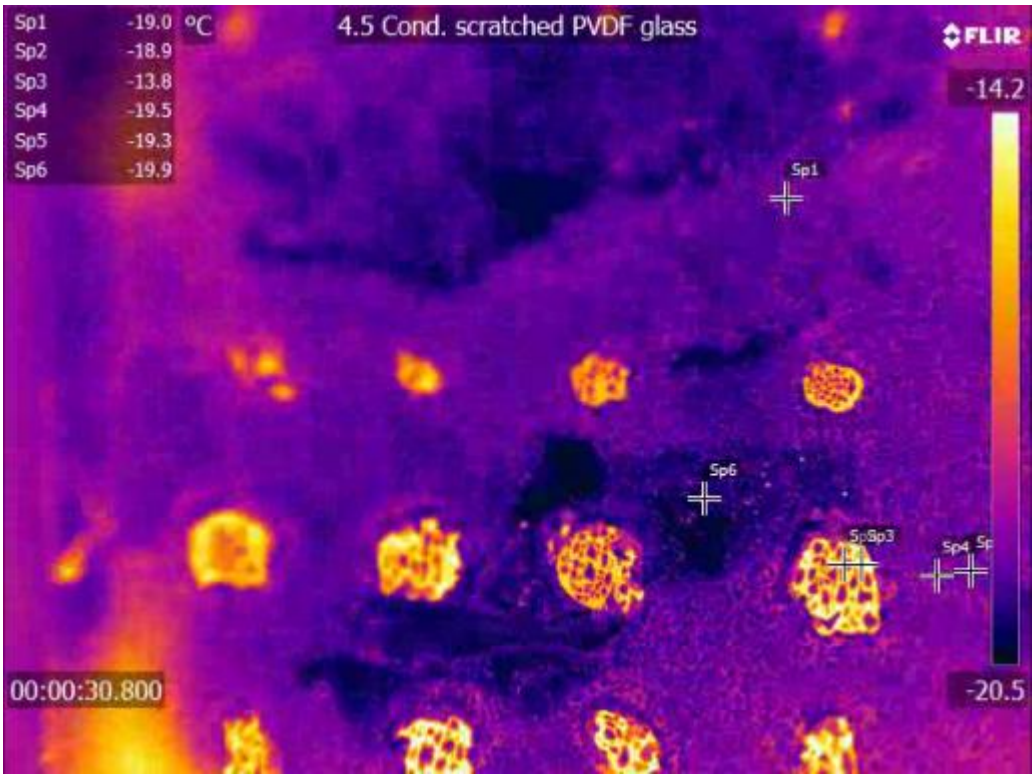

$t = t_n + 1.12s$

J. Measurements coating conductivity

Top-down placement of a glass sample, spincoated with a PVDF thin film.

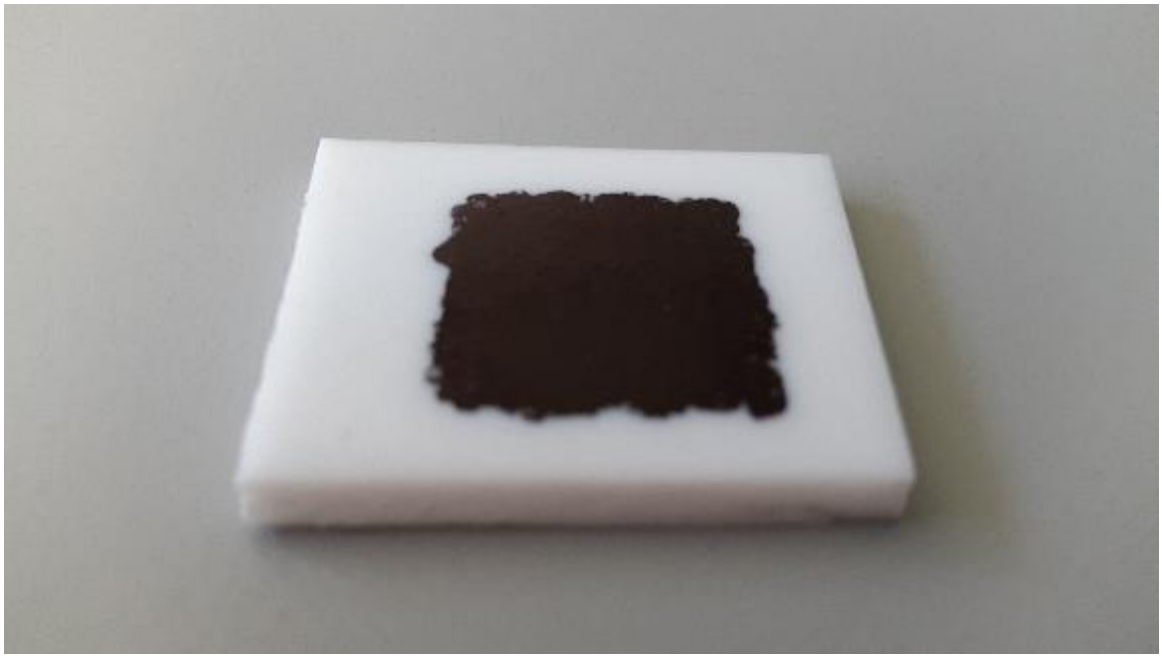

Sample of permanent marker ink on Teflon, made for the testing of conductivity.

K. Alginate islands on PVDF

An alginate (5w%) / water (95w%) was deposited as droplets on a spincoated thin film, prepared by dissolving PVDF (6w%) in DMF (94w%) in an ultrasonic bath. Alginate drops of 1 – 2 mm were deposited on the PVDF thin film after drying with compressed air and cured with a CaCl solution. The samples were placed on the Peltier setup described before in a controlled lab environment with $RH = 60\%$ to 65% and $T_{env} =$

18 – 22℃. Water droplets of diameter $1\ mm$ – $4\ mm$ were deposited next to, in between and on top of the alginate islands. As can be seen in the snapshots below, a droplet marked by Sp3 was caught on top of the crater shaped alginate islands. It remained at a temperature of over $5℃$ above the average droplet temperature, before falling off the alginate island, cooling rapidly and freezing.

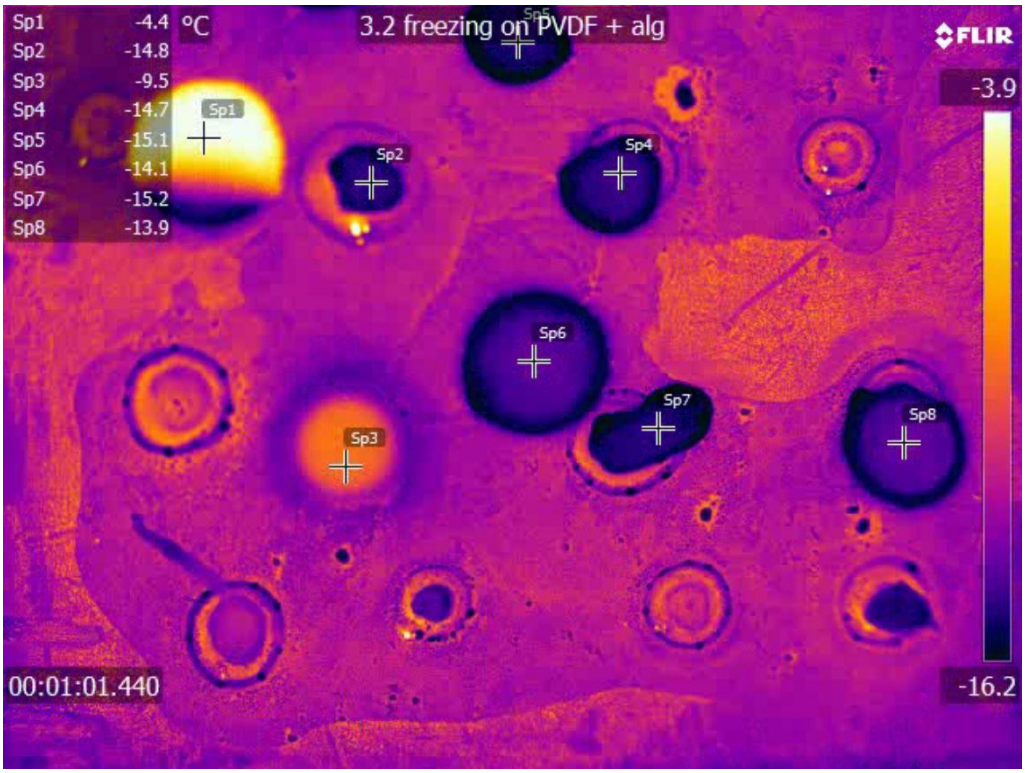

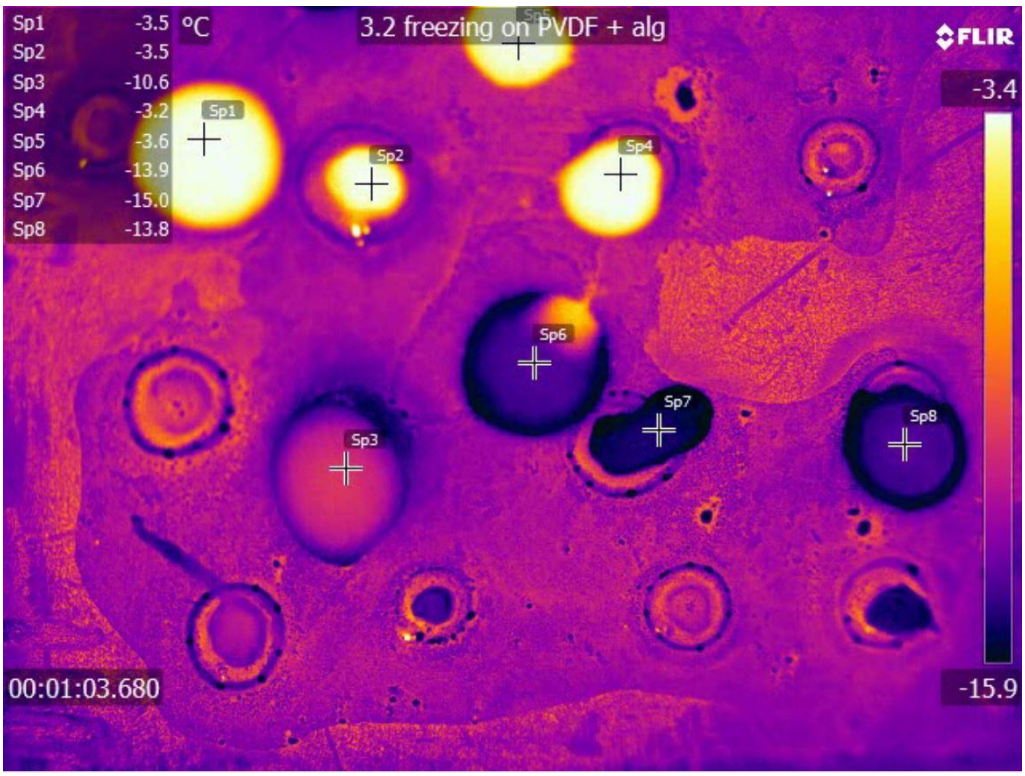

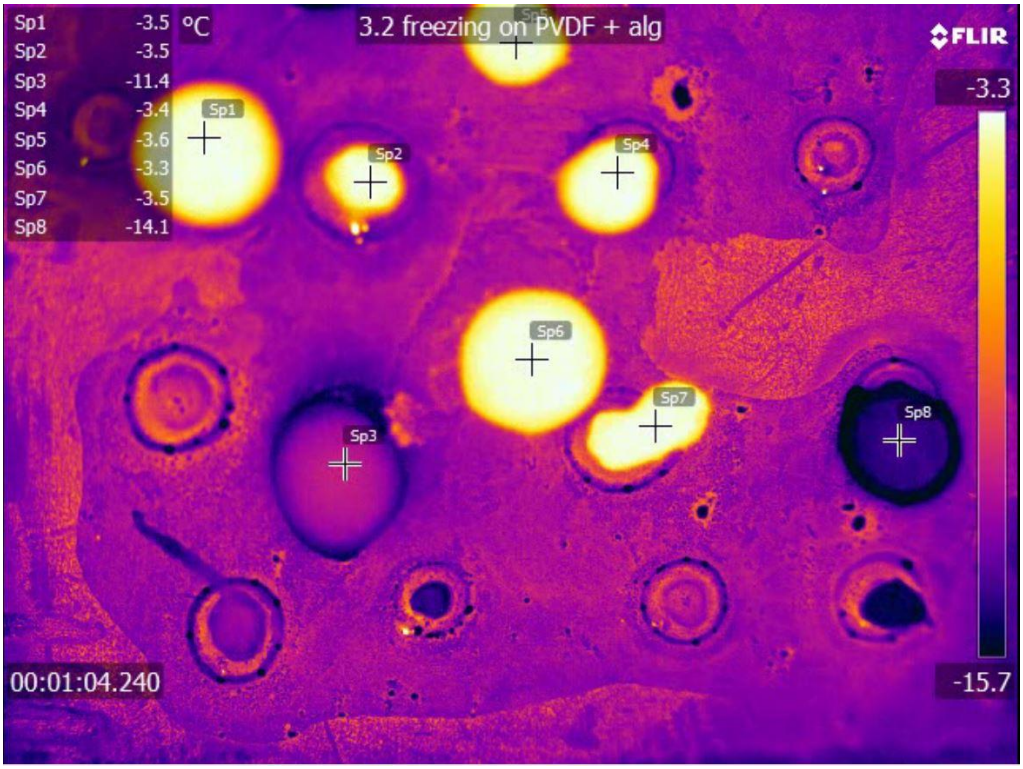
Sp1 -3.5 °C
Sp2 -3.5
Sp3 -11.4
Sp4 -3.4
Sp5 -3.6
Sp6 -3.3
Sp7 -3.5
Sp8 -14.1
3.2 freezing on PVDF + alg
FLIR
-3.3
-15.7
00:01:04.240

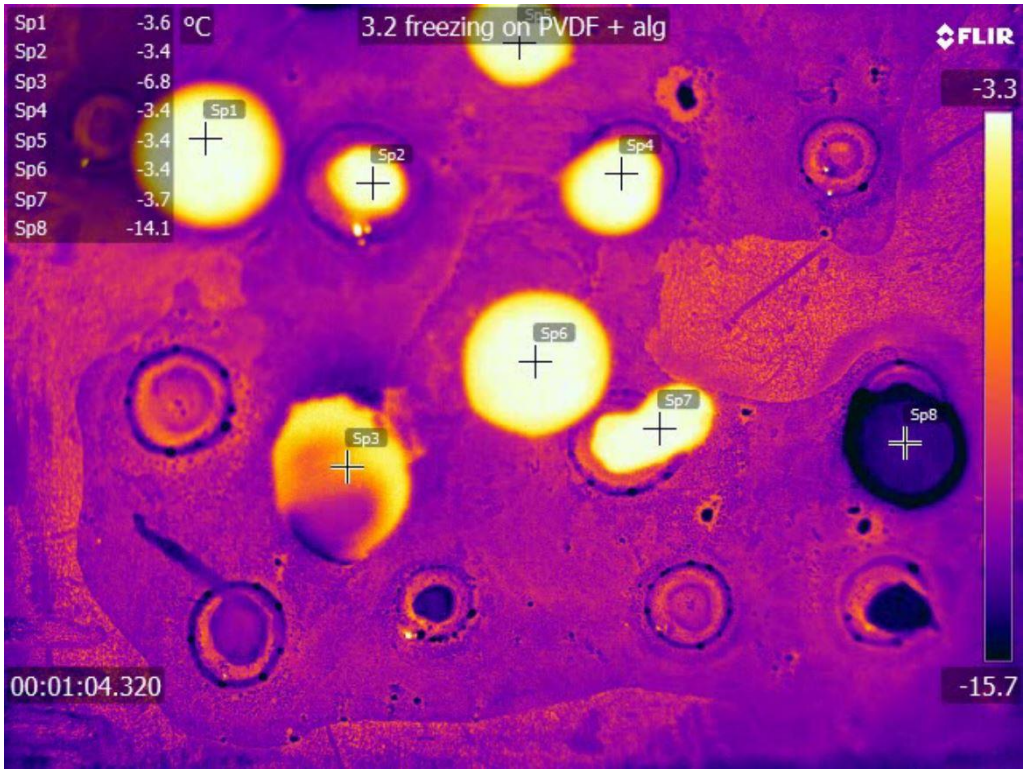
Sp1 -3.6 °C
Sp2 -3.4
Sp3 -6.8
Sp4 -3.4
Sp5 -3.4
Sp6 -3.4
Sp7 -3.7
Sp8 -14.1
3.2 freezing on PVDF + alg
FLIR
-3.3
-15.7
00:01:04.320

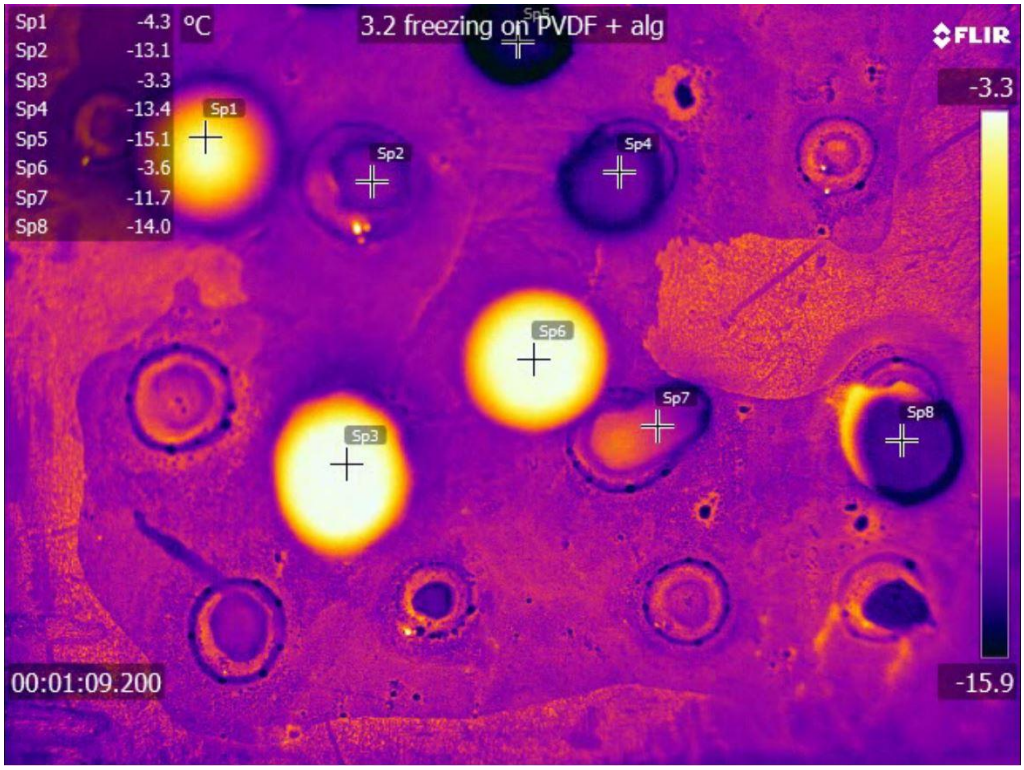

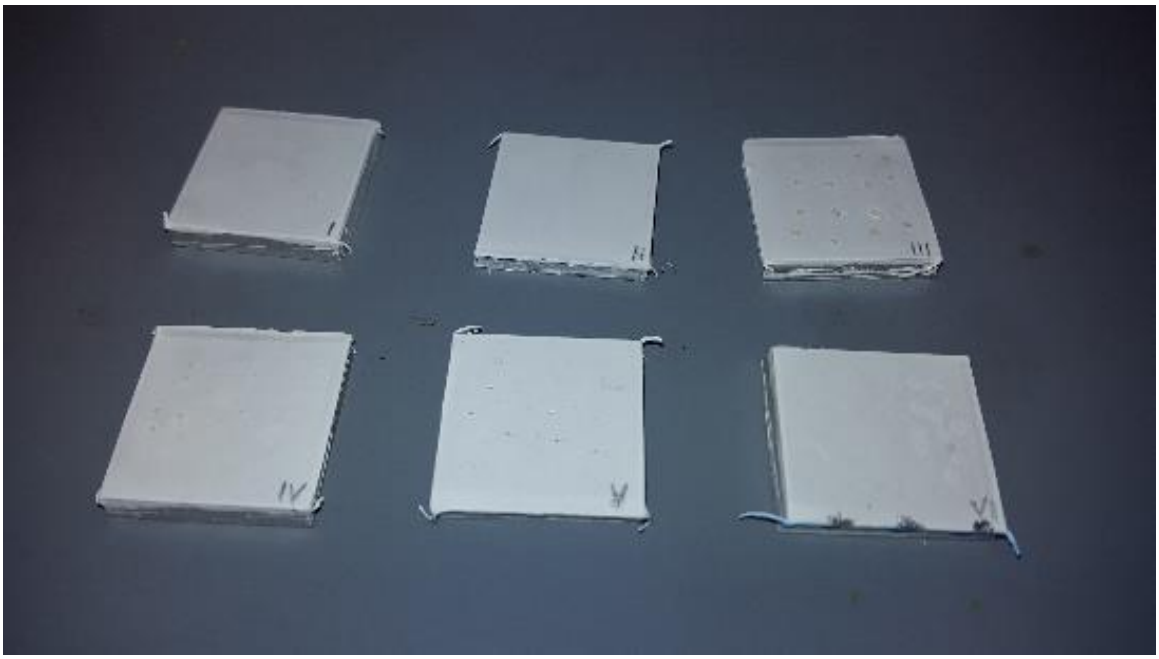

Alginate droplets deposited on spincoated PVDF thin film on glass before it had fully dried, creating streaks around the alginate droplets. A crater shaped microrelief could be found under the cured alginate drop after detachment from the fully dried PVDF film.

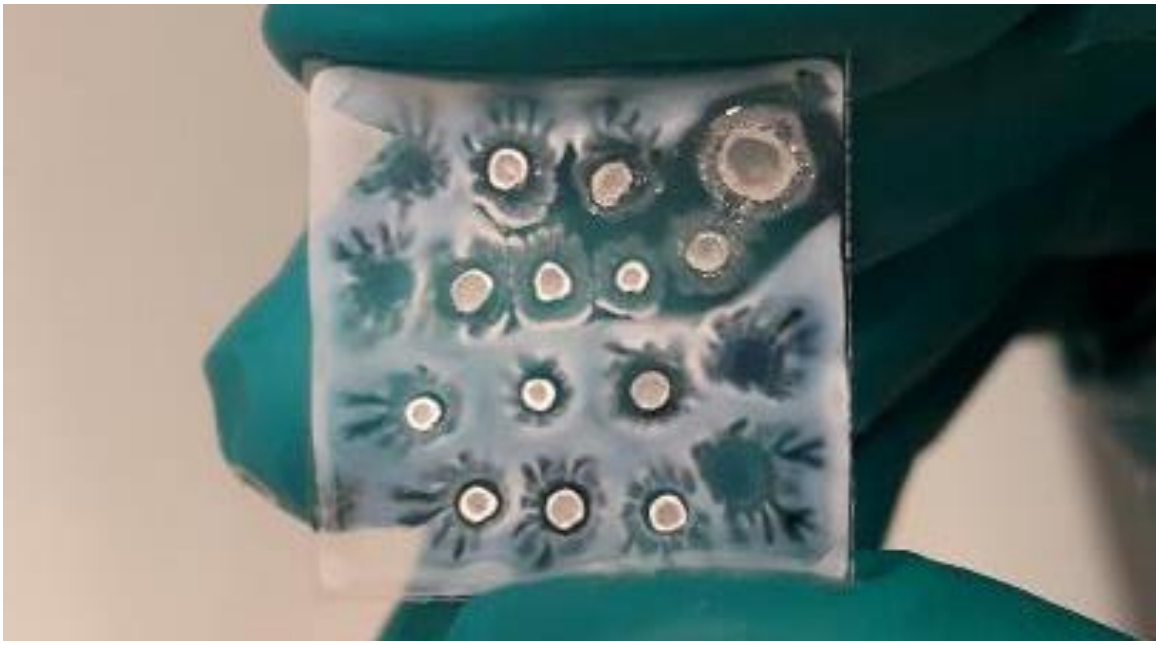

L. Making Surlyn thin film coatings

Pressing Surlyn at $T_{env} = 150°C$, above its melting temperature.

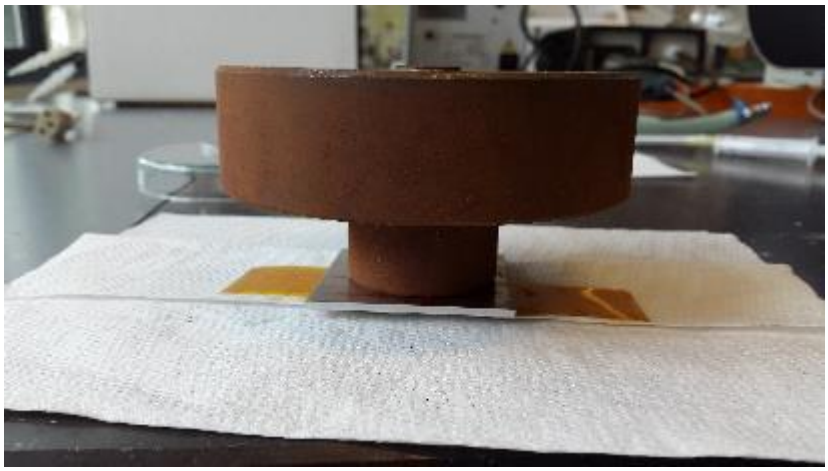

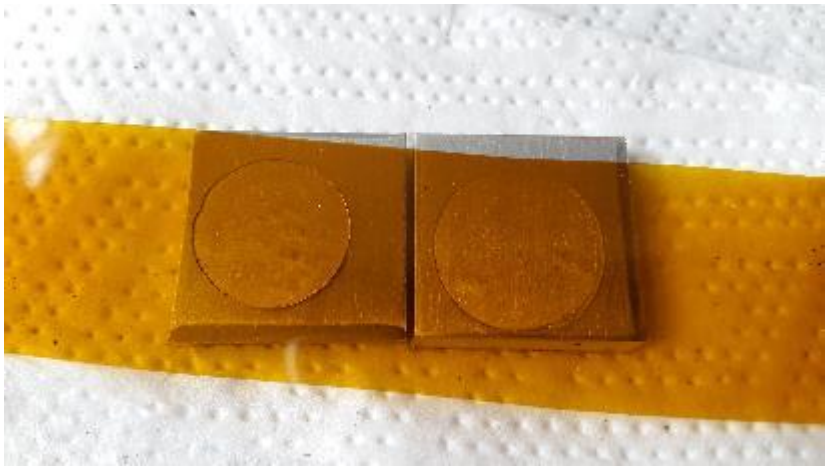

Bibliography

[1] Morawietz, T., Singraber, A., Dellago, C., & Behler, J. (2016). How van der Waals interactions determine the unique properties of water. Proceedings of the National Academy of Sciences, 113(30), 8368-8373.
[2] Antonini, C., Innocenti, M., Horn, T., Marengo, M., & Amirfazli, A. (2011). Understanding the effect of superhydrophobic coatings on energy reduction in anti-icing systems. Cold Regions Science and Technology, 67(1-2), 58-67.
[3] Alizadeh, A., Yamada, M., Li, R., Shang, W., Otta, S., Zhong, S., ... & Vinciquerra, A. J. (2012). Dynamics of ice nucleation on water repellent surfaces. Langmuir, 28(6), 3180-3186.
[4] Kraj, A. G., & Bibeau, E. L. (2006). Impact of mitigation strategies on icing accumulation rate for wind turbines in cold climates. In 2006 Canadian Wind Energy Association Annual Conference, Winnipeg, Manitoba.
[5] Gent, R. W., Dart, N. P., & Cansdale, J. T. (2000). Aircraft icing. Philosophical Transactions of the Royal Society of London A: Mathematical, Physical and Engineering Sciences, 358(1776), 2873-2911.
[6] Mingione, G., & Barocco, M. (1997). Flight in Icing Conditions Summary. French DGAC.
[7] No 1, W. SAFETY ADVISOR. Weather, 88, 2842.
[8] FAA 2006 Anti-icing - Ice protection methods
[9] Sand, W. R., Cooper, W. A., Politovich, M. K., & Veal, D. L. (1984). Icing conditions encountered by a research aircraft. Journal of climate and applied meteorology, 23(10), 1427-1440.
[10] Murphy 2004 (Anti-icing and de-icing equipment, pilot instruction)
[11] Makkonen, L. (2012). Ice adhesion—theory, measurements and countermeasures. Journal of Adhesion Science and Technology, 26(4-5), 413-445.
[12] Zumwalt 1988 .Anti-icing - EIDI Electro-impulsive deicing, principles and test results.
[13] Embry, G. D., Erskine, R. W., Haslim, L. A., Lockyer, R. T., & McDonough, P. T. (1990). Electro-Expulsive Separation System Shipboard Applications. Naval Engineers Journal, 102(5), 55-66.
[14] Stenzel, V., & Rehfeld, N. (2011). Functional coatings (pp. 91-106). Hanover: Vincentz Network.
[15] GKN-Technology 2014. De-icing (current methods, equipment)
[16] Mishchenko, L., Hatton, B., Bahadur, V., Taylor, J. A., Krupenkin, T., & Aizenberg, J. (2010). Design of ice-free nanostructured surfaces based on repulsion of impacting water droplets. ACS nano, 4(12), 7699-7707.
[17] Heydari, G., Thormann, E., Järn, M., Tyrode, E., & Claesson, P. M. (2013). Hydrophobic surfaces: topography effects on wetting by supercooled water and freezing delay. The Journal of Physical Chemistry C, 117(42), 21752-21762.
[18] Li, C., Gao, X., & Li, Z. (2017). Roles of Surface Energy and Temperature in Heterogeneous Ice Nucleation. The Journal of Physical Chemistry C, 121(21), 11552-11559.
[19] Reinhardt, A., & Doye, J. P. (2014). Effects of surface interactions on heterogeneous ice nucleation for a monatomic water model. The Journal of chemical physics, 141(8), 084501.
[20] Schremb, M., Roisman, I. V., & Tropea, C. (2018). Normal impact of supercooled water drops onto a smooth ice surface: experiments and modelling. Journal of Fluid Mechanics, 835, 1087-1107.
[21] Pasieka, J., Nanua, R., Coulombe, S., & Servio, P. (2014). The crystallization of sub-cooled water: Measuring the front velocity and mushy zone composition via thermal imaging. International Journal of Heat and Mass Transfer, 77, 940-945.
[22] Hu, J., Xiao, X. D., Ogletree, D. F., & Salmeron, M. (1995). Imaging the condensation and evaporation of molecularly thin films of water with nanometer resolution. Science, 268(5208), 267-269.
[23] James, M., Darwish, T. A., Ciampi, S., Sylvester, S. O., Zhang, Z., Ng, A., ... & Hanley, T. L. (2011). Nanoscale condensation of water on self-assembled monolayers. Soft Matter, 7(11), 5309-5318.
[24] Park, J., Han, H. S., Kim, Y. C., Ahn, J. P., Ok, M. R., Lee, K. E., ... & Jeon, H. (2015). Direct and accurate measurement of size dependent wetting behaviors for sessile water droplets. Scientific reports, 5, 18150.
[25] Chen, J., Dou, R., Cui, D., Zhang, Q., Zhang, Y., Xu, F., ... & Jiang, L. (2013). Robust prototypical anti-icing coatings with a self-lubricating liquid water layer between ice and substrate. ACS applied materials & interfaces, 5(10), 4026-4030.
[26] Zhang, H., Zhao, Y., Lv, R., & Yang, C. (2016). Freezing of sessile water droplet for various contact angles. International journal of thermal sciences, 101, 59-67.

[27] Bird, J. C., Dhiman, R., Kwon, H. M., & Varanasi, K. K. (2013). Reducing the contact time of a bouncing drop. Nature, 503(7476), 385.
[28] Bharathidasan, T., Kumar, S. V., Bobji, M. S., Chakradhar, R. P. S., & Basu, B. J. (2014). Effect of wettability and surface roughness on ice-adhesion strength of hydrophilic, hydrophobic and superhydrophobic surfaces. Applied Surface Science, 314, 241-250.
[29] He, Z., Xiao, S., Gao, H., He, J., & Zhang, Z. (2017). Multiscale crack initiator promoted super-low ice adhesion surfaces. Soft matter, 13(37), 6562-6568.
[30] Laforte, C., Blackburn, C., & Perron, J. (2015). A review of icephobic coating performances over the last decade (No. 2015-01-2149). SAE Technical Paper.
[31] Carpenter, K., & Bahadur, V. (2015). Saltwater icephobicity: Influence of surface chemistry on saltwater icing. Scientific reports, 5, 17563.
[32] Wang, N., Xiong, D., Lu, Y., Pan, S., Wang, K., Deng, Y., & Shi, Y. (2016). Design and fabrication of the lyophobic slippery surface and its application in anti-icing. The Journal of Physical Chemistry C, 120(20), 11054-11059.
[33] Alizadeh-Birjandi, E., & Kavehpour, H. P. (2017). Plant leaves icephobicity. Journal of Coatings Technology and Research, 14(5), 1061-1067.
[34] Bird, J. C., Dhiman, R., Kwon, H. M., & Varanasi, K. K. (2013). Reducing the contact time of a bouncing drop. Nature, 503(7476), 385.
[35] Sakaue, H., Morita, K., Tanaka, M., & Kimura, S. (2014). Study of Icing Process using Dual-Luminescence Imaging for Aircraft-Icing Prevention. In 52nd Aerospace Sciences Meeting (p. 0929).
[36] Wang, S., Yang, Z., Gong, G., Wang, J., Wu, J., Yang, S., & Jiang, L. (2016). Icephobicity of penguins Spheniscus Humboldti and an artificial replica of penguin feather with air-infused hierarchical rough structures. The Journal of Physical Chemistry C, 120(29), 15923-15929.
[37] Jung, S., Dorrestijn, M., Raps, D., Das, A., Megaridis, C. M., & Poulikakos, D. (2011). Are superhydrophobic surfaces best for icephobicity?. Langmuir, 27(6), 3059-3066.
[38] Yin, L., Xia, Q., Xue, J., Yang, S., Wang, Q., & Chen, Q. (2010). In situ investigation of ice formation on surfaces with representative wettability. Applied Surface Science, 256(22), 6764-6769.
[39] Chen, J., Liu, J., He, M., Li, K., Cui, D., Zhang, Q., ... & Song, Y. (2012). Superhydrophobic surfaces cannot reduce ice adhesion. Applied Physics Letters, 101(11), 111603.
[40] Varanasi, K. K., Deng, T., Smith, J. D., Hsu, M., & Bhate, N. (2010). Frost formation and ice adhesion on superhydrophobic surfaces. Applied Physics Letters, 97(23), 234102.
[41] Cao, L., Jones, A. K., Sikka, V. K., Wu, J., & Gao, D. (2009). Anti-icing superhydrophobic coatings. Langmuir, 25(21), 12444-12448.
[42] Moore, E. B., De La Llave, E., Welke, K., Scherlis, D. A., & Molinero, V. (2010). Freezing, melting and structure of ice in a hydrophilic nanopore. Physical Chemistry Chemical Physics, 12(16), 4124-4134.
[43] Subramanyam, S. B., Rykaczewski, K., & Varanasi, K. K. (2013). Ice adhesion on lubricant-impregnated textured surfaces. Langmuir, 29(44), 13414-13418.
[44] Bengaluru Subramanyam, S., Kondrashov, V., Rühe, J., & Varanasi, K. K. (2016). Low ice adhesion on nano-textured superhydrophobic surfaces under supersaturated conditions. ACS applied materials & interfaces, 8(20), 12583-12587.
[45] Wang, N., Xiong, D., Pan, S., Wang, K., Shi, Y., & Deng, Y. (2017). Robust superhydrophobic coating and the anti-icing properties of its lubricants-infused-composite surface under condensing condition. New Journal of Chemistry, 41(4), 1846-1853.
[46] Wong, T. S., Kang, S. H., Tang, S. K., Smythe, E. J., Hatton, B. D., Grinthal, A., & Aizenberg, J. (2011). Bioinspired self-repairing slippery surfaces with pressure-stable omniphobicity. Nature, 477(7365), 443.
[47] Dong, H., Wang, N., Wang, L., Bai, H., Wu, J., Zheng, Y., ... & Jiang, L. (2012). Bioinspired electrospun knotted microfibers for fog harvesting. ChemPhysChem, 13(5), 1153-1156.
[48] Garrod, R. P., Harris, L. G., Schofield, W. C. E., McGettrick, J., Ward, L. J., Teare, D. O. H., & Badyal, J. P. S. (2007). Mimicking a Stenocara beetle's back for microcondensation using plasmachemical patterned superhydrophobic− superhydrophilic surfaces. Langmuir, 23(2), 689-693.
[49] Ghosh, A., Beaini, S., Zhang, B. J., Ganguly, R., & Megaridis, C. M. (2014). Enhancing dropwise condensation through bioinspired wettability patterning. Langmuir, 30(43), 13103-13115.
[50] White, B., Sarkar, A., & Kietzig, A. M. (2013). Fog-harvesting inspired by the Stenocara beetle—An analysis of drop collection and removal from biomimetic samples with wetting contrast. Applied Surface Science, 284, 826-836.

[51] Zhang, L., Wu, J., Hedhili, M. N., Yang, X., & Wang, P. (2015). Inkjet printing for direct micropatterning of a superhydrophobic surface: toward biomimetic fog harvesting surfaces. Journal of Materials Chemistry A, 3(6), 2844-2852.
[52] Herminghaus, S. (2000). Roughness-induced non-wetting. EPL (Europhysics Letters), 52(2), 165.
[53] Kirillova, A., Ionov, L., Roisman, I. V., & Synytska, A. (2016). Hybrid hairy Janus particles for anti-icing and de-icing surfaces: Synergism of properties and effects. Chemistry of Materials, 28(19), 6995-7005.
[54] Cho, K. L. (2011). Development of superhydrophobic coatings (Doctoral dissertation).
[55] Klyosov, A. A., Philippidis, G. P., James, A. M., & Monovoukas, Y. A. (2000). U.S. Patent No. 6,156,226. Washington, DC: U.S. Patent and Trademark Office.
[56] Fuller, M. P., & Wisniewski, M. (1998). The use of infrared thermal imaging in the study of ice nucleation and freezing of plants1. Journal of Thermal biology, 23(2), 81-89.
[57] Xu, Y., Petrik, N. G., Smith, R. S., Kay, B. D., & Kimmel, G. A. (2016). Growth rate of crystalline ice and the diffusivity of supercooled water from 126 to 262 K. Proceedings of the National Academy of Sciences, 113(52), 14921-14925.
[58] Blake, J., Thompson, D., Raps, D., & Strobl, T. (2015). Simulating the freezing of supercooled water droplets impacting a cooled substrate. AIAA Journal, 53(7), 1725-1739.
[59] Guadarrama-Cetina, J., Mongruel, A., González-Viñas, W., & Beysens, D. (2013). Percolation-induced frost formation. EPL (Europhysics Letters), 101(1), 16009.
[60] Wang, Z., Cong, Y., & Zhang, B. (2016). Liquid crystal compound anti-ice surface. Liquid Crystals, 43(2), 241-248.
[61] Schremb, M., Roisman, I. V., & Tropea, C. (2018). Normal impact of supercooled water drops onto a smooth ice surface: experiments and modelling. Journal of Fluid Mechanics, 835, 1087-1107.
[62] Van Der Kooij, H. M., Fokkink, R., Van Der Gucht, J., & Sprakel, J. (2016). Quantitative imaging of heterogeneous dynamics in drying and aging paints. Scientific reports, 6, 34383.
[63] Wang, Y., Xue, J., Wang, Q., Chen, Q., & Ding, J. (2013). Verification of icephobic/anti-icing properties of a superhydrophobic surface. ACS applied materials & interfaces, 5(8), 3370-3381.
[64] Whitacre, D. L. (2013). Development of an icing research wind tunnel at the University of Toledo. The University of Toledo.
[65] Horstmann, K. H., & Meyer, J. B. (2004). Flight Testing of Anti-Icing and Anti-Contamination Systems for HLFC Surfaces.
[66] Fletcher, N. H. (1970). Water as a Solid.(Book Reviews: The Chemical Physics of Ice). Science, 169, 756.
[67] Zhao, H., & Beysens, D. (1995). From droplet growth to film growth on a heterogeneous surface: condensation associated with a wettability gradient. Langmuir, 11(2), 627-634.
[68] Rabal, H. J., & Braga Jr, R. A. (Eds.). (2008). Dynamic laser speckle and applications. CRC Press.
[69] Schremb, M., & Tropea, C. (2016). Solidification of supercooled water in the vicinity of a solid wall. Physical Review E, 94(5), 052804.
[70] Enríquez, O. R., Marín, Á. G., Winkels, K. G., & Snoeijer, J. H. (2012). Freezing singularities in water drops. Physics of fluids, 24(9), 091102.
[71] Pach, E., Rodríguez, L., & Verdaguer, A. (2017). Substrate Dependence of the Freezing Dynamics of Supercooled Water Films: A High-Speed Optical Microscope Study. The Journal of Physical Chemistry B.
[72] Kulinich, S. A., & Farzaneh, M. (2009). Ice adhesion on super-hydrophobic surfaces. Applied Surface Science, 255(18), 8153-8157.
[73] Yang, S., Xia, Q., Zhu, L., Xue, J., Wang, Q., & Chen, Q. M. (2011). Research on the icephobic properties of fluoropolymer-based materials. Applied Surface Science, 257(11), 4956-4962.
[74] Mccafferty, D. J., Gilbert, C., Thierry, A. M., Currie, J., Le Maho, Y., & Ancel, A. (2013). Emperor penguin body surfaces cool below air temperature. Biology letters, 9(3), 20121192.
[75] Kiani, H., & Sun, D. W. (2011). Water crystallization and its importance to freezing of foods: A review. Trends in Food Science & Technology, 22(8), 407-426.
[76] Bird, L. (1988). U.S. Patent No. 4,732,351. Washington, DC: U.S. Patent and Trademark Office.
[77] Embry, G. D., Erskine, R. W., Haslim, L. A., Lockyer, R. T., & McDonough, P. T. (1990). Electro-Expulsive Separation System Shipboard Applications. Naval Engineers Journal, 102(5), 55-66.
[78] Moláček, J., & Bush, J. W. (2013). Drops walking on a vibrating bath: towards a hydrodynamic pilot-wave theory. Journal of Fluid Mechanics, 727, 612-647.
[79] Walker, J. (1978). Drops of liquid can be made to float on liquid-what enables them to do so. Scientific American, 238(6), 151.

[80] Couder, Y., Protiere, S., Fort, E., & Boudaoud, A. (2005). Dynamical phenomena: Walking and orbiting droplets. Nature, 437(7056), 208.
[81] Gunn, R., & Kinzer, G. D. (1949). The terminal velocity of fall for water droplets in stagnant air. Journal of Meteorology, 6(4), 243-248.
[82] Wang, Y., Xue, J., Wang, Q., Chen, Q., & Ding, J. (2013). Verification of icephobic/anti-icing properties of a superhydrophobic surface. ACS applied materials & interfaces, 5(8), 3370-3381.
[83] Bracco, G., & Holst, B. (Eds.). (2013). Surface science techniques. Springer Science & Business Media.
[84] Chia, H. N., & Wu, B. M. (2015). Recent advances in 3D printing of biomaterials. Journal of biological engineering, 9(1), 4.
[85] Guo, P., Zheng, Y., Wen, M., Song, C., Lin, Y., & Jiang, L. (2012). Icephobic/Anti-Icing Properties of Micro/Nanostructured Surfaces. Advanced materials, 24(19), 2642-2648.
[86] Wang, Z. J., Kwon, D. J., DeVries, K. L., & Park, J. M. (2015). Frost formation and anti-icing performance of a hydrophobic coating on aluminum. Experimental Thermal and Fluid Science, 60, 132-137.